Subduction Zone Blues:

Laboratory and Field Constraints on the Rheology and Deformation Mechanisms of Mafic Blueschist at the Subduction Interface

Jason Ott

A dissertation
submitted in partial fulfillment of the
requirements for the degree of

Doctor of Philosophy

University of Washington
2025

Reading Committee:
Cailey Condit, Chair
Rachel Bernard
J Michael Brown

Program Authorized to Offer Degree:
Department of Earth and Space Sciences

University of Washington

Abstract

Subduction Zone Blues:
Laboratory and Field Constraints on the Rheology and Deformation Mechanisms of Mafic Blueschist at the Subduction Interface

Jason Ott

Chair of the Supervisory Committee:
Cailey Condit
Department of Earth and Space Sciences

Subduction zones are key drivers of plate tectonics, facilitating crustal recycling and deformation. The associated geological hazards of these convergent margins, including megathrust earthquakes and tsunamis, pose significant risks to society. Although these hazards are generated by frictional, seismic slip along the shallow subduction interface, aseismic, ductile deformation plays a critical role by modulating the strength of the subducting slab and transferring stress up-dip to load the seismogenic zone. During subduction, progressive metamorphic transformations of mid-ocean ridge basalt to blueschist and, ultimately, to eclogite alters the chemical and mechanical properties of the subducting crust through changes in its mineralogy, volatile content, density, and rheological strength. Field observations and limited experimental work have offered some insights into the evolution of subducting oceanic crust—

such as a strength hierarchy estimating blueschist to be weaker than both gabbro (basalt) and eclogite—but a substantial knowledge gap persists.

This thesis addresses this knowledge gap by investigating key questions regarding subduction zone dynamics including: (1) Does blueschist generate an observable seismic signal that can improve seismic imaging of blueschist along the subduction interface? (2) What mechanism(s) accommodates blueschist deformation along the subduction interface down-dip of the seismogenic zone and what are the implications for the seismic-aseismic transition? (3) How do chemical and mechanical changes at the blueschist-eclogite transition influence interface subduction zone dynamics during the subduction and exhumation of HP/LT lithologies?

Electron backscatter diffraction (EBSD)-based petrofabric analysis was applied to model the seismic anisotropy generated by a suite of mafic blueschists exhumed from a range of peak P-T conditions relevant to the ductilely deforming interface in active subduction zones. The blueschists displayed a broad range of *P*-wave anisotropies (AVp) up to 20%, correlating positively with the abundance and deformation-produced crystallographic preferred orientation (CPO) of the sodic amphibole mineral, glaucophane. Modeled AVp magnitudes were commonly ~10%, suggesting a common blueschist seismic anisotropy signal with potential to improve mapping of the extent and deformation of blueschists along the subduction interface.

To investigate the underlying deformation that generates observed seismic anisotropies, EBSD techniques—including a novel technique coupling weighted Burgers vector and misorientation analyses—were applied to glaucophane in a lawsonite blueschist from the Catalina Schist that was exhumed from P-T conditions down-dip of the seismogenic zone. The results of this investigation reveal deformation of blueschists at these conditions to be primarily accommodated by the dislocation creep mechanism. A suite of deformation experiments were

performed on glaucophane aggregates to derive a constitutive, power-law relationship (flow law) for dislocation creep in glaucophane and, by extension, blueschist. Extrapolation of flow laws for glaucophane dislocation creep and related subduction lithology flow laws to natural conditions predict deformation by dislocation creep in the subducting slab initiates at ~350°C, evolving to grain-size-sensitive mechanisms with increasing temperatures and pore fluid pressures or finer grain sizes.

Detailed microstructural and petrological investigation were conducted on an exhumed blueschist-eclogite transition on Vroulidia Beach, Sifnos Island, Greece to investigate the complex interplay between deformation, metamorphism, and aqueous fluids in during the subduction and exhumation of blueschists and eclogites. This investigation demonstrates that fluid-deformation feedbacks promote zones of weakness that further localize deformation and fluid flow to enhance retrogression in such zones during exhumation. Together, these investigations advance our understanding of deformation and metamorphic processes in blueschists, eclogites, and at the blueschist-eclogite transition and subduction zone dynamics.

Table of Contents

Author Contributions

This Ph.D. dissertation was written in full by Jason Ott under the advisement of Cailey Condit, and all analyses and interpretations herein were completed by Ott with the noted contributions from co-authors listed below:

Chapter 1: Written in full by Jason Ott, with edits from Cailey Condit

Chapter 2: This chapter was published in the *Journal of Geophysical Research: Solid Earth* with co-authors Cailey Condit, Vera Schulte-Pelkum, Rachel Bernard, and Matěj Peč. The project was conceived and the methodology designed by Jason Ott in collaboration with Cailey Condit. Data collection and analyses were undertaken by Jason Ott. Rachel Bernard assisted Jason Ott through helpful discussions regarding EBSD collection and indexing methods, and Vera Schulte-Pelkum assisted with conceptual discussions regarding the application of petrofabric-based seismic anisotropy models to receiver function analysis. Sarah Brownlee (see Chapter 2 acknowledgements) assisted with the contribution of her base script for implementation of anisotropy symmetry decomposition analysis in the MTEX toolbox for Matlab. With the exception of these contributions, all data analysis and interpretations, and all writing, figure preparation, and editing were completed by Jason Ott with constructive feedback on the analysis, and edits to the text and figures provided by the co-authors.

Chapter 3: This chapter was published in *Geology* with co-authors Cailey Condit, Matěj Peč, and Baptiste Journaux. This project was conceived by Jason Ott in collaboration with Cailey Condit, and the methodology and analyses were designed and implemented by Jason Ott—including the development of novel scripts to implement weighted Burgers vector and mother-daughter inheritance analysis of EBSD-data into MTEX. Thermodynamic equilibrium modeling in Perple_X was conducted by Jason Ott with technical advice from Cailey Condit. Other than these noted exceptions, all data collection, analyses, and interpretations were conducted by Jason Ott. Manuscript and figure preparation and editing were completed by Jason Ott with constructive feedback on the analysis and interpretations, and edits to the text and figures from the co-authors.

Chapter 4: This chapter is in review at *Geophysical Research Letters* with co-authors Cailey Condit and Matěj Peč. This project was conceived by Cailey Condit and Matěj Peč, and the experimental methodology were designed by them as outlined in the grant proposal funded by the National Science Foundation (EAR-2022154 to Condit and EAR-2022928 to Peč). Matěj Peč provided training on the Grigg-type deformation apparatus hosted at the Rock Deformation Laboratory at MIT and the newRig software for analysis of mechanical data collected from the experiments. The EBSD-methodology and microstructural analyses were designed and implemented by Jason Ott. EPMA data were collected by the staff of the microprobe laboratory at MIT and analyzed by Jason Ott. Andrew Cross provided EBSD-indexing assistance on one sample (see Chapter 4 acknowledgements). With the exception of these contributions, all data collection, analyses, and interpretations are by Jason Ott, with constructive feedback provided by the co-authors. Text and figure preparation and editing were completed by Jason Ott with edits provided by the co-authors.

Chapter 5: This chapter is in preparation for *Geochemistry, Geophysics, Geosystems* with co-authors Cailey Condit, Jewel Wass de Czege, and Eirini Poulaki. This project with conceived by Jason Ott in collaboration with Cailey Condit. Field samples and notes were collected by Cailey Condit and Eirini Poulaki. XRF bulk sample compositions were determined on subsamples prepared by Jason Ott and sent to the X-ray Laboratory at Franklin and Marshall College for major- and trace-element analyses. Joel Desormeau provided training and technical assistance on the electron microprobe at University of Nevada, Reno, and Jason Ott collected all EMPA data—which were then compiled and normalized to laboratory standards by Joel Desormeau. EMPA analyses were conducted by Jason Ott and undergraduate researcher Jewel Wass de Czege and classical thermobarometry on samples conducted by Jewel Wass de Czege under the mentorship of Jason Ott. Thermodynamic phase equilibrium models in Perple_X were constructed by Jason Ott with constructive criticism from Cailey Condit and technical assistance from Cailey Condit, Peter Lindquist, and Gabe Epstein. Discussions with Eirini Poulaki provided context on the geologic setting of the Cyclades Islands. With these noted exceptions, all data acquisition and analyses were conducted by Jason Ott. All interpretations, writing, figure preparation, and editing were completed by Jason Ott with constructive criticism and edits from the co-authors.

Acknowledgements

This PhD dissertation is the capstone of eleven and a half years of work, through which I have learned and struggled, overcome many obstacles, and grown as a person as well as a scientist. This is a path I did not see myself taking at the onset of my undergraduate studies, an experience I cannot imagine having missed now that I near its completion, and a journey that I never would have completed without the support, guidance, friendship, and love of so many I know and have met along the way. Below is an extensive, but I fear incomplete, list of the many people who have supported me along the way.

First, I would like to thank my advisor, Cailey B. Condit, who has been my mentor, a brilliant collaborator, and a supportive colleague throughout this project. Over the last six years, Cailey has continually inspired me to grow as a scientist and as a human being, and challenged me to think deeply about data to find compelling stories to tell about the Earth. I am honored to have been Cailey's student, and look forward to our ongoing collaborations.

I would also like to thank all of my committee members: J. Michael Brown, Rachel Bernard, Harold J Tobin, George W. Bergantz, and William Wilcock. I deeply appreciate the time, expertise, and critical feedback you have shared that have improved my ability to do meaningful science and present it effectively.

Additionally, while not on my committee, I would like to thank Matěj Peč, who has been instrumental to my success through his mentorship in experimental rock physics, and a close collaborator throughout my PhD work.

Thank you to all the faculty at the University of Washington Department of Earth and Space Sciences who have contributed to my development of the skills I needed to work, think, write, and present as a scientist during my undergraduate studies and my PhD training, including—but not limited to—Baptiste Journaux, Darrel Cowan, John Stone, Katharine Huntington, Alison Duval, Juliet Crider, Kenneth Creager, Fang-Zhen Teng, Gerard Roe, and David Schmidt.

I am indebted to all the past and present members of the Structural Petrology of the Lithosphere group. It has been an inspiration to share ideals with, learn from, and grow as scientists with you all during my time as a graduate student. I am especially grateful for the mentorship of the postdoctoral researchers who have been a part of the lab, and have learned so much about being a good mentor from the undergraduates I have worked with in the group. Thank you to all the graduate students in the Department of Earth and Space Sciences—the importance of the community within our department, especially during the COVID pandemic, can never be overstated.

I want to thank my family, especially Joyce Ott, my mother, who has encouraged me to follow my dreams all through my life, and to always strive to reach my full potential, despite many missteps along the way.

Most importantly, I would never have found the courage to even start down this path without my supportive partner of more than twenty years (and my wife for the last 2 ½ of them), Jamie Ott. Jamie believed in me and encouraged to start on this academic journey, was there to celebrate with me in the best of times, and helped strengthen my resolve during the most challenging. Your friendship, support, and love are at the core of who I am and who I strive to become.

Funding for this work were provided by the National Science Foundation (EAR-2022154 to Condit, EAR-2022928 to Peč, CAREER grant EAR-2338181 to Condit), the Geological Society of America Graduate Student Research Grant program to Ott, and research awards at the University of Washington through the Anthony Qamar Endowed Memorial Fund to Ott. Part of this work was conducted at the Washington Nanofabrication Facility / Molecular Analysis Facility, a National Nanotechnology Coordinated Infrastructure (NNCI) site at the University of Washington with partial support from the National Science Foundation via awards NNCI-1542101 and NNCI-2025489. I am grateful for the technical expertise of Scott Braswell of the MAF for their technical assistance with the electron microscopy instruments. Microprobe data were collected at the Mackay School of Earth Science and Engineering Microbeam Laboratory at University of Nevada, Reno, with the invaluable assistance of Joel DesOrmeau. We thank Stanley Mertzman at the X-ray Laboratory of Franklin and Marshall College for assistance with bulk sample analyses.

Chapter 1: Introduction

Subduction is a key engine of global plate motion and a major source of geological hazards, responsible for generating megathrust earthquakes and tsunamis with catastrophic impacts. For instance, the 2011 Mw 9.1 megathrust earthquake at the Tohoku-Oki subduction zone—with an estimated recurrence interval of ~500 years (Shibazaki, 2023)—caused the loss of ~20,000 lives and destroyed nearly 122,000 homes (Uchida & Bürgmann, 2021). While megathrust earthquakes are the result of frictional, seismic slip along the subduction interface, aseismic deformation down dip of this zone also plays a critical role in shaping these hazards by controlling the strength of the subducting slab and transferring stress up-dip to load the seismogenic zone (Scholz, 1988; Wech & Creager, 2011). This aseismic slip, which is viscous, is typically accommodated by ductile mechanisms. Therefore, characterizing the flow behavior (rheology) of materials along the subduction interface is essential for understanding the mechanical properties of subducting oceanic crust (Behr et al., 2018) and associated subduction zone hazards. The transition from brittle seismic to viscous, aseismic deformation at the base of the seismogenic zone is broadly coincident with the onset of blueschist-facies metamorphism in most subduction zones (Keken et al., 2018; Peacock, 2004). With deep subduction of mafic oceanic crust, the transition from blueschist to eclogite at sub-arc depths (~80 km) is associated with dehydration reactions that release mineral-bound water that facilitates flux-melting in the overlying mantle wedge and arc volcanism at the surface (Hyndman et al., 1997; Peacock, 1993; Stöckhert, 2002). Furthermore, serpentinization from fluid infiltration into the mantle wedge and the strength contrast between blueschist and eclogite likely play a role in coupling behavior between the subducting slab and overriding mantle wedge and consequently, mantle wedge flow (Arcay et al., 2005; Long & Wirth, 2013; Stünitz et al., 2020). These and other studies indicate that blueschist plays a key role in the processes that govern subduction zone behavior and associated hazards. However, our understanding of the extent of blueschist along the subduction interface and its rheological properties are largely unconstrained.

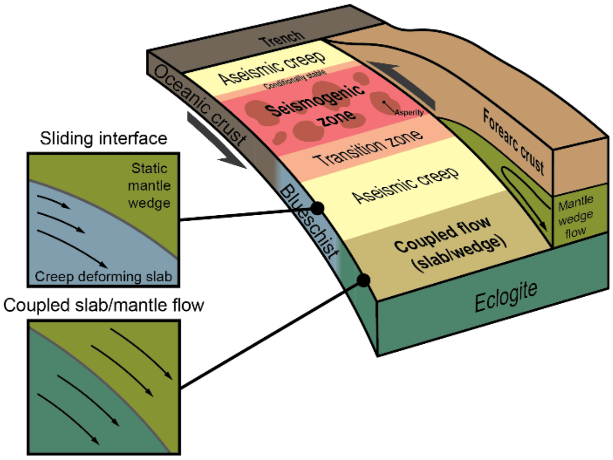

Figure 1. Block diagram of a subduction zone illustrating the role of blueschist in subduction zone structure and dynamics.

Field observations of exhumed subduction terranes suggest a strength hierarchy in which mafic blueschists are stronger than serpentinite but weaker than eclogite and gabbro (Behr et al., 2018; Kotowski & Behr, 2019; Jesús Muñoz-Montecinos et al., 2021), with similar bulk viscosities to quartz-governed lithologies under equivalent conditions (Kotowski & Behr, 2019). The sodic amphibole glaucophane ($Na_2(Mg_3Al_2)Si_8O_{22}(OH)_2$) is ubiquitous in mafic blueschist-facies rocks (Evans, 1990) and geological studies suggest that it is central to accommodating strain and governing the strength of the lithology (Cao et al., 2014; Kim et al., 2013; Kotowski & Behr, 2019; Reynard et al., 1989; Teyssier et al., 2010). Microstructural investigations of naturally deformed blueschists reveal that glaucophane can deform by multiple mechanisms, including dislocation creep (Kim et al., 2013; Kotowski & Behr, 2019; Reynard et al., 1989), diffusion- and dissolution-precipitation creep (De Caroli et al., 2024; Misch, 1969; J. Muñoz-Montecinos et al., 2023), and cataclasis to semi-brittle processes (Ildefonse et al., 1990; J. Muñoz-Montecinos et al., 2023). Experimental constraints on these deformation modes remain limited: laboratory studies have examined semi-brittle deformation in blueschist (Kim et al., 2015; Okazaki & Hirth, 2020), and dislocation glide transitioning to cataclasis and granular flow (Park et al., 2020). Recently, Tokle et al. (2023) proposed a flow law for microboudinage-limited diffusion creep in mafic blueschist. However, a significant gap persists—there are still few experimentally derived flow laws applicable to the deformation mechanisms active in glaucophane, and to date, no published flow law exists for the dislocation-creep regime that is widely observed in naturally deformed glaucophane-bearing blueschists.

To address this knowledge gap, this thesis aims to investigate the extent, deformation mechanisms, and strength of blueschist through a combined field and laboratory approach. A fundamental tool I apply in this work is electron backscatter diffraction (EBSD), a technique that relies on interactions between the electron beam of a scanning electron microscope and the surface of a sample. The electrons are diffracted by the crystal lattice of minerals in the sample and imaged by the EBSD detector, allowing indexing of the mineral phases and their orientation within the sample over large areas in relatively short periods (Prior et al., 1999, 2009). Building on power of this approach, this thesis advances EBSD analyses for glaucophane—a monoclinic mineral that is notoriously difficult to characterize and interpret microstructurally because of its low symmetry and often complex growth and deformation history. Through developing and refining analytical routines, this work establishes new best practices for resolving crystallographic controls on, and interpreting mechanisms that produce deformation fabrics in glaucophane—setting a methodological benchmark for EBSD studies of amphibole and other low-symmetry phases. This technique can be used directly to image microstructures in deformed samples and infer the mechanisms by which a rock or mineral deformed (Wheeler et al., 2001), or combined with other data such as the measured intrinsic elastic properties of a polyphase aggregate to model its physical properties (Mainprice, 2015; Mainprice et al., 2011; Mainprice & Humbert, 1994).

In Chapter 2, I investigate the seismic anisotropy of 14 mafic lawsonite- and epidote-blueschists that span a range of mineralogies, peak P–T conditions, and deformation fabrics from eight exhumed subduction terranes. Seismic anisotropy—the directional dependence of seismic wave velocities—provides a window into subsurface structure when constrained by the range of anisotropy generated by known lithologies (Brownlee et al., 2017; Schulte-Pelkum & Mahan, 2014a, 2014b). In this investigation, **I test the hypothesis that blueschist generates a common seismic anisotropy signal that can be resolved by seismic imaging of the subsurface in subduction zones and will enable mapping of blueschist at the subduction interface**. At depths relevant to blueschists, seismic anisotropy is generated by the deformation induced alignment, or crystallographic preferred orientation (CPO) taken on by anisotropic minerals and their intrinsic elastic properties (Almqvist & Mainprice, 2017; Brownlee et al., 2017; Mainprice et al., 2011). I apply an EBSD-based petrofabric approach to measure the CPOs and modal abundances of blueschist mineral assemblages and integrate these data with the previously measured elastic stiffness tensors of each phase to model the contribution of each blueschist to observed seismic anisotropy (Almqvist & Mainprice, 2017; Mainprice et al., 2011; Mainprice & Humbert, 1994). The resultant anisotropies were evaluated with respect to the crystallographic preferred orientation (CPO) and modal abundance of each phase, as well as the peak metamorphic conditions, to assess how anisotropy depends on lithology and metamorphic history. A key result is that blueschists produce strong seismic anisotropy, with Vp anisotropies (AVp) reaching ~20%, and many of the modeled blueschists displaying AVp values ~10%. The magnitude of the anisotropy scales positively with both the abundance and CPO-intensity of glaucophane. This suggests that **seismic receiver functions may be used to identify the distribution of blueschist along the subduction interface and to constrain the depth of the blueschist–eclogite transition in active subduction zones**. An outstanding question arising from these results that is not addressed in this paper is the exact deformation mechanisms that produce the observed CPOs—which may include synkinematic growth, dislocation creep, or rigid body rotation—a topic explored in detail through field, microstructural, and experimental studies in the following chapters. Chapter 2 has been published as "Seismic Anisotropy of Mafic Blueschists: EBSD-Based Constraints from the Exhumed Rock Record" by Ott, Condit, Schulte-Pelkum, Bernard, and Peč in the *Journal of Geophysical Research: Solid Earth* (2024).

Chapter 3 builds on these findings by examining the deformation mechanisms active at blueschist at conditions relevant to the subduction interface downdip of the seismogenic zone. The study focuses on a garnet-bearing lawsonite blueschist from the mélange unit of the Catalina Schist on Pimu'nga (Santa Catalina Island, CA), equilibrated at ~300°C and ~1 GPa during subduction and characterized by both a strong CPO and a strong modeled seismic anisotropy (AVp ~9%) in Chapter 2. **I test the hypothesis that deformation in subducting oceanic crust at these conditions is governed primarily by dislocation creep following a power-law rheology**. The P–T conditions of equilibration and deformation were confirmed as representative aseismic creep along the viscously deforming portion of the subduction interface using optical petrography and phase equilibrium modeling in Perple_X (Connolly, 1990; Connolly & Petrini, 2002). Detailed EBSD analyses reveal microstructures consistent with dislocation creep, including intragranular strain, subgrain boundary formation, and subgrain rotation (SGR) recrystallization (Karato, 2008; Passchier & Trouw, 1998; Reynard et al., 1989). A key result is the first documentation of significant dislocation-accommodated deformation on hard slip systems in amphibole at low temperatures using the novel EBSD-based weighted Burgers vector (WBV) analysis technique (Wheeler et al., 2009, 2024). **These findings support the interpretation that blueschist deformation near the base of the seismogenic zone is dominated by stress-sensitive dislocation creep**, highlighting the need for further experimental constraints on blueschist rheology to refine models of aseismic, viscous megathrust behavior. Chapter 3 was published as "Dislocation creep of glaucophane in mafic blueschists during subduction: Weighted Burgers vector analysis from the Catalina Schist (California, USA)" by Ott, Condit, Peč, and Journaux in *Geology* (2025).

Chapter 4 builds on the field and microstructural evidence for dislocation creep presented in Chapter 3 by experimentally constraining the rheology of glaucophane under conditions relevant to deformation by aseismic creep. To establish a quantitative relationship between stress and strain rate in blueschist deforming by dislocation creep, I constrained an experimentally derived flow law for glaucophane. Aggregates prepared from a metabasic blueschist host rock from Sifnos Island, Greece, were deformed in a Griggs-type apparatus at high pressures and temperatures to determine the parameters of this flow law. **These experiments test the field-evidence-based hypothesis that blueschists are stronger than serpentinite but weaker than eclogite, exhibiting a rheological strength comparable to quartz at conditions relevant to the viscously deforming subduction interface** (Behr et al., 2018; Kotowski & Behr, 2019; Jesús Muñoz-Montecinos et al., 2021). In these tests, glaucophane aggregates were deformed under three experimental configurations—(1) constant displacement rate, (2) load-stepping, and (3) temperature-stepping—to constrain the parameters of a power-law dislocation creep flow law: stress exponent (n = 5.3), activation energy (Q = 392 kJ mol^{-1}), and pre-exponential factor (A = 160 MPa$^{-5.3}$ s^{-1}). EBSD-based microstructural analysis confirms dislocation creep by documenting microstructures in the experimental products consistent with those reported in naturally deformed blueschist in Chapter 3. Extrapolating these results to natural conditions predicts that aseismic viscous deformation in the subducting slab is accommodated by dislocation creep of glaucophane at ~350 °C, transitioning to grain-size-sensitive mechanisms at higher temperatures, finer grain sizes, and elevated pore-fluid pressures. **A key implications of these results is that models of blueschist deforming by dislocation creep in glaucophane are rheologically weaker than eclogite but substantially stronger than serpentinite (antigorite-bearing) and metasedimentary (quartz-bearing) lithologies.** Chapter 4 has been submitted to *Geophysical Research Letters* as "Experimental constraints on the strength of subducting oceanic crust: a dislocation creep flow law for blueschist (glaucophane)" by Ott, Condit, and Peč, and is currently in peer review.

Chapter 5 extends my investigation of blueschist rheology downdip to the blueschist–eclogite transition through a field-based study of the petrogenesis and significance of this transition at Vroulidia Beach, Sifnos Island, Greece. Previous work on the blueschists and eclogites exposed in the Cherronisos unit of the Cycladic Blueschist Unit on this island has emphasized the role of protolith composition in interpreting the complex as a record of peak high-pressure/low-temperature (HP/LT) subduction conditions and prograde deformation within the preserved unit (Groppo et al., 2009; Matthews & Schliestedt, 1984; Mocek, 2001; Okrusch & Broecker, 1990; Schliestedt, 1986). In this investigation, **I test the hypothesis that the preserved blueschist–eclogite transition at Vroulidia Beach instead represents a retrogressed eclogite–blueschist transition, where the observed mineral assemblages reflect peak eclogite-facies P–T conditions followed by localized, fluid-mediated blueschist-facies retrogression and localized exhumation-related deformation.** Optical petrography, bulk- and mineral-scale geochemical analyses, and phase equilibrium modeling establish the mineral parageneses within the investigated lithologic sequence. EBSD-based analyses of the crystallographic orientations and orientation relationships between the amphibole glaucophane and the pyroxene omphacite provide further insight into the nature and timing of deformation in the blueschist and eclogite samples. **P–T constraints derived from these data reveal a P–T path indicating that limited prograde deformation during subduction established fluid pathways that, during exhumation, channeled fluid flow into the blueschists, selectively promoting retrogression and localized deformation.** These results underscore the importance of integrating petrological and microstructural analyses in interpreting the petrogenesis and tectonometamorphic evolution of exhumed HP/LT terranes. Chapter 5 is in preparation for submission to *Geochemistry, Geophysics, Geosystems* as "Constraining the Nature and Significance of an Exhumed Blueschist–Eclogite Transition, Sifnos Island, Greece" by Ott, Condit, Wass de Czege, and Poulaki.

Chapter 1 References

Almqvist, B. S. G., & Mainprice, D. (2017). Seismic properties and anisotropy of the continental crust: Predictions based on mineral texture and rock microstructure. *Reviews of Geophysics*, *55*(2), 367–433. https://doi.org/10.1002/2016RG000552

Arcay, D., Tric, E., & Doin, M.-P. (2005). Numerical simulations of subduction zones: Effect of slab dehydration on the mantle wedge dynamics. *Physics of the Earth and Planetary Interiors*, *149*(1), 133–153. https://doi.org/10.1016/j.pepi.2004.08.020

Behr, W. M., Kotowski, A. J., & Ashley, K. T. (2018). Dehydration-induced rheological heterogeneity and the deep tremor source in warm subduction zones. *Geology*, *46*(5), 475–478. https://doi.org/10.1130/G40105.1

Brownlee, S. J., Schulte-Pelkum, V., Raju, A., Mahan, K., Condit, C., & Orlandini, O. F. (2017). Characteristics of deep crustal seismic anisotropy from a compilation of rock elasticity tensors and their expression in receiver functions. *Tectonics*, *36*(9), 1835–1857. https://doi.org/10.1002/2017TC004625

Cao, Y., Jung, H., & Song, S. (2014). Microstructures and petro-fabrics of lawsonite blueschist in the North Qilian suture zone, NW China: Implications for seismic anisotropy of subducting oceanic crust. *Tectonophysics*, *628*, 140–157. https://doi.org/10.1016/j.tecto.2014.04.028

Connolly, J. a. D. (1990). Multivariable phase diagrams; an algorithm based on generalized thermodynamics. *American Journal of Science*, *290*(6), 666–718. https://doi.org/10.2475/ajs.290.6.666

Connolly, J. a. D., & Petrini, K. (2002). An automated strategy for calculation of phase diagram sections and retrieval of rock properties as a function of physical conditions. *Journal of Metamorphic Geology*, *20*(7), 697–708. https://doi.org/10.1046/j.1525-1314.2002.00398.x

De Caroli, S., Fagereng, Å., Ujiie, K., Blenkinsop, T., Meneghini, F., & Muir, D. (2024). Deformation microstructures of low- and high-strain epidote-blueschist (Ryukyu arc, Japan): Implications for subduction interface rheology. *Journal of Structural Geology*, *180*, 105041. https://doi.org/10.1016/j.jsg.2023.105041

Evans, B. W. (1990). Phase relations of epidote-blueschists. *Lithos*, *25*(1), 3–23. https://doi.org/10.1016/0024-4937(90)90003-J

Groppo, C., Forster, M., Lister, G., & Compagnoni, R. (2009). Glaucophane schists and associated rocks from Sifnos (Cyclades, Greece): New constraints on the *P*–*T* evolution from oxidized systems. *Lithos*, *109*(3), 254–273. https://doi.org/10.1016/j.lithos.2008.10.005

Hyndman, R. D., Yamano, M., & Oleskevich, D. A. (1997). The seismogenic zone of subduction thrust faults. *Island Arc*, *6*(3), 244–260. https://doi.org/10.1111/j.1440-1738.1997.tb00175.x

Ildefonse, B., Lardeaux, J.-M., & Caron, J.-M. (1990). The behavior of shape preferred orientations in metamorphic rocks: amphiboles and jadeites from the Monte Mucrone area (Sesia-Lanzo zone, Italian Western Alps). *Journal of Structural Geology*, *12*(8), 1005–1011. https://doi.org/10.1016/0191-8141(90)90096-H

Karato, S. (2008). *Deformation of Earth Materials: An Introduction to the Rheology of Solid Earth*. Cambridge: Cambridge University Press. https://doi.org/10.1017/CBO9780511804892

Keken, P. E. van, Wada, I., Abers, G. A., Hacker, B. R., & Wang, K. (2018). Mafic High-Pressure Rocks Are Preferentially Exhumed From Warm Subduction Settings. *Geochemistry, Geophysics, Geosystems*, *19*(9), 2934–2961. https://doi.org/10.1029/2018GC007624

Kim, D., Katayama, I., Michibayashi, K., & Tsujimori, T. (2013). Rheological contrast between glaucophane and lawsonite in naturally deformed blueschist from Diablo Range, California. *Island Arc*, *22*(1), 63–73. https://doi.org/10.1111/iar.12003

Kim, D., Katayama, I., Wallis, S., Michibayashi, K., Miyake, A., Seto, Y., & Azuma, S. (2015). Deformation microstructures of glaucophane and lawsonite in experimentally deformed blueschists: Implications for intermediate-depth intraplate earthquakes. *Journal of Geophysical Research: Solid Earth*, *120*(2), 1229–1242. https://doi.org/10.1002/2014JB011528

Kotowski, A. J., & Behr, W. M. (2019). Length scales and types of heterogeneities along the deep subduction interface: Insights from exhumed rocks on Syros Island, Greece. *Geosphere*, *15*(4), 1038–1065. https://doi.org/10.1130/GES02037.1

Long, M. D., & Wirth, E. A. (2013). Mantle flow in subduction systems: The mantle wedge flow field and implications for wedge processes. *Journal of Geophysical Research: Solid Earth*, *118*(2), 583–606. https://doi.org/10.1002/jgrb.50063

Mainprice, D. (2015). 2.20 - Seismic Anisotropy of the Deep Earth from a Mineral and Rock Physics Perspective. In G. Schubert (Ed.), *Treatise on Geophysics (Second Edition)* (pp. 487–538). Oxford: Elsevier. https://doi.org/10.1016/B978-0-444-53802-4.00044-0

Mainprice, David, & Humbert, M. (1994). Methods of calculating petrophysical properties from lattice preferred orientation data. *Surveys in Geophysics*, *15*(5), 575–592. https://doi.org/10.1007/BF00690175

Mainprice, David, Hielscher, R., & Schaeben, H. (2011). Calculating anisotropic physical properties from texture data using the MTEX open-source package. *Geological Society, London, Special Publications*, *360*(1), 175–192. https://doi.org/10.1144/SP360.10

Matthews, A., & Schliestedt, M. (1984). Evolution of the blueschist and greenschist facies rocks of Sifnos, Cyclades, Greece. *Contributions to Mineralogy and Petrology*, *88*(1), 150–163. https://doi.org/10.1007/BF00371419

Misch, P. (1969). Paracrystalline microboudinage of zoned grains and other criteria for synkinematic growth of metamorphic minerals. *American Journal of Science*, *267*(1), 43–63. https://doi.org/10.2475/ajs.267.1.43

Mocek, B. (2001). Geochemical evidence for arc-type volcanism in the Aegean Sea: the blueschist unit of Siphnos, Cyclades (Greece). *Lithos*, *57*(4), 263–289. https://doi.org/10.1016/S0024-4937(01)00043-3

Muñoz-Montecinos, J., Angiboust, S., Garcia-Casco, A., & Raimondo, T. (2023). Shattered Veins Elucidate Brittle Creep Processes in the Deep Slow Slip and Tremor Region. *Tectonics*, *42*(4), e2022TC007605. https://doi.org/10.1029/2022TC007605

Muñoz-Montecinos, Jesús, Angiboust, S., Garcia-Casco, A., Glodny, J., & Bebout, G. (2021). Episodic hydrofracturing and large-scale flushing along deep subduction interfaces: Implications for fluid transfer and carbon recycling (Zagros Orogen, southeastern Iran). *Chemical Geology*, *571*, 120173. https://doi.org/10.1016/j.chemgeo.2021.120173

Okazaki, K., & Hirth, G. (2020). Deformation of mafic schists from subducted oceanic crust at high pressure and temperature conditions. *Tectonophysics*, *774*, 228217. https://doi.org/10.1016/j.tecto.2019.228217

Okrusch, M., & Broecker, M. (1990). Eclogites associated with high-grade blueschists in the Cyclades archipelago, Greece; a review. *European Journal of Mineralogy*, *2*(4), 451–478.

Ott, J. N., Condit, C. B., & Peč, M. (2025). Experimental constraints on the strength of subducting oceanic crust: a dislocation creep flow law for blueschist (glaucophane). Manuscript submitted to *Journal of Geophysical Research.*

Ott, J. N., Condit, C. B., Peč, M., and Journaux, B. (2025). Dislocation creep of glaucophane in mafic blueschists during subduction: Weighted Burgers vector analysis from the Catalina Schist (California, USA). *Geology*, 53(6), 529-534. https://doi.org/10.1130/G53025.1

Ott, J. N., Condit, C. B., Schulte-Pelkum, V., Bernard, R., & Peč, M. (2024). Seismic Anisotropy of Mafic Blueschists: EBSD-Based Constraints From the Exhumed Rock Record. *Journal of Geophysical Research: Solid Earth,* 129(2), e2023JB027679. https://doi.org/10.1029/2023jb027679

Park, Y., Jung, S., & Jung, H. (2020). Lattice Preferred Orientation and Deformation Microstructures of Glaucophane and Epidote in Experimentally Deformed Epidote Blueschist at High Pressure. *Minerals*, *10*(9), 803. https://doi.org/10.3390/min10090803

Passchier, C. W., & Trouw, R. A. J. (1998). *Microtectonics*. Berlin, Heidelberg: Springer. https://doi.org/10.1007/978-3-662-08734-3

Peacock, S. M. (1993). The importance of blueschist → eclogite dehydration reactions in subducting oceanic crust. *Geological Society of America Bulletin*, *105*(5), 684–694. https://doi.org/10.1130/0016-7606(1993)105%253C0684:TIOBED%253E2.3.CO;2

Peacock, S. M. (2004). Thermal Structure and Metamorphic Evolution of Subducting Slabs. In *Inside the Subduction Factory* (pp. 7–22). American Geophysical Union (AGU). https://doi.org/10.1029/138GM02

Prior, D. J., Boyle, A. P., Brenker, F., Cheadle, M. C., Day, A., Lopez, G., et al. (1999). The application of electron backscatter diffraction and orientation contrast imaging in the SEM to textural problems in rocks. *American Mineralogist*, *84*(11–12), 1741–1759. https://doi.org/10.2138/am-1999-11-1204

Prior, D. J., Mariani, E., & Wheeler, J. (2009). EBSD in the Earth Sciences: Applications, Common Practice, and Challenges. In A. J. Schwartz, M. Kumar, B. L. Adams, & D. P. Field (Eds.), *Electron Backscatter Diffraction in Materials Science* (pp. 345–360). Boston, MA: Springer US. https://doi.org/10.1007/978-0-387-88136-2_26

Reynard, B., Gillet, P., & Willaime, C. (1989). Deformation mechanisms in naturally deformed glaucophanes: a TEM and HREM study. *European Journal of Mineralogy*, *1*(5), 611–624. https://doi.org/10.1127/ejm/1/5/0611

Schliestedt, M. (1986). Eclogite-Blueschist Relationships as Evidenced by Mineral Equilibria in the High-Pressure Metabasic Rocks of Sifnos (Cycladic Islands), Greece. *Journal of Petrology*, *27*(6), 1437–1459. https://doi.org/10.1093/petrology/27.6.1437

Scholz, C. H. (1988). The brittle-plastic transition and the depth of seismic faulting. *Geologische Rundschau*, *77*(1), 319–328. https://doi.org/10.1007/BF01848693

Schulte-Pelkum, V., & Mahan, K. H. (2014a). A method for mapping crustal deformation and anisotropy with receiver functions and first results from USArray. *Earth and Planetary Science Letters*, *402*, 221–233. https://doi.org/10.1016/j.epsl.2014.01.050

Schulte-Pelkum, V., & Mahan, K. H. (2014b). Imaging Faults and Shear Zones Using Receiver Functions. *Pure and Applied Geophysics*, *171*(11), 2967–2991. https://doi.org/10.1007/s00024-014-0853-4

Shibazaki, B. (2023). Progress in modeling the Tohoku-oki megathrust earthquake cycle and associated crustal deformation processes. *Progress in Earth and Planetary Science*, *10*(1), 43. https://doi.org/10.1186/s40645-023-00575-x

Stöckhert, B. (2002). Stress and deformation in subduction zones: insight from the record of exhumed metamorphic rocks. *Geological Society, London, Special Publications*, *200*(1), 255–274. https://doi.org/10.1144/GSL.SP.2001.200.01.15

Stünitz, H., Neufeld, K., Heilbronner, R., Finstad, A. K., Konopásek, J., & Mackenzie, J. R. (2020). Transformation weakening: Diffusion creep in eclogites as a result of interaction of mineral reactions and deformation. *Journal of Structural Geology*, *139*, 104129. https://doi.org/10.1016/j.jsg.2020.104129

Teyssier, C., Whitney, D. L., Toraman, E., & Seaton, N. C. A. (2010). Lawsonite vorticity and subduction kinematics. *Geology*, *38*(12), 1123–1126. https://doi.org/10.1130/G31409.1

Tokle, L., Hufford, L. J., Behr, W. M., Morales, L. F. G., & Madonna, C. (2023). Diffusion Creep of Sodic Amphibole-Bearing Blueschist Limited by Microboudinage. *Journal of Geophysical Research: Solid Earth*, *128*(9), e2023JB026848. https://doi.org/10.1029/2023JB026848

Uchida, N., & Bürgmann, R. (2021). A Decade of Lessons Learned from the 2011 Tohoku-Oki Earthquake. *Reviews of Geophysics*, *59*(2), e2020RG000713. https://doi.org/10.1029/2020RG000713

Wech, A. G., & Creager, K. C. (2011). A continuum of stress, strength and slip in the Cascadia subduction zone. *Nature Geoscience*, *4*(9), 624–628. https://doi.org/10.1038/ngeo1215

Wheeler, J., Prior, D., Jiang, Z., Spiess, R., & Trimby, P. (2001). The petrological significance of misorientations between grains. *Contributions to Mineralogy and Petrology*, *141*(1), 109–124. https://doi.org/10.1007/s004100000225

Wheeler, J., Mariani, E., Piazolo, S., Prior, D. j., Trimby, P., & Drury, M. r. (2009). The weighted Burgers vector: a new quantity for constraining dislocation densities and types using electron backscatter diffraction on 2D sections through crystalline materials. *Journal of Microscopy*, *233*(3), 482–494. https://doi.org/10.1111/j.1365-2818.2009.03136.x

Wheeler, J., Piazolo, S., Prior, D. J., Trimby, P. W., & Tielke, J. A. (2024). Using crystal-lattice distortion data for geological investigations: the weighted Burgers vector method. *Journal of Structural Geology*, *179*, 105040. https://doi.org/10.1016/j.jsg.2023.105040

Chapter 2: Seismic Anisotropy of Mafic Blueschists: EBSD-based constraints from the exhumed rock record

Jason N. Ott[1], Cailey B. Condit[1], Vera Schulte-Pelkum[2], Rachel Bernard[3], and Matěj Peč [4]

[1]Department of Earth and Space Sciences, University of Washington, Seattle, WA, USA

[2]Cooperative Institute for Research in Environmental Sciences and Department of Geological Sciences, University of Colorado, Boulder, CO, USA

[3]Geology Department, Amherst College, Amherst, MA, USA

[4]Department of Earth, Atmospheric and Planetary Sciences, Massachusetts Institute of Technology, Cambridge, MA, USA

Corresponding author: Jason Ott (jasonott@uw.edu)

Key Points:

- Calculated blueschist Vp anisotropy up to ~20% with a plateau at ~10%, with lineation-parallel fast axis and foliation-normal slow axis
- The anisotropy magnitude increases with glaucophane modal abundance/CPO strength and is diluted by epidote/lawsonite abundance
- The glaucophane CPO type correlates with the Vp pattern and increasing AVp magnitude in mafic blueschists

Abstract

Seismic anisotropy constitutes a useful tool for imaging the structure along the plate interface in subduction zones, but the seismic properties of mafic blueschists, a common rock type in subduction zones, remain poorly constrained. We applied the technique of electron backscatter diffraction (EBSD) based petrofabric analysis to calculate the seismic anisotropies of 14 naturally-deformed mafic blueschists at dry, ambient conditions. The ductilely deformed blueschists were collected from terranes with inferred peak P-T conditions applicable to subducting slabs at or near the plate interface in active subduction zones. Epidote blueschists display the greatest *P* wave anisotropy range (AVp ~7–20%), while lawsonite blueschist AVp ranges from ~2–10%. *S* wave anisotropies generate shear wave splitting delay times up to ~0.1 s over a thickness of 5 km. AVp magnitude increases with glaucophane abundance (from areal EBSD measurements), decreases with increasing epidote or lawsonite abundance, and is enhanced by glaucophane crystallographic preferred orientation (CPO) strength. Two-phase rock recipe models provide further evidence of the primary role of glaucophane, epidote, and lawsonite in generating blueschist seismic anisotropy. The symmetry of *P* wave velocity patterns reflects the deformation-induced CPO type in glaucophane—an effect previously observed for hornblende on amphibolite *P* wave anisotropy. The distinctive seismic properties that distinguish blueschist from other subduction zone rock types and the strong correlation between anisotropy magnitude/symmetry and glaucophane CPO suggest that seismic anisotropy may be a useful tool in mapping the extent and deformation of blueschists along the interface, and the blueschist-eclogite transition in active subduction zones.

Plain Language Summary

The directional dependence of seismic wave speeds in the subsurface, or seismic anisotropy, can allow us to map the Earth's structure in subduction zones. To improve the interpretation of seismic data collected in active subduction zones, we characterized the range of seismic anisotropy created by blueschists (a common subduction zone rock-type) that were returned to the surface after being deformed in ancient subduction margins. We calculate the anisotropy of each blueschist rock from mineral orientations collected in the lab combined with the elastic properties of these minerals. Trends in seismic anisotropy were compared to the changes in composition and preferred orientations of minerals (produced by deformation). We found that blueschists can generate a broad range of seismic anisotropy, and that this anisotropy is enhanced by increasing amounts of the mineral glaucophane. The seismic anisotropy is further increased when the glaucophane minerals are more uniformly oriented, as is typical in rocks that have experienced higher levels of deformation. The seismic anisotropy and seismic wave speeds of blueschists are distinctive from those of other common subduction zone rocks. Therefore, these results suggest blueschist seismic anisotropy can be used to improve our ability to map structure and deformation occurring in active subduction zones.

1 Introduction

Subduction zones are complex convergent boundaries where the majority of deformation between two plates is accommodated by periodic, frictional slip in the shallow seismogenic zone, and aseismic, viscous creep at greater depths (Hyndman et al., 1997). This viscous deformation, localized along the plate interface in ductile shear zones with a thickness of up to a few kilometers (Stöckhert, 2002), plays an important role in transferring stress to the seismogenic zone and generating megathrust earthquakes (Wech & Creager, 2011). The transition from brittle to ductile deformation occurs around the same region as the onset of blueschist facies metamorphism in most active subduction zones (Fig. 1a,b; Peacock 2004; van Keken et al., 2018). Observations of exhumed subduction terranes indicate that the thickness of blueschist-metamorphosed oceanic crust at the subduction interface can vary from tens of meters to > one kilometer scales (e.g., Brothers, 1974; Aoki et al., 2008; Topuz et al., 2008; Lamont et al., 2020; Peillod et al., 2021). Deep subduction of mafic blueschist (>70 km) induces a transformation to eclogite through dehydration reactions that release mineral-bound water to enable flux-melting in the overlying mantle-wedge, and arc-volcanism at the surface (Peacock, 1993). Consequently, subducting blueschist-metamorphosed oceanic crust is strongly tied to a range of the mechanical and chemical processes in subduction zones (Fig. 1a), yet cannot be studied *in situ* within active systems. However, we can use geophysical observations of the directional dependence of seismic wave velocities, or seismic anisotropy, in active subduction zones to interpret subsurface structure by constraining the range of seismic anisotropy from exhumed subduction exposures and samples (e.g., Schulte-Pelkum et al., 2005; Schulte-Pelkum & Mahan, 2014a,2014b; Brownlee et al., 2017).

Seismic anisotropy is produced in large part by crystallographic preferred orientation (CPO) of anisotropic minerals at depths below the closure of open cracks (Mainprice & Nicolas, 1989; Mainprice & Humbert, 1994; Brownlee et al., 2017; Almqvist & Mainprice 2017; Jung, 2017). CPO formation is typical of the viscous deformation that occurs along the plate interface below the seismogenic zone (Mainprice & Nicolas, 1989), and thus, parts of the subducting slab may develop significant seismic anisotropy if CPOs are developed in anisotropic phases such as amphibole or mica. Seismology-based studies of subduction zones document evidence of seismic anisotropy including azimuthal anisotropy of *P* wave velocities and observations of shear wave splitting between the fast (Vs_1) and slow (Vs_2) shear waves (e.g., Park & Levin, 2002; Nakajima & Hasegawa, 2004; Wang & Zhao, 2010; Huang et al., 2011; Wei et al., 2016). These studies have proposed various source regions for the observed seismic anisotropy including the subducting slab, the underlying subducting mantle lithosphere, and serpentinized mantle wedge. However, in order to understand the relative contributions of these structural units to the overall seismic anisotropy of subduction zones, we need geologic constraints from the rock record that inform us about the range of potential anisotropies and the contribution of the constituent phases and their orientation in producing these seismic signatures.

Some previous investigations have characterized the seismic anisotropy of mafic blueschists using petrofabrics and laboratory velocity measurements (Bezacier et al., 2010; Fujimoto et al., 2010; Kim et al., 2013; Cao et al., 2013; Cao et al., 2014; Cao & Jung, 2016; Keppler et al., 2017; Ha et al., 2019; Park & Jung, 2022; Zertani et al., 2022). Previous studies calculated the anisotropy of naturally deformed blueschists using petrofabrics determined at ambient conditions with electron backscatter diffraction (EBSD) data and the elastic properties of the constituent minerals, and reported *P* wave anisotropies (AVp) from ~8–30%, and maximum *S* wave anisotropies (AVs) from 4–24% (Bezacier et al., 2010; Kim et al., 2013; Cao et al., 2013; Cao et al., 2014; Cao & Jung, 2016; Ha et al., 2019). Keppler et al. (2017) calculated the anisotropy of two exhumed blueschists using the elastic properties of the minerals and petrofabrics determined by neutron diffraction at ambient conditions, and reported AVp values ~7–12%. In an experimental study, Park and Jung (2022) deformed blueschists under shear in a modified Griggs apparatus at high pressures and temperatures, and calculated anisotropies of AVp ~5-11% and max AVs ~4-6% using the EBSD-determined petrofabrics of the recovered samples (at ambient conditions). Two studies using ultrasonic measurements of mafic blueschist petrophysical properties at high pressures and temperatures report anisotropies up to AVp ~13% (Fujimoto et al., 2010), and AVp and max AVs ~11% (Zertani et al., 2022). Taken together, these studies suggest that blueschist-facies rocks may contribute substantially to the seismic anisotropy observed in active subduction zones by generating *P* wave anisotropies up to 30% and shear wave splitting delay times of up to ~0.3 s (Kim et al., 2013; Cao et al., 2013; Cao et al., 2014). Most previous investigations include only a few blueschists, or blueschists from a single exhumed subduction terrane. Thus, further work to characterize variations in the potential contribution of blueschists to observed seismic anisotropy in subduction zones by investigating elastic anisotropy in blueschists from different exhumed subduction terranes and peak P-T conditions will be invaluable.

Blueschist facies metamorphism of mid-ocean ridge basaltic crust (MORB) produces blueschists with variable mineralogies (e.g., lawsonite blueschist or epidote blueschist subtypes; Evans, 1990) depending on the pressure-temperature gradient of the subduction path. Lawsonite blueschists are produced by metamorphism at low temperatures and remain stable to high pressures, while epidote blueschists are the product of metamorphism at warmer temperatures and moderate pressures (Fig. 1b). Consequently, exhumed lawsonite blueschists and epidote blueschists preserve evidence of the deformation history of these rocks to the peak P-T conditions they experienced during subduction. The seismic anisotropy generated by both blueschist subtypes can be substantial, although the magnitude of lawsonite blueschist anisotropy is generally observed to be weaker than the anisotropy generated by epidote blueschist (e.g., Fujimoto et al, 2010; Kim et al., 2013). Mafic blueschists are primarily composed of the sodic amphibole glaucophane with significant fractions of epidote (epidote blueschist), lawsonite (lawsonite blueschist), and smaller fractions (<10%) of phengite, garnet, and other accessory phases. Single-crystal elastic wave velocity measurements in multiple crystallographic directions have been made using Brillouin spectroscopy to determine elastic moduli of glaucophane (Bezacier et al., 2010), lawsonite (Schilling et al, 2003), epidote (Aleksandrov et al., 1974), and phengite (muscovite, Vaughan & Guggenheim, 1986). The experimentally determined elastic anisotropies of these phases demonstrate that each may contribute substantially to observed seismic anisotropies (Fig. 2a,b).

Other amphiboles, such as the hornblende group, and micas (biotite and muscovite) have been proposed as fundamental contributors to the seismic anisotropy of deep crustal (continental) rocks in texture-based seismic anisotropy studies of rocks from the middle and lower continental crust (e.g., Mahan, 2006; Tatham et al., 2008; Lloyd et al., 2011). Amphibole in naturally deformed rocks has been observed with four different CPO types which were proposed to correlate with the deformation conditions experienced (Ko & Jung, 2015; Kim & Jung, 2019). The type-I amphibole CPO is defined by strong alignment of the [100] crystallographic axes subnormal to the shear plane and the [001] axes subparallel to the shear direction, while the type-II CPO shows the same [100] axes orientation with the [010] axes aligned subparallel to the shear direction (Fig. 2c). The type-III CPO of amphibole is also characterized by strong alignment of the [100] axes subnormal to the shear plane, but the [010] and [001] axes describe a girdle on the shear plane (Fig. 2c). Amphibole with a type-IV CPO displays a strong alignment of the [001] axes subparallel to the shear direction with the [100] and [010] axes describing a girdle subnormal to the shear direction (Fig. 2c). Laboratory deformation experiments on amphibolites yielded correlations between amphibole CPO type and the magnitude of seismic anisotropy predicted in the samples (Kim & Jung, 2019; Kim & Jung, 2020), and studies of naturally deformed amphibolites reported further correlations between the amphibole CPO type and the symmetry of the Vp anisotropy patterns (Ji et al., 2013; Kim & Jung 2020; Liu & Cao, 2023). In contrast, the contribution of glaucophane to the seismic properties of mafic blueschists is not as well understood due to the limited number of petrofabric based seismic anisotropy studies on mafic blueschists, and the potential contribution of other anisotropic phases to the bulk anisotropy (e.g., epidote, lawsonite, and phengite).

Here, we extend and build up this previous work by creating a catalog of EBSD derived seismic anisotropies for 14 mafic epidote and lawsonite blueschists spanning a large range of P-T conditions from eight exhumed subduction terranes (Fig. 1b). We use the electron backscatter diffraction (EBSD) based approach to calculate seismic anisotropy at dry, ambient conditions, which combines measured CPOs, modal abundances derived from indexed regions of EBSD maps, and the elastic properties of each phase to calculate the elastic anisotropy of the aggregate; these microstructural-based calculations provide constraints on the potential contribution of blueschists to seismic anisotropy (Mainprice & Humbert, 1994; Mainprice et al., 2011; Mainprice et al., 2015). We then investigated the anisotropy trends with respect to modal abundance, CPO type, and CPO strength for glaucophane, epidote, lawsonite, and phengite within each sample assemblage to assess the contribution of the modal abundance and CPO of each phase to the seismic properties. We leveraged the variability in peak metamorphic conditions across our samples to investigate the potential of a correlation between the magnitude of anisotropy and increasing metamorphic grade due to increasing depth of subduction. We find that glaucophane's influence on blueschist seismic anisotropy is similar to that of previous observations of hornblende group amphiboles on the anisotropy of deep crustal rocks; the modal abundance and CPO strength of the amphibole glaucophane exerts a key control on the magnitude of seismic anisotropy in mafic blueschist and the pattern of *P* wave anisotropy reflects the CPO type of glaucophane.

2 Materials and Methods

2.1 Sample description and preparation

We investigated the elastic anisotropy of 14 mafic blueschists covering a wide range of mineralogies, pressure-temperature conditions, and fabrics. This included nine epidote blueschists and five lawsonite blueschists, collected from eight exhumed subduction terranes that experienced peak metamorphic conditions ranging from 200 to 600°C and 0.6 to 2.6 GPa (Table 1), spanning much of the blueschist facies stability field (Fig. 1b). The blueschists were metamorphosed from mafic protoliths and exhibit mineralogies dominantly composed of glaucophane and lawsonite or epidote, with variable amounts of garnet, phengite, pyroxene (jadeite or omphacite), quartz, chlorite, and minor rutile or titanite. Average grain size of the samples ranges from 10 to 80 μm in diameter with some blueschists containing porphyroblasts up to 5 mm in diameter. The samples selected for this study display evidence of ductile deformation, including well-defined foliations and lineations. Photos of hand samples illustrating the macroscopic fabrics are shown in Figure 3.

Thin sections were prepared following the common methodology employed in petrofabric based anisotropy studies (e.g., Ward et al., 2012; Cao et al., 2013; Kim et al., 2013; Brownlee et al., 2017; Kang & Jung, 2019; Liu & Cao, 2023). One structurally oriented thin section, cut parallel

Table 1: *Samples, Localities, and P-T Estimates*

Sample	Locality[a]	P (GPa)	T (°C)	Reference
Epidote Blueschist				
BAN09	Bandon, Oregon, USA	0.6–0.7	400–550	Coleman and Lanphere, 1971
BAN15	Bandon, Oregon, USA	0.6–0.7	400–550	Coleman and Lanphere, 1971
CY106	Tinos, Cycladic Islands, Greece	1.52–1.97	468–510	Lamont et al., 2020
CY107	Tinos, Cycladic Islands, Greece	1.52–1.97	468–510	Lamont et al., 2020
DR221	Diablo Range, California, USA	0.75–1.0	200–300	Patrick and Day, 1989
LAB34	Diablo Range, California, USA	0.75–1.0	200–300	Patrick and Day, 1989
LAB555	Pam Peninsula, New Caledonia	1.26 ±0.12	570 ±36	Clarke et al., 1997
LAB570	Pam Peninsula, New Caledonia	1.26 ±0.12	570 ±36	Clarke et al., 1997
LAB572	Pam Peninsula, New Caledonia	1.26 ±0.12	570 ±36	Clarke et al., 1997
Lawsonite Blueschist				
C18G1003C01	Corsica, France	1.5–1.8	350–480	Brovarone et al., 2014
DR265	Diablo Range, California, USA	0.75–1.0	200–300	Patrick and Day, 1989
GB15-02A	Catalina Schist, California, USA	0.7–1.0	200–300	Grove and Bebout, 1995
SV01-49A	Sivrihisar Massif, Turkey	1.2–2.6	380–520	Davis and Whitney, 2006
01GSN2-3	S. Motagua Fault Zone, Guatemala	0.9–1.6	370–460	Harlow et al., 2003

[a] Sample location coordinates are available for samples: C18G1003C01(42°23'30.4"N 9°19'22.9"E), GB15(33°22'N 118°28'W), and SV01(39°36'00.7"N 31°15'26.9"E). Remaining sample details are available only for the locality.

to the lineation and perpendicular to the foliation, where the X-Z plane is contained in the thin section, was cut for each sample. Optical microscopy was used to select target regions for EBSD data collection in each thin section that were representative of the mineralogy, grain sizes, and fabric of the full section and hand sample. Examples of selected representative regions and their microstructures are presented in Figure 4 and photomicrographs of larger areas containing the target regions of samples are included in Figure S1.

2.2 EBSD data acquisition

The EBSD technique relies on the interaction of an incident electron beam with a flat sample mounted with the normal vector of the surface oriented at a high angle to the electron beam. The electrons interact with the sample at a shallow depth (~1 μm), and electrons diffracted by the lattice planes of mineral phases in the sample are imaged as bands on the phosphor screen of the EBSD detector. Prior et al. (1999) provides a detailed review of the electron backscatter diffraction technique. Multiple bands are imaged at each indexed point, forming a Kikuchi pattern that can be matched with a crystallographic database to identify the phase and its orientation within the sample (e.g., Lloyd et al., 1991; Britton et al., 2016). Improvements in automated data collection, Kikuchi pattern recognition, and indexing of EBSD data allows for the collection of dense phase-and-orientation datasets over large areas in thin sections prepared from geologic samples, making EBSD a powerful tool for the study of physical properties that are connected to rock microstructures (Krieger Lassen et al., 1992; Prior et al., 1999; Wright, 2000).

EBSD data were collected at the University of Washington Molecular Analysis Facility using a ThermoFisher-Scientific Apreo variable-pressure scanning electron microscope (SEM) equipped with an Oxford Instruments Symmetry EBSD detector. Prior to data collection, samples were polished for two to six hours with a 0.06 µm-diameter amorphous, colloidal silica suspension in a Buehler VibroMet 2 vibratory polisher. Samples with an indexing rate less than 75% after a test map were polished for an additional two hours before data collection.

EBSD data for 13 of the 14 samples were collected at SEM chamber pressure of 160 Pa with a pressure-limiting apparatus installed on the beam column, resulting in a limited working distance of 18 mm. All samples were mounted to the stage with a fixed 70° tilt, and data was collected at an accelerating voltage of 20 kV and 32 nA current. Sample LAB555 was coated in a 10 nm layer of carbon to dissipate sample charging and run at high-vacuum conditions with no pressure-limiting apparatus and a shorter working distance of 16 mm to improve the indexing rate of this fine grained sample.

EBSD patterns were collected on a grid with a step size selected to optimize sample characterization and collection time. Selected step sizes ranged from 1.5–10 µm based on the average observed grain size in the sample, and the exposure time at each step was 20 ms. EBSD-map areas varied from 1.3 mm by 1.7 mm to 3.6 mm by 9.3 mm. The EBSD patterns were indexed using the Oxford HKL and American Mineralogist databases loaded in the Oxford AZtec software. Inclusion of the jadeite and/or omphacite match units during EBSD data collection and sample indexing was based on the presence of calcium (suggesting omphacite) in qualitative energy-dispersive X-ray spectroscopy (EDS) on test maps of sample regions containing pyroxene.

2.3 EBSD data analysis

Microstructural analysis and calculation of the seismic anisotropy were done with the MTEX 5.7.0 toolbox for MATLAB (Bachmann et al., 2010; Mainprice et al., 2011). Each EBSD map was processed to remove low confidence data with a mean angular deviation (MAD) greater than 1.0° from the crystallographic database reference data. Grains were reconstructed with a threshold of greater than 10° between neighboring EBSD measurements. We removed grains with fewer than three indexed points. These reduced EBSD datasets were used in all subsequent analyses.

2.3.1 Seismic anisotropy calculations

To calculate seismic anisotropy, we combined the quantitative measure of the CPOs from the full set of indexed orientations with published single crystal elastic tensors for the constituent phases (Table 2) to calculate the effective elastic properties of each multiphase crystalline aggregate (Mainprice & Humbert, 1994; Mainprice et al., 2011; Mainprice et al., 2015). Stress is linked to strain through the general tensor form of Hooke's law as

$$\sigma_{ij} = C_{ijkl}\varepsilon_{kl} \tag{1}$$

where σ_{ij} is the stress tensor, ε_{kl} is the strain tensor and C_{ijkl} is the full elastic stiffness tensor. The elastic stiffness tensor is a fourth-rank tensor with 81 components, but the symmetry of the stress and strain tensors requires that $C_{ijkl} = C_{jikl}$ and $C_{ijkl} = C_{ijlk}$, reducing the number of independent entries to 36. The resultant 6 x 6 Voigt matrix representation of the elastic stiffness tensor may be further reduced to 21 independent elastic constants due to thermodynamic strain energy conditions that require $C_{ijkl} = C_{klij}$. In this work, we will present the elastic stiffness constants for each phase and the polyphase aggregates in the Voigt matrix representation as

$$C_{IJ} = C_{ijkl} = \begin{vmatrix} C_{11} & C_{12} & C_{13} & C_{14} & C_{15} & C_{16} \\ & C_{22} & C_{23} & C_{24} & C_{25} & C_{26} \\ & & C_{33} & C_{34} & C_{35} & C_{36} \\ & & & C_{44} & C_{45} & C_{46} \\ & & & & C_{55} & C_{56} \\ & & & & & C_{66} \end{vmatrix} \tag{2}$$

A detailed description of the reduction of a full elastic stiffness tensor into its reduced Voigt matrix representation (Voigt stiffness matrix) is included in Almqvist and Mainprice (2017). While grain size, shape, crystallographic orientation, and distribution of phases may be heterogeneous at microscopic scales, we treat the samples as representative of the macroscopic structure and composition and assume that stress and strain vary slowly and continuously with position, and are linked through the effective elastic stiffness tensor, C^* (Mainprice et al., 1994, Mainprice, 2015).

To determine C^* for each phase, the full set of indexed orientations for each phase was fitted in MTEX by an orientation distribution function (ODF)—a mathematical function in spherical harmonics that weighs each possible orientation by the fraction of the phase with that orientation (Bunge, 1985). The single crystal Voigt elastic stiffness matrix for each phase (Table 2) were integrated over the ODF in MTEX to calculate the effective elastic Voigt stiffness matrix C^* for each phase using three averaging schemes: (1) the Voigt average that assumes uniform strain throughout the sample (Voigt, 1928), (2) the Reuss average that assumes uniform stress throughout the sample (Reuss, 1929), and (3) the Voigt-Reuss-Hill (VRH) average, which is the arithmetic mean of the Voigt and Reuss averages (Hill, 1952), using the method of Mainprice et al. (2011). The calculated seismic anisotropy values using the Voigt and Reuss averages were within 2% of the VRH-averaged results for all samples, therefore, we report the VRH-averaged elastic stiffness matrices throughout this work. The C^* matrix and the density of each phase (Table 2) weighted by volume fraction are used to calculate the effective elastic stiffness matrix and density of each polyphase aggregate. While recent theoretical work has proposed a first-principals-based model of elastic stiffness constants for titanite (Das et al., 2021), no single-crystal elasticity measurements are available, so this phase was excluded from the anisotropy calculations; given its low modal abundance (<7% in all blueschist samples), the exclusion of the phase in our calculations introduces some minor systematic error into these calculations.

The calculated polyphase aggregate effective elastic stiffness matrix and density were used in MTEX to solve the Christoffel (1877) equation to predict the plane wave speeds and polarizations in three dimensions; a derivation of this solution appears in the review paper by Almqvist and Mainprice (2017). The percentage of *P* wave seismic anisotropy (AVp) for each sample was calculated in MTEX as

$$\text{AVp}\ \% = [(\text{Vp}_{\text{max}} - \text{Vp}_{\text{min}})/0.5(\text{Vp}_{\text{max}} + \text{Vp}_{\text{min}})]*100 \tag{3}$$

The percentage of *S* wave seismic anisotropy was calculated for the fast shear waves (AVs_1) and the slow shear waves (AVs_2) as

$$\text{AVs}i\ \% = [(\text{Vs}i_{\text{max}} - \text{Vs}i_{\text{min}})/0.5(\text{Vs}i_{\text{max}} + \text{Vs}i_{\text{min}})]*100 \tag{4}$$

where i is 1 (fast shear wave) or 2 (slow shear wave). The shear wave splitting percentage (AVs %) for all orientations in each sample was determined as

$$\text{AVs(g)}\ \% = [(\text{Vs}_{1(\text{g})} - \text{Vs}_{2(\text{g})})/0.5(\text{Vs}_{1(\text{g})} + \text{Vs}_{2(\text{g})})]*100 \tag{5}$$

Where g is the orientation at which the shear wave splitting is being calculated. Maximum delay times between the fast and slow shear waves are calculated as

$$dt_{max} = (T * AVs_{max})/(100 * \langle Vs\rangle) \tag{6}$$

where dt_{max} is the maximum delay time, *T* is the thickness of the anisotropic layer, AVs_{max} is the calculated maximum shear wave splitting percentage, and $\langle Vs\rangle$ is the simple average of the shear wave phase speeds in the three principal directions (after Silver & Chan, 1991).

2.3.2 CPO strength measurement by texture index

The CPO strength of glaucophane, epidote, lawsonite, and phengite were measured using three different texture indices to test for correlation between the magnitude of seismic anisotropy and the CPO strength of these anisotropic phases. The CPO strength for each principal crystallographic axis was calculated by the pole-figure J-index (pfJ-index) as

$$pfJ_{[hkl]} = \int P_{[hkl]}(\alpha,\beta)^2 d\omega \tag{7}$$

where $[hkl]$ is the Miller index of a crystallographic axis, α and β are the spherical coordinates of an orientation within the pole figure, $P_{[hkl]}(\alpha,\beta)$ is the fraction of the measured orientations of

Table 2: *Referenced Single-Crystal Elastic Constants in Voigt Matrix Notation*[a] *(in GPa)*

Chlorite (density = 2.54 g/cm^3) — Mookherjee & Mainprice, 2014

198.4	57.3	14.0	0	3.0	0
	197.7	19.6	0	-0.5	0
		138.1	0	0.1	0
			25.9	0	0.1
				24.6	0
					71.0

Epidote (density = 3.45 g/cm^3) — Aleksandrov et al., 1974

211.5	65.6	43.2	0	-6.5	0
	239.0	43.6	0	-10.4	0
		202.1	0	-20.0	0
			39.1	0	-2.3
				43.4	0
					79.5

Garnet(almandine) (density = 3.8 g/cm^3) — Chai et al., 1997

306.7	106.7	111.9	0	0	0
	306.7	111.9	0	0	0
		306.7	0	0	0
			94.9	0	0
				94.9	0
					94.9

Glaucophane (density = 3.07 g/cm^3) — Bezacier et al., 2010

122.3	46.7	37.2	0	2.3	0
	231.5	74.9	0	-4.8	0
		254.6	0	-23.7	0
			79.6	0	8.9
				52.8	0
					51.2

Jadeite (density = 3.33 g/cm^3) — Kandelin & Weidner, 1988

274.0	94.0	71.0	0	4.0	0
	253.0	82.0	0	14.0	0
		282.0	0	28.0	0
			88.0	0	13.0
				65.0	0
					94.0

Lawsonite (density = 3.09 g/cm^3) — Schilling et al., 2003

226.0	66.0	64.0	0	0	0
	216.0	83.0	0	0	0
		262.0	0	0	0
			64.0	0	0
				59.0	0
					18.0

Phengite(muscovite) (density = 2.73 g/cm^3) — Vaughan & Guggenheim, 1986

181.0	48.8	25.6	0	-14.2	0
	178.4	21.2	0	1.1	0
		58.6	0	1.0	0
			16.5	0	-5.2
				19.5	0
					72.0

Omphacite (density = 3.33 g/cm^3) — Bhagat et al., 1992

257.3	85.9	76.2	0	7.1	0
	216.2	71.8	0	13.3	0
		260.2	0	33.7	0
			80.2	0	10.2
				70.6	0
					85.8

Quartz (density = 2.65 g/cm^3) — Ogi et al., 2016

86.8	6.87	11.9	-18.0	0	0
	86.8	11.9	18.0	0	0
		105.5	0	0	0
			58.1	0	0
				58.1	-18.0
					39.9

Rutile (density = 4.30 g/cm^3) — Isaak et al., 1998

267.3	174.1	146.4	0	0	0
	0	0	0	0	0
		483.9	0	0	0
			123.9	0	0
				0	0
					190.4

[a] Voigt matrix notation formulation shown in Eq. 2

the crystallographic axis with that orientation, and $d\omega$ is the differential element (Michibayashi & Mainprice, 2004). The pfJ-index is a quantitative measure of the fabric strength of each crystallographic axis for a phase and ranges from 1 in phases with a random CPO to infinity for a single crystal orientation. The CPO strength was also calculated using the J-index, defined as

$$J = \int f(g)^2 dg \qquad (8)$$

Where $f(g)$ is the value of the ODF at orientation g, and the resulting J-index also ranges from 1 for a random CPO to infinity for a single crystal (Bunge, 1985). Fabric strength was also calculated using the misorientation angle distribution, or M-index. The misorientation angle is the minimum angle of rotation about a common axis between two grains of the same phase that are not in direct contact that will bring their respective crystal lattices into alignment (Wheeler et al., 2001). The M-index is defined as the difference between the observed misorientation angle distribution and a random distribution of misorientation angles for that phase, and is calculated as

$$M = \frac{1}{2}\int |R^T(\theta) - R^O(\theta)| d\theta \tag{9}$$

where $R^T(\theta)$ is the theoretical value of a random misorientation distribution and $R^O(\theta)$ is the observed misorientation distribution at angle θ (Skemer et al., 2005). The M-index varies from 0 for a random distribution of misorientation angles to 1 for a single crystal fabric. Functions for the calculation of these texture indices are implemented in the MTEX toolbox (Mainprice et al., 2015).

3 Results

3.1 Microstructural description

The mineral modal analysis of the blueschists used in our seismic anisotropy calculations was conducted using the indexed areas of the EBSD maps collected on the selected representative regions of the structural reference frame-oriented thin sections. The modal abundance of the mineral phases was estimated by measuring the area fractions of each individual phase in the indexed 2-D sections of the EBSD maps. The modal abundance calculations exclude the low confidence data removed during data cleaning (section 2.3) and the indexed titanite data (section 2.3.1), and are used in the elastic stiffness matrix and density calculations for all samples. As discussed in section 2.1, the mapped regions were selected to be representative of the mineralogy of the hand samples and are treated as volume fractions in the 3-D rock volumes (after Heilbronner & Barrett, 2014). Glaucophane comprises a significant fraction of all indexed phases in the EBSD maps (37–96%), and the sample foliations and lineations are largely defined by the orientation of elongate glaucophane grains (Figs. 3, 4a-d,g,h). Eight of the nine epidote blueschist samples contain less than 40% epidote, while sample LAB572 contains a dominant fraction of epidote (55%; Fig. 4e,f). Elongate epidote grains are most often aligned with their longest dimension parallel to the sample foliation. The lawsonite blueschists are composed of lawsonite modes ranging from 19–56% occurring either as lawsonite-rich layers of anhedral grains elongated with the foliation, or subhedral porphyroblasts with no strong preferred orientations (Fig. 4c,d). Garnet (<15%), when present, often occurs as small, anhedral grains distributed in glaucophane-rich layers, or as porphyroblasts up to 5 mm in diameter with fractures filled by glaucophane, epidote, phengite, quartz, and/or chlorite (Fig. 4g,h). Phengite is often present in minor abundances (<2%) in these mafic-protolith blueschists (Fig. 4a-f). When present in greater abundances, phengite is associated with epidote or glaucophane, or concentrated in garnet pressure-shadows (up to ~9%; Fig. 4g,h). Jadeite, omphacite, quartz, chlorite, rutile, and titanite typically appear in the samples in modes <5% with limited exceptions. The error percentage of the modal abundance calculations was determined relative to the number of grains indexed for each phase as

$$error\ \%\ (phase) = \left(\frac{1}{\sqrt{N}}\right) * (areal\ modal\ \%) \tag{10}$$

where *N* is the number of grains indexed for the phase (Heilbronner & Barrett, 2014). The error of the modal abundances is << 1% for most phases in all samples, with a maximum error of ~4%

for the garnet fraction in LAB570 due to a significant volume of garnet (9%) contained in 5 grains (Table S1). The areal modal analysis of the indexed EBSD maps used in our anisotropy calculations is included in Table 3.

Table 3: *EBSD-based Areal Modal Analysis*[a,b]

Sample	Gln %	Ep %	Lws %	Ph %	Grt %	Jd %	Omp %	Qz %	Chl %	Rt %
Epidote Blueschist										
BAN09	60.86	38.10		0.01	0.31	0.01		0.71		
BAN15	85.78	10.35		3.80						0.07
CY106	58.89	11.29		0.78	14.48		4.64	1.32	7.68	0.93
CY107	77.87	0.28		8.57	11.93		0.12	0.51	0.69	0.04
DR221	81.60	5.59		0.28	11.91			0.08	0.13	0.41
LAB34	62.18	28.89		8.12	0.49		0.02		0.14	0.15
LAB555	95.75	0.58		0.08		0.08	0.10	3.07	0.28	0.06
LAB570	54.65	32.63		0.20	9.33			2.34	0.29	0.56
LAB572	36.94	55.39		0.91	1.77	3.27	0.06	0.29	0.05	1.32
Lawsonite Blueschist										
C18G1003C01	43.02		56.26	0.03	0.28	0.31	0.05	0.01	0.04	
DR265	64.22	0.07	18.84	0.68	0.77	14.90	0.10	0.41		
GB15-02A	61.56		20.64	0.56	4.46		0.01	12.74		0.02
SV01-49A	41.61		42.94	1.51	0.85	2.69	0.08	9.89	0.21	0.22
01GSN2-3	45.74	0.03	18.70	4.04	3.13	3.17	0.12	24.83	0.04	0.21

[a] Mineral abbreviations after Whitney & Evans (2010): Gln = glaucophane, Ep = epidote, Lws = lawsonite, Ph = phengite, Grt = garnet, Jd = jadeite, Omp = omphacite, Qz = quartz, Chl = chlorite, Rt = rutile

[b] All mineral percentages are expressed as the indexed area % of each mineral from reduced EBSD dataset reported by MTEX to 2 decimal places that were used in subsequent seismic anisotropy calculations (section 3.1)

3.2 Crystallographic Preferred Orientations (CPOs)

Fabric development was evaluated for the minerals glaucophane, epidote, lawsonite, and phengite in each blueschist sample by calculating the pfJ-index, the J-index, and the M-index as described in section 2.3.2. These texture indices were calculated by two different procedures: (1) using the complete set of indexed EBSD orientations, and (2) as one point-per-grain (1ppg) using the mean orientation calculated from the set of all indexed orientations in each grain. The pfJ-indices (Eq. 7) were determined for the [100], [010], and [001] crystallographic axes (the *a*-, *b*-, and *c*-axes, respectively) from pole figures calculated for each phase (complete orientation set pole figures, Fig. S2; 1ppg pole figures, Fig. S3). The CPO projections for the full EBSD orientation datasets are qualitatively similar to the 1ppg results, and the calculated pfJ-indices display only small deviations between the full EBSD datasets and 1ppg values. Here, we report the pfJ-index for the full sets of indexed orientations that are utilized in the seismic anisotropy calculations, but will reference the 1ppg pfJ-indices (Table S2) in our discussion of *P* wave seismic anisotropy and CPO strength (section 4.2) to remain consistent with previous investigations (e.g., Fujimoto et al., 2010; Kim et al., 2013; Cao & Jung, 2016). While our analysis will focus on the correlation between the pfJ-indices of each phase and the anisotropy, we have included all pfJ-index, J-index, and M-index values for each sample calculated by both procedures in Table S2 for completeness.

3.2.1 Glaucophane CPOs

The glaucophane CPO in five of the samples displays the type-I amphibole CPO most prevalent in the rock record (e.g., Kim and Jung, 2019; Figs. 2c, 5a), which is defined by density maxima in each of the [100], [010], and [001] principal crystallographic axes. The [001] axes display a density maximum oriented parallel to the X-direction in the specimen reference frame (the lineation direction) while the density maximum of the [100] axes is oriented normal to the foliation plane (Z-direction). The [010]-axis density maximum lies in the foliation plane, parallel to the Y-direction (defining the foliation; e.g., Fig. 5a). The glaucophane in sample DR265 (Fig. 5b) displays the type-III amphibole CPO (Fig. 2c) that was developed in two of the samples, with an [100]-axis density maximum oriented normal to the foliation as in the type-I CPO, but is distinguished by a girdle composed of the [010] and [001] axes contained within the foliation plane. The type-IV glaucophane CPO (Fig. 2c) in seven of the samples is also characterized by a [001]-axis density maximum parallel to the lineation, but differs from the type-I CPO in the [100] and [010] axes, which describe a girdle in the Y-Z plane, normal to the lineation (e.g., Fig. 5c). The fabric strength of the glaucophane in the blueschist samples ranges from $pfJ_{[100]}$ = 1.05–1.65, $pfJ_{[010]}$ = 1.01–1.52, and $pfJ_{[001]}$ = 1.11–2.05 (Table S2).

3.2.2 Epidote CPOs

The CPO of epidote in the epidote blueschist samples most frequently occurs with a density maximum of the [010] axis oriented parallel to the lineation (Figs. S2, S3). Several samples with a strong epidote fabric additionally show density maxima of the [001] and [100] axes oriented normal to the sample foliation (Z-direction) and normal to the lineation within the foliation plane (Y-direction), respectively (Figs. S2, S3). This epidote CPO was previously described in Ile de Groix blueschists by Bezacier et al. (2010). Two of the New Caledonia epidote blueschists alternatively display a girdle of [001] and [100] axes normal to the sample lineation in the Y-Z plane (e.g., LAB570 & LAB572 in Figs. S2, S3). Interestingly, the observed CPOs in the nine epidote-bearing blueschists in this compilation are not reproduced in experimentally-deformed blueschists (e.g., Park et al., 2020). The fabric strength of epidote in the epidote blueschists ranges from $pfJ_{[100]}$ = 1.03–2.56, $pfJ_{[010]}$ = 1.12–2.73, and $pfJ_{[001]}$ = 1.14–2.70 (Table S2).

3.2.3 Lawsonite CPOs

Lawsonite displays one of two fabrics depending on the distribution of the phase within the sample. In samples with large lawsonite porphyroblasts separated in a matrix of fine-grained glaucophane, the lawsonite displays a random CPO (e.g., Fig. 5c). Lawsonite in samples with similar grain-size distributions as glaucophane and layers composed primarily of interconnected lawsonite grains develop a CPO with the [001]-axis density maximum oriented normal to the foliation (Z-direction) and the [100] and [010] axes oriented either as density maxima within the foliation (e.g., Fig. 5b) or as a girdle parallel to the foliation plane (e.g., 01GSN2-3, Figs. S2, S3). Cao and Jung (2016) described this lawsonite CPO as the “normal-type” fabric, which has been frequently observed in naturally deformed lawsonite blueschists (e.g., Cao et al., 2014;

Choi et al., 2021). Lawsonite fabric strength in the lawsonite blueschists covers a range of $\mathrm{pfJ}_{[100]} = 1.03–1.99$, $\mathrm{pfJ}_{[010]} = 1.02–2.30$, and $\mathrm{pfJ}_{[001]} = 1.09–2.01$ (Table S2).

3.2.4 Phengite CPOs

Phengite frequently occurs in small volumes with a weak fabric/CPO (e.g., Fig. 5c). In samples with larger phengite fractions (~3–10%), the CPO has a [001]-axis density maximum oriented normal to the foliation (Z-direction) and the [100] and [010] axes oriented in a girdle in the foliation plane (e.g., CY107, Figs. S2, S3). Phengite fabric strength in the blueschists ranges from $\mathrm{pfJ}_{[100]} = 1.05–2.70$, $\mathrm{pfJ}_{[010]} = 1.06–2.70$, and $\mathrm{pfJ}_{[001]} = 1.24–2.78$ (Table S2). This is typical of CPOs in micas (Mahan, 2006; Lloyd et al., 2011).

3.3 Seismic anisotropy

The VRH-averaged effective elastic stiffness matrices in Voigt notation are shown in Table 4. The calculated Voigt matrices were used as inputs to solve the Christoffel equation (Christoffel, 1877) for the *P* and *S* plane wave velocities and polarizations, and to calculate the resultant seismic anisotropies at dry, ambient P-T conditions (AVp %, AVs_1 %, AVs_2 %, and AVs %; Eqs. 3-5). All calculated seismic properties including maximum/minimum Vp, Vs_1, and Vs_2 velocities, anisotropies, and maximum shear wave splitting orientation are included in Table 5, and stereographic projections of all calculated seismic properties are included in Figure S4.

The symmetry decomposition method of Browaeys and Chevrot (2004) was used to evaluate the symmetry of the Voigt elastic stiffness matrices of each sample, and the resultant anisotropy, by progressively subtracting out the isotropic, hexagonal, tetragonal, orthorhombic, and monoclinic symmetry components—leaving the triclinic component. The results of the symmetry decomposition are included in Table S3 as the percentage of the Voigt elastic stiffness matrix represented by the isotropic, hexagon, orthorhombic, and remaining (tetragonal, monoclinic, and triclinic) symmetry classes. The anisotropic symmetry components of the Voigt matrices were plotted on a ternary diagram to display the extent to which each sample can be represented by hexagonal, orthorhombic, or other (tetragonal + monoclinic + triclinic) symmetry (Fig. S5). The symmetry of all the Voigt matrices is predominantly hexagonal, with LAB570 displaying the largest orthorhombic with ~2.7 % orthorhombic symmetry and ~3.7 % hexagonal symmetry. This dominant contribution of hexagonal symmetry to anisotropy in blueschists is consistent with the results of Brownlee et al. (2017) for amphibole-rich deep crustal rocks.

3.3.1 *P* wave seismic anisotropy

The maximum *P* wave velocities of all blueschists in the compilation are oriented within the sample foliation and parallel to sub-parallel to the lineation and range from $\mathrm{Vp}_{\mathrm{max}} = 7.82$ km s^{-1} (LAB34) to 8.47 km s^{-1} (CY107). The minimum *P* wave velocities of the samples are oriented

Table 4: *VRH-Averaged Effective Elastic Stiffness Matrices in Voigt Notation[a] (in GPa)*

C18G1003C01 Lawsonite blueschist (AVp = 1.5%)
(density = 3.08 g/cm^3)

193.2	74.4	76.3	0.6	-0.6	0.3
	188.1	71.6	-0.1	-0.4	-0.1
		188.8	-0.1	-0.3	0.5
			58.3	0	-0.0
				57.2	-0.2
					57.2

SV01-49A Lawsonite blueschist (AVp = 3.8%)
(density = 3.05 g/cm^3)

187.0	64.7	66.1	0.1	-3.1	1.3
	176.5	66.0	1.1	0.4	0.0
		181.8	0.9	-1.5	0.2
			58.0	-0.2	0.1
				58.4	0.5
					56.8

LAB572 Epidote blueschist (AVp = 6.8%)
(density = 3.31 g/cm^3)

204.5	61.1	61.9	0.6	4.3	3.0
	183.1	60.7	-0.6	0.3	1.3
		185.5	-0.2	2.2	0.4
			61.8	0.8	0.8
				65.7	0.3
					64.1

GB15-02A Lawsonite blueschist (AVp = 9.0%)
(density = 3.05 g/cm^3)

193.9	56.0	61.2	0.3	4.5	-2.2
	165.8	54.7	0.5	0.7	-0.4
		181.6	0.4	3.0	-0.9
			58.7	-0.1	0.5
				63.0	0.0
					59.4

CY106 Epidote blueschist (AVp = 9.5%)
(density = 3.19 g/cm^3)

219.3	61.8	65.6	1.5	2.7	1.8
	184.7	61.7	3.0	0.1	1.1
		198.9	1.2	3.3	0.1
			64.9	0.5	0.8
				69.5	2.0
					67.6

DR265 Lawsonite blueschist (AVp = 10.1%)
(density = 3.12 g/cm^3)

211.6	59.9	75.4	-0.0	0.3	0.8
	175.8	61.3	0.2	0.2	0.4
		208.7	0.6	0.9	0.8
			62.2	0.3	-0.6
				70.9	0.3
					62.0

LAB570 Epidote blueschist (AVp = 10.2%)
(density = 3.26 g/cm^3)

215.8	58.6	63.5	0.5	-0.8	-3.4
	177.1	59.8	0.5	-0.1	-1.2
		192.8	2.1	0.4	-0.1
			62.9	-0.4	-0.4
				68.4	1.3
					64.5

01GSN2-3 Lawsonite blueschist (AVp = 10.3%)
(density = 2.99 g/cm^3)

182.8	47.9	56.1	1.8	3.0	3.0
	152.5	48.0	1.1	-0.1	1.3
		175.1	2.0	1.2	1.3
			56.4	0.5	0.3
				61.0	0.9
					56.4

DR221 Epidote blueschist (AVp = 10.7%)
(density = 3.18 g/cm^3)

218.8	60.8	63.1	1.0	-1.8	3.5
	179.7	58.6	2.3	0.1	2.0
		193.2	2.4	-1.5	0.9
			63.7	0.6	-0.7
				70.3	1.1
					67.7

LAB34 Epidote blueschist (AVp = 10.9%)
(density = 3.16 g/cm^3)

191.7	55.3	57.5	2.7	1.3	0.6
	172.6	52.9	6.8	0.1	-0.4
		169.9	8.3	0.2	-0.4
			58.6	-0.2	0.1
				62.0	4.0
					62.7

BAN09 Epidote blueschist (AVp = 12.8%)
(density = 3.21 g/cm^3)

205.1	54.7	60.4	2.0	0.4	-4.4
	162.1	54.7	3.3	-0.3	-2.2
		187.8	4.2	0.3	-0.7
			59.6	-1.4	-0.1
				66.9	2.0
					60.9

BAN15 Epidote blueschist (AVp = 13.8%)
(density = 3.10 g/cm^3)

198.7	50.5	58.5	-1.4	2.5	-3.7
	154.4	51.9	-2.1	0.7	-2.0
		189.4	-3.2	1.8	-1.1
			58.1	-1.3	0.3
				68.2	-0.8
					60.2

CY107 Epidote blueschist (AVp = 17.4%)
(density = 3.12 g/cm^3)

220.7	55.5	64.2	3.4	-5.1	-0.2
	161.0	55.9	4.6	0.2	0.4
		195.7	7.4	-3.2	-0.5
			60.4	-0.1	-0.9
				71.4	3.3
					62.1

LAB555 Epidote blueschist (AVp = 19.9%)
(density = 3.06 g/cm^3)

211.4	49.0	59.3	3.2	-1.8	6.9
	147.5	48.8	5.5	0.1	3.7
		188.2	7.8	-1.4	1.6
			58.4	1.6	0.0
				69.6	2.7
					60.5

[a] Voigt matrix notation formulation shown in Eq. 2

normal to the foliation plane and range from Vp_{min} = 6.84 km s^{-1} (LAB555) to 7.81 km s^{-1} (C18G1003C01). Figure 6a displays the patterns of the *P* wave velocities for each sample plotted as contoured, equal-area, upper-hemisphere spherical projections in order of increasing AVp.

The blueschists in this study display a broad range of *P* wave anisotropies extending from a minimum AVp = 1.5% for the lawsonite blueschist C18G1003C01 from Corsica, France to a maximum AVp = 19.9% for the epidote blueschist LAB555 from the Pam Peninsula, New Caledonia (Table 5). The salient feature of the *P* waves anisotropies in Figure 6a is that half of the blueschist samples show AVp values ~10%, despite their variance in mineral assemblages (Fig. 6b).

The upper-hemisphere spherical projections of the *P* wave velocities display three different seismic anisotropy patterns that were previously observed in amphibolite facies deep crustal rocks (Ji et al., 2013; Kim & Jung 2020; Liu & Cao, 2023). We describe the patterns using the terminology of Liu and Cao (2023) where Vp(X) is the velocity in the X-direction (parallel to the lineation), Vp(Y) is the velocity in Y-direction (normal to the lineation in the foliation plane), and Vp(Z) is the velocity in the Z-direction (normal to the foliation plane). In the blueschists with the highest AVp % magnitudes, the Vp pattern is Vp(X) > Vp(Y) > Vp(Z) and is correlated to a type-I CPO in glaucophane (Fig. 5a). The two blueschists in our study with a type-III CPO in glaucophane display Vp patterns with Vp(X) ≈ Vp(Y) > Vp(Z) (Fig. 5b). Blueschists with the lowest AVp % magnitudes display Vp patterns with Vp(X) > Vp(Y) ≈ Vp(Z) and glaucophane with a type-IV CPO (Fig. 5c). In the remainder of the text, these Vp patterns will be referred to as Vp-pattern I (Vp(X) > Vp(Y) > Vp(Z)), Vp-pattern III (Vp(X) ≈ Vp(Y) > Vp(Z)), and Vp-pattern IV (Vp(X) > Vp(Y) ≈ Vp(Z)) based on their association with the observed CPO types of the same number.

3.3.2 *S* wave seismic anisotropy

The fast and slow shear wave maximum/minimum velocities are included in Table 5, and result in calculated seismic anisotropies ranging from AVs_1 = 1% and AVs_2 = 0.9% (C18G1003C01) to AVs_1 = 9.2% and AVs_2 = 5.7% (LAB555). The calculated AVs_1, AVs_2, and AVs percentages do not follow the same trend of increasing magnitude that is observed in the blueschist AVp percentages (Fig. S6), and two of the samples yield AVs_2 percentages that are larger than AVs_1 (e.g., Fig. S6, CY106 and DR221). For all samples other than C18G1003C01, the fast shear wave polarization is contained within the foliation for S_1 waves propagating along the X-Y plane and parallel to the lineation for S_1 waves propagating in the Z-direction (Figs. 5, S4). In the lawsonite blueschist C18G1003C01, the polarizations of the fast shear waves are reversed from that observed in the other blueschists of the compilation (Fig. S4).

The Corsican lawsonite blueschist, C18G1003C01, displays the lowest magnitude of maximum shear wave splitting (AVs_{max} = 1.3 %) and the epidote blueschist LAB555 from New Caledonia displays the highest magnitude of shear wave splitting (AVs_{max} = 10.4%). The maximum shear wave splitting percentage of most samples is less than 7% and most often is contained within the foliation plane with orientations varying from lineation-parallel to lineation normal (Table 5, Fig. S4). The calculated AVs magnitudes generate modest Vs_1/Vs_2 delay times in blueschist layers with thicknesses observed in exhumed subduction terranes or with thicknesses of the same order as oceanic crust (~7 km) except for steep subduction angles (~45–60°; e.g., Cao et al., 2013; Ha et al., 2019; Park & Jung, 2022).

Table 5: *P and S Wave Velocities and Seismic Anisotropies at Room Temperature and Pressure*

Sample	Rock Type[a]	Location[b]	Vp (km/s)		AVp (%)	Vp Pattern	Gln CPO	Vs_1 (km/s)		AVs_1 (%)	Vs_2 (km/s)		AVs_2 (%)	AVs max (%)	Max shear wave splitting orientation[c]
			max	min				max	min		max	min			
C18G1003C01	LBS	Corsica, FR	7.92	7.81	1.5	Vp(X)>Vp(Y)≈Vp(Z)	type-IV	4.36	4.31	1.0	4.34	4.30	0.9	1.3	lineation-⊥, ∠ to foliation
SV01-49A	LBS	Sivr. Mas. TR	7.90	7.60	3.8	Vp(X)>Vp(Y)≈Vp(Z)	type-IV	4.44	4.32	2.8	4.36	4.27	2.2	4.0	lineation-∥, ∠to foliation
LAB572	EBS	Pam Penins. NC	7.93	7.40	6.8	Vp(X)>Vp(Y)≈Vp(Z)	type-IV	4.51	4.39	2.8	4.42	4.30	2.7	3.8	∠ to lineation, foliation-∥
GB15-02A	LBS	Catalina CA	8.06	7.37	9.0	Vp(X)>Vp(Y)>Vp(Z)	type-IV	4.57	4.41	3.5	4.49	4.37	2.7	4.2	∠ to lineation, foliation-∥
CY106	EBS	Tinos GR	8.32	7.56	9.5	Vp(X)>Vp(Y)>Vp(Z)	type-IV	4.74	4.59	3.2	4.65	4.46	4.3	5.0	∠ to lineation, ∠ to foliation
DR265	LBS	Diablo Rng. CA	8.31	7.51	10.1	Vp(X)≈Vp(Y)>Vp(Z)	type-III	4.77	4.49	6.2	4.61	4.44	3.8	6.8	lineation-∥, foliation-∥
LAB570	EBS	Pam Penins. NC	8.16	7.37	10.2	Vp(X)>Vp(Y)>Vp(Z)	type-IV	4.67	4.43	5.2	4.53	4.35	4.2	6.2	∠ to lineation, foliation-∥
01GSN2-3	LBS	S. Motagua GT	7.90	7.13	10.3	Vp(X)>Vp(Y)>Vp(Z)	type-I	4.56	4.34	5.0	4.44	4.33	2.9	5.3	∠ to lineation, foliation-∥
DR221	EBS	Diablo Rng. CA	8.32	7.48	10.7	Vp(X)>Vp(Y)>Vp(Z)	type-IV	4.75	4.60	3.2	4.63	4.47	3.7	5.6	lineation-⊥, foliation-∥
LAB34	EBS	Diablo Rng. CA	7.82	7.01	10.9	Vp(X)≈Vp(Y)>Vp(Z)	type-III	4.60	4.32	6.4	4.34	4.27	1.7	6.7	lineation-∥, foliation-∥
BAN09	EBS	Bandon OR	8.01	7.05	12.8	Vp(X)>Vp(Y)>Vp(Z)	type-I	4.61	4.32	6.5	4.44	4.29	3.5	7.0	lineation-⊥, foliation-∥
BAN15	EBS	Bandon OR	8.08	7.04	13.8	Vp(X)>Vp(Y)>Vp(Z)	type-I	4.70	4.40	6.7	4.48	4.32	3.6	8.4	lineation-⊥, foliation-∥
CY107	EBS	Tinos GR	8.47	7.12	17.4	Vp(X)>Vp(Y)>Vp(Z)	type-I	4.84	4.43	8.8	4.60	4.35	5.7	10.0	lineation-⊥, foliation-∥
LAB555	EBS	Pam Penins. NC	8.36	6.84	19.9	Vp(X)>Vp(Y)>Vp(Z)	type-I	4.82	4.40	9.2	4.53	4.33	4.4	10.4	lineation-⊥, foliation-∥

[a] Rock Type: LBS = lawsonite blueschist, EBS = epidote blueschist

[b] Sample peak P-T condition estimates from the literature included in Table 1

[c] Max shear-splitting orientation notations: ⊥ = normal, ∥ = parallel, ∠ = at an angle (~30-60 degrees)

4. Discussion

Below, we explore the effect of variations in modal mineralogy and CPO strength on the seismic anisotropy of mafic blueschists. *S* wave anisotropy, and the resultant shear wave splitting delay times between Vs_1 and Vs_2, are tools that are useful to understanding the seismic anisotropy of the mantle wedge (Long, 2013). However, the technique is a path-integrated measurement that provides weak constraints on the depth of the anisotropic layer; application of the technique is further complicated by the small delay times our AVs results generate in blueschist units with thicknesses observed in exhumed blueschist units (10s to a few 1000s of m). In contrast, receiver function analysis of *P* to *S* conversions of teleseismic waves can resolve contrasts in anisotropy to ~2km in thickness (Schulte-Pelkum & Mahan, 2014b), and shows potential for imaging blueschist-metamorphosed oceanic crust (Long, 2013), therefore, we focus on AVp, while reporting calculated shear wave splitting values in Fig. S4. We first consider the effect of modal composition and CPO strength independently on the resulting AVp. Next, we consider the combined effects of mineralogy and CPO strength by modeling two-phase aggregates, and the impact of increasing metamorphic grade on the *P* wave anisotropy. Lastly, we explore the implications of blueschist anisotropy for the investigation of subduction zones.

4.1 AVp % and modal composition

While the blueschists of our study display a wide range of *P* wave anisotropy (1.5–19.9%; Fig. 6a; Table 5), we note that the samples are composed primarily (>70%) of the minerals glaucophane, epidote, lawsonite, and phengite—each of which is strongly anisotropic (Fig. 6b). We plotted the AVp as a function of the modal composition of each phase and found a clear positive correlation between the abundance of glaucophane and the resultant AVp of the sample (Fig. 7a). Increasing fractions of either epidote (Fig. 7b) or lawsonite (Fig. 7c) correspond to a reduction of the sample AVp. Although phengite is the most anisotropic phase commonly found in blueschists, we observed no trend between increasing modal abundance of phengite and the AVp magnitude of the samples (Fig. 7d). This lack of clear correlation between increasing fractions of phengite and AVp magnitude is likely due to weak phengite fabrics and a relatively low phengite abundance (typical of mafic blueschists). The four samples containing phengite fractions greater than 3% display *P* wave anisotropy magnitudes > 10% (Table 5), signifying a potential contribution by phengite to the magnitude and symmetry of the anisotropy if it occurs in higher abundances. The increase in AVp with increasing glaucophane modal abundance and decreasing AVp with increasing epidote or lawsonite are consistent with the measured single-crystal seismic properties of each phase (Fig. 2b; Bezacier et al., 2010; Aleksandrov et al., 1974; Schilling et al., 2003), where glaucophane is the most anisotropic mineral of the three with respect to *P* waves.

To evaluate the extent to which each mineral phase enhances or dilutes the bulk seismic anisotropy, we modeled the relationship between the AVp and mineral mode by linear regression for glaucophane, epidote, and lawsonite (Fig. 7a-c). Multivariate linear regression would be a tool to model the trend in AVp as a contribution from multiple uncorrelated variables, however, the modal fractions of an aggregate do not vary independently, thus precluding this approach. Consequently, we modeled the relationship between each phase and the bulk AVp by single linear regression. Best-fit lines to the anisotropy trends in glaucophane and epidote display slopes of +0.22 for the AVp % versus glaucophane abundance and -0.10 for the AVp % versus epidote abundance, respectively (Fig. 7a,b), a relationship that reflects the contrast in single-crystal *P* wave anisotropy between glaucophane (max AVp = 38.1%) and epidote (max AVp = 26.5%). The single-crystal anisotropy of lawsonite (max AVp = 24.1%) is similar to that of epidote, and so a similar trend might be expected. However, the best-fit line for AVp versus lawsonite abundance shows a slope of -0.23 (Fig. 7c). The dilution of the bulk anisotropy cannot be explained solely by the difference in mode between glaucophane and lawsonite, or by glaucophane mode alone; some samples with similar modes have large variations in anisotropy. Thus, we must include the effect of CPO on the seismic anisotropy generated by each phase, a relationship we explore below.

4.2 AVp % and CPO strength

Previous work on the seismic anisotropy of deformed rocks links the development of significant seismic anisotropy to the creation of strong CPOs by plastic deformation processes (e.g., Mainprice & Nicolas, 1989; Almqvist & Mainprice, 2017). We observe a strong correlation between the glaucophane CPO type (Figs. 2c, 5, S2, S3), the AVp magnitude, and symmetry of the AVp patterns (Fig. 6a; Table 5). Blueschists with a type-I glaucophane CPO display Vp-pattern I, and result in AVp percentages from 10.3–19.9%. The two blueschists with type-III glaucophane CPOs display Vp-pattern III, and yield AVp percentages of 10.1% and 10.9%. Blueschists with type-IV glaucophane-CPOs transition from Vp-pattern IV in samples with the lowest *P* wave anisotropy (AVp = 1.5–6.8%) to Vp-pattern I with higher *P* wave anisotropies (AVp = 9–10.7%). This transition in the Vp pattern is accompanied by increased density of the [100] and [010] crystallographic axes in the Z- and Y-directions respectively that implies a transition between the type-IV and type-I amphibole CPOs in these samples. The magnitude of AVp percentages of the blueschists in our compilation can be broadly ordered as AVp(Vp-pattern I) > AVp(Vp-pattern III) > AVp(Vp-pattern IV) in agreement with the trend observed for the hornblende-group amphiboles in amphibolites (Fig. 8a; Ji et al., 2013; Kim & Jung 2020; Liu & Cao, 2023). We infer from these results that the glaucophane CPO strength and type exerts a strong control on the magnitude and symmetry of the *P* wave seismic anisotropy in blueschists.

To explore the effects of CPO strength of each crystallographic axis on the magnitude of the *P* wave seismic anisotropy, we plotted the AVp versus the pfJ-index (calculated as 1ppg) for the [100], [010], and [001] crystallographic axes for glaucophane, epidote, lawsonite, and phengite. We colored each datapoint by Vp pattern and modeled the AVp versus pfJ-index trends using linear regression to assess the dependence of the seismic anisotropy magnitude on the CPO strength of each phase (Fig. 8). After performing a Pearson correlation test (Freedman et al., 2007), we determined the strength of correlation between the pfJ-indices and AVp magnitude and the confidence interval of the fit did not justify a multivariate linear regression, therefore, we used single linear regression for this analysis. We excluded two outliers (DR265 and 01GSN2-3; Fig. 8a, open circles) from the best-fit results for glaucophane. We observed steep increases in AVp with the pfJ-index of the glaucophane axes, with a positive correlation in the [100] axis (slope = 33.84, $R^2 = 0.77$), and a weak AVp to pfJ-index relationship for the [010] axis (slope = 44.07, $R^2 = 0.41$) and [001] axis (slope = 13.47, $R^2 = 0.33$; Fig. 8a). In epidote and lawsonite, the increase in pfJ-index of each crystallographic axis weakly correlates with shallow increases in AVp (slopes < 10; Fig. 8b-c), and phengite does not display a clear linear relationship between CPO strength and sample AVp (Fig. 8d).

The qualitative relationship between glaucophane CPO type, the Vp pattern symmetry, and AVp magnitude implies that strong alignment of the glaucophane [100] and [010] axes enhances blueschist anisotropy. It is notable that we do find a moderately strong CPO in the [001] axis in all of our samples, even when the [100] and [010] axes are weakly oriented. Alignment of the [001] axis generates low-magnitude seismic anisotropy which is typical in the early stages of ductile deformation of blueschists (Park et al., 2020). The strong increase in AVp with CPO strength in the glaucophane [100] and [010] axes (Fig. 8a) suggests that strong alignment of these axes exerts a key control on the resultant anisotropy magnitude (and Vp pattern). To evaluate the relative importance of the glaucophane [100] and [010] axes to the bulk anisotropy, we plotted each sample's calculated maximum, minimum, and median *P* wave velocities versus the AVp percentage in Figure 8e. Vp_{max} increased by ~5.5% (from 7.92 km s^{-1} to 8.36 km s^{-1}) between the least anisotropic sample (C18G1003C01, AVp = 1.5%) and most anisotropic sample (LAB555, AVp = 19.9%). We observed decreases in Vp_{min} and the median *P* wave velocity (Vp_{med}) of ~12.4% (from 7.81 km s^{-1} to 6.84 km s^{-1}) and ~3.4% (from 7.87 to 7.6 km s^{-1}), respectively, between the two samples. We associate the reduction in Vp_{min}—the greatest change in Vp in our results—with stronger alignment of the glaucophane [100] axis after the single-crystal elasticity measurements of Bezacier et al. (2010). Based on this analysis, we assert that the strength of the CPO in the [100] axis exerts the strongest control on the magnitude and symmetry of seismic anisotropy in mafic blueschists, once the [001] axis is already aligned.

4.3 AVp % of two-phase rock recipe models

Based on the restrictions that exclude the application of multivariate regression analysis of our data, we applied an alternative approach of rock recipe modelling to explore the relative contributions of mineral abundances and CPO strength to the bulk seismic anisotropy of our compilation samples (e.g., Lloyd et al., 2011; Ward et al., 2012; Bernard et al., 2021). We constructed two-phase rock recipe models for each sample using the ODFs that were calculated for glaucophane and epidote or lawsonite in the full mineral assemblage. We then modeled the Vp anisotropy patterns and AVp percentage by the same method as for the full mineral assemblages, but limited to normalized ratios of glaucophane/epidote (Gln/Ep; epidote blueschists) or glaucophane/lawsonite (Gln/Lws; lawsonite blueschists) ranging from 0 to 100 percent glaucophane (Figs. 9, S7). Our methodology assumes that the CPO strength of each phase in the naturally-deformed polyphase rocks will remain constant across the range of compositions in the modelled two-phase aggregates. *In situ*, strain-partitioning in a naturally-deformed rock depends on the total magnitude of strain and strain-rate experienced by the rock, the temperature under which the rock was deformed, and strength contrasts between adjacent phases (Lloyd et al., 2011; Park et al., 2020). These limitations should be considered when extending these modeling results to natural samples.

4.3.1 Epidote blueschist AVp modeling

The Vp anisotropy pattern modeling results for a representative epidote blueschist sample (LAB555) are displayed in Figure 9a for the glaucophane/epidote ratios: 0/100, 20/80, 40/60, 60/40, 80/20, and 100/0. The glaucophane and epidote in this sample have moderately strong, complementary CPOs (Figs. S2, S3; Table S2), consequently, the AVp is substantial for all modeled Gln/Ep ratios and monotonically increases from 11.0% to 20.5% with increasing glaucophane fraction (Fig. 9a,c). Vp_{max} and Vp_{min} remain oriented parallel to the lineation and normal to the foliation respectively for all modeled Gln/Ep ratios.

Our rock recipe models of the remaining epidote blueschists in this compilation similarly show monotonic increases in AVp on the order of ~5–10% between the pure epidote and pure glaucophane models (Fig. 9c) with the exception of CY106. This sample is composed of strongly aligned epidote and glaucophane with a weak type-IV CPO (Figs. S2, S3), and exhibits a decrease in AVp with increasing glaucophane. While CY106 contains ~8% chlorite with a preferred orientation (Figs. S2, S3), a phase that also may contribute substantially to seismic anisotropy (Kim & Jung, 2015; Kang & Jung, 2019; Kim et al., 2020), the AVp prediction of our two-phase model is ~5% higher in magnitude than for the bulk assemblage calculation (Fig. 9c; Table 5). Though CPOs of glaucophane and epidote are not fully complementary in all samples (e.g., Figs. S2, S3, LAB34 and LAB572), we found the orientation of the maximum and minimum P-wave velocities reflected the glaucophane CPO in all models with 20% or greater fractions of glaucophane (Fig. S7), meaning it controls the anisotropy orientation. The 100 % glaucophane models in Figure 9c display ~10% difference in AVp magnitude between a sample with a weak type-IV glaucophane CPO (LAB572) and a strong type-I glaucophane CPO (CY107). Taken together with our discussion of AVp dependence on modal abundance and CPO for the full sample mineral assemblages, these models imply that the seismic anisotropy of epidote blueschists is largely controlled by the modal abundance and CPO of glaucophane.

4.3.2 Lawsonite blueschist AVp modeling

Vp anisotropy pattern models for sample 01GSN2-3, a lawsonite blueschist with strong type-I glaucophane CPO and normal-type lawsonite CPO, are presented in Figure 9b across a range of glaucophane/lawsonite ratios. The antithetically aligned fast-velocity axes of glaucophane and lawsonite in the sample (Figs. 2b, S2, S3; Table S2) result in a concave AVp profile with maximums of 7.9% and 22.7% for models with Gln/Lws ratios of 0/100 and 100/0, respectively (Fig. 9b,d). The minimum AVp ~2.5% occurs at a modeled composition of ~25% glaucophane; below this threshold the orientation the *P* wave velocities are controlled by the lawsonite CPO with Vp_{max} oriented normal to the foliation and Vp_{min} contained within the foliation plane (Figs. 2b, 9d). With >25% glaucophane, the velocity structure reflects the glaucophane CPO, with Vp_{max} parallel to the lineation and Vp_{min} normal to the foliation (Figs. 2b, 9d).

The concave AVp profile of the 01GSN2-3 models was observed previously in lawsonite blueschists (e.g., Kim et al, 2013), and we found similar profiles in the rock recipe modeling for four of the five lawsonite blueschists included in this work (Fig. 9d). The minimum AVp of these models ranged from ~1% to 4.2% and occurred at glaucophane fractions of 20% to 40%. We note that the glaucophane/lawsonite ratio of the AVp minimum, and the accompanying shift of the anisotropy orientation from lawsonite CPO to the glaucophane CPO, does not trend with the pfJ-indices of either phase (Table S2), but depends on the combined CPO strengths of both phases. The AVp profile of sample SV01-49a differs from the other lawsonite blueschists in our compilation. This sample from the Sivrihisar Massif contains larger (>200 μm), unaligned lawsonite porphyroblasts in a matrix of glaucophane with a weak type-IV CPO (Fig. 5c). With no contradictory CPO in lawsonite, our models display a weakly increasing AVp with larger fractions of glaucophane (Fig. 9d) peaking at an AVp of 7.2%, and an anisotropy profile similar to our models for epidote blueschists (Fig. 9c). In this case, unaligned lawsonite acts to dilute the seismic anisotropy, inversely proportional to glaucophane mode.

These results demonstrate that the effect of lawsonite on blueschist seismic anisotropy can be considerable. The contradictory alignment of Vp_{max} and Vp_{min} in strongly aligned lawsonite versus glaucophane rapidly diminishes the contribution of glaucophane to the anisotropy and produces the steeply negative slope in AVp for our samples with increasing lawsonite abundance relative to epidote (Fig. 7b,c). Dilution of the anisotropy by strongly aligned lawsonite has been invoked previously to explain generally lower magnitude of seismic anisotropy observed in lawsonite blueschists (Kim et al., 2013; Cao & Jung, 2016). However, our models demonstrate that lawsonite blueschists with dominant fractions of glaucophane (>80%) may generate AVp anisotropies indistinguishable from epidote blueschists. The dependence of AVp magnitude on glaucophane CPO strength is further supported in our 100% glaucophane models; we observed a broader range of AVp magnitudes (~15%) than found in our epidote blueschist two-phase models (Fig. 9d).

4.3.3 Modeled AVp versus bulk sample AVp

Comparison of the AVp of our two-phase models with the AVp of the bulk sample composition illustrates that the presence of significant fractions of phases with lower elastic anisotropies or weak CPOs may dilute the anisotropy of blueschists. For each modeled AVp profile, we plotted the Gln/Ep (Fig. 9c) or Gln/Lws (Fig. 9d) ratio of the respective sample. Figure 9e is a comparison plot of the AVp of the two-phase model versus the bulk sample calculations for all samples. The AVp percentage of the two-phase models and bulk sample calculations matched within 2% for 8 of 14 blueschists (Fig. 9c,d, circles). The AVp of the remaining 6 models were 2–5% higher than bulk sample calculations (Fig. 9c,d, triangles). Two-phase models with high AVp compared to the bulk sample calculations correlated to samples containing significant fractions of garnet (up to ~15%; CY106, CY107, DR221, DR265, 01GSN2-3), phengite (up to ~9%; CY107, 01GSN2-3), jadeite (~15%; DR265), chlorite (~8%; CY106), or quartz (up to ~24%; LAB570, 01GSN2-3). While the dilution of the anisotropy may be attributed to the high abundance and low elastic anisotropy of garnet in some cases (e.g., CY106, CY107, DR221), in DR265 the lower AVp of the bulk sample calculation stems from the CPO and lower elastic anisotropy of jadeite (Table 3, Figs. S2,S3). The differences between our two-phase models and the bulk samples shows we should regard such two-phase models as a maximum bound on the anisotropy generated by blueschists. However, it is notable that the two-phase models produce similar AVp % predictions as the full mineral assemblages in most models, highlighting the key role played by the glaucophane, lawsonite, and epidote in generating seismic anisotropy in mafic blueschists (Fig. 9e).

4.4 Seismic anisotropy and increasing metamorphic grade

Lawsonite is stable in the lowest grade and coldest temperatures to high pressure conditions of blueschist-facies rocks (lawsonite blueschist facies), while epidote is stable in the warmer, moderate pressure epidote blueschist-facies rocks (Evans, 1990). Therefore, we examined our data for trends in the magnitude of the anisotropy in AVp, AVs_1 , AVs_2 , and AVs as a function of pressure, temperature, and temperature/pressure (Fig. S8). The epidote blueschists display generally higher *P* and *S* wave anisotropies than lawsonite blueschists, in agreement with the observations of other workers (e.g., Bezacier et al., 2010; Fujimoto et al., 2010; Kim at al., 2013; Cao et al., 2013; Park et al., 2020), but we observe no clear trends between the peak P-T conditions experienced by our samples and the magnitude of the seismic anisotropy.

The relationship between seismic anisotropy and increasing metamorphic grade is further complicated by the poorly constrained effects of pressure and temperature on each phase and the full mineral assemblages of each sample. The elastic stiffness constants for many of the constituent phases in blueschist have been measured at only ambient conditions, with few experimental studies to evaluate the sensitivity of the elastic constants to high pressures (e.g., garnet by Chai et al., 1997) or temperatures (e.g., rutile by Isaak et al., 1998). Therefore, our anisotropy calculations were conducted at dry, ambient conditions. An experimental study on an epidote blueschist and two lawsonite blueschists shows decreasing AVp until pressures ~0.7 GPa (attributed to the closing of microcracks in the samples), a weakly decreasing AVp at pressures of 0.7–1 GPa at a constant temperature of 20°C, and weakly increasing AVp at temperatures of 20–400°C at a constant confining pressure of 1 GPa (Fujimoto et al., 2010). In contrast, a density functional theory based study of glaucophane's elasticity at high pressures reports a significant reduction in AVp from ~36% at ambient pressure to ~27% at 4 GPa (Mookherjee & Bezacier, 2012). Combined with the key role glaucophane plays in our AVp models, this suggests pressure effects on the magnitude of seismic anisotropy may be important well beyond the depth of microcrack closure.

Because of the contrary alignment of the fast and slow velocity directions in typical glaucophane and lawsonite CPOs, replacement of lawsonite by epidote with increasing temperatures might enhance the seismic anisotropy. Such enhancement of the anisotropy is dependent on growth of epidote in the complementary CPO to glaucophane frequently observed in epidote blueschists. There are examples in the rock record of epidote pseudomorphs after lawsonite (e.g., Hamelin et al., 2018), but we found no examples of studies that considered the CPOs of lawsonite and epidote in such replacement reactions. If we treat the range of epidote, lawsonite, and glaucophane CPOs in this study as representative and consider an example with a significant lawsonite composition of 40% with the simplifying assumption that all lawsonite is replaced by epidote, then our two-phase rock recipe models yield AVp ranges of 3–10% for lawsonite blueschists and higher anisotropies of 8–17% for epidote blueschists (Fig. 9c,d). This dilution of the anisotropy due to the lawsonite CPO in our models diminishes with decreasing lawsonite abundance.

A more complete understanding of the seismic anisotropy of blueschists with increasing metamorphic grade will require ongoing collaborative work between the geology and rock and mineral physics communities, including elasticity measurements of the constituent phases of blueschists to high pressures and temperatures to facilitate extrapolation of petrofabric-based anisotropy calculations to P-T conditions at the subduction interface in active subduction zones. Texture-related seismic anisotropy studies of samples from exhumed subduction terranes spanning the lawsonite-epidote blueschist transition are needed to assess if these models are representative of the evolution of the anisotropy during the transition. Finally, this work needs to be validated by additional *in situ* measurements of anisotropy in mafic blueschists with varying mineralogies and fabric strengths under dry and wet conditions to account for the effects of pressure, temperature, and fluid pressure on seismic anisotropy.

4.5 Implications for seismic anisotropy of subduction zones

P wave seismic tomography models of subducting crust under Java (Koulakov et al., 2009), Japan (Wang & Zhao, 2008; Wang & Zhao 2012; Wang & Zhao, 2021), and Alaska (Tian & Zhao, 2012) yield azimuthal anisotropies ranging from ~3–10%. While our calculated *P* wave anisotropies do extend to greater magnitudes than the tomographic models, it has been noted that the actual magnitude of the seismic anisotropy may be reduced by the damping and smoothing routines applied in tomographic inversions (e.g., Wang & Zhao, 2021). The blueschists in our compilation typically display higher AVp values than eclogites (< 6%; e.g., Mauler et al, 2000; Bezacier et al., 2010; Worthington et al, 2013, Cao et al., 2016), and while the range of AVp overlaps with peridotites (up to ~15%), the *P* wave velocity of blueschists are typically lower (blueschist Vp_{min}–Vp_{max} = 6.8–8.5 km/s; peridotite Vp_{min}–Vp_{max} = 7.6–8.9 km/s; e.g., Worthington et al., 2013; Liu et al., 2019; Bernard at al., 2021). The *P* wave velocities and anisotropies in this work are useful as natural constraints to differentiate blueschist from other anisotropic lithological units in subduction zones.

The plateau observed at AVp ~10% in seven of our samples merits additional consideration as this represents a potential constraint on the *P* wave anisotropy of blueschist in active subduction zones. While EBSD-based petrofabric studies of seismic anisotropy report AVp values up to 30%, AVp values ~10% are frequently calculated for blueschists in the literature (Kim et al., 2013; Cao et al., 2014; Cao & Jung, 2016; Park & Jung, 2022). Our EBSD-based results predict the *P* wave anisotropy using rock textures measured at mm scales under ambient conditions, but are consistent with AVp values determined by petrophysical methods using larger sample volumes in the literature. Keppler et al. (2017) measured the CPOs of two mafic blueschists using neutron diffraction and calculated AVp values ~ 6.5% and 12%. Fujimoto et al. (2010) and Zertani et al. (2022) measured AVp values ~11% using ultrasonic pulse transmission at elevated P-T conditions (up to 400°C at 1 GPa and 600°C at 600 MPa, respectively). Application of these constraints to interpretation of geophysical data requires consideration of macroscopic geological structure and rock heterogeneities, which can reduce the magnitude and change the symmetry of the observed anisotropy (Okaya et al., 2017; Zertani et al., 2020). Further work integrating micro to outcrop scale observations with macroscale structural features of exhumed, coherent subduction terranes is needed to assess the effects of meso-scale structures on this reported suite of microstructural-based constraints.

Shear wave splitting delay times have been reported in subduction zones ranging from 0.3 s in the Nicaragua subduction zone up to 4.5 s in the Hikurangi subduction zone (e.g., Currie et al., 2004; Long & van der Hilst, 2006; Greve et al., 2008; Abt et al., 2009). The orientation of the fast shear wave, Vs_1, is most frequently observed parallel to the trench (Long, 2013), but trench-normal Vs_1 orientations have been observed in a limited number of subduction zones including the Cascadia subduction zone (Currie et al., 2004) and the Nicaragua subduction zone (Abt et al., 2009). Taking the lineation direction as indicative of the direction of subduction with a 5-km thick anisotropic layer, the New Caledonian blueschist LAB555 can generate trench-parallel anisotropy with a delay time of $dt_{max} \sim 0.1\ s$ (Eq. 6). The Diablo Range blueschist, LAB34, can generate trench-normal anisotropy delay times approaching $dt_{max} \sim 0.07\ s$ with the same parameters and slab subduction at a steep angle (>60°). The low magnitude of the potential shear wave splitting times for the samples in this compilation, in combination with the difficulties inherent in assigning depths to the source of the splitting for path-integrated geophysical measurements (Long, 2013), creates a challenge for the application of shear wave splitting to map blueschist at the subduction interface.

Receiver function analysis provides an alternative approach to image blueschist at the subduction interface. Previous work demonstrated that analysis of receiver functions can resolve variances in the arrival time of teleseismic waves associated with dipping anisotropic layers with thickness and AVp magnitudes applicable to blueschist at the subduction interface (Schulte-Pelkum & Mahan, 2014a, 2014b). Recent work has demonstrated that synthetic receiver function models incorporating blueschist layers with thickness, fabric strength, and anisotropy magnitudes consistent with observations from exhumed blueschists can reproduce observed velocity structure in active subduction zones (e.g., Schulte-Pelkum et al., 2005; Cossette et al., 2016; Kang & Kim, 2019). Our seismic anisotropy results, and the connection between the AVp magnitude, the Vp pattern, and the glaucophane CPO together suggest that receiver function analysis can improve mapping of blueschist and deformation along the subduction interface between the seismogenic zone and the sub-arc (Fig. 1a). The observed dilution of the *P* wave seismic anisotropy with increasing fractions of garnet, jadeite, and quartz in our samples illustrates an additional application of receiver functions to subduction zones. Garnet, pyroxene, and quartz are common reaction products of the blueschist-eclogite transition at the high-temperature limit of the blueschist facies (Evans, 1990), therefore, the accompanying reduction in AVp with eclogitization of blueschist along the interface may facilitate imaging of this transition in individual subduction zones.

5 Conclusions

Our calculations of seismic anisotropy for a range of blueschists from an inventory of globally expansive, exhumed subduction terranes range from 1.5–19.9% for *P* wave anisotropies, with seven samples displaying *P* wave anisotropies ~10%. The AVp magnitude is positively correlated with increasing glaucophane modal abundance, and diluted by increasing modal abundance of epidote or lawsonite. AVp magnitude is similarly enhanced by stronger CPO development in the glaucophane [100] and [010] crystallographic axes. We also observed a relationship between increasing AVp magnitude, the glaucophane CPO type (IV→III→I), and the Vp pattern (IV→III→I). Two-phase rock recipe modeling of glaucophane/epidote and glaucophane/lawsonite aggregates illustrates that CPO production by ductile deformation of glaucophane plays a similarly important role in the magnitude of seismic anisotropy as modal abundances of the phase. We calculated shear wave splitting percentages from 1.3–10.4% that result in trench-parallel and trench-normal shear wave splitting delay times up to 0.1 s and 0.07 s, respectively. Finally, we presented implications for this work including the potential of using seismic receiver functions to map the extent and deformation of blueschists along the subduction interface and determine the depth of the blueschist-eclogite transition in active subduction zones.

Acknowledgments

Part of this work was conducted at the Molecular Analysis Facility, which is supported in part by funds from the Molecular Engineering & Sciences Institute, the Clean Energy Institute, the National Science Foundation (NNCI-2025489 and NNCI-1542101). Funding for portions of this work were provided by the Geological Society of America Graduate Student Research Grant program. The authors are indebted to Darrel S. Cowan, Bruce Nelson, Donna Whitney, Christian Teyssier, Kayleigh Harvey, Sarah Penniston-Dorland, George Harlow, and Joshua M. Garber for their contribution of samples included in this study. The authors also thank Sarah Brownlee for the invaluable assistance with the implementation of the symmetry decomposition analysis.

Conflicts of Interest

The authors declare that they have no conflicts of interest.

Open Research

Datasets for this research are available at this in-text data citation reference: Ott et al. (2023).

Chapter 2 Figures

Figure 1. a) Subduction zone schematic showing distribution of blueschist facies rocks. b) Pressure-temperature conditions of blueschist samples. Facies boundaries from Peacock (2009). Mineral abbreviations after Whitney & Evans (2010) used in metamorphic facies designations (b): Act = actinolite, Amp = amphibole, Ep = epidote, Grt = garnet, Jd = jadeite, Lws = lawsonite, Prh = prehnite, Pmp = pumpellyite; rock type abbreviations used in metamorphic facies designations (b): BS = blueschist; Ecl = eclogite; Amph = amphibolite.

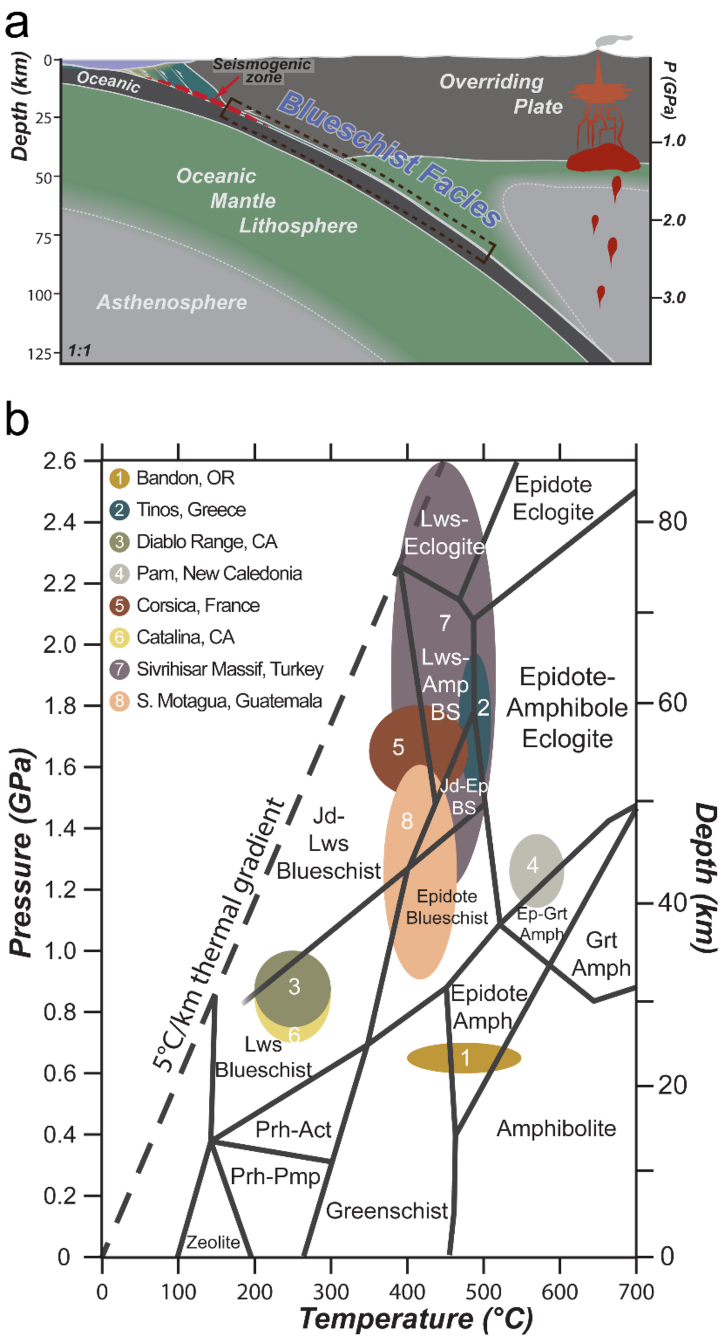

Figure 2. a) Diagrams of the crystal morphology of glaucophane, epidote, lawsonite, and phengite labelled with the [100], [010], and [001] crystallographic axes in common preferred orientation typical for blueschists in this compilation. Vp velocities of the crystallographic axes on the upper hemisphere stereographic projections (red circles = slow-axis, white circle = intermediate-axis, blue circle = fast-axis). b) The respective single-crystal Vp seismic velocities projections (upper hemisphere) and seismic anisotropy percentages (AVp) for phases and orientations in (a). Black squares and white circles are maximum and minimum *P* wave velocity orientations, respectively. c) Diagram of CPO types previously observed in the amphibole glaucophane in naturally and experimentally deformed samples (modified after Kim & Jung, 2019).

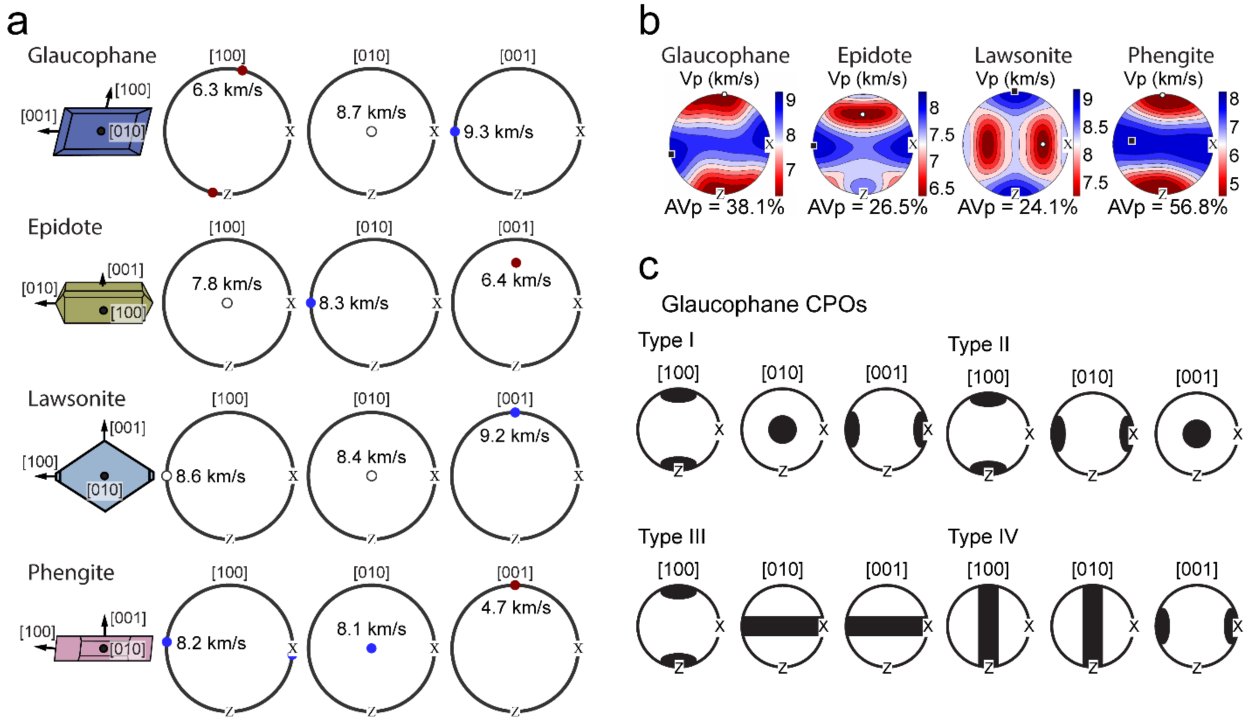

Figure 3. Photos of blueschist hand samples representative of the macroscopic fabrics observed in the samples selected for this study. The approximately horizontal foliation and lineation (subhorizontal in the plane of the page) in the epidote blueschists from a) Tinos, Greece and b) the Diablo Range, California is largely defined by the volumetrically dominant elongate glaucophane grains. Scale bar is applicable to both samples.

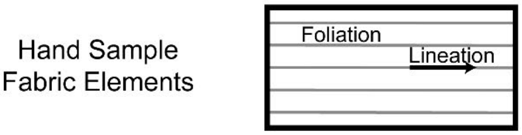

a **Epidote blueschist** CY107 Tinos, GR

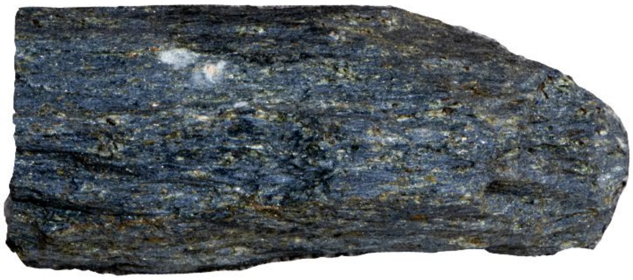

b **Epidote blueschist** DR221 Diable Range, CA

Figure 4. a,b) Bandon, OR epidote blueschist showing foliation defined by shape preferred orientation of glaucophane and epidote grains; c,d) Sivrihisar Massif, TUR lawsonite blueschist with lawsonite porphyroblasts in matrix of fine-grained glaucophane; e,f) epidote blueschist from Pam Peninsula, NC, with foliation defined by compositional layers of fine-grained epidote and large glaucophane grains; g,h) epidote blueschist from Tinos, GRC, with strong foliation in elongate glaucophane grains and phengite in garnet pressure-shadows.

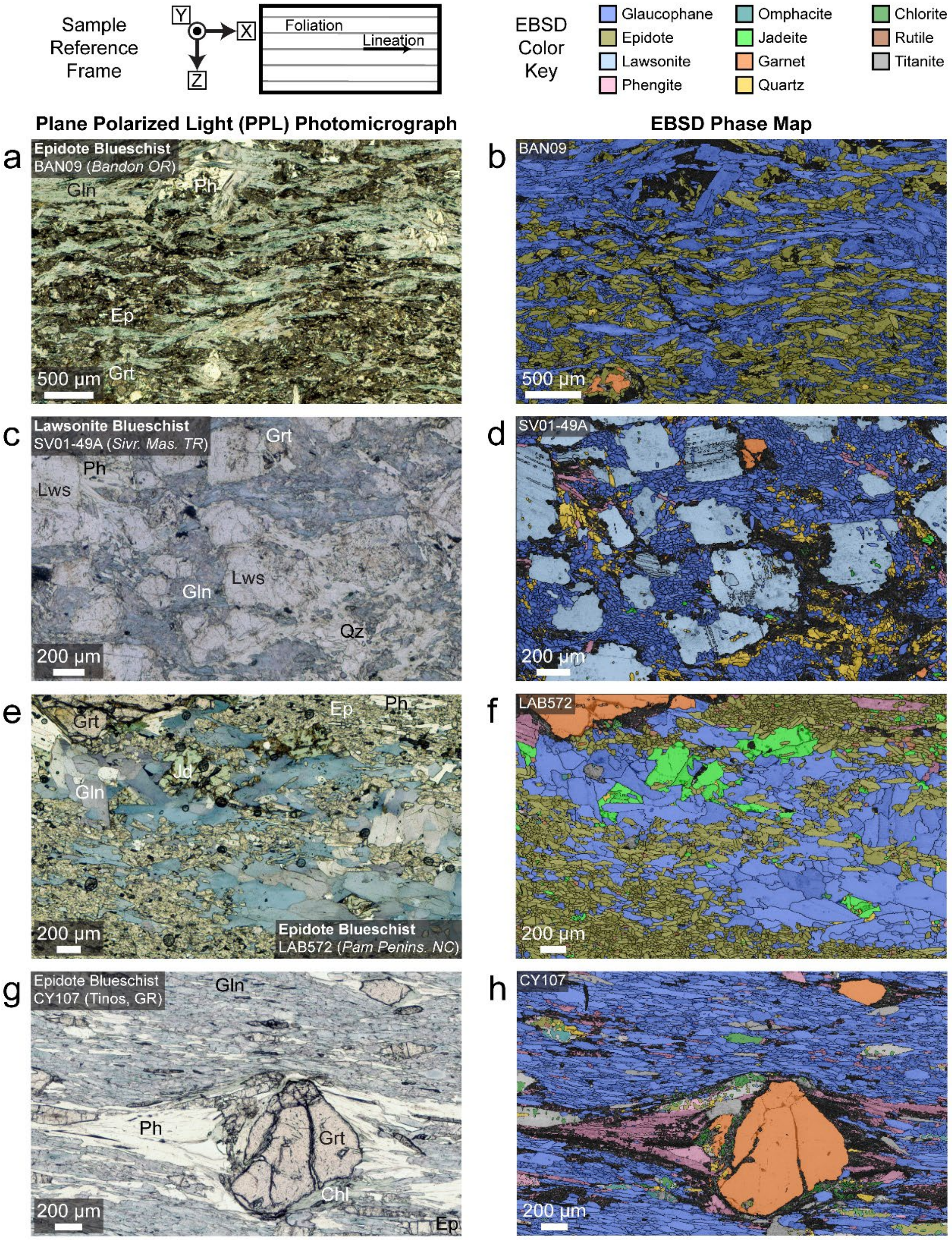

Figure 5. The CPOs in glaucophane, epidote, lawsonite, and phengite and the calculated seismic anisotropies for the full mineral assemblage for representative examples of a) a type-I glaucophane CPO, b) a type-III glaucophane CPO, and c) a weak type-IV glaucophane CPO. All CPO and seismic anisotropy calculations use the full set of EBSD-indexed orientations. Pole figures are plotted as equal-area upper-hemisphere projections with multiple of uniform distribution (m.u.d.) density contours and the pole-figure J-index (pfJ-index) calculated for *n* indexed points of each phase. Phengite modal abundance is < 1% in sample DR265 and is excluded from the figure. Seismic anisotropies are plotted as equal-area upper-hemisphere projections. Orientations of maximum and minimum *P* and *S* wave velocities and shear wave splitting (AVs) percentages are shown with black squares (maxima) and white circles (minima).

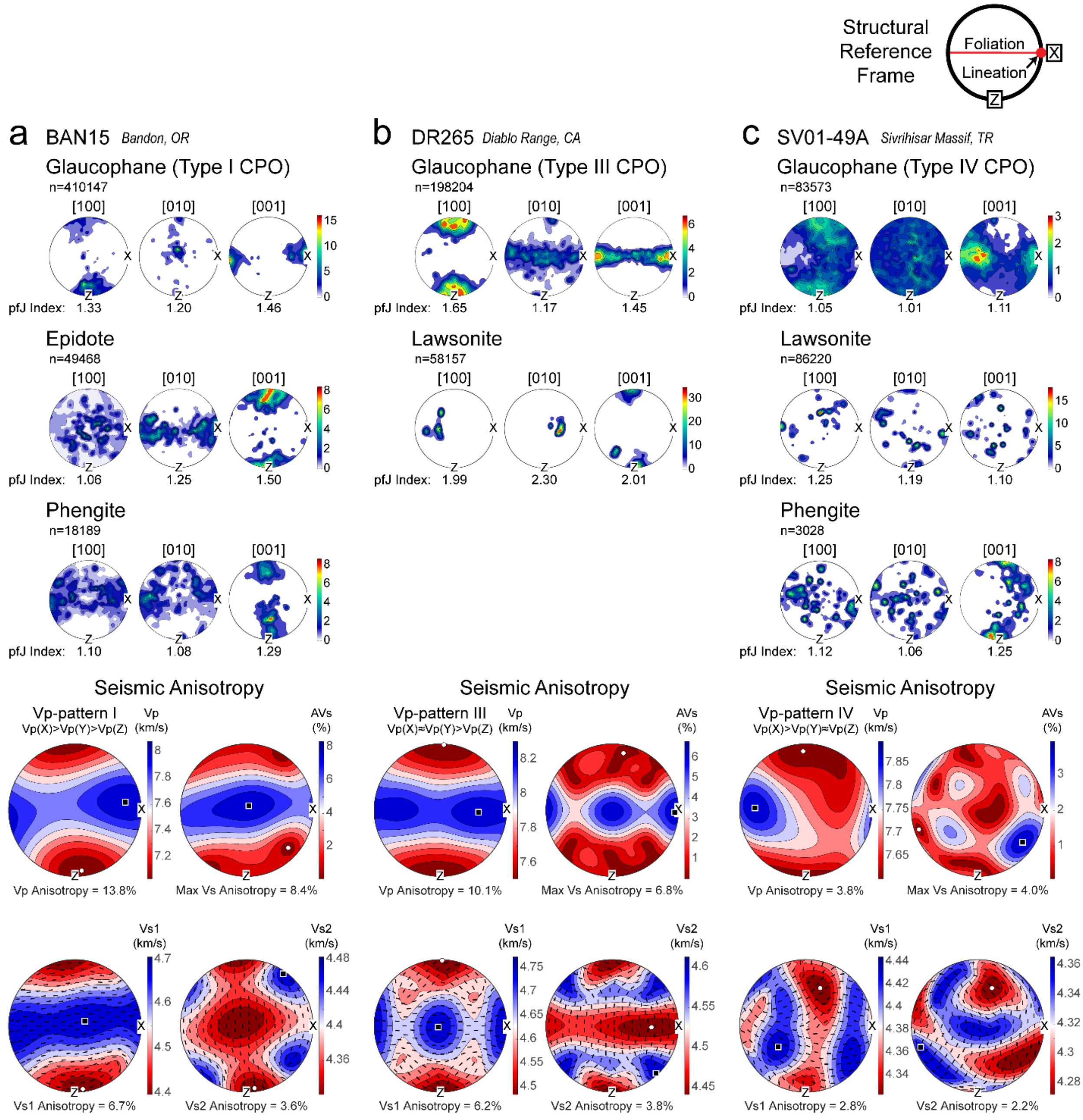

Figure 6. a) The calculated upper-hemisphere *P* wave velocity projections plotted in order of increasing maximum Vp anisotropy (AVp %) displays the broad range of seismic anisotropy presented in the compilation samples. The *P* wave anisotropy patterns are positively correlated with the CPO type observed in glaucophane for each sample. b) The modal composition of each sample follows a general trend of increasing AVp with increasing glaucophane modal abundance.

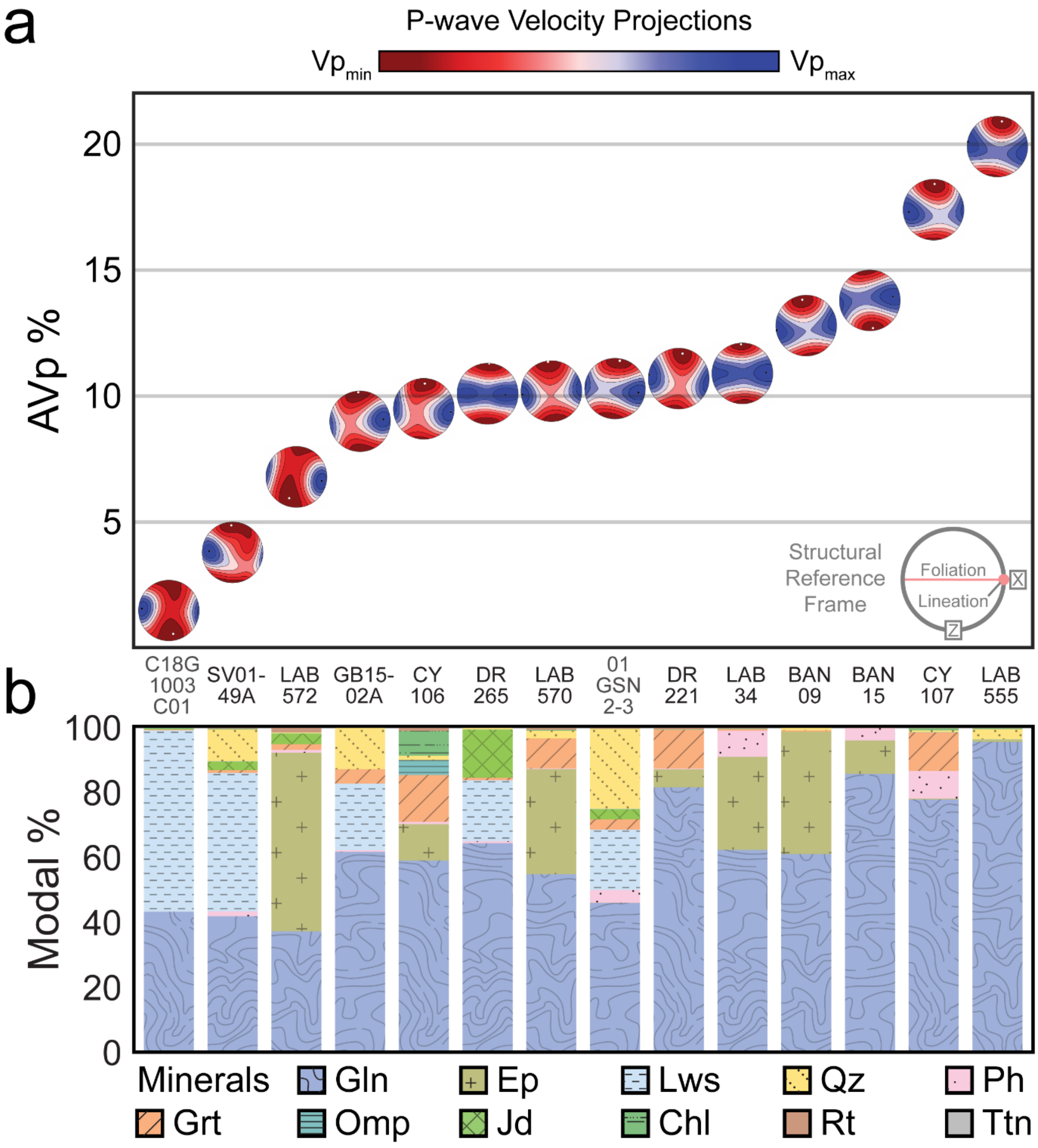

Figure 7. AVp % versus mineral mode (%) of samples for a) glaucophane, b) epidote, c) lawsonite, and d) phengite. AVp trends for glaucophane, epidote, and lawsonite are fit by linear regression and the equations of the best-fit line (with M = modal abundance of the phase), and the R^2 quality of fit statistic shown.

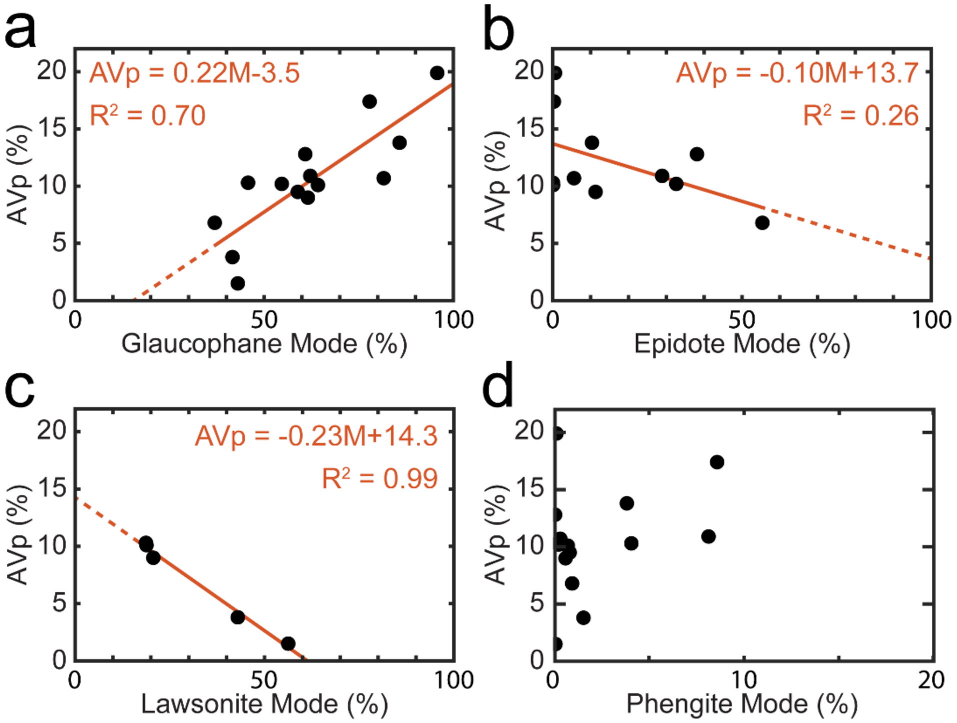

Figure 8. AVp % versus the pfJ-Index for the [100] axis, [010] axis, and [001] axis for a) glaucophane, b) epidote, c) lawsonite, and d) phengite. Best-fit linear regression AVp/pfJ-index trendlines are shown with R^2 quality of fit statistic shown for glaucophane, epidote, and lawsonite. $R^2 = 1$ if 100% of data explained by fit, and decreases to 0 for lower fit-quality. Markers are colored by Vp pattern (see text) and open markers (a) are excluded from the linear regression fit (see text); e) $Vp_{maximum}$, Vp_{median}, and $Vp_{minimum}$ versus AVp % for all blueschists in this study.

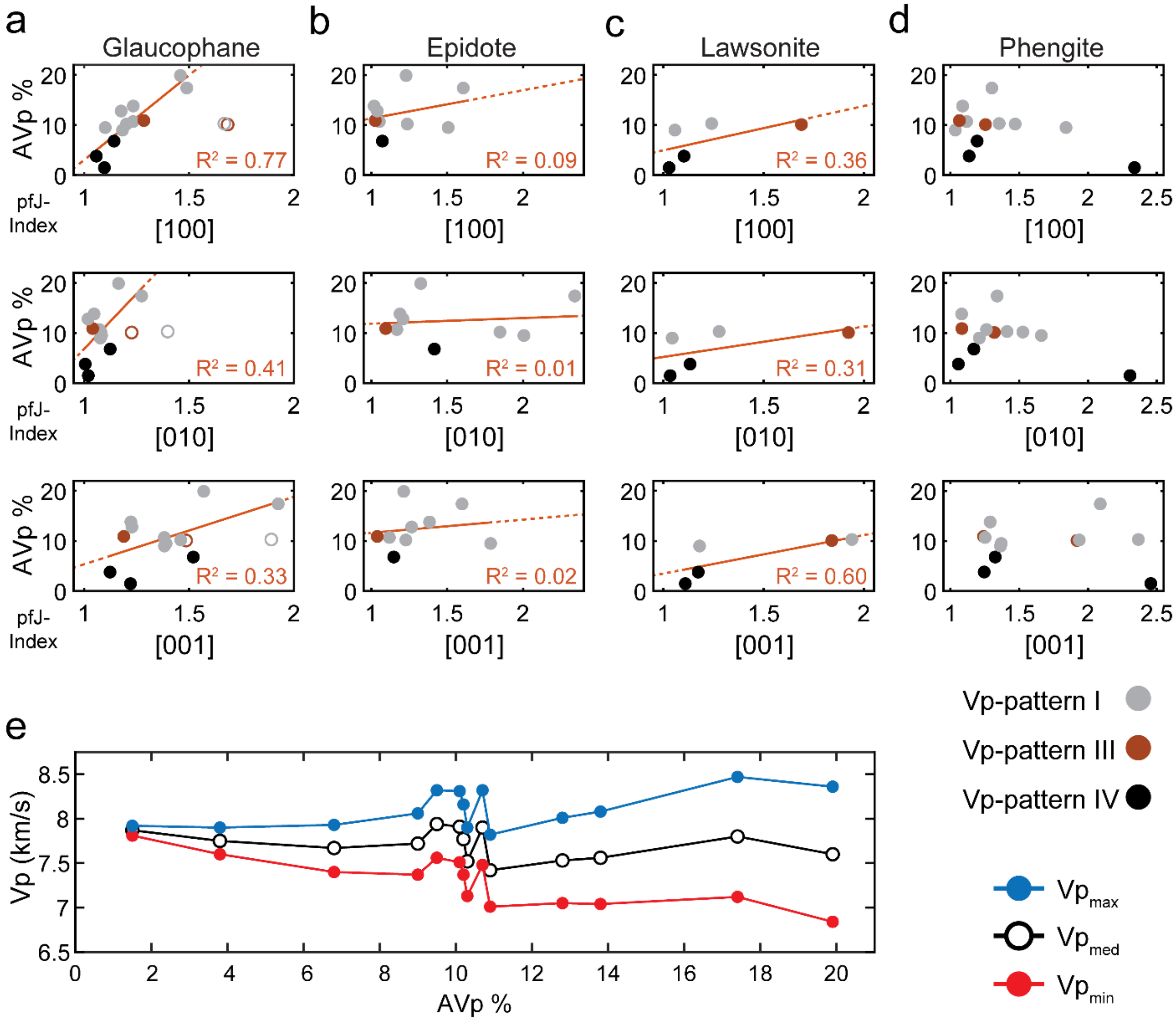

Figure 9. Equal-area upper hemisphere stereographic projections of *P* wave velocities (in km/s) and AVp % for a) the range of Gln/Ep ratios for epidote blueschist LAB555 and b) the range of Gln/Lws ratios for lawsonite blueschist 01GSN2-3. Projections show increasing glaucophane proportion from left-to-right and maximum and minimum *P* wave velocity orientation with black and white markers, respectively; c) AVp trends with increasing glaucophane in 2-phase models for all epidote blueschists in the study and d) AVp trends with increasing glaucophane in 2-phase models for all lawsonite blueschists. Markers on each profile in part c and d correspond to Gln/Ep or Gln/Lws ratio in bulk sample and are represented as circles for models matching bulk AVp within 2%, and triangles for modeled AVp higher (up to ~5%) than bulk sample AVp %. e) Scatterplot of the calculated AVp % for bulk sample versus the calculated AVp % of the 2-phase models at the Gln/Ep or Gln/Lws ratios in the bulk sample. The 1:1 correlation line illustrates where samples would plot if the calculated AVp % coincides for both methods.

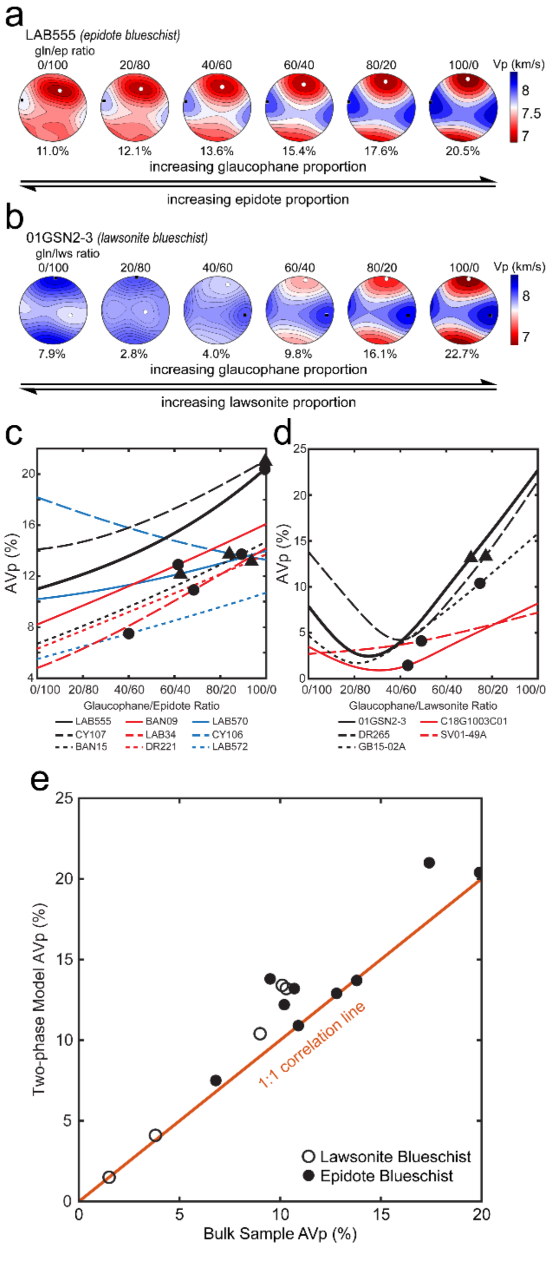

Chapter 2 References

Abt, D. L., Fischer, K. M., Abers, G. A., Strauch, W., Protti, J. M., & González, V. (2009). Shear wave anisotropy beneath Nicaragua and Costa Rica: Implications for flow in the mantle wedge. Geochemistry, Geophysics, Geosystems, 10(5). https://doi.org/10.1029/2009GC002375

Aleksandrov, K. S., Alchikov, U. V., Belikov, B. P., Zaslavskii, B. I., & Krupnyi, A. I. (1974), Velocities of elastic waves in minerals at atmospheric pressure and increasing precision of elastic constants by means of EVM [in Russian], Izv. Acad. Sci. USSR, Geo. Ser., 10, 15–24.

Almqvist, B. S. G., & Mainprice, D. (2017). Seismic properties and anisotropy of the continental crust: Predictions based on mineral texture and rock microstructure. Reviews of Geophysics, 55(2), 367–433. https://doi.org/10.1002/2016RG000552

Aoki, K., Itaya, T., Shibuya, T., Masago, H., Kon, Y., Terabayashi, M., et al. (2008). The youngest blueschist belt in SW Japan: implication for the exhumation of the Cretaceous Sanbagawa high-P/T metamorphic belt. Journal of Metamorphic Geology, 26(5), 583–602. https://doi.org/10.1111/j.1525-1314.2008.00777.x

Bachmann, F., Hielscher, R., & Schaeben, H. (2010). Texture Analysis with MTEX – Free and Open Source Software Toolbox. Solid State Phenomena, 160, 63–68. https://doi.org/10.4028/www.scientific.net/SSP.160.63

Bernard, R. E., Schulte-Pelkum, V., & Behr, W. M. (2021). The competing effects of olivine and orthopyroxene CPO on seismic anisotropy. Tectonophysics, 814, 228954. https://doi.org/10.1016/j.tecto.2021.228954

Bezacier, L., Reynard, B., Bass, J. D., Wang, J., & Mainprice, D. (2010). Elasticity of glaucophane, seismic velocities and anisotropy of the subducted oceanic crust. Tectonophysics, 494(3), 201–210. https://doi.org/10.1016/j.tecto.2010.09.011

Bhagat, S. S., Bass, J. D., & Smyth, J. R. (1992). Single-crystal elastic properties of omphacite-C2/c by Brillouin spectroscopy. Journal of Geophysical Research: Solid Earth, 97(B5), 6843–6848. https://doi.org/10.1029/92JB00030

Britton, T. B., Jiang, J., Guo, Y., Vilalta-Clemente, A., Wallis, D., Hansen, L. N., et al. (2016). Tutorial: Crystal orientations and EBSD — Or which way is up? Materials Characterization, 117, 113–126. https://doi.org/10.1016/j.matchar.2016.04.008

Brothers, R. N. (1974). High-pressure schists in Northern New Caledonia. Contributions to Mineralogy and Petrology, 46(2), 109–127. https://doi.org/10.1007/BF00377499

Brovarone, A. V., Picatto, M., Beyssac, O., Lagabrielle, Y., & Castelli, D. (2014). The blueschist–eclogite transition in the Alpine chain: P–T paths and the role of slow-spreading extensional structures in the evolution of HP–LT mountain belts. Tectonophysics, 615–616, 96–121. https://doi.org/10.1016/j.tecto.2014.01.001

Browaeys, J. T., & Chevrot, S. (2004). Decomposition of the elastic tensor and geophysical applications. Geophysical Journal International, 159(2), 667–678. https://doi.org/10.1111/j.1365-246X.2004.02415.x

Brownlee, S. J., Schulte-Pelkum, V., Raju, A., Mahan, K., Condit, C., & Orlandini, O. F. (2017). Characteristics of deep crustal seismic anisotropy from a compilation of rock elasticity tensors and their expression in receiver functions. Tectonics, 36(9), 1835–1857. https://doi.org/10.1002/2017TC004625

Bunge, H. J. (1985). 4 - Representation of Preferred Orientations. In H.-R. Wenk (Ed.), Preferred Orientation in Deformed Metal and Rocks (pp. 73–108). San Diego: Academic Press. https://doi.org/10.1016/B978-0-12-744020-0.50009-2

Cao, Y., Jung, H., & Song, S. (2013). Petro-fabrics and seismic properties of blueschist and eclogite in the North Qilian suture zone, NW China: Implications for the low-velocity upper layer in subducting slab, trench-parallel seismic anisotropy, and eclogite detectability in the subduction zone. Journal of Geophysical Research: Solid Earth, 118(6), 3037–3058. https://doi.org/10.1002/jgrb.50212

Cao, Y., Jung, H., & Song, S. (2014). Microstructures and petro-fabrics of lawsonite blueschist in the North Qilian suture zone, NW China: Implications for seismic anisotropy of subducting oceanic crust. Tectonophysics, 628, 140–157. https://doi.org/10.1016/j.tecto.2014.04.028

Cao, Y., & Jung, H. (2016). Seismic properties of subducting oceanic crust: Constraints from natural lawsonite-bearing blueschist and eclogite in Sivrihisar Massif, Turkey. Physics of the Earth and Planetary Interiors, 250, 12–30. https://doi.org/10.1016/j.pepi.2015.10.003

Chai, M., Brown, J. M., & Slutsky, L. J. (1997). The elastic constants of a pyrope-grossular-almandine garnet to 20 GPa. Geophysical Research Letters, 24(5), 523–526. https://doi.org/10.1029/97GL00371

Choi, S., Fabbri, O., Topuz, G., Okay, A. I., & Jung, H. (2021). Twin Induced Reduction of Seismic Anisotropy in Lawsonite Blueschist. Minerals, 11(4), 399. https://doi.org/10.3390/min11040399

Christoffel, E. B. (1877). Über die fortpflanzung van stössen durch elastische feste körper. Annali di Matematica pura ed applicata, Serie II 8, 193–243.

Clarke, G. L., Aitchison, J. C., & Cluzel, D. (1997). Eclogites and blueschists of the Pam Peninsula, NE New Caledonia: a Reappraisal. Journal of Petrology, 38(7), 34.

Coleman, R. G., & Lanphere, M. A. (1971). Distribution and age of high-grade blueschists, associated eclogites, and amphibolites from Oregon and California. Geological Society of America Bulletin, 82(9), 2397. https://doi.org/10.1130/0016-7606(1971)82[2397:DAAOHB]2.0.CO;2

Cossette, É., Audet, P., Schneider, D., & Grasemann, B. (2016). Structure and anisotropy of the crust in the Cyclades, Greece, using receiver functions constrained by in situ rock textural data. Journal of Geophysical Research: Solid Earth, 121(4), 2661–2678. https://doi.org/10.1002/2015JB012460

Currie, C. A., Cassidy, J. F., Hyndman, R. D., & Bostock, M. G. (2004). Shear wave anisotropy beneath the Cascadia subduction zone and western North American craton. Geophysical Journal International, 157(1), 341–353. https://doi.org/10.1111/j.1365-246X.2004.02175.x

Das, P. Kr., Mondal, S. K., & Mandal, N. (2021). First principles prediction of exceptional mechanical and electronic behaviour of Titanite (CaTiSiO5). Materialia, 15, 100964. https://doi.org/10.1016/j.mtla.2020.100964

Davis, P. B., & Whitney, D. L. (2006). Petrogenesis of lawsonite and epidote eclogites and blueschist, Sivrihisar Massif, Turkey. Journal of Metamorphic Geology, 24(9), 823–849. https://doi.org/10.1111/j.1525-1314.2006.00671.x

Evans, B. W. (1990). Phase relations of epidote-blueschists. Lithos, 25(1), 3–23. https://doi.org/10.1016/0024-4937(90)90003-J

Freedman, D., Pisani, R., & Purves, R. (2007). Statistics (international student edition). New York, NY: WW Norton & Company.

Fujimoto, Y., Kono, Y., Hirajima, T., Kanagawa, K., Ishikawa, M., & Arima, M. (2010). P-wave velocity and anisotropy of lawsonite and epidote blueschists: Constraints on water transportation along subducting oceanic crust. Physics of the Earth and Planetary Interiors, 183(1), 219–228. https://doi.org/10.1016/j.pepi.2010.09.003

Getsinger, A. J., & Hirth, G. (2014). Amphibole fabric formation during diffusion creep and the rheology of shear zones. Geology, 42(6), 535–538. https://doi.org/10.1130/G35327.1

Greve, S. M., Savage, M. K., & Hofmann, S. D. (2008). Strong variations in seismic anisotropy across the Hikurangi subduction zone, North Island, New Zealand. Tectonophysics, 462(1), 7–21. https://doi.org/10.1016/j.tecto.2007.07.011

Grove, M., & Bebout, G. E. (1995). Cretaceous tectonic evolution of coastal southern California: Insights from the Catalina Schist. Tectonics, 14(6), 1290–1308. https://doi.org/10.1029/95TC01931

Ha, Y., Jung, H., & Raymond, L. A. (2019). Deformation fabrics of glaucophane schists and implications for seismic anisotropy: the importance of lattice preferred orientation of phengite. International Geology Review, 61(6), 720–737. https://doi.org/10.1080/00206814.2018.1449142

Hamelin, C., Brady, J. B., Cheney, J. T., Schumacher, J. C., Able, L. M., & Sperry, A. J. (2018). Pseudomorphs after Lawsonite from Syros, Greece. Journal of Petrology, 59(12), 2353–2384. https://doi.org/10.1093/petrology/egy099

Harlow, G. E., Sisson, V. B., Lallemant, H. G. A., Sorensen, S. S., & Seitz, R. (2003). High-pressure, metasomatic rocks along the Motagua Fault Zone, Guatemala. Ofioliti, 28(2), 115–120. https://doi.org/10.4454/ofioliti.v28i2.199

Heilbronner, R., & Barrett, S. (2014). Volume Determinations. In R. Heilbronner & S. Barrett (Eds.), Image Analysis in Earth Sciences: Microstructures and Textures of Earth Materials (pp. 173–185). Berlin, Heidelberg: Springer. https://doi.org/10.1007/978-3-642-10343-8_10

Hill, R. (1952). The Elastic behaviour of a crystalline aggregate. Proceedings of the Physical Society. Section A, 65(5), 349–354. https://doi.org/10.1088/0370-1298/65/5/307

Huang, Z., Zhao, D., & Wang, L. (2011). Shear wave anisotropy in the crust, mantle wedge, and subducting Pacific slab under northeast Japan. Geochemistry, Geophysics, Geosystems, 12(1). https://doi.org/10.1029/2010GC003343

Hyndman, R. D., Yamano, M., & Oleskevich, D. A. (1997). The seismogenic zone of subduction thrust faults. Island Arc, 6(3), 244–260. https://doi.org/10.1111/j.1440-1738.1997.tb00175.x

Isaak, D. G., Carnes, J. D., Anderson, O. L., Cynn, H., & Hake, E. (1998). Elasticity of TiO2 rutile to 1800 K. Physics and Chemistry of Minerals, 26(1), 31–43. https://doi.org/10.1007/s002690050158

Ji, S., Shao, T., Michibayashi, K., Long, C., Wang, Q., Kondo, Y., et al. (2013). A new calibration of seismic velocities, anisotropy, fabrics, and elastic moduli of amphibole-rich rocks. Journal of Geophysical Research: Solid Earth, 118(9), 4699–4728. https://doi.org/10.1002/jgrb.50352

Jung, H. (2017). Crystal preferred orientations of olivine, orthopyroxene, serpentine, chlorite, and amphibole, and implications for seismic anisotropy in subduction zones: a review. Geosciences Journal, 21(6), 985–1011. https://doi.org/10.1007/s12303-017-0045-1

Kandelin, J., & Weidner, D. J. (1988). The single-crystal elastic properties of jadeite. Physics of the Earth and Planetary Interiors, 50(3), 251–260. https://doi.org/10.1016/0031-9201(88)90106-9

Kang, H., & Jung, H. (2019). Lattice-preferred orientation of amphibole, chlorite, and olivine found in hydrated mantle peridotites from Bjørkedalen, southwestern Norway, and implications for seismic anisotropy. Tectonophysics, 750, 137–152. https://doi.org/10.1016/j.tecto.2018.11.011

Kang, H., & Kim, Y. (2019). Localized Anisotropic Subduction-Zone Structure in Southern Peru: Constraints from Teleseismic Receiver Functions and Forward Modeling. Seismological Research Letters, 90(5), 1820–1835. https://doi.org/10.1785/0220180384

Keken, P. E. van, Wada, I., Abers, G. A., Hacker, B. R., & Wang, K. (2018). Mafic high-pressure rocks are preferentially exhumed from warm subduction settings. Geochemistry, Geophysics, Geosystems, 19(9), 2934–2961. https://doi.org/10.1029/2018GC007624

Keppler, R., Behrmann, J. H., & Stipp, M. (2017). Textures of eclogites and blueschists from Syros island, Greece: Inferences for elastic anisotropy of subducted oceanic crust. Journal of Geophysical Research: Solid Earth, 122(7), 5306–5324. https://doi.org/10.1002/2017JB014181

Kim, D., & Jung, H. (2015). Deformation microstructures of olivine and chlorite in chlorite peridotites from Almklovdalen in the Western Gneiss Region, southwest Norway, and implications for seismic anisotropy. International Geology Review, 57(5–8), 650–668. https://doi.org/10.1080/00206814.2014.936054

Kim, D., Jung, H., & Lee, J. (2020). Strain-Induced Fabric Transition of Chlorite and Implications for Seismic Anisotropy in Subduction Zones. Minerals, 10(6), 503. https://doi.org/10.3390/min10060503

Kim, D., Katayama, I., Michibayashi, K., & Tsujimori, T. (2013). Deformation fabrics of natural blueschists and implications for seismic anisotropy in subducting oceanic crust. Physics of the Earth and Planetary Interiors, 222, 8–21. https://doi.org/10.1016/j.pepi.2013.06.011

Kim, J., & Jung, H. (2019). New crystal preferred orientation of amphibole experimentally found in simple shear. Geophysical Research Letters, 46, 12,996–13,005. https://doi.org/10.1029/2019GL085189

Kim, J., & Jung, H. (2020). Lattice Preferred Orientation(LPO) and Seismic Anisotropy of Amphibole in Gapyeong Amphibolites. Korean Journal of Mineralogy and Petrology, 33(3), 259–272. https://doi.org/10.22807/KJMP.2020.33.3.259

Ko, B., & Jung, H. (2015). Crystal preferred orientation of an amphibole experimentally deformed by simple shear. Nature Communications, 6(1), 6586. https://doi.org/10.1038/ncomms7586

Koulakov, I., Jakovlev, A., & Luehr, B. G. (2009). Anisotropic structure beneath central Java from local earthquake tomography. Geochemistry, Geophysics, Geosystems, 10(2). https://doi.org/10.1029/2008GC002109

Krieger Lassen, N. C., Jensen, D. J., & Conradsen, K. (1992). Image Processing Procedures for Analysis of Electron Back Scattering Patterns. Scanning Microscopy, 6(1). Retrieved from https://digitalcommons.usu.edu/microscopy/vol6/iss1/7

Lamont, T. N., Searle, M. P., Gopon, P., Roberts, N. M. W., Wade, J., Palin, R. M., & Waters, D. J. (2020). The Cycladic Blueschist Unit on Tinos, Greece: Cold NE subduction and SW directed extrusion of the Cycladic Continental Margin under the Tsiknias Ophiolite. Tectonics, 39(9), e2019TC005890. https://doi.org/10.1029/2019TC005890

Liu, J., & Cao, S. (2023). Development of Amphibole Crystal Preferred Orientations (CPOs) and Their Effects on Seismic Anisotropy in Deformed Amphibolites. Journal of Geophysical Research: Solid Earth, 128(4), e2022JB026136. https://doi.org/10.1029/2022JB026136

Liu, S., Tommasi, A., Vauchez, A., & Mazzucchelli, M. (2019). Deformation, annealing, melt-rock interaction, and seismic properties of an old domain of the Equatorial Atlantic Lithospheric Mantle. Tectonics, 38(4), 1164–1188. https://doi.org/10.1029/2018TC005373

Lloyd, G. E., Butler, R. W. H., Casey, M., Tatham, D. J., & Mainprice, D. (2011). Constraints on the seismic properties of the middle and lower continental crust. Geological Society, London, Special Publications, 360(1), 7–32. https://doi.org/10.1144/SP360.2

Lloyd, G. E., Schmidt, N.-H., Mainprice, D., & Prior, D. J. (1991). Crystallographic textures. Mineralogical Magazine, 55(380), 331–345. https://doi.org/10.1180/minmag.1991.055.380.04

Long, M. D., & van der Hilst, R. D. (2006). Shear wave splitting from local events beneath the Ryukyu arc: Trench-parallel anisotropy in the mantle wedge. Physics of the Earth and Planetary Interiors, 155(3), 300–312. https://doi.org/10.1016/j.pepi.2006.01.003

Mahan, K. (2006). Retrograde mica in deep crustal granulites: Implications for crustal seismic anisotropy. Geophysical Research Letters, 33(24). https://doi.org/10.1029/2006GL028130

Mainprice, D. (2015). 2.20 - Seismic Anisotropy of the Deep Earth from a Mineral and Rock Physics Perspective. In G. Schubert (Ed.), Treatise on Geophysics (Second Edition) (pp. 487–538). Oxford: Elsevier. https://doi.org/10.1016/B978-0-444-53802-4.00044-0

Mainprice, D., Bachmann, F., Hielscher, R., & Schaeben, H. (2015). Descriptive tools for the analysis of texture projects with large datasets using MTEX : strength, symmetry and components. Geological Society, London, Special Publications, 409(1), 251–271. https://doi.org/10.1144/SP409.8

Mainprice, D., Hielscher, R., & Schaeben, H. (2011). Calculating anisotropic physical properties from texture data using the MTEX open-source package. *Geological Society, London, Special Publications*, 360(1), 175–192. https://doi.org/10.1144/SP360.10

Mainprice, D., & Humbert, M. (1994). Methods of calculating petrophysical properties from lattice preferred orientation data. Surveys in Geophysics, 15(5), 575–592. https://doi.org/10.1007/BF00690175

Mainprice, D., & Nicolas, A. (1989). Development of shape and lattice preferred orientations: application to the seismic anisotropy of the lower crust. Journal of Structural Geology, 11(1), 175–189. https://doi.org/10.1016/0191-8141(89)90042-4

Mauler, A., Burlini, L., Kunze, K., Philippot, P., & Burg, J.-P. (2000). P-wave anisotropy in eclogites and relationship to the omphacite crystallographic fabric. Physics and Chemistry of the Earth, Part A: Solid Earth and Geodesy, 25(2), 119–126. https://doi.org/10.1016/S1464-1895(00)00020-X

Michibayashi, K., & Mainprice, D. (2004). The Role of Pre-existing Mechanical Anisotropy on Shear Zone Development within Oceanic Mantle Lithosphere: an Example from the Oman Ophiolite. Journal of Petrology, 45(2), 405–414. https://doi.org/10.1093/petrology/egg099

Mookherjee, M., & Bezacier, L. (2012). The low velocity layer in subduction zone: Structure and elasticity of glaucophane at high pressures. Physics of the Earth and Planetary Interiors, 208–209, 50–58. https://doi.org/10.1016/j.pepi.2012.07.007

Mookherjee, M., & Mainprice, D. (2014). Unusually large shear wave anisotropy for chlorite in subduction zone settings. Geophysical Research Letters, 41(5), 1506–1513. https://doi.org/10.1002/2014GL059334

Nakajima, J., & Hasegawa, A. (2004). Shear-wave polarization anisotropy and subduction-induced flow in the mantle wedge of northeastern Japan. Earth and Planetary Science Letters, 225(3), 365–377. https://doi.org/10.1016/j.epsl.2004.06.011

Nicolas, A., & Poirier, J. P. (1976). Crystalline plasticity and solid state flow in metamorphic rocks. J. Wiley and Sons, London.

Ogi, H., Ohmori, T., Nakamura, N., & Hirao, M. (2016). Elastic, anelastic, and piezoelectric coefficients of α-quartz determined by resonance ultrasound spectroscopy. Journal of Applied Physics, 100(5), 053511. https://doi.org/10.1063/1.2335684

Okaya, D., Vel, S. S., Song, W. J., & Johnson, S. E. (2018). Modification of crustal seismic anisotropy by geological structures ("structural geometric anisotropy"). Geosphere, 15(1), 146–170. https://doi.org/10.1130/GES01655.1

Ott, J. N., Condit, C., Schulte-Pelkum, V., Bernard, R., & Pec, M. (2023). Supplemental Files and Data for Seismic Anisotropy of Mafic Blueschists: constraints from the exhumed rock record [Data set]. Zenodo. https://doi.org/10.5281/zenodo.10270076

Park, Y., & Jung, H. (2022). Seismic velocity and anisotropy of glaucophane and epidote in experimentally deformed epidote blueschist and implications for seismic properties in warm subduction zones. Earth and Planetary Science Letters, 598, 117822. https://doi.org/10.1016/j.epsl.2022.117822

Park, Y., Jung, S., & Jung, H. (2020). Lattice Preferred Orientation and Deformation Microstructures of Glaucophane and Epidote in Experimentally Deformed Epidote Blueschist at High Pressure. Minerals, 10(9), 803. https://doi.org/10.3390/min10090803

Park, J., & Levin, V. (2002). Seismic Anisotropy: Tracing Plate Dynamics in the Mantle. Science, 296(5567), 485–489. https://doi.org/10.1126/science.1067319

Passchier, C. W., & Trouw, R. A. J. (2005). Microtectonics. Berlin, Heidelberg: Springer-Verlag. https://doi.org/10.1007/3-540-29359-0

Patrick, B. E., & Day, H. W. (1989). Controls on the first appearance of jadeitic pyroxene, northern Diablo Range, California. Journal of Metamorphic Geology, 7(6), 629–639. https://doi.org/10.1111/j.1525-1314.1989.tb00623.x

Peacock, S. M. (1993). The importance of blueschist → eclogite dehydration reactions in subducting oceanic crust. Geological Society of America Bulletin, 105(5), 684–694. https://doi.org/10.1130/0016-7606(1993)105<0684:TIOBED>2.3.CO;2

Peacock, S. M. (2004). Thermal structure and metamorphic evolution of subducting slabs. In Inside the Subduction Factory (pp. 7–22). American Geophysical Union (AGU). https://doi.org/10.1029/138GM02

Peacock, S. M. (2009). Thermal and metamorphic environment of subduction zone episodic tremor and slip. Journal of Geophysical Research: Solid Earth, 114(B8). https://doi.org/10.1029/2008JB005978

Peillod, A., Majka, J., Ring, U., Drüppel, K., Patten, C., Karlsson, A., et al. (2021). Differences in decompression of a high-pressure unit: A case study from the Cycladic Blueschist Unit on Naxos Island, Greece. Lithos, 386–387, 106043. https://doi.org/10.1016/j.lithos.2021.106043

Prior, D. J., Boyle, A. P., Brenker, F., Cheadle, M. C., Day, A., Lopez, G., et al. (1999). The application of electron backscatter diffraction and orientation contrast imaging in the SEM to textural problems in rocks. American Mineralogist, 84(11–12), 1741–1759. https://doi.org/10.2138/am-1999-11-1204

Reuss, A. (1929). Berechnung der Fließgrenze von Mischkristallen auf Grund der Plastizitätsbedingung für Einkristalle . ZAMM - Journal of Applied Mathematics and Mechanics / Zeitschrift Für Angewandte Mathematik Und Mechanik, 9(1), 49–58. https://doi.org/10.1002/zamm.19290090104

Reynard, B., Gillet, P., & Willaime, C. (1989). Deformation mechanisms in naturally deformed glaucophanes: a TEM and HREM study. European Journal of Mineralogy, 1(5), 611–624. https://doi.org/10.1127/ejm/1/5/0611

Schilling, F. R., Sinogeikin, S. V., & Bass, J. D. (2003). Single-crystal elastic properties of lawsonite and their variation with temperature. Physics of the Earth and Planetary Interiors, 136(1), 107–118. https://doi.org/10.1016/S0031-9201(03)00024-4

Schmid, S. M. (1994). Textures of geological materials: Computer model predictions versus empirical interpretations based on rock deformation experiments and field studies. In H. J. Bunge, S. Siegesmund, W. Skrotzki, & K. Weber (Eds.), Texture of geological materials. (pp. 279– 301). Oberursel: Deutsch gesellschaft für materialkunde.

Schmidt, M. W., & Poli, S. (2014). 4.19 - Devolatilization during subduction. In H. D. Holland & K. K. Turekian (Eds.), Treatise on Geochemistry (Second Edition) (pp. 669–701). Oxford: Elsevier. https://doi.org/10.1016/B978-0-08-095975-7.00321-1

Schulte-Pelkum, V., & Mahan, K. H. (2014a). A method for mapping crustal deformation and anisotropy with receiver functions and first results from USArray. Earth and Planetary Science Letters, 402, 221–233. https://doi.org/10.1016/j.epsl.2014.01.050

Schulte-Pelkum, V., & Mahan, K. H. (2014b). Imaging Faults and Shear Zones Using Receiver Functions. Pure and Applied Geophysics, 171(11), 2967–2991. https://doi.org/10.1007/s00024-014-0853-4

Schulte-Pelkum, V., Monsalve, G., Sheehan, A., Pandey, M. R., Sapkota, S., Bilham, R., & Wu, F. (2005). Imaging the Indian subcontinent beneath the Himalaya. Nature, 435(7046), 1222–1225. https://doi.org/10.1038/nature03678

Silver, P. G., & Chan, W. W. (1991). Shear wave splitting and subcontinental mantle deformation. Journal of Geophysical Research: Solid Earth, 96(B10), 16429–16454. https://doi.org/10.1029/91JB00899

Skemer, P., Katayama, I., Jiang, Z., & Karato, S. (2005). The misorientation index: Development of a new method for calculating the strength of lattice-preferred orientation. Tectonophysics, 411(1), 157–167. https://doi.org/10.1016/j.tecto.2005.08.023

Stöckhert, B. (2002). Stress and deformation in subduction zones: insight from the record of exhumed metamorphic rocks. Geological Society, London, Special Publications, 200(1), 255–274. https://doi.org/10.1144/GSL.SP.2001.200.01.15

Tatham, D. J., Lloyd, G. E., Butler, R. W. H., & Casey, M. (2008). Amphibole and lower crustal seismic properties. Earth and Planetary Science Letters, 267(1), 118–128. https://doi.org/10.1016/j.epsl.2007.11.042

Teyssier, C., Whitney, D. L., Toraman, E., & Seaton, N. C. A. (2010). Lawsonite vorticity and subduction kinematics. Geology, 38(12), 1123–1126. https://doi.org/10.1130/G31409.1

Tian, Y., & Zhao, D. (2012). Seismic anisotropy and heterogeneity in the Alaska subduction zone. Geophysical Journal International, 190(1), 629–649. https://doi.org/10.1111/j.1365-246X.2012.05512.x

Topuz, G., Okay, A. I., Altherr, R., Satir, M., & Schwarz, W. H. (2008). Late Cretaceous blueschist facies metamorphism in southern Thrace (Turkey) and its geodynamic implications. Journal of Metamorphic Geology, 26(9), 895–913. https://doi.org/10.1111/j.1525-1314.2008.00792.x

Tsujimori, T., Matsumoto, K., Wakabayashi, J., & Liou, J. G. (2006). Franciscan eclogite revisited: Reevaluation of the P–T evolution of tectonic blocks from Tiburon Peninsula, California, U.S.A. Mineralogy and Petrology, 88(1), 243. https://doi.org/10.1007/s00710-006-0157-1

Vaughan, M. T., & Guggenheim, S. (1986). Elasticity of muscovite and its relationship to crystal structure. Journal of Geophysical Research: Solid Earth, 91(B5), 4657–4664. https://doi.org/10.1029/JB091iB05p04657

Voigt, W. (1928). Lehrbuch der Kristallphysik. Teubner-Verlag. Leipzig. https://doi.org/10.1007/978-3-663-15884-4

Wang, J., & Zhao, D. (2008). P-wave anisotropic tomography beneath Northeast Japan. Physics of the Earth and Planetary Interiors, 170(1), 115–133. https://doi.org/10.1016/j.pepi.2008.07.042

Wang, J., & Zhao, D. (2010). Mapping P-wave anisotropy of the Honshu arc from Japan Trench to the back-arc. Journal of Asian Earth Sciences, 39(5), 396–407. https://doi.org/10.1016/j.jseaes.2010.04.009

Wang, J., & Zhao, D. (2012). P wave anisotropic tomography of the Nankai subduction zone in Southwest Japan. Geochemistry, Geophysics, Geosystems, 13(5). https://doi.org/10.1029/2012GC004081

Wang, Z., & Zhao, D. (2021). 3D anisotropic structure of the Japan subduction zone. Science Advances, 7(4), eabc9620. https://doi.org/10.1126/sciadv.abc9620

Ward, D., Mahan, K., & Schulte-Pelkum, V. (2012). Roles of quartz and mica in seismic anisotropy of mylonites. Geophysical Journal International, 190(2), 1123–1134. https://doi.org/10.1111/j.1365-246X.2012.05528.x

Wech, A. G., & Creager, K. C. (2011). A continuum of stress, strength and slip in the Cascadia subduction zone. Nature Geoscience, 4(9), 624–628. https://doi.org/10.1038/ngeo1215

Wei, W., Zhao, D., Xu, J., Zhou, B., & Shi, Y. (2016). Depth variations of P-wave azimuthal anisotropy beneath Mainland China. Scientific Reports, 6(1), 29614. https://doi.org/10.1038/srep29614

Wenk, H.-R., & Christie, J. M. (1991). Comments on the interpretation of deformation textures in rocks. Journal of Structural Geology, 13(10), 1091–1110. https://doi.org/10.1016/0191-8141(91)90071-P

Wheeler, J., Prior, D., Jiang, Z., Spiess, R., & Trimby, P. (2001). The petrological significance of misorientations between grains. Contributions to Mineralogy and Petrology, 141(1), 109–124. https://doi.org/10.1007/s004100000225

Whitney, D. L., & Evans, B. W. (2010). Abbreviations for names of rock-forming minerals. American Mineralogist, 95(1), 185–187. https://doi.org/10.2138/am.2010.3371

Worthington, J. R., Hacker, B. R., & Zandt, G. (2013). Distinguishing eclogite from peridotite: EBSD-based calculations of seismic velocities. Geophysical Journal International, 193(1), 489–505. https://doi.org/10.1093/gji/ggt004

Wright, S. I. (2000). Fundamentals of Automated EBSD. In A. J. Schwartz, M. Kumar, & B. L. Adams (Eds.), Electron Backscatter Diffraction in Materials Science (pp. 51–64). Boston, MA: Springer US. https://doi.org/10.1007/978-1-4757-3205-4_5

Zertani, S., Vrijmoed, J. C., Tilmann, F., John, T., Andersen, T. B., & Labrousse, L. (2020). P Wave Anisotropy Caused by Partial Eclogitization of Descending Crust Demonstrated by Modeling Effective Petrophysical Properties. Geochemistry, Geophysics, Geosystems, 21(6), e2019GC008906. https://doi.org/10.1029/2019GC008906

Zertani, S., Pleuger, J., Motra, H. B., & John, T. (2022). Highly variable petrophysical properties in felsic high-pressure rocks of the continental crust. Lithos, 410–411, 106572. https://doi.org/10.1016/j.lithos.2021.106572

Chapter 3: Dislocation creep of glaucophane in mafic blueschists during subduction: weighted Burgers vector analysis from the Catalina Schist

Jason N. Ott[1], Cailey B. Condit[1], Matěj Peč[2], and Baptiste Journaux[1]

[1]*Department of Earth & Space Sciences, University of Washington, Seattle, Washington, USA*

[2]*Department of Earth, Atmospheric & Planetary Sciences, Massachusetts Institute of Technology, Cambridge, Massachusetts, USA*

Abstract

Mafic blueschist is ubiquitous along the plate interface from the base of the seismogenic zone to blueschist to eclogite transition depths in many subduction zones. Currently, the deformation mechanisms of the rheology-controlling mineral glaucophane in blueschists are controversial. Dislocation creep, diffusion creep, and semi-brittle deformation have all been proposed, with specific implications for each in modulating slip behavior. We document the preserved deformation mechanisms in a lawsonite blueschist that equilibrated at ~300°C and 1.0 GPa in the Catalina Schist on Pimu'nga through a novel method coupling weighted Burgers vector (WBV) and misorientation analyses of glaucophane. Electron backscattered diffraction-based analyses reveal strong crystallographic and shape preferred orientations in glaucophane and dislocations organized into subgrain boundaries. Misorientation distributions further illustrate dislocation-accommodated deformation and dynamic recrystallization by subgrain rotation (SGR). Subgrain boundaries show WBVs composed primarily of <100>, <010>, and <110> components, with lower representation of 'easy' slip on <001> WBVs. Misorientation analysis demonstrates mother-daughter relationships between elongated core grains and recrystallized grains. Limited chemical zoning along microfractures suggests subsidiary diffusion creep during exhumation. Our results clearly document blueschist deformation primarily accommodated by dislocation creep and SGR recrystallization at P-T conditions of the base of the seismogenic zone.

1. Introduction

Subducting oceanic crust is a key contributor to the rheological behavior and state of stress along the subduction megathrust (Behr et al., 2022). The onset of blueschist-facies metamorphism often coincides with the base of the seismogenic zone, yet the rheological properties of mafic blueschists remain poorly understood (Hyndman et al., 1997; Stöckhert, 2002; Behr et al., 2018). Glaucophane (Gln), a sodic amphibole, is an abundant and ubiquitous mineral in mafic blueschist-facies rocks (Evans, 1990), and the major strain-accommodating phase in these lithologies (e.g., Teyssier et al., 2010). Despite Gln's importance for blueschist strength, its deformation mechanisms and rheology remain controversial: microstructural observations reveal a range of proposed deformation mechanisms from dislocation creep (Reynard et al., 1989; Kotowski and Behr, 2019), diffusion or dissolution-precipitation creep (Misch, 1969; De Caroli et al., 2024), and brittle/semi-brittle deformation (Ildefonse et al., 1990). These mechanisms and their resultant rheologies have important implications for slip behaviors and subduction dynamics (Platt et al., 2018; Behr and Becker, 2018). For example, if subducting crust has a power-law rheology (e.g., dislocation creep), it will behave in a more sensitive way to stress changes and may affect subduction velocities or slip behaviors compared to crust governed by a linear-viscous rheology (e.g., diffusion creep; Agard et al., 2018; Behr and Becker, 2018).

Microstructural studies of deformed rocks are key to unraveling active deformation mechanisms, but using textural data to infer specific mechanisms in low-symmetry, anisotropic minerals is challenging. Often, a strong crystallographic preferred orientation (CPO) is interpreted to reflect deformation by dislocation creep (e.g., Kotowski and Behr, 2019), but recent work demonstrates that CPOs and shape preferred orientations (SPOs) can develop by alternative mechanisms in elongate-grain minerals such as amphibole (e.g., Díaz Aspiroz et al., 2007; Getsinger and Hirth, 2014), and are not solely diagnostic of dislocation creep. Electron backscatter diffraction (EBSD)-based techniques, including weighted Burgers vector (WBV) and misorientation analyses, are effective in differentiating between deformation mechanisms (Wheeler et al., 2009, 2024).

We present novel microstructural analyses that document dislocation creep accommodated deformation of Gln in mafic blueschist at lawsonite blueschist (LBS)-facies conditions during subduction (~300°C and 1.0 GPa). WBV analysis diagnoses dislocation creep by identifying the distribution and direction of dislocations, with geometrically necessary dislocations (GNDs) accommodating lattice distortions such as subgrain boundaries (Supplemental Material; Wheeler et al., 2009, 2024). Here, we use the WBV to establish the lower bounds of the GND content and direction (slip-vector) in EBSD maps (Supplemental Material; Wheeler et al., 2009, 2024). Our results illustrate the formation of subgrain boundaries through dislocation glide on multiple slip systems and reveal dynamic recrystallization occurred via subgrain rotation. We document evidence for pervasive dislocation creep in Gln with limited evidence for diffusion creep. This offers a snapshot of deformation governed by a power-law rheology within subducted oceanic crust at the subduction interface downdip of the seismogenic zone.

2. Geological Framework and Methods

We focus on a deformed polymetamorphic metabasaltic garnet blueschist (GB) block within the mélange of the LBS unit (Fig. S1) of the Catalina Schist subduction complex on

Pimu'nga (Santa Catalina Island; Platt, 1976; Grove and Bebout, 1995). Previous workers proposed that this block subducted to eclogite-facies metamorphic conditions during the late Jurassic-early Cretaceous (165-135 Ma) to peak P-T conditions of 635 ± 14℃ at 1.65 ± 0.10 GPa (Grove and Bebout, 1995; Harvey et al., 2021). The block was subsequently exhumed and entrained in the LBS unit mélange, where it equilibrated and deformed at the P-T conditions of the surrounding LBS unit of 327 ± 8°C and 1 GPa P-T (Platt and Schmidt, 2024), between 100–90 Ma (Grove and Bebout, 1995). Together, these data support a history of prograde eclogitic metamorphism followed by an LBS-facies overprint of the GB block during a later stage of subduction and ductile deformation in the Cretaceous.

The deformed GB block contains >50% Gln with minor lawsonite, phengite, garnet, quartz, and titanite. A foliation is defined by the SPO and layer segregation of Gln, Lws, and Ph, with elongated Gln and Lws grains up to ~1 mm in length (Fig. S2A; mineral abbr. after Whitney and Evans, 2010). We observe textural equilibrium between Gln and Lws, Ttn in the matrix and as Gln/Lws inclusions, and intragranular deformation microstructures (undulatory extinction and subgrain structures), and core-mantle structures in Gln (Supplemental Material; Fig. S2).

We quantified these microstructural observations and interpreted deformation mechanisms in Gln using EBSD data, paired with scanning electron microscopy (SEM) imaging with the forescatter detector (FSD). FSD-imaged intragranular contrast gradients in Gln were targeted for energy dispersive spectroscopy (EDS) mapping of chemical zoning patterns. Operating conditions, analytical methods and data reduction are detailed in the Supplemental Material. We coupled microstructural analysis with pseudosection modeling to confirm the P-T conditions of Gln deformation (Supplemental Material; Fig. S3).

3. Microstructures and Deformation Mechanisms of Glaucophane

3.1 Dislocation-accommodated deformation of glaucophane

We used EBSD to measure the CPO and SPO produced by intra- and inter-granular deformation of Gln (Fig. 1). Larger, elongate Gln grains are mantled by smaller (equivalent diameter <5 μm) Gln grains (Fig. 1A). Glaucophane displays a type-IV CPO (Kim and Jung, 2019), commonly found both in natural (Díaz Aspiroz et al., 2007; Ott et al., 2024) and experimentally deformed amphiboles (e.g., Kim and Jung, 2019). The CPO-strength of each crystallographic axis (pfJ-index, after Michibayashi and Mainprice, 2004), reveal that the large Gln grains have a slightly stronger CPO (Fig. 1B), and SPOs (Fig. 1D) than the small grains.

Misorientations in Gln and Lws are revealed by kernel average misorientation (KAM; Fig. 1C) maps and pervasively organized into low-angle boundaries consistent with subgrain boundary formation by the migration of dislocations during recovery processes (Passchier and Trouw, 1998). Misorientation angle distributions for random and neighboring pairs of Gln grains are significantly different from each other and the theoretical distribution for an untextured CPO (Fig. 1E). The neighboring grain-pair misorientation angle distribution displays a peak at low-angles. These misorientation data suggest the activation of subgrain rotation (SGR) recrystallization in Gln, a recovery-recrystallization process associated with dislocation creep (e.g., Wheeler et al., 2001).

We use WBV analysis (after Wheeler et al., 2009, 2024) on selected grains (Fig. 2) to image significant dislocation densities concentrated along subgrain boundaries (~0.1–0.2 μm^{-1}; Figs. 2A,D). The WBV directions frequently correspond to GNDs on the great circle connecting the <100>, <010>, and <110> crystallographic directions, with less frequent documentation of a WBV with a component in the <001>-direction frequently observed in amphiboles (insets, Figs. 2A,D; Reynard 1989). There is no systematic chemical zonation (Fig. 2B), and the changes in orientation are not associated with microfractures (Fig. 2C inset; Fig. S4). Extending the WBV analysis to larger maps yielded evidence of the same slip vectors observed in the individual grains (Figs. S5-12). The alignment of the WBV clusters along this great circle supports subgrain boundary formation in Gln by dislocation glide on multiple slip systems, which is consistent with the mechanism of dislocation creep (Karato, 2008).

Comparison of the orientations of core Gln grains to surrounding mantle grains reveal groupings of small, misorientation-free grains (lower left, Figs. 2C,E) proximal to subgrain structures in the core grains. These groups display CPOs clustered near the central grain orientation, suggesting an inherited orientation, or mother-daughter relationship, between grains (lower left, Figs. 2C,E). This relationship supports the inference of SGR recrystallization from the misorientation angle distributions. In conjunction with widespread evidence of dislocation glide on multiple slip systems, we interpret dislocation creep as the primary Gln deformation mechanism recorded in the GB sample (Reynard et al., 1989; Passchier and Trouw, 1998).

3.2 Minor diffusion-mediated deformation of glaucophane

We observe limited evidence of chemical zoning associated with microfractures in Gln oriented ~subnormal to the foliation (Fig. 3A), with a decrease in Mg and Al coupled to an Fe increase (Fig. 3B). This change in amphibole composition away from Gln toward riebeckite likely stems from retrogression at lower pressures (Wood, 1980). Chemically zoned Gln is only found with relatively rare microfractures—no core-rim zoning was observed (e.g., De Caroli et al., 2024)—implying the involvement of a diffusion-mediated process in tandem with the development of the microfractures in Gln, a phenomenon more pervasively observed in recent experiments (Tokle et al., 2023).

4. Discussion

4.1 P-T conditions of glaucophane deformation

Textural equilibrium between Gln and Lws (Figs. S2A,C-D), and Ttn in the matrix and inclusions in Gln and Lws poikiloblasts suggest significant Gln growth occurred within the Lws and Ttn stability fields. Idiomorphic Grts primarily occur as Gln-inclusions (Fig. S2B), while matrix Grts display partial resorption textures (Fig. S2A)—suggesting that Grt was unstable during the LBS metamorphism, consistent with our PerpleX modeling results (Fig. 4A; Supplemental Material). Thus, we interpret the majority of deformation in the Gln to have occurred during fabric development defined by the LBS mineral assemblage at or near LBS-facies conditions of ~300°C and 1.0 GPa.

4.2 Dislocation creep of glaucophane at lawsonite blueschist conditions

Our WBV-analysis of Gln subgrain boundaries reveals glide on slip systems previously identified by TEM (Reynard et al., 1989). A key distinction is that our most frequently observed WBVs align with slip on the (010)[100],{110}1/2<110>, and (001)1/2<110> systems, with infrequent evidence for the systems with [001]-slip vectors that are expected to dominate at low temperatures (Reynard et al., 1989). This preferential preservation of 'hard' over 'easy' slip systems stems from the occurrence of SGR recrystallization. Progressive rotation of subgrains through the addition of dislocations with a [001]-Burgers vector to the subgrain boundary leads to recrystallization (Karato, 2008), such that the dislocations are recorded only by their influence on CPO-development (Fig. 1B). Indeed, the prevalence of recrystallized daughter-grains at grain boundary segments associated with the [001]-axis are consistent with dislocation creep in Gln dominated by glide on the (100)[001], {110}[001], and (010)[001] systems (Reynard et al., 1989). Figure 4B illustrates the development of dislocation creep-related microstructures in Gln by the activation of dislocation glide on multiple slip systems, subgrain boundary development, and subsequent SGR recrystallization. This is consistent with previous studies of intragranular deformation of Gln by dislocation creep (Reynard et al., 1989; Kotowski and Behr, 2019). This first application of WBV analysis to Gln illustrates its utility to resolve slip-vectors on large sample areas (compared to TEM) and provides the first evidence of significant dislocation motion on hard slip-systems at low temperatures.

4.3 Retrograde minor diffusion-mediated deformation of glaucophane

Microboudinage/dissolution-precipitation creep has been observed previously in the rock record and in experimental samples (Misch, 1969; Tokle et al., 2023). Metasomatism is well documented in the mélange of the Catalina schist, and may have modulated the strength of blueschist in the presence of reactive fluids at LBS conditions (Bebout and Barton, 2002). This diffusion-mediated deformation, while observed, was not pervasive in these samples.

5. Implications for Glaucophane Rheology and Behavior During Subduction

Previous work has demonstrated evidence for Gln deformation primarily by diffusive mechanisms at epidote blueschist conditions (e.g., 400°C at <1 GPa, De Caroli et al., 2024). In contrast, our results reveal Gln deformation dominated by dislocation creep at LBS conditions. The microstructural evidence and our WBV analysis show dislocation creep is an important deformation mechanism in blueschist with large grain sizes at the onset of blueschist-facies metamorphism at the subduction interface. A key implication of our results is that dislocation creep (a power law rheology) is highly stress-sensitive. Mafic blueschist in the subducting slab likely plays an important role in plate coupling and convergence velocities, and could contribute to slow slip behaviors at the base of the seismogenic zone (Bürgmann and Dresen, 2008; Wech and Creager, 2011; Behr and Becker, 2018). Our results demonstrate that blueschist deformation at subduction conditions is readily accommodated by dislocation creep in Gln modulated by external controls such as P-T conditions or internal factors such as Gln grain size. Ongoing experimental work to quantify the rheology of blueschist are, therefore, critical to constraining the mechanical behavior of the subduction megathrust.

Acknowledgments

Funding provided by NSF EAR-2022154 and NSF EAR-2022928. We acknowledge the Molecular Analysis Facility, a National Nanotechnology Coordinated Infrastructure (NNCI) site at UW, which is supported in part by funds from NSF (awards NNCI-2025489, NNCI-1542101), the Molecular Engineering & Sciences Institute, and the Clean Energy Institute. We thank K. Harvey and S. Penniston-Dorland for sample access and J. Wheeler, E. Miranda and an anonymous reviewer for constructive comments that improved this contribution.

Chapter 3 Figures

Figure 1. A. EBSD map representative of GB block sample. B. Pole figures of [100], [010], and [001] axes of all Gln, large Gln grains, and small Gln grains. C. Kernel average misorientation (KAM) illustrating subgrain structure. D. Glaucophane SPO rose diagram (orientation of the longest diameter of grains weighted by area). E. Random-pair (left) and neighbor-pair (right) misorientation angle distributions for all Gln in (A).

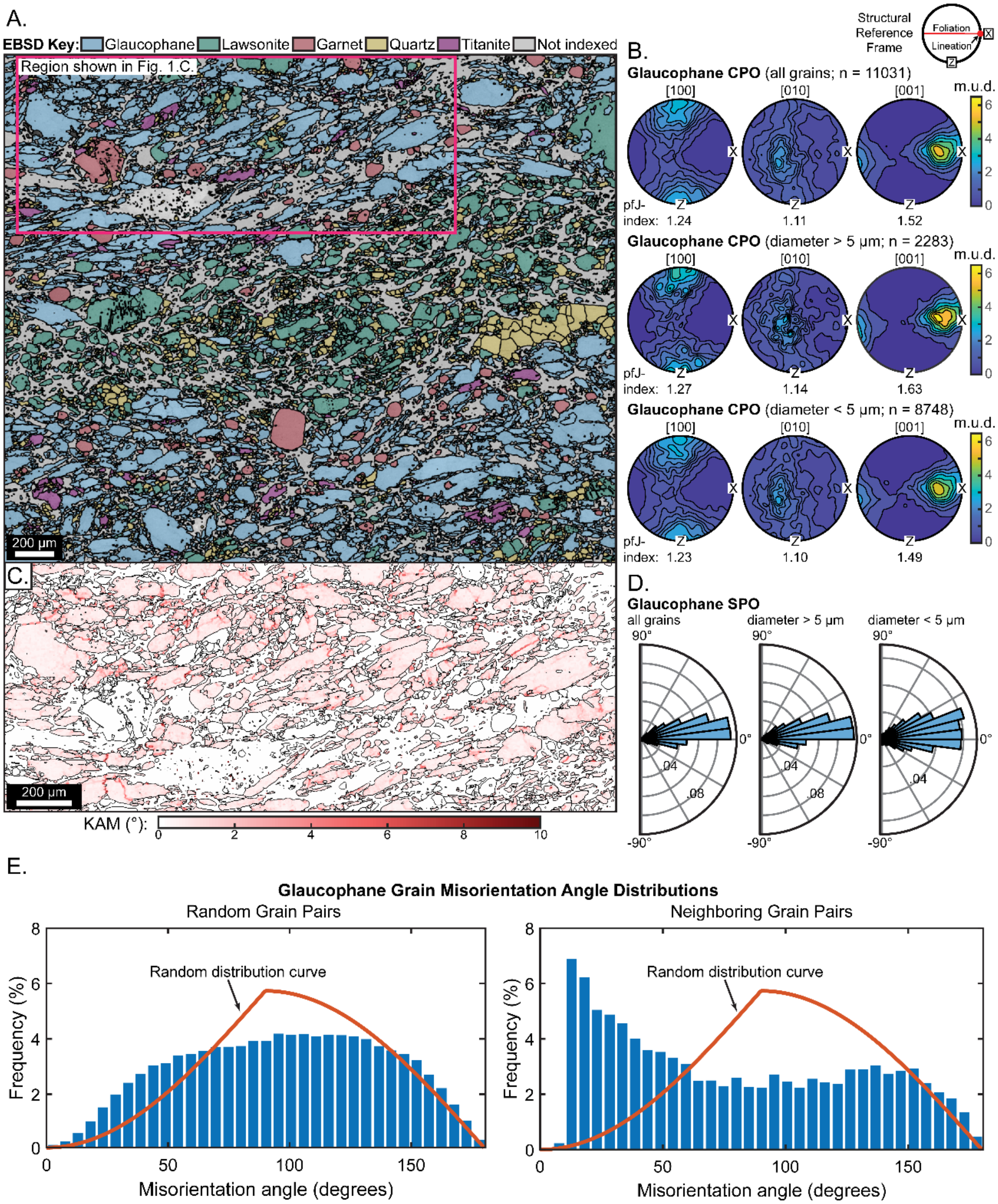

Figure 2. A. Differential method WBV magnitude map for selected Gln grain from region 5 (Fig. S11). Integral method WBV directions for red boxed subgrain boundary segments are plotted as inverse pole figures. B. EDS maps of subgrain-containing region in (A). C. KAM map of Gln core grain (A) and mantle grains with all indexed orientations shown on pole figures (right) colored by grain boundary. The FSD image inset. D. WBV magnitude and directions for select Gln grain from region 1 (Fig. S7) calculated as in (A). E. KAM of Gln core (D) and mantle grains calculated as in (C).

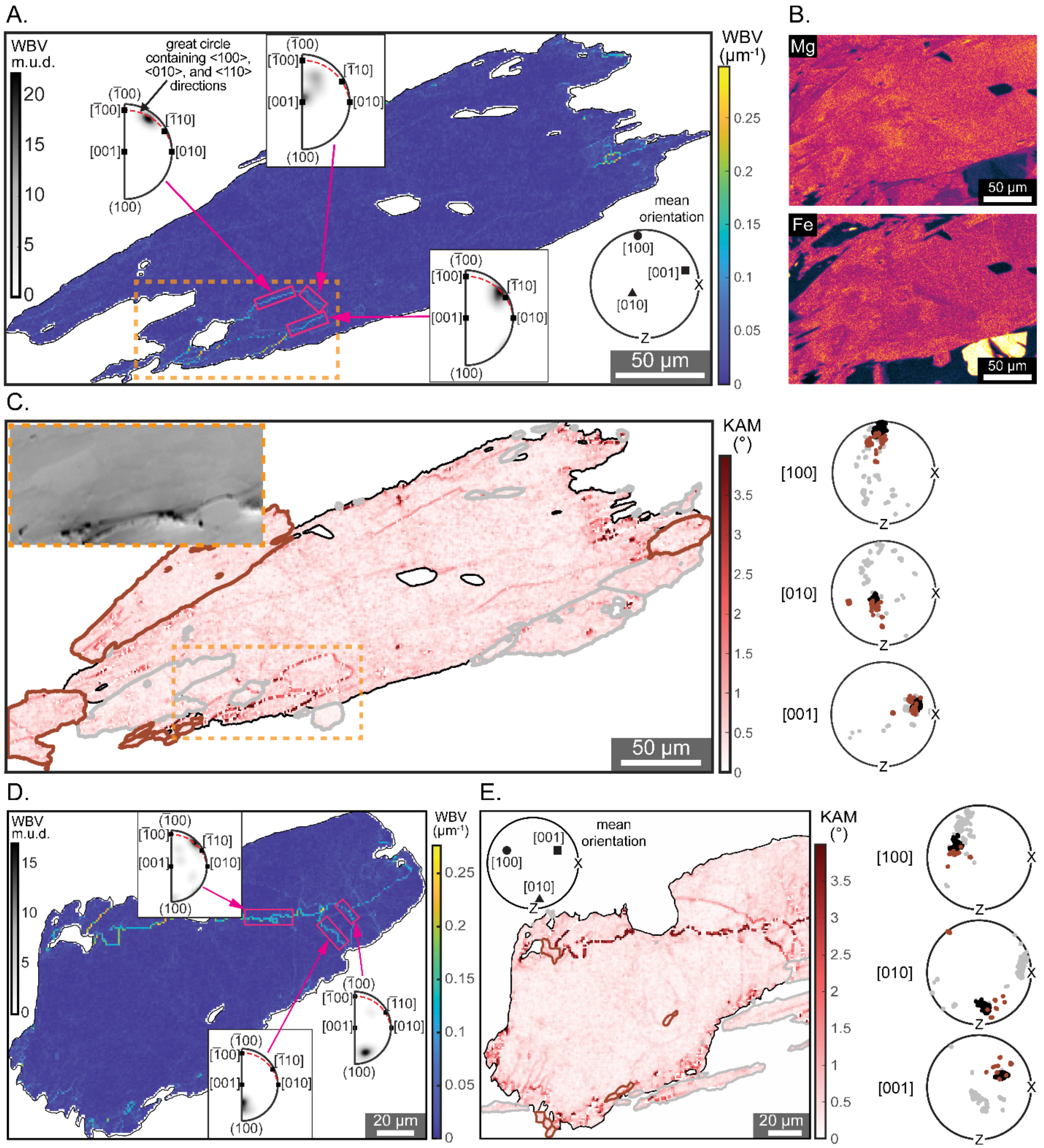

Figure 3. A. BSE image of selected Gln grain from region 3 (Fig. S9) B. EDS maps.

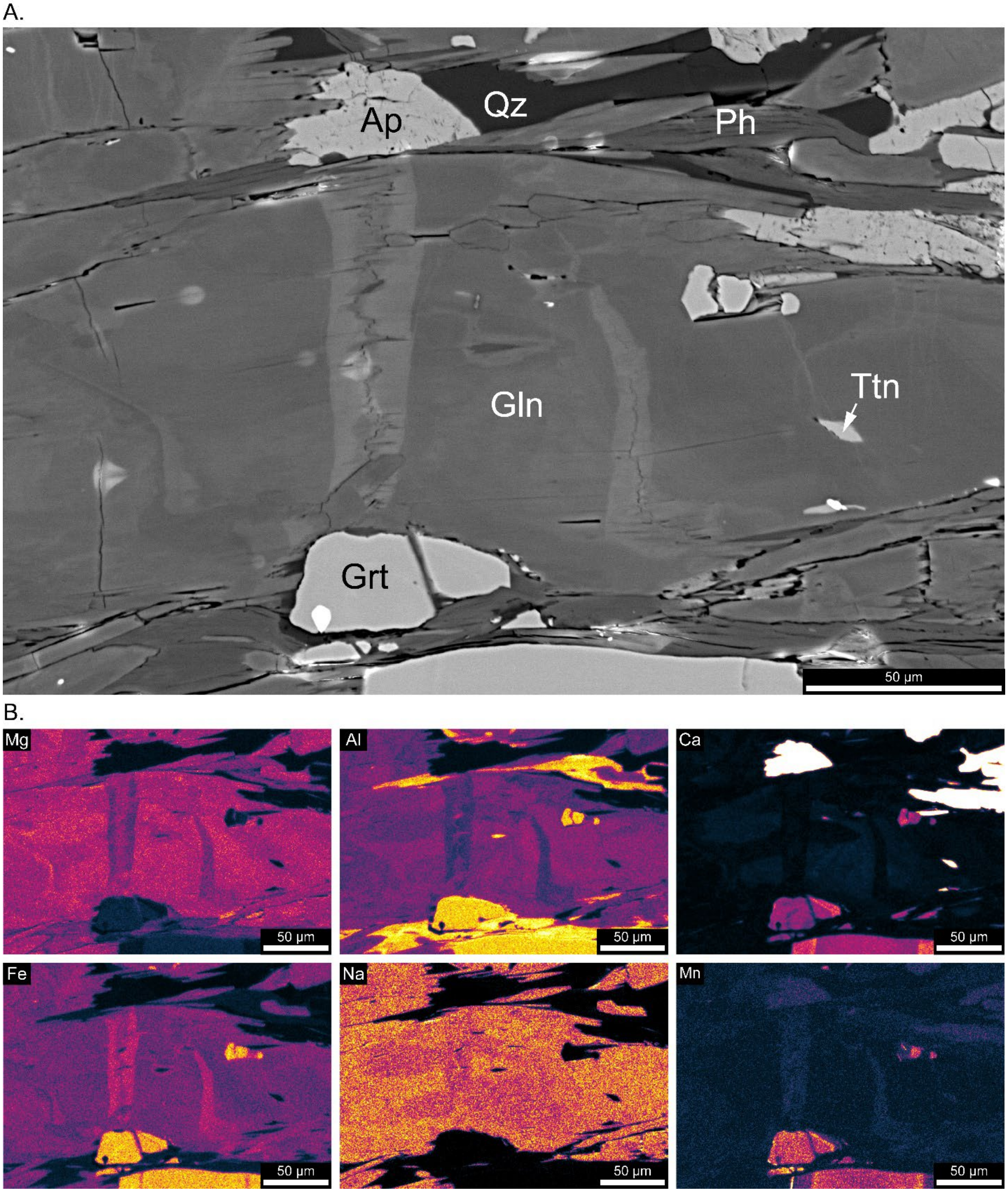

Figure 4. A. P-T diagram of occurrence of Lws, Ttn, Rt, and Grt from pseudosection models of bulk composition (Fig. S3; Supplemental Material) and estimated peak GB block and LBS mélange P-T conditions. B. Schematic representation of development of dislocation creep and SGR recrystallization microstructures: i. disorganized dislocation defects in the crystal lattice created by stress ii. mobile dislocations become organized into subgrain boundaries, reducing grain energy iii. progressive addition of dislocations to subgrain boundary increases misorientation by subgrain rotation iv. boundary evolves into high-angle grain boundary (~10° misorientation angle) from large mismatch in the crystal lattices across boundary.

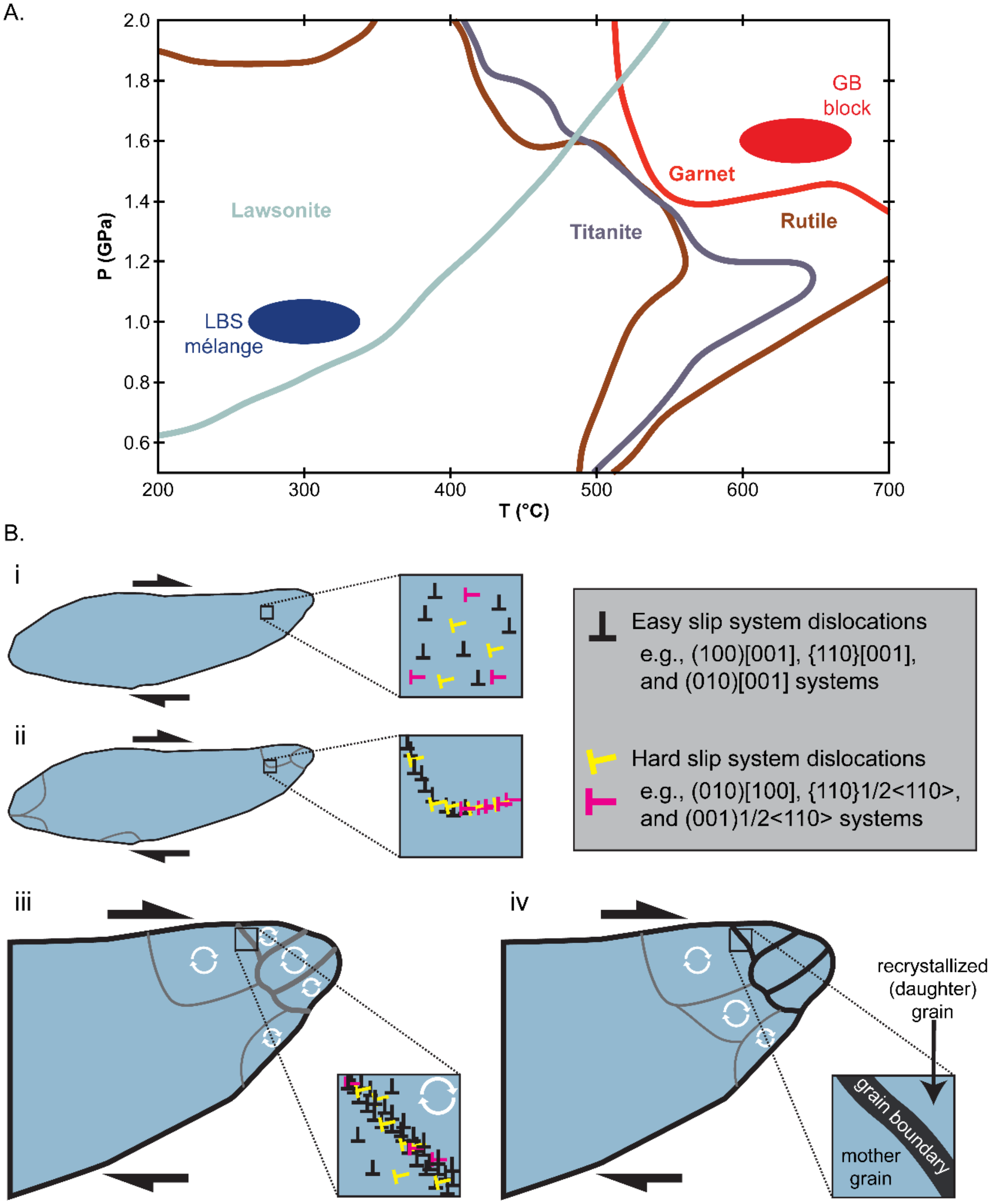

Chapter 3 References

Agard, P., Plunder, A., Angiboust, S., Bonnet, G., and Ruh, J., 2018, The subduction plate interface: rock record and mechanical coupling (from long to short timescales): Lithos, v. 320–321, p. 537–566, doi:10.1016/j.lithos.2018.09.029.

Bebout, G.E., and Barton, M.D., 2002, Tectonic and metasomatic mixing in a high-*T*, subduction-zone mélange—insights into the geochemical evolution of the slab–mantle interface: Chemical Geology, v. 187, p. 79–106, doi:10.1016/S0009-2541(02)00019-0.

Behr, W.M., and Becker, T.W., 2018, Sediment control on subduction plate speeds: Earth and Planetary Science Letters, v. 502, p. 166–173, doi:10.1016/j.epsl.2018.08.057.

Behr, W.M., Holt, A.F., Becker, T.W., and Faccenna, C., 2022, The effects of plate interface rheology on subduction kinematics and dynamics: Geophysical Journal International, v. 230, p. 796–812, doi:10.1093/gji/ggac075.

Behr, W.M., Kotowski, A.J., and Ashley, K.T., 2018, Dehydration-induced rheological heterogeneity and the deep tremor source in warm subduction zones: Geology, v. 46, p. 475–478, doi:10.1130/G40105.1.

Bürgmann, R., and Dresen, G., 2008, Rheology of the Lower Crust and Upper Mantle: Evidence from Rock Mechanics, Geodesy, and Field Observations: Annual Review of Earth and Planetary Sciences, v. 36, p. 531–567, doi:10.1146/annurev.earth.36.031207.124326.

De Caroli, S., Fagereng, Å., Ujiie, K., Blenkinsop, T., Meneghini, F., and Muir, D., 2024, Deformation microstructures of low- and high-strain epidote-blueschist (Ryukyu arc, Japan): Implications for subduction interface rheology: Journal of Structural Geology, v. 180, p. 105041, doi:10.1016/j.jsg.2023.105041.

Díaz Aspiroz, M., Lloyd, G.E., and Fernández, C., 2007, Development of lattice preferred orientation in clinoamphiboles deformed under low-pressure metamorphic conditions. A SEM/EBSD study of metabasites from the Aracena metamorphic belt (SW Spain): Journal of Structural Geology, v. 29, p. 629–645, doi:10.1016/j.jsg.2006.10.010.

Evans, B.W., 1990, Phase relations of epidote-blueschists: Lithos, v. 25, p. 3–23, doi:10.1016/0024-4937(90)90003-J.

Getsinger, A.J., and Hirth, G., 2014, Amphibole fabric formation during diffusion creep and the rheology of shear zones: Geology, v. 42, p. 535–538, doi:10.1130/G35327.1.

Grove, M., and Bebout, G.E., 1995, Cretaceous tectonic evolution of coastal southern California: Insights from the Catalina Schist: Tectonics, v. 14, p. 1290–1308, doi:10.1029/95TC01931.

Harvey, K.M., Penniston-Dorland, S.C., Kohn, M.J., and Piccoli, P.M., 2021, Assessing P-T variability in mélange blocks from the Catalina Schist: Is there differential movement at the subduction interface? Journal of Metamorphic Geology, v. 39, p. 271–295, doi:10.1111/jmg.12571.

Hyndman, R.D., Yamano, M., and Oleskevich, D.A., 1997, The seismogenic zone of subduction thrust faults: Island Arc, v. 6, p. 244–260, doi:10.1111/j.1440-1738.1997.tb00175.x.

Ildefonse, B., Lardeaux, J.-M., and Caron, J.-M., 1990, The behavior of shape preferred orientations in metamorphic rocks: amphiboles and jadeites from the Monte Mucrone area (Sesia-Lanzo zone, Italian Western Alps): Journal of Structural Geology, v. 12, p. 1005–1011, doi:10.1016/0191-8141(90)90096-H.

Karato, S., 2008, Deformation of Earth Materials: An Introduction to the Rheology of Solid Earth: Cambridge, Cambridge University Press, doi:10.1017/CBO9780511804892.

Kim, J., and Jung, H., 2019, New Crystal Preferred Orientation of Amphibole Experimentally Found in Simple Shear: Geophysical Research Letters, v. 46, p. 12996–13005, doi:10.1029/2019GL085189.

Kotowski, A.J., and Behr, W.M., 2019, Length scales and types of heterogeneities along the deep subduction interface: Insights from exhumed rocks on Syros Island, Greece: Geosphere, v. 15, p. 1038–1065, doi:10.1130/GES02037.1.

Michibayashi, K., and Mainprice, D., 2004, The Role of Pre-existing Mechanical Anisotropy on Shear Zone Development within Oceanic Mantle Lithosphere: an Example from the Oman Ophiolite: Journal of Petrology, v. 45, p. 405–414, doi:10.1093/petrology/egg099.

Misch, P., 1969, Paracrystalline microboudinage of zoned grains and other criteria for synkinematic growth of metamorphic minerals: American Journal of Science, v. 267, p. 43–63, doi:10.2475/ajs.267.1.43.

Ott, J.N., Condit, C.B., Schulte-Pelkum, V., Bernard, R., and Pec, M., 2024, Seismic Anisotropy of Mafic Blueschists: EBSD-Based Constraints From the Exhumed Rock Record: Journal of Geophysical Research: Solid Earth, v. 129, p. e2023JB027679, doi:10.1029/2023JB027679.

Passchier, C.W., and Trouw, R.A.J., 1998, Microtectonics: Berlin, Heidelberg, Springer, doi:10.1007/978-3-662-08734-3.

Platt, J.P., 1976, The petrology, structure, and geologic history of the Catalina Schist terrain, Southern California: Berkeley, University of California Press, University of California publications in geological sciences, 111 p.

Platt, J.P., and Schmidt, W.L., 2024, Is the Inverted Field Gradient in the Catalina Schist Terrane Primary or Constructional? Tectonics, v. 43, p. e2023TC008021, doi:10.1029/2023TC008021.

Platt, J.P., Xia, H., and Schmidt, W.L., 2018, Rheology and stress in subduction zones around the aseismic/seismic transition: Progress in Earth and Planetary Science, v. 5, p. 24, doi:10.1186/s40645-018-0183-8.

Reynard, B., Gillet, P., and Willaime, C., 1989, Deformation mechanisms in naturally deformed glaucophanes: a TEM and HREM study: European Journal of Mineralogy, v. 1, p. 611–624, doi:10.1127/ejm/1/5/0611.

Stöckhert, B., 2002, Stress and deformation in subduction zones: insight from the record of exhumed metamorphic rocks: Geological Society, London, Special Publications, v. 200, p. 255–274, doi:10.1144/GSL.SP.2001.200.01.15.

Teyssier, C., Whitney, D.L., Toraman, E., and Seaton, N.C.A., 2010, Lawsonite vorticity and subduction kinematics: Geology, v. 38, p. 1123–1126, doi:10.1130/G31409.1.

Tokle, L., Hufford, L.J., Behr, W.M., Morales, L.F.G., and Madonna, C., 2023, Diffusion Creep of Sodic Amphibole-Bearing Blueschist Limited by Microboudinage: Journal of Geophysical Research: Solid Earth, v. 128, p. e2023JB026848, doi:10.1029/2023JB026848.

Wech, A.G., and Creager, K.C., 2011, A continuum of stress, strength and slip in the Cascadia subduction zone: Nature Geoscience, v. 4, p. 624–628, doi:10.1038/ngeo1215.

Wheeler, J., Mariani, E., Piazolo, S., Prior, D. j., Trimby, P., and Drury, M. r., 2009, The weighted Burgers vector: a new quantity for constraining dislocation densities and types using electron backscatter diffraction on 2D sections through crystalline materials: Journal of Microscopy, v. 233, p. 482–494, doi:10.1111/j.1365-2818.2009.03136.x.

Wheeler, J., Piazolo, S., Prior, D.J., Trimby, P.W., and Tielke, J.A., 2024, Using crystal-lattice distortion data for geological investigations: the weighted Burgers vector method: Journal of Structural Geology, v. 179, p. 105040, doi:10.1016/j.jsg.2023.105040.

Wheeler, J., Prior, D., Jiang, Z., Spiess, R., and Trimby, P., 2001, The petrological significance of misorientations between grains: Contributions to Mineralogy and Petrology, v. 141, p. 109–124, doi:10.1007/s004100000225.

Whitney, D.L., and Evans, B.W., 2010, Abbreviations for names of rock-forming minerals: American Mineralogist, v. 95, p. 185–187, doi:10.2138/am.2010.3371.

Wood, R.M., 1980, Compositional zoning in sodic amphiboles from the blueschist facies: Mineralogical Magazine, v. 43, p. 741–752, doi:10.1180/minmag.1980.043.330.07.

Chapter 4: Experimental constraints on the strength of subducting oceanic crust: a dislocation creep flow law for blueschist (glaucophane)

Jason. N. Ott[1], Cailey B. Condit[1], and Matěj Peč[2]

[1] Department of Earth and Space Sciences, University of Washington, Seattle, WA, USA

[2] Department of Earth, Atmospheric and Planetary Sciences, Massachusetts Institute of Technology, Cambridge, MA, USA

Corresponding author: Jason Ott (jasonott@uw.edu)

Key Points:

- An experimentally derived flow law for dislocation creep in glaucophane
- The onset of viscous deformation in subducting slab occurs via glaucophane dislocation creep at downdip limit of seismogenic zone
- Temperature, grain-size, and pore-fluid pressure contribute to switching between dislocation creep and grain-size sensitive deformation

Abstract

We experimentally derived a flow law for dislocation creep in glaucophane, the defining mineral of mafic blueschists in subducting oceanic crust at the downdip limit of the seismogenic zone. Glaucophane aggregates were deformed in general shear at 1.5 GPa, 575–750°C, and strain rates of ~10^{-4}–10^{-5} s^{-1}, yielding a stress exponent $n = 5.3$ and activation energy $Q = 392$ kJ mol^{-1}. The prefactor $A = 160$ $MPa^{-5.3}$ s^{-1} was determined by global fitting of mechanical data. Microstructural analyses of experimental products document dislocation creep through dislocation-accommodated deformation and subgrain rotation recrystallization. Extrapolation to natural conditions predict viscous deformation in subducting slab initiates by glaucophane dislocation creep at ~350°C, transitioning to grain-size-sensitive mechanisms at higher temperatures, finer grain sizes, and elevated pore-fluid pressures. These rheological constraints highlight the role of blueschist in controlling the strength and slip behavior of the subduction interface.

Plain Language Summary

Subduction zones, where one tectonic plate sinks beneath another, generate major geological hazards including megathrust earthquakes and tsunamis. Below megathrust earthquake depths, the descending plate deforms by continuous, viscous deformation, but the strength of rocks at these conditions are largely unknown. We conducted high-pressure, high-temperature deformation experiments on glaucophane—a key mineral in subducting oceanic crust—to determine how it deforms under geologic conditions. Our experiments show that glaucophane deforms by a stress-sensitive process called dislocation creep at conditions relevant to the onset of viscous flow in the slab. At higher temperatures, smaller grain sizes, or elevated pore-fluid pressures, deformation becomes grain-size dependent. These results provide new experimental evidence for how and where the subducting slab weakens, offering insight into the transition from brittle, earthquake-generating slip to stable sliding along the plate boundary fault with increasing depth.

1 Introduction

Subduction drives plate tectonics and generates deadly geohazards, including megathrust earthquakes and tsunamis, during abrupt failure of the locked seismogenic zone along subduction megathrust faults. Viscous deformation downdip of this zone modulates slab strength and transfers stress updip, loading the megathrust (Scholz, 1988; Wech & Creager, 2011). The viscous rheology of the subducting slab therefore can exert a first-order control on stress and slip distribution (Behr et al., 2022). The onset of blueschist-facies metamorphism within subducting oceanic crust commonly coincides with the base of the seismogenic zone, but the strength and deformation behavior of these mafic blueschists remain poorly constrained (Behr & Becker, 2018; Hyndman et al., 1997; Stöckhert, 2002). Glaucophane, a sodic amphibole, is the defining phase in these rocks (Evans, 1990) and ubiquitously localizes strain (e.g., Kim et al., 2015; Kotowski & Behr, 2019; Teyssier et al., 2010). Field evidence suggests blueschists are stronger than serpentinite and weaker than eclogite (Behr et al., 2018; Muñoz-Montecinos et al., 2021), with bulk viscosities similar to quartz under equivalent conditions (Kotowski & Behr, 2019). Despite these insights, the rheology of glaucophane—and by extension blueschist—remains largely unquantified.

Microstructural studies show that glaucophane in natural blueschists deforms by multiple mechanisms. Dislocation creep has been observed by coupled crystallographic preferred orientations (CPOs), intragranular misorientations, undulose extinction, and subgrains (Kim et al., 2013; Kotowski & Behr, 2019; Ott et al., 2025a; Reynard et al., 1989). Dislocation glide on multiple slip systems is documented by TEM (Reynard et al., 1989) and EBSD-based weighted Burgers vector (WBV) analysis (Ott et al., 2025a). Diffusion- and dissolution-precipitation creep microstructures include observed amphibole-filled microboudin necks (Misch, 1969; Muñoz-Montecinos et al., 2023), development of shape preferred orientations (SPOs) of elongated grains aligned to the shear plane, and chemical zoning (De Caroli et al., 2024). Cataclasis and brittle to semi-brittle processes are also reported (Ildefonse et al., 1990; Muñoz-Montecinos et al., 2023). These diverse microstructures record deformation mechanisms that reflect distinct rheological regimes with important implications for megathrust slip and subduction dynamics (Behr & Becker, 2018; Platt et al., 2018): dislocation creep produces power-law stress-sensitive flow, whereas diffusion creep yields linear-viscous stress dependence. Both influence slip mode and convergence rate (Agard et al., 2018; Behr & Becker, 2018).

Experimental constraints on glaucophane and mafic blueschists are sparse. Kim et al. (2015) and Okazaki and Hirth (2020) reported semi-brittle deformation in blueschists at 1–2 GPa at ~400–500°C, at laboratory strain rates ~10^{-4} to 10^{-5} s^{-1}—all conditions relevant to intermediate-depth seismicity. Epidote blueschists under similar conditions showed dislocation glide and creep at moderate strain, transitioning to cataclasis and granular flow at shear strains $\gamma > 2$ (Park et al., 2020). Tokle et al. (2023) derived a microboudinage limited diffusion-creep flow law in mafic blueschists deformed at 1 GPa, 650–700°C, and strain rates of ~10^{-5} to 10^{-7} s^{-1}. Their microstructures record diffusion-limited growth in sodic-calcic amphibole. While these studies advance understanding, the strength of glaucophane under dislocation creep—commonly observed in natural rocks—still remains poorly quantified.

We performed high-pressure, high-temperature deformation experiments on glaucophane aggregates under conditions favorable for dislocation creep. General shear tests were conducted in a Griggs-type apparatus at 1.5 GPa, 575–750°C, and shear strain rates of ~10^{-4} to 10^{-5} s^{-1}. Recovered microstructures reveal dislocation creep, which is consistent with a derived flow law using stress- and temperature-stepping experiments combined with global parameter fitting returning a stress exponent, n, of ~5. Extrapolating this flow law to conditions expected in nature, we find that glaucophane-rich blueschists deform primarily by dislocation creep below ~500°C, transitioning to grain-size-sensitive mechanisms at higher temperatures and finer grain sizes. These results suggest that viscous deformation in the subducting slab initiates by stress-sensitive dislocation creep near the downdip limit of the seismogenic zone, and likely evolves toward grain-size-sensitive creep with increasing depth and temperature.

2 Materials and Methods

2.1 Starting material

The glaucophane starting material was separated from a metabasic blueschist from Sifnos Island, Greece (Supplemental Information S1). The host rock was crushed and sieved to select a particle size range of 100–120 μm, and the particles were passed through a Franz magnetic separator and hand-picked with an optical microscope to isolate glaucophane with minimal inclusions. The picked glaucophane was ground by mortar-and-pestle, and we used Stokes settling in ethanol (Ronde, 2004) to select a starting particle size of 10–20 μm. The starting material is primarily glaucophane (>90%), with quartz (~8%), rutile (~2%), and oxide (<<1%) impurities.

2.2 Experimental methods

The experiments were conducted in a Sanchez (Griggs-type) triaxial deformation apparatus at MIT's Rock Deformation Laboratory (Ghaffari & Peč, 2020). For each experiment, 0.15 g of the starting material was loaded between two alumina forcing blocks precut to a 45° angle and weld-sealed in a 0.2 mm-thick gold jacket (Fig. 1a). The sample was placed between top and bottom alumina pistons within a solid NaCl-salt confining medium. The temperature was controlled with a graphite resistivity furnace and a K-type thermocouple positioned at the center of the sample. The sample assembly was placed in a water-cooled pressure vessel and capped with a lead plug to transmit the load from the σ_1 and σ_3 pistons to the sample and the full assembly was loaded into the Sanchez apparatus.

Table 1. Mechanical Data

Sample	T [°C]	P (σ_3) [MPa]	Shear Stress (σ_{shear}) [MPa]	[a]Equiv. Stress (σ_{eq}) [MPa]	Shear Strain Rate ($\dot{\gamma}$) [1/s]	[b]Equiv. Strain Rate ($\dot{\varepsilon}_{eq}$) [1/s]	Test Type
100JO	650	1500	701.6	1215.2	5.54e-4	3.20e-4	constant displacement rate
101JO	650	1500	285.4	494.3	2.89e-6	1.67e-6	load stepping
			346.2	599.7	4.57e-6	2.64e-6	
			412.1	713.8	1.16e-5	6.70e-6	
			480.8	832.8	3.91e-5	2.26e-5	
102JO	650	1500	273.2	473.2	8.00e-5	4.62e-5	constant displacement rate
103JO	750	1500	114.4	198.1	7.68e-4	4.44e-4	constant displacement rate
104JO	700	1500	211.5	366.3	8.15e-4	4.71e-4	constant displacement rate
105JO	700	1500	176.6	305.8	8.14e-5	4.70e-5	constant displacement rate
115JO	650	1500					hot press (16 hours)
152JO	650	1500	459.9	796.6	3.77e-5	2.18e-5	temperature stepping
	625	1500	459.9	796.6	7.91e-6	4.57e-6	
	600	1500	459.9	796.6	2.87e-6	1.66e-6	
	575	1500	459.9	796.6	3.55e-7	2.05e-7	

[a] Equivalent stress (σ_{eq}) determined as: $\sigma_{eq} = \sqrt{3} * \sigma_{shear}$ (after Paterson & Olgaard, 2000)
[b] Equivalent strain rate ($\dot{\varepsilon}_{eq}$) determined as: $\dot{\varepsilon}_{eq} = \dot{\gamma}/\sqrt{3}$ (after Paterson & Olgaard, 2000)

During the experiments, the pressure and temperature were gradually increased to 1.5 GPa and 650°C, and the samples were hot-pressed for 16 hours. After hot-pressing, the samples were deformed by (1) constant displacement rate at a constant temperature, (2) load-stepping at a constant temperature, or (3) temperature-stepping at a constant load. At the end of each experiment, the sample was quenched while reducing the differential stress to preserve the deformation microstructures and minimize unloading cracks. One experiment was quenched immediately after hot-pressing to preserve the predeformation microstructures. The experimental conditions are summarized in Table 1, and the experimental methods are fully described in Supporting Information S1–2.

2.3 Data analysis methods

2.3.1 Mechanical data analysis

Experimental data were sampled at 1 Hz and processed in the Matlab application, newRig (Peč, 2018). The data were corrected for rig stiffness, sample thinning, friction, and decreasing forcing-block overlap, and the shear strain, strain rate, and stress were calculated using the sample geometry. The shear stress was corrected using the calibration of Holyoke and Kronenberg (2010), which has been validated for the MIT-based Sanchez apparatus (discussed in Supporting Information of Ortega-Arroyo et al., 2025). The mechanical data analysis is discussed in detail in Supporting Information S3.

2.3.2 Microstructural data analysis

The experimental microstructures were analyzed using electron backscatter diffraction (EBSD), complemented by scanning electron microscopy (SEM) with backscatter electron (BSE) imaging. Analytical procedures, software, instrument settings, and data reduction protocols are described in Supporting Information S4.

3 Results and Discussion

3.1 Mechanical data

Mechanical data from the deformation experiments are summarized in Figure 1 and Table 1. Constant-strain-rate tests were conducted at 1.5 GPa, 650–750 °C, and strain rates of ~5×10^{-4} to 5×10^{-5} s^{-1} (Fig. 1b) show peak shear stress of ~700 MPa at 650 °C and ~5×10^{-4} s^{-1}. Increasing temperature by 100 °C reduced peak stress by ~80%, and an order-of-magnitude decrease in strain rate lowered it by ~60%. At 700 °C, the strain-rate sensitivity diminishes but remains substantial (~20% weaker at the lower strain rate). This strong sensitivity to temperature and strain rate indicates activation of viscous creep under our experimental conditions. Results from the load-stepping test at 650°C are shown in Figure 1c, where log equivalent shear stress is plotted against log equivalent strain rate. The inverse slope of the best-fit line yields a stress exponent of $n \sim 5.3$ ($R^2 = 0.94$), consistent with power-law creep. Figure 1d shows the temperature dependence of creep rate at a constant load stepping down from 650˚C to 575˚C in 25˚C increments (log equivalent strain rate versus 1000/T). A linear regression yields a slope of $-Q/R$, corresponding to an activation energy of $Q = 392$ kJ/mol ($R^2 = 0.98$) under the tested conditions.

3.2 Microstructural analyses

Figure 2 presents the EBSD-based microstructural analyses of the hot-pressed sample (115JO), and samples deformed at a strain rate of 5×10^{-4} s^{-1} at 650°C (100JO) and 700°C (104JO).

Glaucophane exhibits generally low intragranular strain in the hot-pressed sample, with a few highly-strained grains and low-angle boundaries that suggest minor dislocation-accommodated deformation (Figs. 2a; S1, S2). Despite nominally isostatic conditions, glaucophane developed a type-III CPO with the [100]-direction normal to the foliation and the [010]- and [001]-directions aligned to the foliation plane (Fig. 2b), similar to experimentally deformed amphiboles at low differential stress and T ≥ 650°C (Fig. 2m; after Ko & Jung, 2015). As commonly observed in amphiboles, the elongated axis of glaucophanes in the sample displays a strong SPO aligned with the [001]-direction of the CPO, which is contained in the foliation plane (e.g., De Caroli et al., 2024; Getsinger & Hirth,2014; Ott et al., 2025a). However, SPO strength is visibly weaker in the smallest grains (equivalent diameter d < 5 μm; Figs. 2c; S3). Misorientation angle distributions for neighboring and random glaucophane grain pairs are similar, though neighboring pairs display a peak at low angles (Fig. 2d). We attribute these microstructures to pressurization and annealing during hot pressing, activating minor contributions from dislocation creep to accommodate densification.

In the deformed samples, glaucophane grains exhibit progressively increasing intragranular strain and networks of lobate, low-angle boundaries with increasing temperature (Figs. 2e,i; S4–S7), even though both samples were deformed to shear strains of $\gamma \sim 2$–2.5 (Fig. 1b). The CPO and SPO of glaucophane in these deformed samples closely resembled those of the hot-pressed sample (Figs. 2f–k; S8, S9). The only significant difference is observable in the fine-grained fraction (d < 5 μm) of the 700 °C sample. Here, the [010]- and [001]-axes CPO transitioned from girdles to weak density maxima characteristic of a type-I amphibole CPO (Fig. 2j,m; Ko & Jung, 2015), while the SPO showed stronger alignment of grain long axes normal to the shear direction (Figs. 2k; S9). Relative to the hot-pressed sample, neighboring-pair misorientation distributions deviated more strongly from the random distribution with increasing temperature, exhibiting progressively enhanced low-angle peaks. (Figs. 2h,l).

Mechanical and microstructural evidence indicates glaucophane in our samples deformed predominantly by dislocation creep. Intragranular misorientations and low-angle boundaries reflect dislocation migration and subgrain formation (Passchier & Trouw, 1998). Elevated dislocation densities—WBV magnitudes commonly ~2 μm^{-1} at low-angle boundaries—and dominant WBV directions match pure and mixed-character dislocation systems in naturally deformed amphiboles (e.g., Ott et al., 2025a; Reynard et al., 1989; Figs. S5,S7). Low-angle peaks in the neighboring grain-pair misorientation angle distributions imply an inherited orientation relationship signifying recovery via subgrain rotation (SGR) recrystallization (e.g., Tullis, 2002). The development of rounded/lobate grain boundaries in deformed samples (Figs. S10–S13), grain-size reduction (Fig. S14), and preserved subgrain walls in recrystallized grains (Figs. S5, S7) further support SGR recrystallization. Together with the stress exponent of $n \sim 5.3$ from mechanical data, these features confirm deformation by dislocation creep (Karato, 2008).

We assessed the experimental products for potential metamorphic reactions and additional phases and their possible contribution to sample rheology. Glaucophane compositions (Fig. S15) fall within the range of previously studied Sifnos blueschists (Schliestedt, 1986), indicating no evidence of reaction-driven rheological changes. At $T \geq 700$ °C, glaucophane–quartz boundaries show phase mixing, most pervasive at 750 °C (103JO; Figs. S12-S13). Increasing temperature promotes increasing recrystallization rates (Cross & Skemer, 2019), which may enhance phase boundary mixing and result in rheological weakening by driving a transition into a grain-size-sensitive mechanism (Condit & Mahan, 2018; Cross & Skemer, 2017). Accordingly, tests at $T > 650$°C were excluded from the global fit parameters of the glaucophane dislocation creep flow law.

3.3 Experimental flow law for glaucophane aggregate

The constitutive relation for deformation of a material following a power-law rheology is expressed empirically as:

$$\dot{\varepsilon} = A\sigma^{n} exp\left(^{-Q}/_{RT}\right) \tag{1}$$

where $\dot{\varepsilon}$ is the strain rate (s^{-1}), A is the pre-exponential factor ($MPa^{-n}\ s^{-1}$), σ is the differential stress (MPa), n is the stress exponent, Q is the activation energy (kJ/mol), R is the gas constant, and T is the temperature (K). From load-stepping (Fig. 1c) and temperature-stepping (Fig. 1d) experiments, we obtained $n = 5.3 \pm 0.34$ and $Q = 392 \pm 30$ kJ/mol. A global fit to all mechanical data for $T \leq 650$°C yielded $A = 160\ MPa^{-5.3}\ s^{-1}$. The experimentally derived flow law for glaucophane, based on this suite of deformation experiments, is:

$$\dot{\varepsilon} = 160\ MPa^{-5.3}s^{-1}\sigma^{5.3}exp\left(^{-392\ kJ/mol}/_{RT}\right) \tag{2}$$

This relation is plotted in Figure 1e, along with all mechanical data.

Experiments at $T \leq 650$°C are generally well reproduced by the dislocation creep flow law, except for sample 102JO, deformed at 650°C and $\dot{\varepsilon} = 5 \times 10^{-5}\ s^{-1}$ (Fig. 1b,e). Post-experiment inspections revealed ~2 mm displacement of the thermocouple tip relative to the center of the shear zone (Fig. S16), introducing temperature uncertainty that may explain the deviation from the predicted stress-strain rate relationship (Fig. 1e; Dixon & Durham, 2018; Moarefvand et al., 2021). At temperatures > 650°C, measured stresses are ~200-400 MPa lower than predicted, consistent with microstructural evidence for rheological weakening due to a transition from dislocation creep to grain-size-sensitive deformation (Fig. 1e).

4 Implications

In Figure 3, we compare flow law predictions for subduction zone lithologies by extrapolating laboratory-derived flow laws to stresses, strain rates, and temperatures expected along the subduction interface. To represent mafic oceanic crust, we include our experimentally derived glaucophane dislocation creep law together with models for microboudinage-limited diffusion creep in glaucophane (Tokle et al., 2023), and dislocation creep in omphacite (Zhang et al., 2006) and eclogite (Zhang & Green, 2007). Although the flow law of Tokle et al. describes diffusion controlled by microboudin neck length rather than grain size, it provides the only available constraint on a diffusion creep mechanism in blueschist. For comparison, we also model quartz dislocation creep to represent subducted metasediments (Tokle et al., 2019), and antigorite dislocation creep (Hilairet et al., 2007) and low-temperature plasticity (Burdette & Hirth, 2022) for serpentinized mantle.

4.1 Strength of subduction interface lithologies

The transition from brittle to viscous deformation along the subduction interface is commonly associated with temperatures ~350-450°C (Hyndman et al., 1997; Peacock & Hyndman, 1999). At the onset of this range, and for strain rates relevant to subduction interface shear zones (10^{-14}–$10^{-11}\ s^{-1}$; e.g., Abila et al., 2024), lower stresses favor viscous deformation of glaucophane by dislocation creep (Fig. 3a) over other mechanisms. Predicted stresses required to activate dislocation creep deformation in mafic crust (glaucophane) are approximately two orders of magnitude greater than those for quartz and antigorite, suggesting that strain immediately downdip of the seismogenic zone along the subduction interface will be accommodated primarily in any metasediments or serpentinite present. At 450°C, stresses for dislocation creep and for microboudinage-limited diffusion creep in glaucophane are similar (Fig. 3b), signaling the onset of a transition to grain-size-sensitive deformation in mafic crust. However, metasediments and serpentinite are still predicted to be substantially weaker until ~550°C, when the strength of microboudinage-limited diffusion creep approaches that of metasediments and serpentinite (Fig. 3c).

4.2 Viscosity of the subduction interface

In Figure 3d, we plot effective viscosity versus temperature for the representative set of flow laws at a strain rate of 10^{-12} s^{-1} to represent a 1 km-thick shear zone with a 4 cm/year convergence rate. Our glaucophane dislocation creep flow law predicts viscosities that decrease from ~10^{21} to ~10^{19} Pa s between 350°C and 600°C, intermediate between eclogite and serpentinite. Above 450°C, the grain-size-dependent transition from dislocation creep to diffusion-accommodated deformation produces a steeper reduction in viscosity, and blueschist crust becomes nearly isoviscous with metasediments and serpentinite near 550°C. These results suggests a general rheological hierarchy of metasediment/serpentinite strength < blueschist strength < eclogite strength, in broad agreement with observations from the rock record (Behr et al., 2018; Davis & Whitney, 2006; Kotowski & Behr, 2019; Muñoz-Montecinos et al., 2021).

Given a reference asthenospheric viscosity of ~4×10^{20} Pa s (e.g., Peltier, 2004) and geodetically estimated strain rates at the asthenosphere of ~10^{-14} s^{-1} (Fagereng & Biggs, 2019) corresponding to stresses ~40 MPa, deformation along the subduction interface is likely accommodated within metasedimentary or serpentinite units, whose viscosities are markedly lower than that of the overriding asthenosphere (Behr & Becker, 2018). Predicted creep viscosities of glaucophane indicate that blueschist may also accommodate substantial strain in sediment-poor margins lacking a strongly serpentinized interface or up dip of the slab-mantle wedge corner (Fig. 3b), though this would require elevated stresses at the lowest temperatures along the viscous interface (Fig. 3a). After slab-top eclogitization initiates coupled flow of the slab and mantle wedge at ~80 km depths (Abers et al., 2020), blueschist may host intraslab creep deformation in the lower-temperature core of the slab where blueschist assemblages are preserved to deeper depths.

4.3 Pore fluid pressure and viscous creep in blueschist

Elevated pore-fluid pressures reduce the strength of the subduction interface, deepen the brittle–ductile transition, and are often invoked to explain slow-slip events (French & Condit, 2019; Houston, 2015; Leeman et al., 2016). Figure 3c shows strength profiles for glaucophane dislocation creep and microboudinage-limited diffusion creep, plotted against brittle strength profiles for pore fluid pressure factors ranging from $\lambda = 0.4$ (hydrostatic) to 0.95 (near-lithostatic; e.g., Bedford et al., 2021). Crustal strength profiles are calculated along slab-top P–T paths from Holt and Condit (2021) to assess the combined effects of pore pressure and thermal evolution on deformation mode in the subducting slab (van Keken et al., 2011; Sibson, 1992).

In the hot slab-top model, viscous strength profiles favor glaucophane dislocation creep over diffusion-accommodated creep only at sub-hydrostatic pore pressures and large grain sizes. With progressive cooling to an intermediate warm slab-top, dislocation creep is predicted over a wider range of pore pressures, extending to $\lambda \approx 0.6$. For the cold, mature subduction zone, dislocation creep is predicted over an even broader range (approaching $\lambda \approx 0.8$), but the strengths predicted by dislocation creep and microboudinage-limited diffusion creep converge. This suggests that both mechanisms could operate in the slab depending on grain size and stress state in a cold subduction zone.

4.4 Bridging the laboratory-field gap in subduction rheology

Rheological models based on our glaucophane dislocation creep flow law, together with those for other subduction-zone lithologies, indicate conditions under which glaucophane may deform viscously along the subduction interface. The models suggest that dislocation creep may dominate blueschist deformation at relatively low temperatures and high stresses, while increasing temperature, elevated pore-fluid pressure, and grain-size reduction promote grain-size-sensitive mechanisms (Fig. 3). Recent studies support these general trends, with natural blueschists displaying microstructural evidence of dislocation creep at low temperatures or large grain sizes (Choi et al., 2024; Ott et al., 2025a), and diffusion creep accompanied by reaction weakening at higher temperatures and smaller grain sizes (De Caroli et al., 2024).

A key complication is that laboratory creep experiments require stresses much higher than estimates for the downdip subduction interface to achieve deformation on laboratory time-scales. Stress estimates for the creeping zone are typically ~10–100 MPa, based on grain-size paleopiezometry, microstructural and constitutive-relation analysis, and integrated heat-flow models (Condit et al., 2022; Gao & Wang, 2014; Koyama et al., 2024; Lamb, 2006; Platt et al., 2018). Modeling creep with a monomineralic flow law of the weakest phase may apply in some systems (e.g., Stipp et al., 2002; Tokle et al., 2019; Tullis, 2002), but this approach neglects processes such as chemical and mechanical phase mixing, grain- and phase-boundary sliding, grain pinning, fluid-mediated mechanisms, and reactions that control the rheology of polyphase rocks (Condit & Mahan, 2018; Cross & Skemer, 2017; Cross et al., 2020; Soret et al., 2025; Zhao et al., 2019). The departure of our high-temperature data from the predicted stress–strain-rate relation for glaucophane dislocation creep underscores the importance of these processes in mafic blueschists (Fig. 1e). This dislocation creep flow law for glaucophane represents a key constraint in improving our understanding of the strength and deformation mechanisms active along the viscous subduction interface. However, future studies integrating polyphase rheology, fluid behavior, and field constraints are needed to predict deformation more accurately along subduction interfaces that are dominated by polyphase naturally deformed rocks in a fluid-rich environment.

Acknowledgments

Part of this work was conducted at the Washington Nanofabrication Facility / Molecular Analysis Facility, a National Nanotechnology Coordinated Infrastructure (NNCI) site at the University of Washington with partial support from the National Science Foundation via awards NNCI-1542101 and NNCI-2025489. The authors are indebted to Andrew Cross for EBSD-indexing assistance. The authors declare no conflicts of interest relevant to this study.

Open Research

Data sets for this research are available at this in-text data citation reference: Ott et al. (2025b)

Chapter 4 Figures

Figure 1. (a) Schematic of sample geometry for glaucophane deformation experiments in Sanchez deformation apparatus. (b) Shear stress versus shear strain curves of all constant displacement rate experiments. (c) Plot (logscale) of load-stepping experiment as equivalent (eq) stress ($\sigma_{eq} = \sqrt{3} * \sigma_{shear}$) versus equivalent strain rate ($\dot{\varepsilon}_{eq} = \dot{\gamma}/\sqrt{3}$) where n is determined as the reciprocal of the slope of a linear regression fit to the data. Equivalent stress and strain rate transformations are detailed in Paterson & Olgaard (2000) (d) Semi-log plot of equivalent strain rate versus inverse temperature at constant equivalent stress ~ 797 MPa. Slope of linear regression fit to data yields activation energy Q. (e) Dislocation creep flow law for glaucophane with A derived by global fit to mechanical data for $T \leq$ 650°C.

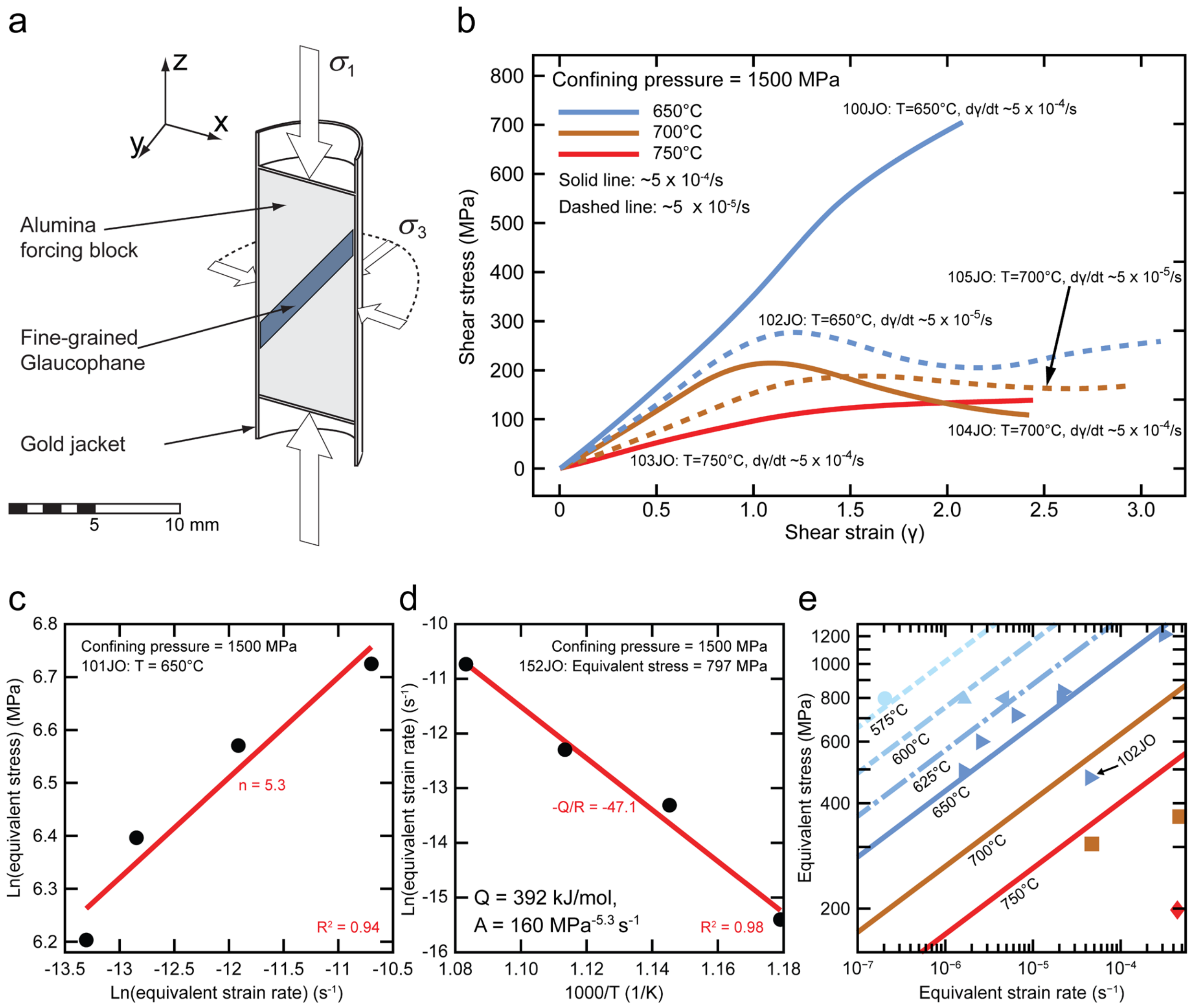

Figure 2. Electron backscattered diffraction (EBSD)-based microstructural analysis of samples 115JO, 100JO, and 104JO. (a-d) Sample 115JO: (a) misorientation-to-mean-orientation (mis2mean) and subgrain boundary (SGB) map of glaucophane, (b) pole figures of [100], [010], and [001] axes of all glaucophane, large glaucophane (effective diameter d > 5μm), and small glaucophane grains (d < 5μm), (c) rose diagrams of shape preferred orientation of glaucophane (SPO; orientation of longest diameter of grains weighted by area) for all, large, and small grains, and (d) misorientation angle distributions for neighbor and random glaucophane grain pairs. (e-h) Sample 100JO, same as (a-d). (i-l) Sample 104JO, same as (a-d). (m) Amphibole CPO types after Ko and Jung (2015). All pole figures are upper-hemisphere, equal-angle projections; contours are multiples of uniform distribution (m.u.d.). CPO—crystallographic preferred orientation; pfj—pole figure J-index, measured CPO strength of each crystallographic axis (e.g., Michibayashi & Mainprice, 2004).

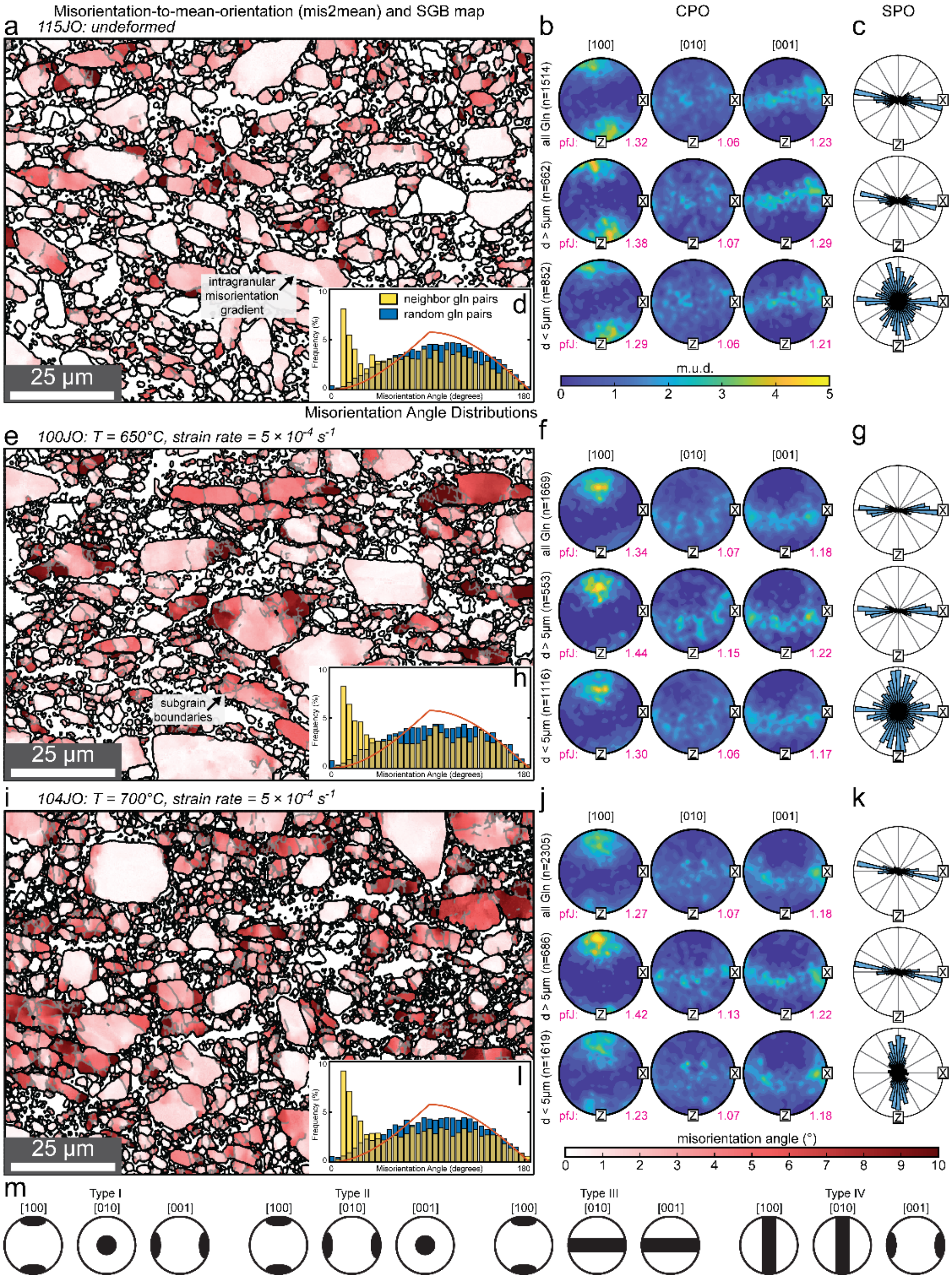

Figure 3. Rheological modeling of experiment-derived flow laws for minerals and lithologies relevant to subduction zone interface displayed as (a-c) stress versus strain rate for *T* = 350°, 450°, and 550°C respectively, (d) viscosity versus temperature at 10^{-12} s^{-1} strain rate, and (e) blueschist crustal strength profiles along hot (top), warm (middle), and cold (bottom) slab top subduction P-T paths (right panel; from representative paths in Fig. 3 of Holt & Condit, 2021) at 10^{-12} s^{-1} strain rate with brittle strength profiles predicted by Byerlee's rule with frictional coefficient μ = 0.6 and pore fluid pressure factors of λ = 0.4 (hydrostatic), 0.6, 0.8, and 0.95 (near-lithostatic). Quartz and omphacite dislocation creep strength profiles included for reference.

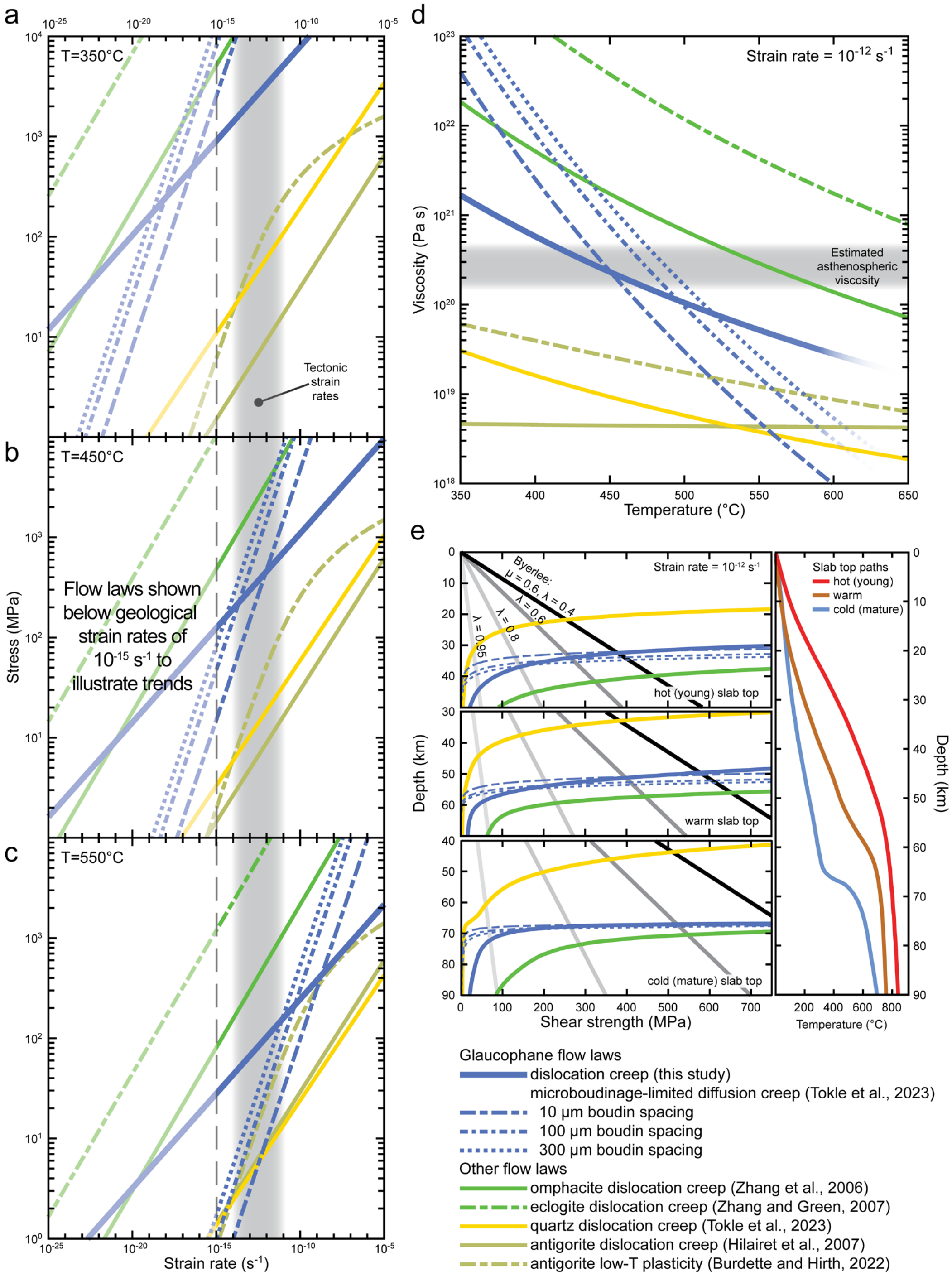

Chapter 4 References

Abers, G. A., Keken, P. E. van, & Wilson, C. R. (2020). Deep decoupling in subduction zones: Observations and temperature limits. *Geosphere*, *16*(6), 1408–1424. https://doi.org/10.1130/GES02278.1

Abila, A. L., Behr, W. M., & Ruh, J. (2024). Strength of viscous subduction interfaces: A global compilation. *Geology*. https://doi.org/10.1130/G52518.1

Agard, P., Plunder, A., Angiboust, S., Bonnet, G., & Ruh, J. (2018). The subduction plate interface: rock record and mechanical coupling (from long to short timescales). *Lithos*, *320–321*, 537–566. https://doi.org/10.1016/j.lithos.2018.09.029

Bedford, J. D., Faulkner, D. R., Allen, M. J., & Hirose, T. (2021). The stabilizing effect of high pore-fluid pressure along subduction megathrust faults: Evidence from friction experiments on accretionary sediments from the Nankai Trough. *Earth and Planetary Science Letters*, *574*, 117161. https://doi.org/10.1016/j.epsl.2021.117161

Behr, W. M., & Becker, T. W. (2018). Sediment control on subduction plate speeds. *Earth and Planetary Science Letters*, *502*, 166–173. https://doi.org/10.1016/j.epsl.2018.08.057

Behr, W. M., Kotowski, A. J., & Ashley, K. T. (2018). Dehydration-induced rheological heterogeneity and the deep tremor source in warm subduction zones. *Geology*, *46*(5), 475–478. https://doi.org/10.1130/G40105.1

Behr, W. M., Holt, A. F., Becker, T. W., & Faccenna, C. (2022). The effects of plate interface rheology on subduction kinematics and dynamics. *Geophysical Journal International*, *230*(2), 796–812. https://doi.org/10.1093/gji/ggac075

Burdette, E., & Hirth, G. (2022). Creep Rheology of Antigorite: Experiments at Subduction Zone Conditions. *Journal of Geophysical Research: Solid Earth*, *127*(7), e2022JB024260. https://doi.org/10.1029/2022JB024260

Choi, S., Park, Y., Han, S., Jung, S., Fabbri, O., & Jung, H. (2024). Deformation microstructures of blueschists in Alpine Corsica, France, and implications for seismic anisotropy and the low-velocity layer in subducting oceanic crust. *Tectonophysics*, *877*, 230297. https://doi.org/10.1016/j.tecto.2024.230297

Condit, C. B., & Mahan, K. H. (2018). Fracturing, fluid flow and shear zone development: Relationships between chemical and mechanical processes in Proterozoic mafic dykes from southwestern Montana, USA. *Journal of Metamorphic Geology*, *36*(2), 195–223. https://doi.org/10.1111/jmg.12289

Condit, C. B., French, M. E., Hayles, J. A., Yeung, L. Y., Chin, E. J., & Lee, C.-T. A. (2022). Rheology of Metasedimentary Rocks at the Base of the Subduction Seismogenic Zone.

Geochemistry, Geophysics, Geosystems, *23*(2), e2021GC010194. https://doi.org/10.1029/2021GC010194

Cross, A. J., & Skemer, P. (2017). Ultramylonite generation via phase mixing in high-strain experiments. *Journal of Geophysical Research: Solid Earth*, *122*(3), 1744–1759. https://doi.org/10.1002/2016JB013801

Cross, A. J., & Skemer, P. (2019). Rates of Dynamic Recrystallization in Geologic Materials. *Journal of Geophysical Research: Solid Earth*, *124*(2), 1324–1342. https://doi.org/10.1029/2018JB016201

Cross, Andrew J., Olree, E., Couvy, H., & Skemer, P. (2020). How Does Viscosity Contrast Influence Phase Mixing and Strain Localization? *Journal of Geophysical Research: Solid Earth*, *125*(8), e2020JB020323. https://doi.org/10.1029/2020JB020323

Davis, P. B., & Whitney, D. L. (2006). Petrogenesis of lawsonite and epidote eclogite and blueschist, Sivrihisar Massif, Turkey. *Journal of Metamorphic Geology*, *24*(9), 823–849. https://doi.org/10.1111/j.1525-1314.2006.00671.x

De Caroli, S., Fagereng, Å., Ujiie, K., Blenkinsop, T., Meneghini, F., & Muir, D. (2024). Deformation microstructures of low- and high-strain epidote-blueschist (Ryukyu arc, Japan): Implications for subduction interface rheology. *Journal of Structural Geology*, *180*, 105041. https://doi.org/10.1016/j.jsg.2023.105041

Dixon, N. A., & Durham, W. B. (2018). Measurement of Activation Volume for Creep of Dry Olivine at Upper-Mantle Conditions. *Journal of Geophysical Research: Solid Earth*, *123*(10), 8459–8473. https://doi.org/10.1029/2018JB015853

Evans, B. W. (1990). Phase relations of epidote-blueschists. *Lithos*, *25*(1), 3–23. https://doi.org/10.1016/0024-4937(90)90003-J

Fagereng, Å., & Biggs, J. (2019). New perspectives on ‘geological strain rates’ calculated from both naturally deformed and actively deforming rocks. *Journal of Structural Geology*, *125*, 100–110. https://doi.org/10.1016/j.jsg.2018.10.004

French, M. E., & Condit, C. B. (2019). Slip partitioning along an idealized subduction plate boundary at deep slow slip conditions. *Earth and Planetary Science Letters*, *528*, 115828. https://doi.org/10.1016/j.epsl.2019.115828

Gao, X., & Wang, K. (2014). Strength of stick-slip and creeping subduction megathrusts from heat flow observations. *Science*, *345*(6200), 1038–1041. https://doi.org/10.1126/science.1255487

Getsinger, A. J., & Hirth, G. (2014). Amphibole fabric formation during diffusion creep and the rheology of shear zones. *Geology*, *42*(6), 535–538. https://doi.org/10.1130/G35327.1

Ghaffari, H. O., & Peč, M. (2020). An ultrasound probe array for a high-pressure, high-temperature solid medium deformation apparatus. *Review of Scientific Instruments*, *91*(8), 085117. https://doi.org/10.1063/5.0004035

Hilairet, N., Reynard, B., Wang, Y., Daniel, I., Merkel, S., Nishiyama, N., & Petitgirard, S. (2007). High-Pressure Creep of Serpentine, Interseismic Deformation, and Initiation of Subduction. *Science*, *318*(5858), 1910–1913. https://doi.org/10.1126/science.1148494

Holt, A. F., & Condit, C. B. (2021). Slab Temperature Evolution Over the Lifetime of a Subduction Zone. *Geochemistry, Geophysics, Geosystems*, *22*(6), e2020GC009476. https://doi.org/10.1029/2020GC009476

Holyoke, C. W., & Kronenberg, A. K. (2010). Accurate differential stress measurement using the molten salt cell and solid salt assemblies in the Griggs apparatus with applications to strength, piezometers and rheology. *Tectonophysics*, *494*(1), 17–31. https://doi.org/10.1016/j.tecto.2010.08.001

Houston, H. (2015). Low friction and fault weakening revealed by rising sensitivity of tremor to tidal stress. *Nature Geoscience*, *8*(5), 409–415. https://doi.org/10.1038/ngeo2419

Hyndman, R. D., Yamano, M., & Oleskevich, D. A. (1997). The seismogenic zone of subduction thrust faults. *Island Arc*, *6*(3), 244–260. https://doi.org/10.1111/j.1440-1738.1997.tb00175.x

Ildefonse, B., Lardeaux, J.-M., & Caron, J.-M. (1990). The behavior of shape preferred orientations in metamorphic rocks: amphiboles and jadeites from the Monte Mucrone area (Sesia-Lanzo zone, Italian Western Alps). *Journal of Structural Geology*, *12*(8), 1005–1011. https://doi.org/10.1016/0191-8141(90)90096-H

Karato, S. (2008). *Deformation of Earth Materials: An Introduction to the Rheology of Solid Earth*. Cambridge: Cambridge University Press. https://doi.org/10.1017/CBO9780511804892

van Keken, P. E., Hacker, B. R., Syracuse, E. M., & Abers, G. A. (2011). Subduction factory: 4. Depth-dependent flux of H2O from subducting slabs worldwide. *Journal of Geophysical Research: Solid Earth*, *116*(B1). https://doi.org/10.1029/2010JB007922

Kim, D., Katayama, I., Michibayashi, K., & Tsujimori, T. (2013). Rheological contrast between glaucophane and lawsonite in naturally deformed blueschist from Diablo Range, California. *Island Arc*, *22*(1), 63–73. https://doi.org/10.1111/iar.12003

Kim, D., Katayama, I., Wallis, S., Michibayashi, K., Miyake, A., Seto, Y., & Azuma, S. (2015). Deformation microstructures of glaucophane and lawsonite in experimentally deformed blueschists: Implications for intermediate-depth intraplate earthquakes. *Journal of Geophysical Research: Solid Earth*, *120*(2), 1229–1242. https://doi.org/10.1002/2014JB011528

Ko, B., & Jung, H. (2015). Crystal preferred orientation of an amphibole experimentally deformed by simple shear. *Nature Communications*, *6*(1), 6586. https://doi.org/10.1038/ncomms7586

Kotowski, A. J., & Behr, W. M. (2019). Length scales and types of heterogeneities along the deep subduction interface: Insights from exhumed rocks on Syros Island, Greece. *Geosphere*, *15*(4), 1038–1065. https://doi.org/10.1130/GES02037.1

Koyama, Y., Wallis, S. R., & Nagaya, T. (2024). Subduction plate interface shear stress associated with rapid subduction at deep slow earthquake depths: example from the Sanbagawa belt, southwestern Japan. *Solid Earth*, *15*(2), 143–166. https://doi.org/10.5194/se-15-143-2024

Lamb, S. (2006). Shear stresses on megathrusts: Implications for mountain building behind subduction zones. *Journal of Geophysical Research: Solid Earth*, *111*(B7). https://doi.org/10.1029/2005JB003916

Leeman, J. R., Saffer, D. M., Scuderi, M. M., & Marone, C. (2016). Laboratory observations of slow earthquakes and the spectrum of tectonic fault slip modes. *Nature Communications*, *7*(1), 11104. https://doi.org/10.1038/ncomms11104

Michibayashi, K., & Mainprice, D. (2004). The Role of Pre-existing Mechanical Anisotropy on Shear Zone Development within Oceanic Mantle Lithosphere: an Example from the Oman Ophiolite. *Journal of Petrology*, *45*(2), 405–414. https://doi.org/10.1093/petrology/egg099

Misch, P. (1969). Paracrystalline microboudinage of zoned grains and other criteria for synkinematic growth of metamorphic minerals. *American Journal of Science*, *267*(1), 43–63. https://doi.org/10.2475/ajs.267.1.43

Moarefvand, A., Gasc, J., Fauconnier, J., Baïsset, M., Burdette, E., Labrousse, L., & Schubnel, A. (2021). A new generation Griggs apparatus with active acoustic monitoring. *Tectonophysics*, *816*, 229032. https://doi.org/10.1016/j.tecto.2021.229032

Muñoz-Montecinos, J., Angiboust, S., Garcia-Casco, A., & Raimondo, T. (2023). Shattered Veins Elucidate Brittle Creep Processes in the Deep Slow Slip and Tremor Region. *Tectonics*, *42*(4), e2022TC007605. https://doi.org/10.1029/2022TC007605

Muñoz-Montecinos, Jesús, Angiboust, S., & Garcia-Casco, A. (2021). Blueschist-facies paleo-earthquakes in a serpentinite channel (Zagros suture, Iran) enlighten seismogenesis in Mariana-type subduction margins. *Earth and Planetary Science Letters*, *573*, 117135. https://doi.org/10.1016/j.epsl.2021.117135

Okazaki, K., & Hirth, G. (2020). Deformation of mafic schists from subducted oceanic crust at high pressure and temperature conditions. *Tectonophysics*, *774*, 228217. https://doi.org/10.1016/j.tecto.2019.228217

Ortega-Arroyo, D., O'Ghaffari, H., Peč, M., Gong, Z., Fu, R. R., Ohl, M., et al. (2025). "Lab-Quakes": Quantifying the Complete Energy Budget of High-Pressure Laboratory Failure. *AGU Advances*, *6*(5), e2025AV001683. https://doi.org/10.1029/2025AV001683

Ott, J. N., Condit, C. B., Peč, M., & Journaux, B. (2025a). Dislocation creep of glaucophane in mafic blueschists during subduction: Weighted Burgers vector analysis from the Catalina Schist (California, USA). *Geology*, *53*(6), 529–534. https://doi.org/10.1130/G53025.1

Ott, J., Condit, C., & Pec, M. (2025b). EBSD and Mechanical Data for: Experimental constraints on the strength of subducting oceanic crust: a dislocation creep flow law for blueschist (glaucophane) [Data set]. Zenodo. https://doi.org/10.5281/zenodo.17478083

Park, Y., Jung, S., & Jung, H. (2020). Lattice Preferred Orientation and Deformation Microstructures of Glaucophane and Epidote in Experimentally Deformed Epidote Blueschist at High Pressure. *Minerals*, *10*(9), 803. https://doi.org/10.3390/min10090803

Passchier, C. W., & Trouw, R. A. J. (1998). *Microtectonics*. Berlin, Heidelberg: Springer. https://doi.org/10.1007/978-3-662-08734-3

Paterson, M. S., & Olgaard, D. L. (2000). Rock deformation tests to large shear strains in torsion. *Journal of Structural Geology*, *22*(9), 1341–1358. https://doi.org/10.1016/S0191-8141(00)00042-0

Peacock, S. M., & Hyndman, R. D. (1999). Hydrous minerals in the mantle wedge and the maximum depth of subduction thrust earthquakes. *Geophysical Research Letters*, *26*(16), 2517–2520. https://doi.org/10.1029/1999GL900558

Peč, M. (2018). newRig (Version Beta) [Software]. Retrieved from https://mpec.scripts.mit.edu/peclab/software/

Peltier, W. R. (2004). Global Glacial Isostasy and the Surface of the Ice-Age Earth: The ICE-5G (VM2) Model and GRACE. *Annual Review of Earth and Planetary Sciences*, *32*(Volume 32, 2004), 111–149. https://doi.org/10.1146/annurev.earth.32.082503.144359

Platt, J. P., Xia, H., & Schmidt, W. L. (2018). Rheology and stress in subduction zones around the aseismic/seismic transition. *Progress in Earth and Planetary Science*, *5*(1), 24. https://doi.org/10.1186/s40645-018-0183-8

Reynard, B., Gillet, P., & Willaime, C. (1989). Deformation mechanisms in naturally deformed glaucophanes: a TEM and HREM study. *European Journal of Mineralogy*, *1*(5), 611–624. https://doi.org/10.1127/ejm/1/5/0611

Ronde, A. A. de. (2004). *Mineral reaction and deformation in Plagioclase-Olivine composites : an experimental study* (Thesis). University_of_Basel. https://doi.org/10.5451/unibas-003550982

Schliestedt, M. (1986). Eclogite-Blueschist Relationships as Evidenced by Mineral Equilibria in the High-Pressure Metabasic Rocks of Sifnos (Cycladic Islands), Greece. *Journal of Petrology*, *27*(6), 1437–1459. https://doi.org/10.1093/petrology/27.6.1437

Scholz, C. H. (1988). The brittle-plastic transition and the depth of seismic faulting. *Geologische Rundschau*, *77*(1), 319–328. https://doi.org/10.1007/BF01848693

Sibson, R. H. (1992). Implications of fault-valve behaviour for rupture nucleation and recurrence. *Tectonophysics*, *211*(1), 283–293. https://doi.org/10.1016/0040-1951(92)90065-E

Soret, M., Précigout, J., Stünitz, H., Raimbourg, H., Plümper, O., Osselin, F., et al. (2025). Deep crustal deformation driven by reaction-induced weakening. *Nature Communications*, *16*(1), 6407. https://doi.org/10.1038/s41467-025-60692-7

Stipp, M., Stünitz, H., Heilbronner, R., & Schmid, S. M. (2002). Dynamic recrystallization of quartz: Correlation between natural and experimental conditions. In S. de Meer, M. R. Drury, J. H. P. de Bresser, & G. M. Pennock (Eds.), *Deformation Mechanisms, Rheology and Tectonics: Current Status and Future Perspectives* (Vol. 200, p. 0). Geological Society of London. https://doi.org/10.1144/GSL.SP.2001.200.01.11

Stöckhert, B. (2002). Stress and deformation in subduction zones: insight from the record of exhumed metamorphic rocks. *Geological Society, London, Special Publications*, *200*(1), 255–274. https://doi.org/10.1144/GSL.SP.2001.200.01.15

Teyssier, C., Whitney, D. L., Toraman, E., & Seaton, N. C. A. (2010). Lawsonite vorticity and subduction kinematics. *Geology*, *38*(12), 1123–1126. https://doi.org/10.1130/G31409.1

Tokle, L., Hirth, G., & Behr, W. M. (2019). Flow laws and fabric transitions in wet quartzite. *Earth and Planetary Science Letters*, *505*, 152–161. https://doi.org/10.1016/j.epsl.2018.10.017

Tokle, Leif, Hufford, L. J., Behr, W. M., Morales, L. F. G., & Madonna, C. (2023). Diffusion Creep of Sodic Amphibole-Bearing Blueschist Limited by Microboudinage. *Journal of Geophysical Research: Solid Earth*, *128*(9), e2023JB026848. https://doi.org/10.1029/2023JB026848

Tullis, J. (2002). Deformation of Granitic Rocks: Experimental Studies and Natural Examples. *Reviews in Mineralogy and Geochemistry*, *51*(1), 51–95. https://doi.org/10.2138/gsrmg.51.1.51

Warren, J. M., & Hirth, G. (2006). Grain size sensitive deformation mechanisms in naturally deformed peridotites. *Earth and Planetary Science Letters*, *248*(1), 438–450. https://doi.org/10.1016/j.epsl.2006.06.006

Wech, A. G., & Creager, K. C. (2011). A continuum of stress, strength and slip in the Cascadia subduction zone. *Nature Geoscience*, *4*(9), 624–628. https://doi.org/10.1038/ngeo1215

Zhang, J., & Green, H. W. (2007). Experimental Investigation of Eclogite Rheology and Its Fabrics at High Temperature and Pressure. *Journal of Metamorphic Geology*, *25*(2), 97–115. https://doi.org/10.1111/j.1525-1314.2006.00684.x

Zhang, Junfeng, Green, H. W., & Bozhilov, K. N. (2006). Rheology of omphacite at high temperature and pressure and significance of its lattice preferred orientations. *Earth and Planetary Science Letters*, *246*(3), 432–443. https://doi.org/10.1016/j.epsl.2006.04.006

Zhao, N., Hirth, G., Cooper, R. F., Kruckenberg, S. C., & Cukjati, J. (2019). Low viscosity of mantle rocks linked to phase boundary sliding. *Earth and Planetary Science Letters*, *517*, 83–94. https://doi.org/10.1016/j.epsl.2019.04.019

Chapter 5: Constraining the Nature and Significance of an Exhumed Blueschist-Eclogite Transition, Sifnos Island, Greece

Jason N. Ott[1], Cailey B. Condit[1], Jewel Wass de Czege[1], and Eirini M. Poulaki[2]

[1]Department of Earth and Space Sciences, University of Washington, Seattle, WA, USA

[2]Department of Geology and Geophysics, Louisiana State University, Baton Rouge, LA, USA

Corresponding author: Jason Ott (jasonott@uw.edu)

Abstract

In mafic rocks, the metamorphic transformation from blueschist to eclogite represents a location of profound rheological and density changes and volatile release. It can exert first-order controls on the behavior of the deep subduction interface. Despite this transition's central role in subduction zone dynamics, the mechanical and metamorphic evolution of the lithologies in the slab at the blueschist-eclogite transition remain largely unconstrained. The exhumed, coherent section of the Eclogite-Blueschist Complex exposed at Vroulidia Beach on Sifnos Island, Greece represents a natural laboratory to investigate the complex interactions between deformation, metamorphism, and aqueous fluids in blueschists and eclogites through subduction and exhumation, and have long been suggested to represent a prograde blueschist to eclogite transition. We reassess the relationship between mafic blueschists and eclogites petrologically and rheologically to better constrain the nature and effects of this transition. This study focuses on a ~10 m section on Vroulidia Beach displaying repeated transitions between blueschist and eclogite lithologies at centimeter- to decimeter-scales. Blueschist domains display penetrative foliations and lineations, defined by alignment of the modally abundant phases glaucophane and white mica. In contrast, eclogites domains occur with massive or weakly foliated textures, defined by omphacite and white mica. Garnet zoning and compositions reveal that blueschist, eclogites, and mixed blueschist-eclogite samples experienced the same P-T history. EBSD-based microstructural analysis show early prograde fabric development is preserved within omphacite inclusions in blueschist garnets. Within the blueschist matrix, microstructural and chemical observations imply retrograde growth of glaucophane on peak omphacite in the presence of an oxidizing fluid to produce blueschist. Using these observations combined with thermodynamic equilibrium modeling, we map a P-T path of this eclogite-blueschist transition in which (1) prograde deformation during subduction initiated zones of weakness, (2) fluid released from near peak to early retrograde eclogitization was localized within these weakened, permeable domains allowing for early retrogression of previously deformed eclogites into blueschists, and (3) strain localization during further retrogression and exhumation produced strongly deformed blueschist layers intercalated with weakly deformed metastable eclogites that preserved near-peak conditions. Our work reveals that at least portions of the CBU's eclogite-blueschist rocks do not represent a prograde transition, but rather a retrogression of eclogite to blueschist during early exhumation, complicating the use of these rocks to reconstruct prograde subduction processes. These results also demonstrate the effectiveness of a combined microstructural and petrological approach in re-evaluating the deformation and metamorphic history of previously-investigated, exhumed subduction terranes.

1 Introduction

Subduction zones are nexuses of crustal recycling and deformation, where cold, dense oceanic lithosphere converges with a buoyant overriding plate which results in slab subduction into the mantle (Hacker et al., 2003; Peacock, 2004; Stern, 2002). As oceanic crust is subducted, it progresses through a series of metamorphic transformations from the mid-ocean ridge basalt (MORB) at the trench, through blueschist-facies assemblages at ~30 km depths—often associated with the transition from seismic to aseismic deformation—and, ultimately, to eclogite-facies metamorphic assemblages at sub-arc depths > 80 km (Agard et al., 2009; Ernst, 1975; Hacker, 2008; Peacock, 1993, 2004). Metamorphic reactions within the subducting slab lead to changes in density, hydration state, and rheological strength (Duesterhoeft et al., 2014; Smye & England, 2023; Wang et al., 2019) that exert first-order controls on the mechanical and chemical evolution of subduction zones (Behr et al., 2018). These processes govern the transition from brittle (seismic) to viscous (aseismic) behavior along the slab interface, facilitate hydration and partial melting of the mantle wedge, and drive corner flow in the mantle wedge and arc volcanism at the surface (Hacker, 2008; van Keken et al., 2011; Peacock, 2004). Despite their central role in controlling subduction zone rheology and fluid release, the mechanical and metamorphic evolution of blueschist, eclogite, and the transitions between them remain incompletely understood.

A major obstacle in understanding this transition is the scarcity of subduction-related terranes where a prograde blueschist to eclogite exposure is preserved. In many exhumed settings, blueschists and eclogites are juxtaposed tectonically after recording different peak conditions. For example, Clarke et al. (1997) investigated exhumed blueschists and eclogites of the Pam Peninsula, New Caledonia and found that while peak temperatures were comparable (~600°C), eclogite pods recording peak pressures ~2.4 GPa are enclosed within a blueschist zone that experienced a peak pressure of ~1.3 GPa. This disparity indicates that deformation and metamorphism occurred under differing P-T conditions, complicating direct rheological or geodynamic comparisons between the two facies.

In contrast, the exposure of the Cycladic Blueschist Unit (CBU) on Sifnos Island, Greece represents a world-class exposure of a coherent blueschist-eclogite section that has been proposed to represent peak metamorphic conditions of blueschist and eclogites metamorphosed from protoliths of different compositions (Groppo et al., 2009; Matthews & Schliestedt, 1984; Mocek, 2001; Okrusch & Broecker, 1990; Schliestedt, 1986). The preservation of the high-pressure assemblages within the Cherronisos Unit of the CBU on northern Sifnos is attributed to its structural position between two marble units that limited external fluid infiltration (Schliestedt, 1986). Ensuing studies have proposed additional controls on the production and preservation of HP-lithologies including dehydration reactions and fluid activity, deformation partitioning, P-T path and thermal heterogeneity, and oxidation state (Brooks et al., 2019; Dragovic et al., 2012, 2015; Groppo et al., 2009; Mocek, 2001). These contrasting models continue to drive debate over the fundamental controls—compositional, thermal, and fluid-mediated—on the formation and preservation of blueschist- and eclogite-facies lithologies on Sifnos.

The coherent exposure of high-pressure blueschist–eclogite units at Vroulidia Beach, Sifnos Island, provides a natural laboratory to investigate the rheological behavior and relative strength contrast between lithologies that experienced a shared pressure–temperature history. The section comprises intercalated blueschists, eclogites, jadeitic felsic gneisses, quartzites, metacherts, metapelites, and occasional marbles, forming an approximately 800-m-thick sequence of centimeter- to decimeter-scale layering (Okrusch & Broecker, 1990; Schliestedt, 1986). Deformation within this sequence is pervasive yet heterogeneously distributed among different lithologies (Lister & Raouzaios, 1996; Roche et al., 2016) and is demonstrably syn-metamorphic during both subduction and exhumation (Groppo et al., 2009; Trotet et al., 2001). These relationships imply that compositional and rheological contrasts between blueschist and eclogites led to the observed strain localization and fabric development. Consequently, an integrated microstructural, petrological, and geochemical investigation of these rocks can directly address the relative strength of blueschists and eclogites within the framework of the subduction to exhumation history of the Vroulidia Beach exposure.

In this study, we present an integrated petrological and microstructural analysis of an exhumed blueschist–eclogite transition at Vroulidia Beach, Sifnos Island, Greece. We use optical petrography and electron backscatter diffraction (EBSD) to characterize deformation and textural relationships among blueschist, eclogite, and intermediate mixed-facies samples, and link these observations to the metamorphic evolution through electron microprobe analyses (EMPA). Thermodynamic equilibrium modeling in Perple_X (Connolly, 1990; Connolly & Petrini, 2002) is used to reconstruct the P-T history of the samples and evaluate the timing and conditions of deformation. We interpret these results as evidence that the study area records an exhumation-related eclogite-blueschist transition, in which deformation localized within weak domains developed during prograde subduction. Fluid infiltration along these zones enhanced retrogression and rheological weakening in blueschists, while eclogite domains remained relatively strong and fluid-poor. These results highlight the key role of fluid-deformation feedbacks in controlling strain localization and metamorphic re-equilibration during exhumation, and underscore the importance of integrated microstructural and petrological analyses in distinguishing prograde from retrograde blueschist assemblages in exhumed high-pressure terranes.

2 Geologic Setting

2.1 Hellenic subduction zone

Sifnos Island is one of the Cyclades Islands situated in the Aegean Sea southeast of Greece (Fig. 1a, inset). The Cyclades form part of the lower unit of Attic-Cycladic Crystalline Complex (ACCC), a subduction-related accretionary complex of the Hellenic subduction zone (Avigad, 1993; Roche et al., 2016). The Hellenic subduction zone is characterized by ongoing convergence between the African plate and Aegean microplate, with estimates for the timing of subduction initiation ranging from Cenozoic to Mesozoic age (Catlos & Cemen, 2023). Southward propagation of thrusting and the resultant nappe stacking (van Hinsbergen et al., 2005; Jolivet & Brun, 2010) were followed by exhumation driven by back-arc extension and wedge extrusion (Avigad, 1993; Jolivet & Brun, 2010; Poulaki et al., 2019; Ring et al., 2007). The ACCC records a two-stage history of metamorphic events during the Cenozoic: high-pressure/low-temperature blueschist to eclogite facies metamorphism during Eocene subduction, and Oligocene to Miocene aged retrogression at greenschist to amphibolite facies conditions during slab rollback and trench migration (Bröcker, 1990; Bröcker et al., 2022; Jolivet & Brun, 2010; Poulaki et al., 2019; Schliestedt, 1986). Exhumation of the ACCC was largely accomplished along low-angle detachment faults during the Eocene and back-arc extension in the late Miocene (Laurent et al., 2018; Poulaki et al., 2019; Ring et al., 2007, 2011).

2.2 Cycladic Blueschist Unit

The ACCC is composed of three main tectonometamorphic units. The structurally lowest unit is the Cycladic Basement, comprised of granitic and metasedimentary rocks of at least Carboniferous ages, that crops out primarily in the southern-central Cyclades (Flansburg et al., 2019; Poulaki et al., 2019; Zlatkin et al., 2018). The Cycladic Basement is structurally overlain by the CBU, which is exposed through much of the central Cyclades. Examples of significant outcrops of well-preserved, high-pressure metasedimentary and metabasite lithologies include Sifnos, Syros, Andros, Tinos, Sikinos, and Ios (e.g., Kotowski et al., 2022; Kotowski & Behr, 2019; Lamont et al., 2020; Poulaki et al., 2019; Schliestedt, 1986). The upper unit of the ACCC is the Pelagonian Upper Unit composed of ophiolitic rocks with high-temperature gneisses and amphibolites that did not undergo high-pressure metamorphism (Altherr et al., 1994).

The CBU is structurally and compositionally complex, composed of multiple nappes and thrust sheets derived from oceanic and continental protoliths, volcanic-sedimentary sequences, and metasedimentary units (Lamont et al., 2020; Poulaki et al., 2019). The broad range of inputs into the CBU creates significant protolith heterogeneity that results in variability in bulk compositions that have been invoked to explain the range of preserved lithologies and mineral assemblages documented in exposures in the Cyclades (e.g., Kotowski et al., 2022; Laurent et al., 2018; Roche et al., 2016; Schliestedt, 1986; Schliestedt et al., 1987). Peak metamorphic conditions vary widely across the CBU, with estimates ranging from peak P-T conditions of ~1.8 GPa and 550°C on Sifnos, Syros, and Ios (Spear et al., 2024) to higher peak pressures approaching ~2.6 GPa at 500°C on Tinos (Lamont et al., 2020). Peak metamorphic conditions were frequently overprinted by greenschist facies retrogression ($T \sim 450$°C and $P < 700$ MPa) facilitated by fluid infiltration during underplating (Avigad, 1993; Matthews & Schliestedt, 1984; Schliestedt & Matthews, 1987). Studies of underplating kinematics report exhumation was often accompanied by syn-metamorphic deformation through thrusting and nappe stacking, coeval with or succeeded by extensional deformation along low angle detachment faults and shear zones associated with back-arc extension and normal faulting until the Miocene (Lamont et al., 2020; Roche et al., 2016).

2.3 Sifnos Island

Sifnos is notable for the well-preserved, largely coherent section of the CBU exposed on the island (Fig. 1a). The Cherronisos Unit, forming the northern part of Sifnos Island includes (from structural top-to-bottom) the Upper Marble Complex, the Eclogite-Blueschist Complex (EBC), and the Main Marble Complex (Ring et al., 2011; Roche et al., 2016; Trotet et al., 2001). The Upper Marble Complex at the northwestern extent of the island consists of interbedded calcitic and dolomitic marbles with thin intercalations of quartzite, calcareous schist, and metabasite lenses. The Upper Marble Complex displays isoclinal folds and a pervasive foliation indicating a top-to-the-northeast shear sense (Ring et al., 2007; Roche et al., 2016; Trotet et al., 2001). The EBC structurally underlies the Upper Marble Complex, and is composed of centimeter- to meter - thick layers of high-pressure/low-temperature metabasites including blueschists, eclogites, actinolite-bearing schists, and jadeite-bearing felsic gneisses with local marble, quartzite, and metapelite intercalations (Dragovic et al., 2015; Roche et al., 2016; Schliestedt, 1986). Previous workers estimate the peak metamorphic conditions of the EBC as ~1.4–2.4 GPa and ~500–600°C (Fig. 1b; Avigad et al., 1992; Dragovic et al., 2012; Groppo et al., 2009; Schmädicke & Will, 2003; Spear et al., 2006; Trotet et al., 2001) during the Eocene (~55–45 Ma; Dragovic et al., 2012, 2015; Laurent et al., 2018). The EBC overlays the Main Marble Complex, which is extensively exposed through much of central and western Sifnos. The Main Marble Complex is composed of thick marbles interlayered with metabasites and metasediments metamorphosed to blueschist- or greenschist-facies conditions. Overturned isoclinal folds and ductile shear kinematic indicators within the Main Marble Complex record northward exhumation of the CBU (Ring et al., 2011).

The Farros Unit, exposed in the southeast on Sifnos, is the structurally lowest unit of the CBU on the island. The Farros Unit is separated from the Cherronisos by a low-angle, northward-dipping normal fault that juxtaposed the two units during top-to-the-northeast exhumation (Avigad, 1993; Ring et al., 2007, 2011). The Farros Unit consists predominantly of metasediments including mica-schists, quartzofeldspathic gneisses, and calc-silicates with a pervasive greenschist-facies overprint facilitated by fluid-infiltration during exhumation (Dragovic et al., 2015; Roche et al., 2016; Schliestedt, 1986; Trotet et al., 2001). The greenschist-facies overprint is estimated as Miocene in age, ~24-18 Ma, based on ^{40}Ar/^{39}Ar and Rb-Sr white mica ages (M. Bröcker et al., 2013).

2.3.1 Vroulidia Beach exposure of CBU on Sifnos Island

The Cherronisos Unit exposure of the EBC at Vroulidia Beach, on the north side of Vroulidia Bay (Fig. 2) displays repeated transitions between eclogite and blueschist lithologies derived from metamafic and metasedimentary protoliths (Fig. 2a). Schliestedt (1986) proposed that the high-pressure lithologies exposed on Vroulidia Beach represent peak P-T conditions during subduction, based on variation of bulk rock chemistry indicating different protoliths for blueschists and eclogites and the lack of reaction textures between omphacite and amphibole in the specimens examined. Later work on Sifnos by Mocek (2001) reinforces the interpretation that protolith composition is a primary control on eclogite and blueschist parageneses, but concludes it is modulated by fluid-rock interactions or metasomatism based on geochemical evidence for chemical alteration. At Vroulidia Beach, the eclogites commonly occur as massive, weakly to un-foliated aggregates comprised primarily of omphacite, garnet, and white mica, locally containing minor glaucophane and epidote (Fig. 2b). These layers commonly grade through apparent reaction zones characterized by alternating omphacite-rich and glaucophane-rich domains (Fig. 2c) to glaucophane-rich blueschists with similar modal proportions of white mica and garnet as observed in the eclogites (Fig. 2d). Transitions between eclogite and blueschist occur repeatedly at centimeter- to decimeter-scales (Figs. 2c,e), defining a rhythmic layering. More recently, studies of garnet growth and fluid inclusions suggest locally derived fluids from dehydration reactions during eclogitization played a role in promoting blueschist-facies retrogression during exhumation of the CBU on Sifnos (Brooks et al., 2019; Dragovic et al., 2012, 2015). The blueschist layers exhibit a strong foliation and mineral lineation defined by aligned glaucophane and phengite, indicating strain partitioning preferentially into blueschist domains (Figs. 2c–e). Eclogite also occurs as competent, massive pods associated with pervasively deformed mica-schists and blueschists (Fig. 2f). These field-relationships at Vroulidia Beach are consistent with a potential role for fluid-assisted retrogression and rheological weakening in producing the observed interlayering, reaction textures, and deformation partitioning that characterize the high-pressure metamorphic rocks of the EBC on Sifnos (Angiboust et al., 2017; Condit & Mahan, 2018; Donna L. Whitney et al., 2014).

3 Methods and materials

3.1 Sample preparation

The samples included in the study were collected along ~10 m transect of a single outcrop of the EBC on the north side of Vroulidia Beach, Sifnos Island, Greece (Figs. 1, 2; Ring et al., 2011; Roche et al., 2016; Schliestedt, 1986). Samples were metamorphosed from metabasite protoliths and were classified as blueschist, eclogite, or mixed blueschist-eclogite lithologies based on the mineral assemblages (Table 1). Selected for this study were a blueschist (V01a; Fig. 2d,3a,3d), a mixed blueschist-eclogite sample (V01c; Fig. 2c,3b,3e), and an eclogite (V01d; Fig. 2b,3c,3f). The blueschist and, to a lesser extent, the mixed blueschist-eclogite sample display penetrative foliations and lineations defined by glaucophane, and white mica, while the eclogite displays a weaker foliation defined by white mica and omphacite. Hand sample textures are porphyroblastic, with all samples composed of fine-to-coarse grained matrices (< 1 mm) with garnet porphyroblasts up to 5 mm in diameter (Fig. 3 a–c). Glaucophane typically occurs as acicular grains < 1 mm length in blueschist, while mixed blueschist-eclogite samples contain glaucophane porphyroblasts up to ~5 mm in length.

Table 1

Classification and Estimated Major Mineral Modes of Metabasite Hand Samples from Vroulidia Beach Exposure

	Sample Name (CBU23 Sif)		
Mineral (vol. %)	V01a	V01c	V01d
Glaucophane	35	20	3
Omphacite	5	10	35
White Mica	40	45	45
Garnet	5	15	10
Epidote	10	9	6
Quartz	5	1	1
Lithology	Blueschist	Mix	Eclogite

Sample location coordinates for CBU23 Sif V samples: 37.023968, 24.654570

Structurally oriented thin sections were prepared from the samples with the X-Z plane contained in the section (i.e., perpendicular to the foliation and parallel to the lineation). Two thin sections were prepared from the blueschist and three from the mixed blueschist-eclogite sample to ensure representative coverage of sample heterogeneities, and one thin section was prepared for the eclogite, which is homogeneous at the scale of the hand sample. Thin sections were used for optical petrography, and for electron probe microanalysis (EMPA; section 3.2) and electron backscatter diffraction (EBSD; section 3.3) data collection.

3.2 Bulk sample and mineral compositions

Bulk major- and trace-element compositions and ferrous iron contents were determined at the X-ray Laboratory at Franklin and Marshall College. Starting material was obtained by cutting ~100 g subsamples from hand specimens; these were subsequently crushed and sieved through an 80-mesh screen. Loss on ignition (LOI) was measured by heating ~1.0 g of powdered sample at 950 °C for 1.5 h, cooling in a desiccator, and re-weighing. Major elements were analyzed on fused glass discs prepared from 0.40 g of ignited sample mixed with 3.60 g of lithium tetraborate flux, fused in Pt crucibles, and cast into glass disks. Discs were analyzed on a Malvern Panalytical Zetium X-ray fluorescence (XRF) vacuum spectrometer calibrated against international geochemical standards, with matrix and inter-element interference corrections applied. Ferrous iron contents were determined separately by a modified Reichen & Fahey (1962) titration, and combined with XRF totals to calculate FeO and Fe_2O_3 speciation. Trace element concentrations were measured from pressed powder briquettes prepared by mixing ~7.0 g of powder with 1.4 g of high-purity copolywax binder, homogenizing, and pressing at 50,000 psi. Elements determined included Rb, Sr, Y, Zr, V, Ni, Cr, Nb, Ga, Cu, Zn, Co, Ba, U, Th, La, Ce, Sc, Pb, and Mo. Analytical precision and accuracy were monitored by replicate analyses of certified reference materials (Abbey, 1980; Govindaraju, 1994). Major oxides are reported on a 100% volatile-free basis, and typical uncertainties are ±0.1–0.3 wt% for major oxides and 5–10% for trace elements, with detection limits of ~0.01 wt% (majors) and 1–10 ppm (traces).

The compositions of key minerals including glaucophane, omphacite, garnet, and mica- and epidote-group minerals were obtained to characterize phase relationships and chemical zoning to constrain the P-T history of the blueschist-eclogite unit at Vroulidia Beach on Sifnos. These were determined by electron microprobe analysis (EMPA) at the Microbeam Laboratory at Mackay School of Earth Science and Engineering, University of Nevada, Reno using a JEOL iHP 200F instrument equipped with five wavelength-dispersive spectrometers. Analyses were performed with an accelerating voltage of 15 kV, a beam current of 20 nA, and a focused beam diameter of 1 μm (garnet and pyroxene), 5 μm (amphibole and epidote), or 7 μm (mica). Counting times were 20 s (garnet and pyroxene) or 15–70 s (amphibole, epidote, mica) on peak and 15 s on backgrounds. Calibration employed natural and synthetic standards (listed in the Supporting Information), with intensity corrections carried out using the ZAF routine. Detection limits for most elements were between a few to several hundred parts per million, with precision ~1% for major elements based on repeated analyses of standards. Data were screened to exclude analyses with oxide totals deviating by more than 2 wt% from expected anhydrous totals (98% for hydrous phases, 100 wt% for anhydrous phases) with the exception of measured epidote compositions. REE standards were not available for EMPA measurements of epidote, therefore measured totals are included in the table but not discussed in the text. Mineral formula recalculations were performed in the application MinPlotX (Walters & Gies, 2025), with Fe^{3+} estimated from the stoichiometry and a TiOH correction applied to amphibole based on measured Ti-contents.

Modal mineralogy of the samples was quantified by point counting on composite, position-rectified images constructed from optical micrographs (plane- and cross-polarized light) and energy-dispersive X-ray spectroscopy (EDS) maps using the JMicroVision application (Roduit, 2019). The qualitative EDS maps were collected at the Molecular Analysis Facility (MAF) at the University of Washington on a ThermoFisher-Scientific Apreo variable-pressure scanning electron microscope (SEM) equipped with an Oxford Instruments Ultim Max Infinity EDS detector. Maps were collected at operating conditions of 15 kV accelerating voltage and 0.8 nA current at a working distance of 10 mm, and processed using Oxford AZtec software. The elemental maps were stacked in Adobe Illustrator and an RGB false color scheme applied and the resulting images imported into JMicroVision with the optical micrographs. The modal abundances of each phase were determined by identifying the phases at 2000 random points on the position-rectified images over the full thin section. For heterogeneous samples, the point counting method was applied to multiple thin sections and the average modal abundances reported. These two-dimensional modal abundances were used in combination with XRF-determined bulk compositions and EMPA data to determine effective bulk compositions for petrological modeling (section 3.4).

3.3 Electron backscatter diffraction (EBSD) methods

3.3.1 Data collection

EBSD analyses were performed at the MAF, University of Washington, using a ThermoFisher Scientific Apreo variable-pressure SEM equipped with an Oxford Instruments Symmetry 2 detector. Thin sections were polished for 1–2 h on a Buehler Vibromet 2 vibratory polisher with 0.06 μm colloidal silica and coated with ~5 nm of carbon to reduce charging. Samples were mounted at a fixed 70° tilt. Operating conditions were 20 kV accelerating voltage, 3.2 nA beam current, and a 13 mm working distance.

EBSD maps were acquired over areas of 3 mm^2–5 mm^2 with a 5 μm step size and 20 ms exposure time. Kikuchi patterns were indexed using the Oxford HKL database (quartz) and the American Mineralogist database (other phases) in Oxford AZtec. Data were used for microstructural analyses including crystallographic preferred orientation (CPO), shape preferred orientation (SPO), and interphase misorientation-angle distributions.

3.3.2 Data reduction and microstructural analysis

EBSD data reduction and analysis were performed in MATLAB with the MTEX 5.10.0 toolbox (Bachmann et al., 2010; Mainprice et al., 2015). Orientation measurements with a mean angular deviation > 1° were excluded from the dataset. Grain reconstruction was performed using thresholds of ≥ 2° threshold for low-angle boundaries and ≥ 10° for high-angle (grain boundaries), and grains with fewer than three measured orientations were discarded.

Glaucophane and omphacite CPOs are shown as equal-area, upper-hemisphere pole figures of the mean orientation of each grain (one-point-per-grain). The pole figures are contoured as multiples of uniform distribution (m.u.d.), with consistent scaling across all pole figures of each phase. Texture strength is measured using the pole-figure J-index (pfJ-index; Michibayashi & Mainprice, 2004), defined as:

$$pfJ_{hkl} = \int P_{hkl}(\alpha,\beta)^2 d\omega$$

where *hkl* designates the Miller index, (α,β) are spherical coordinates, $P_{hkl}(\alpha,\beta)$ denotes the fraction of all poles for the Miller index *hkl* at a given orientation, and *dω* is the differential element. Random CPOs yield a pfJ-index measurement of one, while a single-crystal orientation is valued at infinity. Polar plot histograms (rose diagrams) are plotted to illustrate the SPO of the longest axis of glaucophane and omphacite grains, weighted by grain area. Misorientation angle distributions for neighboring glaucophane-omphacite pairs were calculated from orientation distribution functions (ODFs) fit to the sets of glaucophane and omphacite grain mean orientations by an 8° half-width.

3.4 Petrological modeling

Petrological modeling was used to constrain the P-T history of the blueschist and eclogite samples. Phase diagrams were constructed for the end-member blueschist (V01a) and eclogite (V01d) bulk compositions using Perple_X 6.6.6 (Connolly & Petrini, 2002) and the Holland and Powell (2011) hp62ver thermodynamic database with the components SiO2-TiO2-Al2O3-FeO-Fe2O3-MnO-MgO-CaO-Na2O-K2O. The pure phases ilmenite (ilm; ilm_nol), margarite (ma), and andradite (andr) were excluded from the models based on the requirements of implemented solution models. The thermodynamic models include the following solid solution models: feldspar (Fuhrman & Lindsley, 1988), olivine (Holland & Powell, 1998), spinel (White et al., 2002), omphacite (Green et al., 2007), epidote (Holland & Powell, 2011), antigorite (Padrón-Navarta et al., 2013), biotite, chlorite, chloritoid, ilmenite, garnet, mica, and orthopyroxene (White et al., 2014), and clinoamphibole (Green et al., 2016). Brucite, stilpnomelane, and pumpellyite were treated as ideal solid solutions.

The effective compositions for the blueschist and eclogite were determined by subtracting the garnet-core chemistry from the XRF-determined bulk compositions. The total volume of garnet cores were estimated by the following method. All garnets observed in full thin-section micrographs prepared from the blueschist (2 sections) and the eclogite (1 section) samples were segmented manually in ImageJ (Schneider et al., 2012) and the modal percentages of garnet were calculated. The 2D garnet areas were treated as 3D volumes for the following calculations (after Heilbronner & Barrett, 2014). Rim-core-rim garnet traverses collected on eight garnets by EMPA were used to determine the diameter of the cores and thickness of the rims on each of the measured garnets based on the almandine, grossular, pyrope, and spessartine components of the garnet chemistry. The core-rim ratio of each garnet was determined by calculating the area of the garnet as a circle with an effective radius equal to ½ the length of the traverse, and the area of the core as a circle with an effective radius equal to ½ the diameter of the core. The mean of the garnet core/garnet ratios (60.6 ± 3.2%) were multiplied by mode of garnet in each sample determined from the segmented thin section images. This calculated garnet core fraction of the full thin section area was multiplied by the average microprobe-measured garnet-core chemistry to determine the contribution of the garnet core to the bulk composition. The garnet contributions were subtracted from the XRF-determined bulk composition to determine the effective compositions to be used as inputs in the Perple_X models.

The blueschist was modeled using the effective composition as discussed above, assuming fluid-saturated conditions with a 99:1 molar ratio of H_2O:CO_2 to produce a model where the grossular, pyrope, and spessartine garnet compositions of the model converged with the EMPA-measured average garnet-rim chemistry in the phase diagram field consistent with the observed assemblage of phases preserved as inclusions within garnet. To model the eclogite, the effective composition was further modified by removing 2.24 wt% calcite from the XRF-measured bulk composition based on the observation that the modal abundance of calcite in the thin section (4%) was confined to a few small regions of the sample and textural evidence that it precipitated in the eclogite late during exhumation. Based on the preservation of the eclogite facies mineral assemblage and scarcity of hydrated minerals in the final assemblage, the eclogite was modeled by including four wt% H_2O in the effective composition. This prevented stabilization of albite and plagioclase feldspars to high pressures as the phases were not observed in the final mineral assemblage.

Additional P-T constraints were determined using classical thermobarometry. The geothermometer of Ellis and Green (1979), which is based on Fe-Mg exchange between garnet and clinopyroxene, and is dependent on the Ca-content of garnet, is expressed as the empirical relationship:

$$T(°K) = \frac{3104 * X_{Ca}^{Grt} + 3030 + 10.86 * P(kb)}{\ln K_D + 1.9034} \qquad (1)$$

where *T(°K)* is the temperature in degrees Kelvin, X_{Ca}^{Grt} is the fraction of Ca in garnet determined as the ratio: Ca/(Ca + Mg + Fe), *P(kb)* is the pressure in kilobars, and K_D is the partitioning coefficient:

$$K_D = \left(\frac{\left[{Fe^{2+}}/{Mg} \right]^{Grt}}{\left[{Fe^{2+}}/{Mg} \right]^{Cpx}} \right) \qquad (2)$$

where the numerator and denominator are the Fe^{2+}:Mg ratios in garnet and clinopyroxene, respectively. EMPA measured compositions of mineral pairs interpreted to be in equilibrium were used to determine temperature estimates for early and late garnet growth. Early growth was constrained using garnet–omphacite pairs in the garnet core, while late growth was constrained using garnet-rim–matrix-omphacite pairs in the eclogite (e.g., Nowlan et al., 2000). Pressure estimates were determined using Si-in-phengite thermobarometry for average of EMPA measurements of Si atoms per formula unit (Si p.f.u.) for phengite inclusions in garnet cores and phengite rims in eclogite matrix. Pressure was estimated from Si-in-phengite compositional isopleths extracted from pseudosection models of the bulk composition for early garnet growth (Fig. S1) and the effective composition of the eclogite as described above for late garnet growth. The blueschist was not used for an estimate of P-T conditions during late garnet growth due to the lack of equilibrated garnet-rim–matrix-omphacite pairs in the blueschist.

4 Results

4.1 Bulk rock analyses

The XRF-determined bulk rock major- and trace-element compositions for the blueschist, mixed, and eclogite samples included in this study are shown in Table 2 and Fig. 4a. All three samples are compositionally similar with respect to the major elements, with the largest variations in SiO_2 (~2 wt%), Al_2O_3 (~1 wt%), MgO (~2 wt%), and CaO (~3 wt%; Table 2; Fig. 4a). The trace element distributions are also similar in all three samples, with the largest

Table 2

Bulk Rock (in wt% Oxides) and Trace Element Compositions (in ppm) of Metabasites from Vroulidia Beach Exposure

	Sample Name (CBU23 Sif)		
Oxides (wt%)	V01a (blueschist)	V01c (mixed)	V01d (eclogite)
SiO_2	51.69	50.73	49.58
TiO_2	0.88	0.93	0.86
Al_2O_3	17.64	18.64	17.40
FeO	6.18	7.34	5.66
Fe_2O_3	9.52	10.63	10.12
MnO	0.12	0.13	0.09
MgO	5.71	3.58	4.24
CaO	6.09	7.54	8.98
Na_2O	3.06	2.18	3.85
K_2O	4.37	4.47	3.66
P_2O_5	1.17	1.29	1.10
Total	100.25	100.12	99.88
LOI	6.30	5.03	3.35
Trace elements (ppm)			
Rb	116.6	118.7	94.3
Sr	177	476	395
Y	16.6	35.4	23.6
Zr	250	251	207
V	323	325	302
Ni	45	54	54
Cr	61	28	21
Nb	32.9	40.4	44.4
Ga	13.1	14.5	13.4
Cu	41	43	51
Zn	100	87	104
Co	33	27	26
Ba	1672	1852	1534
La	66	83	87
Ce	62	72	56
U	4.5	2.7	4.7
Th	19.9	21.3	22.1
Sc	26	28	27
Pb	4	8	9

Procedure for determining bulk major- and trace-element compositions and ferrous/ferric iron contents is described in methods 3.2 variation found in Sr and Ba (~200 ppm). Figure 4b shows the trace element distributions normalized to a mid-ocean ridge basalt (after Pearce, 1979; Schliestedt, 1986). The trace element distributions of the three samples are most similar to the average compositions of Sifnos eclogites analyzed by Schliestedt (1986), although the samples from this study are depleted in Sr, Ce, Sc, and Cr with respect to their analyses.

Table 3

Estimated Modal Mineral Abundances of Metabasites from Vroulidia Beach Exposure

	Sample Name (CBU23 Sif)		
Mineral (%)	V01a (blueschist)	V01c (mixed)	V01d (eclogite)
Glaucophane	34.99	20.69	1.22
Omphacite	4.77	5.81	32.26
White Mica	40.68	37.05	40.38
Garnet	4.39	13.88	7.80
Epidote	2.67	3.73	8.71
Quartz	2.98	5.59	0.98
Chlorite	0.46	-	-
Titanite	2.63	2.78	2.99
Rutile	0.02	0.02	0.10
Apatite	2.54	3.36	3.39
Calcite	3.87	7.09	2.16

Procedure for determining modal abundances is described in methods 3.2

Figure 4c displays the blueschist, mixed, and eclogite samples from this study on an Alkalis–Fe–Mg (AFM) ternary diagram with the blueschist, eclogite, and actinolite-bearing metabasites analyzed by Schliestedt (1986) and the basaltic magma series results of Kuno (1968) and Irvine and Baragar (1971). The blueschist, mixed, and eclogite samples all plot alongside the eclogites and actinolite-bearing metabasites, indicating all were metamorphosed from protoliths with a calc-alkaline magma affinity.

4.2 Petrography

The modal mineral abundances are shown in Table 3. The blueschist, mixed, and eclogite samples are all composed of glaucophane + omphacite + white mica + garnet + epidote + quartz + titanite + apatite + calcite + minor rutile ± chlorite. The foliation and lineation of the samples is defined primarily by the shape preferred orientation and layer segregation of glaucophane, white mica, and omphacite. The foliation is well developed in the blueschist, becoming progressively weaker in the mixed blueschist-eclogite and eclogite samples (Figs. 3a–f). Poikiloblastic garnets are common in all of the samples as idiomorphic to hypidiomorphic grains up to 5 mm in diameter (Figs. 3d–f). Titanium-bearing phases in all samples occur as rutile inclusions within garnet cores (Figs. 3g–h) and as titanite in the matrix (Fig. 3i). Epidote appears as tabular masses associated with white mica (phengite) when included in garnets (Figs. 3g–h), and as zoned, acicular grains often > 500 µm in length in the matrix of both eclogites and blueschist (Fig. 3i).

4.2.1 Blueschist V01a

The fabric in the blueschist is predominantly composed of domains of optically zoned glaucophane (~35%) and domains of white mica (phengite, ~41%), with grains typically up to ~1–2 mm in length. Both phases display an SPO formed by alignment of the elongated axis of the grains to the sample foliation (Figs. 3i–j). Glaucophane typically is devoid of undulatory extinction or core-mantle relationships indicative of dislocation accommodated deformation and dynamic recrystallization, respectively, but frequently displays dilated fractures indicating microboudinage (Figs. 3i–j). Calcite appears as untwinned masses and as fill in glaucophane boudin necks (Figs. 3i–j). Titanite crystals are typically aligned with the blueschist fabric, appearing both as wedge-shaped crystals and as synkinematic deformed, elongated grains (Fig. 3i). Omphacite is a minor constituent of the blueschist matrix, commonly associated with glaucophane and displaying reaction textures consistent with replacement by glaucophane (Fig. 3k). Omphacite in the matrix is often heavily fractured with replacement by chlorite along fractures (Fig. 3k). Garnets in the more strongly deformed regions of the blueschist (Fig. 3d,l) are unique in preserving elongated omphacite-grain inclusions that display a shape preferred orientation that is aligned oblique to the predominant foliation defined by glaucophane and phengite (Fig. 3l).

4.2.2 Mixed blueschist-eclogite V01c

The mixed blueschist-eclogite sample fabric is also defined primarily by glaucophane (~21%) and phengite (~37%), and has a foliation fabric that is substantially weaker than that observed in the blueschist. Glaucophane grains in the section display no optical zoning, and are found as elongated grains and basal sections up to ~5 mm in length (Figs. 3e, 5a–b). Glaucophane in the mixed sample is inclusion-rich, with frequent examples of enclosed, acicular epidote and omphacite grains and quartz blebs (Figs. 5a–b). Phengite occurs as platelets in a variety of orientations with cleavage planes normal to the plane of the thin section or as basal planes parallel to the surface of the section (Figs. 5a–e). Matrix omphacite typically appears as acicular to tabular crystals up to ~500 µm in length, and is often fractured, but does not display evidence of replacement by chlorite as found in the blueschist (Figs. 5a–e). Omphacite elongation direction is typically aligned with the weak, approximately horizontal foliation (Figs. 5c–e). Titanite occurs as synkinematic, deformed grains aligned to the foliation (Fig. 5d), but also is found as large wedge-shaped crystals growing across the foliation (Fig. 5c). Calcite is more abundant in the mixed blueschist-eclogite sample than in the blueschist, occurring as localized, untwinned masses, but it does not show the filled-fracture relationship with glaucophane grains observed in the blueschist (Figs. 5d–e).

4.2.3 Eclogite V01d

The eclogite matrix is composed primarily of omphacite (~32%) and phengite (~40%) and displays an indistinct foliation that is approximately horizontal to the thin section (Fig. 3f). Omphacite appears as acicular to tabular grains < 500 µm in length with the long axis oriented in a variety of orientations (Figs. 5f–j). As in the blueschist-eclogite mixed sample, the long axis phengite grains similarly show a broad range of orientations and commonly are found as platelets with visible cleavage planes or basal planes aligned to the thin section plane (Figs. 5f–j). Glaucophane is rare (~1%), appearing as unzoned, single grains in the matrix that replace omphacite or capture omphacite inclusions (Fig. 5j). Small masses of untwinned calcite are distributed through the sample, sometimes associated with Fe-oxide masses (Figs 5f–g). Titanite is the titanium-hosting phase in the eclogite matrix, appearing as found in the blueschist and mixed samples as synkinematically deformed masses and idiomorphic wedges (Figs. 5h–j). Quartz is scarce in the eclogite, with most occurrences as inclusions in garnet associated with epidote and phengite (Figs. 5k–l).

4.3 Microprobe (EMPA) analyses

Mineral compositions of glaucophane, omphacite, garnet, epidote, and phengite were analyzed in the blueschist, mixed blueschist-eclogite, and eclogite samples. The average compositions of the cores and rims of the minerals in the matrix and contained as inclusions in garnets, and the average garnet core and rim chemistry are presented in Table 4. The average chemistry of glaucophane shows little variation across domains and samples, showing only minor FeO enrichment in the mixed blueschist-eclogite sample (V01c). Omphacite chemistry is also fairly homogeneous in the matrix and as inclusions in garnet for the samples with the exception of omphacite inclusions within the eclogite. Here, the average composition of omphacite inclusions shows a substantial increase in Na_2O paired with reduced MgO and CaO, suggesting that omphacite inclusions in the eclogite contain a larger jadeite component than found in the matrix or in the blueschist and mixed samples (Table 4). Garnet chemistry is very consistent across all the samples, with the average garnet cores displaying enriched FeO relative to the rims, inversely correlated with increasing CaO in the average rims relative to the cores (Table 4). Average epidote chemistry is highly variable throughout the samples, although there is a general trend toward higher fractions of FeO in the cores. In contrast, the average phengite chemistry is very homogeneous. Detailed petrological analyses of the garnets, phengite, glaucophane, and omphacite are included in the following sections (4.3.1–4.3.4).

4.3.1 Garnet analyses

Core-to-rim transects of microprobe spot analyses were conducted on two garnets from the blueschist, four garnets from the mixed blueschist–eclogite (two from glaucophane-rich domains of sample V01c1 and two from the more omphacite-rich domains of sample V01c2), and two garnets from the eclogite. Representative garnets from each sample are shown in Figure 6, with recalculated garnet component fractions. Garnet cores are almandine-rich ($X_{\mathrm{Alm}} \approx 0.7$; mineral abbreviations after Whitney & Evans, 2010) and remain relatively flat from core to rim before showing a steep decrease in almandine content from $X_{\mathrm{Alm}} \approx 0.7$ to 0.6 across the outermost ~500 µm of the garnet rim. This decline is accompanied by a complementary increase of similar magnitude in grossular from $X_{\mathrm{Grs}} \approx 0.2$ to 0.3. The pyrope component increases smoothly from $X_{\mathrm{Prp}} \approx 0.05$ to 0.10 from core to rim in all samples, with a slight decrease to $X_{\mathrm{Prp}} \approx 0.08$ at the rims of the blueschist and mixed samples. In contrast, the eclogite garnet exhibits a second, late-stage increase in pyrope content from $X_{\mathrm{Prp}} \approx 0.08$ to 0.1, signifying renewed Mg uptake under relatively dry eclogite-facies conditions where hydrous Mg-bearing phases were absent. The spessartine component decreases steadily from $X_{\mathrm{Sps}} \approx 0.03$ at the core to $X_{\mathrm{Sps}} \approx 0.01$ at the rim in all samples, consistent with prograde garnet growth, but shows a minor rimward increase to $X_{\mathrm{Sps}} \approx 0.02$ in the blueschist and mixed samples and a perturbation (increase to $X_{\mathrm{Sps}} \approx 0.02$ followed by decrease to $X_{\mathrm{Sps}} \approx 0.01$) in the eclogite.

4.3.2 Phengite analyses

White mica occurs both as inclusions within garnet (Fig. 7a) and as a major constituent of the matrix (Fig. 7b) in all samples. Compositions plot predominantly along the phengite solid-solution between muscovite and celadonite (Fig. 7c). Quantitative electron microprobe analyses show that phengite inclusions enclosed in garnet have relatively restricted compositions of ~3.25–3.40 Si atoms per formula unit (Si p.f.u.; Fig. 7d). Matrix phengite exhibits a broader range of core compositions (~3.30–3.65 Si p.f.u.), whereas most rims are again limited to ~3.30–3.40 Si p.f.u. These compositional variations are consistent with multistage phengite growth during the metamorphic evolution of the samples—where inclusions in garnet likely record earlier, lower-grade conditions, followed by prograde to retrograde growth and recrystallization of matrix phengite. Some phengite inclusions occur with quartz and epidote (e.g., Figs. 5k–l) and may alternatively reflect lawsonite breakdown via the reaction lawsonite + omphacite → epidote + quartz + phengite (Schliestedt, 1986). However, the frequent occurrence of isolated, elongate (rather than tabular) phengite inclusions (e.g., Figs. 3g–h) is evidence for the progressive growth through successive metamorphic stages.

4.3.3 Glaucophane analyses

Quantitative electron microprobe analyses were conducted on optically zoned sodic amphibole in the blueschist sample (Figs. 8a–b) and on unzoned amphibole in the mixed blueschist–eclogite sample (Fig. 8c). Sparse, fine-grained amphibole also occurs in the eclogite sample (e.g., Fig. 8d), but these grains appear unzoned and were not analyzed due to their small size and limited abundance. Amphibole compositions plot within the glaucophane field, with two analyses lying near the glaucophane–ferro-glaucophane boundary (Figs. 8e,g). Glaucophane from both the blueschist and mixed samples exhibits a similar range in total alkali contents in the amphibole A-site ($Na + K + 2Ca \approx 0.09 \pm 0.07$; Figs. 8f,h). In contrast, the Fe^{2+} and Fe^{3+} content of glaucophane in the mixed blueschist–eclogite sample is restricted to a narrow range of $Fe^{2+}/(Fe^{2+} + Mg + Mn) \approx 0.43 \pm 0.02$ and $Fe^{3+}/(Fe^{3+} + Al + Ti) \approx 0.07 \pm 0.03$, whereas glaucophane in the blueschist sample displays greater variation of $Fe^{2+}/(Fe^{2+} + Mg + Mn) \approx 0.36–0.51$ and $Fe^{3+}/(Fe^{3+} + Al + Ti) \approx 0.03–0.17$ reflecting changes in the Fe oxidation state (Figs. 8e,g). This variability is consistent with crystallization under fluid-saturated conditions in the blueschist, where changing redox conditions during growth likely produced the observed chemical zoning.

4.3.4 Omphacite analyses

Microprobe measurements were made on omphacite in the blueschist and the eclogite on matrix grains and inclusions within garnets (e.g., Figs 3k–l, 5f–j, 9). Omphacite occurring in the eclogite matrix, in the blueschist matrix, and as inclusions within garnets in the blueschist display homogeneous compositions within the omphacite field (Fig. 9). Projected to the jadeite-diopside-aegirine (Jd-Di-Aeg) system, the average compositions of the omphacite are $Jd_{56}Di_{21}Aeg_{22}$ in the eclogite, $Jd_{56}Di_{24}Aeg_{21}$ in the mixed blueschists-eclogite, and $Jd_{58}Di_{21}Aeg_{22}$ in the blueschist. Omphacite inclusions in garnets within the eclogite are split into two populations of omphacitic and jadeitic composition (Fig. 9a). Backscattered electron (BSE) imaging of the omphacite inclusions in the eclogite garnets display lamellae with contrasting brightnesses stemming from chemical composition. Calculating a simple jadeite fraction as $X_{Jd} = Na\ (apfu)/(Na\ (apfu) + Ca\ (apfu)$, the lamellae correspond to omphacitic ($X_{Jd} \approx 0.84$) and jadeitic ($X_{Jd} \approx 0.93$) pyroxene domains representative of unmixing of omphacite during slow cooling that occurs due to the previously documented miscibility gap in the omphacite solid solution ~500°C (Matsumoto & Hirajima, 2005; Tsujimori et al., 2005).

4.4 EBSD data

EBSD data were collected on representative blueschist and eclogite samples spanning the blueschist–eclogite transition to quantify the CPO strength of glaucophane and omphacite. These analyses allow assessment of the relationship between CPO and the foliation/lineation defined by the SPO of these phases, as well as the orientation relationships between glaucophane and omphacite that record partitioning of deformation between the blueschist- and eclogite-facies lithologies (Behr et al., 2018; Keppler et al., 2017; Kotowski & Behr, 2019).

Table 4

*EMPA-Measured Oxides (wt%) of Minerals in Metabasites**

Mineral	Glaucophane					Omphacite										Garnet					
	V01a (BS)			V01c (Mix)		V01a (BS)				V01c (Mix)		V01d (Ecl)				V01a (BS)		V01c (Mix)		V01d (Ecl)	
	Matrix		Incl.	Matrix		Matrix		Incl.		Matrix		Matrix		Incl.							
	Core	Rim	Rim	Core	Rim	Core	Rim	Core	Rim	Core	Rim	Core	Rim	Core	Rim	Core	Rim	Core	Rim	Core	Rim
SiO_2	56.60	56.28	56.14	56.28	55.74	56.00	56.04	55.75	55.61	55.72	56.38	55.79	56.30	56.67	56.53	37.67	38.07	37.58	37.93	37.67	37.94
TiO_2	0.00	0.00	0.00	0.00	0.00	0.03	0.03	0.03	0.04	0.04	0.03	0.03	0.03	0.03	0.01	0.07	0.04	0.08	0.06	0.07	0.09
Al_2O_3	11.24	11.24	11.92	11.39	11.38	9.46	9.70	9.15	8.74	9.52	10.65	8.91	10.48	13.63	13.54	20.74	21.09	20.65	21.08	21.00	21.09
FeO	12.31	12.84	11.95	12.96	13.26	10.23	9.31	10.56	10.61	11.41	9.34	10.04	8.15	10.80	13.40	32.20	29.97	32.72	29.76	32.76	29.55
MnO	0.02	0.01	0.02	0.03	0.03	0.03	0.02	0.03	0.04	0.02	0.01	0.02	0.01	0.02	0.01	1.00	0.56	0.84	0.64	0.82	0.61
MgO	8.98	8.69	8.95	8.47	8.40	5.46	5.99	5.64	5.89	4.73	5.07	6.23	6.14	2.29	0.79	1.46	2.08	1.26	1.59	1.38	1.89
CaO	0.33	0.38	0.45	0.44	0.41	10.71	11.22	11.07	11.65	9.85	9.86	11.65	11.15	4.21	1.75	7.60	9.01	7.55	9.70	7.34	9.61
Na_2O	7.16	7.15	7.21	7.16	7.19	8.14	7.90	7.88	7.53	8.46	8.63	7.53	7.93	11.85	13.00	0.01	0.00	0.01	0.01	0.01	0.00
K_2O	0.01	0.02	0.02	0.01	0.01	0.00	0.00	-0.01	-0.01	0.00	0.00	0.00	0.00	0.00	0.00	-0.01	-0.01	-0.01	-0.01	-0.01	-0.01
Total	96.65	96.61	96.66	96.74	96.42	100.06	100.23	100.12	100.10	99.74	99.97	100.19	100.21	99.49	99.03	100.74	100.81	100.68	100.77	101.04	100.77

Mineral	Epidote												Phengite										
	V01a (BS)				V01c (Mix)				V01d (Ecl)				V01a (BS)			V01c (Mix)				V01d (Ecl)			
	Matrix		Incl.		Matrix		Incl.		Matrix		Incl.		Matrix		Incl.	Matrix		Incl.		Matrix		Incl	
	Core	Rim	Core	Rim	Core	Rim	Core	Rim	Core	Rim	Core	Rim	Core	Rim	Core	Core	Rim	Core	Rim	Core	Rim	Core	Rim
SiO_2	34.38	36.77	37.78	38.91	35.10	37.33	37.87	37.66	35.48	37.25	37.17	37.64	50.45	50.55	49.73	50.13	49.29	49.64	49.35	49.45	49.30	49.82	49.97
TiO_2	0.27	0.08	0.07	0.17	0.19	0.10	0.11	0.12	0.21	0.08	0.16	0.11	0.19	0.20	0.17	0.20	0.20	0.21	0.18	0.19	0.16	0.19	0.19
Al_2O_3	22.77	26.03	29.52	29.03	23.84	26.97	28.86	28.38	24.30	26.40	29.10	29.35	26.18	26.60	27.84	26.91	27.87	28.13	28.03	28.36	28.42	27.43	27.54
FeO	10.99	9.51	6.34	7.87	10.52	9.09	7.41	8.04	10.94	10.20	7.24	6.91	3.12	3.03	2.76	3.19	3.00	3.46	4.19	3.42	3.57	3.17	3.39
MnO	0.13	0.09	0.07	0.04	0.07	0.03	0.07	0.12	0.09	0.07	0.09	0.09	0.00	0.00	0.00	0.00	0.00	0.00	0.00	0.00	0.00	0.00	0.00
MgO	0.16	0.09	0.08	0.08	0.14	0.06	0.06	0.06	0.12	0.05	0.07	0.06	3.59	3.54	3.29	3.31	3.08	2.89	2.56	2.84	2.76	3.19	3.08
CaO	18.64	22.02	22.98	23.20	18.96	22.18	23.50	23.46	20.00	22.68	23.29	23.66	0.00	0.01	0.00	0.00	0.01	0.05	0.07	0.01	0.01	0.03	0.00
Na_2O	0.04	0.01	0.02	0.02	0.04	0.01	0.00	0.00	0.03	0.00	0.00	0.00	0.33	0.40	0.41	0.43	0.50	0.52	0.48	0.58	0.57	0.46	0.44
K_2O	0.01	0.01	0.00	0.01	0.02	0.00	0.00	0.00	0.01	0.00	0.00	0.00	10.92	10.86	10.77	10.81	10.74	10.55	9.96	10.69	10.66	10.80	10.88
Total	87.39	94.60	96.87	99.34	88.88	95.78	97.88	97.84	91.18	96.72	97.11	97.83	94.78	95.18	94.97	94.98	94.70	95.46	94.82	95.54	95.44	95.09	95.49

**Note: BS = blueschist, Mix = blueschist-eclogite mix, Ecl = eclogite, Incl. = inclusions*

4.4.1 Omphacite CPO in blueschist garnet inclusions

EBSD data were collected on omphacite inclusions in garnet in the blueschist displaying a foliation defined by the elongation direction of the omphacite grains that is oblique to the dominant foliation of the blueschist sample (Figs. 3l, 10a–b). The omphacite inclusions display a moderately strong CPO in which the [001] axis (c-axis) shows the strongest alignment ($pfJ_{[001]}$ = 1.76; Fig. 10c), which is coincident with the orientation of the long axis of the omphacite grains (Fig. 10d). This relict CPO in the omphacite [001] axis is oblique to the subhorizontal foliation of the matrix (Fig. 10a). The CPO strength is weaker in the [010] and [100] axes (b- and a-axes, respectively) with respective fabric strengths of $pfJ_{[010]}$ = 1.60 and $pfJ_{[100]}$ = 1.51.

4.4.2 Omphacite and glaucophane CPO in eclogite matrix

Omphacite and glaucophane were mapped by EBSD in a representative region of the eclogite matrix to assess the CPO strength of the phases and their orientation relationship (Fig. 11a). The mapped omphacite grain sizes span a range from ~10 μm-diameter nearly equant grains to elongated grains > 500 μm in length in a subhorizontal orientation that defines the weak foliation observed in the eclogite (Figs. 5f–l). Glaucophane in the eclogite EBSD-map are equant to elongated with grain sizes up to tens of μm for the largest elongated grains. Glaucophane appear as single grains or clusters of a few grains that are associated with omphacite junctions of three or more grains, or embayment of omphacite porphyroblasts (Fig. 11a).

Pole figures display the CPO of omphacite (Fig. 11b) and glaucophane (Fig. 11c) for the full populations of indexed grains, larger grains (effective diameter d > 5 μm) and smaller grains (d < 5 μm). The c-axis ([001]) of omphacite and glaucophane are both aligned with the weak subhorizontal foliation and lineation (approximately in the X-direction) of the eclogite. The a-axis ([100]) and b-axis ([010]) of omphacite describe a weak girdle normal to the alignment of the c-axis, with larger omphacite porphyroblasts showing a density maxima in the [010] axis aligned subnormal to the foliation plane. This omphacite CPO has been previously attributed to S-type fabrics in omphacite (Lee & Jung, 2021). The glaucophane CPO is comprised of density maxima in the glaucophane a- and b-axes that are approximately aligned with the corresponding crystallographic directions in omphacite (Figs. 11b–c), but are not consistent with commonly observed glaucophane CPOs in which the [100] axis (a-axis) is oriented normal to the foliation or within a girdle normal to the lineation (Kim & Jung, 2019; Ko & Jung, 2015). Both omphacite and glaucophane display slightly stronger CPOs in larger grains than in smaller (d < 5 μm) grains. The SPO of omphacite and glaucophane are displayed as rose diagrams weighted by grain area in Fig. 11d. Both phases show a similar, subhorizontal alignment of the grain elongation direction that is slightly oblique relative to the alignment of their c-axes (Figs. 11b–c). The misorientation relationship between neighboring grains of omphacite and glaucophane in the eclogite is shown as the misorientation angle distribution function in Fig. 11e. The misorientation angle distribution deviates significantly from a theoretical, random distribution for pairs of neighboring grains with monoclinic symmetry, with approximately 35% of omphacite-glaucophane pairs displaying a 180° misorientation angle.

4.4.3 Omphacite and glaucophane CPO in blueschist matrix

A representative region of the blueschist matrix was mapped by EBSD to investigate the orientations and orientation relationship of omphacite and glaucophane (Fig. 12a). Omphacite in the mapped region is heavily fragmented, with the fractures commonly filled by chlorite (e.g., Fig.

3k; chlorite was not well-indexed in EBSD due to surface preparation difficulties that are common in phyllosilicates and high mean angular deviations from pseudosymmetry). Glaucophane occurs as elongated grains up to > 500 µm in length, commonly associated with omphacite at grain boundaries, or as inclusions in glaucophane (Fig. 12a).

The CPO of omphacite (Fig. 12b) and glaucophane (Fig. 12c) both feature density maxima of the [001] axis (c-axis) aligned with the local foliation of the sample (Fig. 12a), with stronger c-axis alignment in glaucophane ($pfJ_{[001]} = 2.14$ in glaucophane, $pfJ_{[001]} = 1.88$ in omphacite). The [100] and [010] axes (a- and b-axes, respectively) of omphacite also display density maxima, with the b-axis oriented subnormal to the foliation, and the a-axis aligned with the foliation plane. CPO strength is weaker in the smallest omphacite grains relative to the larger fragments/porphyroblasts (Fig. 12b). Glaucophane displays density maxima in the a- and b-axes that are aligned with the omphacite CPO—with the b-axis subnormal to the sample foliation and the a-axis aligned with the foliation plane. As observed in the eclogite, this CPO is not commonly reported for amphibole (Kim & Jung, 2019; Ko & Jung, 2015). The glaucophane CPO displays similar strength in the population of the smallest grains (d < 5 µm) as the measured CPO-strength of the full orientation dataset. In contrast, the larger glaucophane porphyroblasts display stronger alignment of the c-axis ($pfJ_{[001]} = 2.28$) with the a- and b-axes dispersed into girdles subnormal to the lineation direction of the sample (X-direction). Rose diagrams of the omphacite and glaucophane SPOs are included in Fig. 12d and show that the SPO defined by the elongation direction of omphacite and glaucophane grains are coincident with the c-axis CPO of each phase and the local foliation. The misorientation relationship observed between omphacite and glaucophane in the eclogite is more pervasive in the blueschist, with ~75% of neighboring omphacite-glaucophane pairs displaying a 180° misorientation angle.

4.5 Petrological models

The effective compositions of the blueschist (V01a) and eclogite (V01d) used as inputs for phase equilibria modeling were determined as described in the methods (section 3.4) and are shown in Table 5. Subtraction of the early-growth garnet cores accounts for sequestration of major elements into the garnet cores during prograde growth approximating the effective bulk composition of the matrix during late garnet growth facilitating more accurate modeling of phase equilibria and reaction relations during exhumation (Dragovic et al., 2012; Manzotti et al., 2025; Tinkham & Ghent, 2005; Zuluaga et al., 2005).

Table 5

Effective Rock Compositions (in wt% Oxides) of Metabasites from Vroulidia Beach Exposure used as Inputs for Pseudosection Models

	Sample Name (CBU23 Sif)	
Oxides (wt%)	V01a (blueschist)	V01d (eclogite)
SiO_2	50.61	47.97
TiO_2	0.88	0.86
Al_2O_3	17.04	16.50
FeO	5.26	4.26
Fe_2O_3	2.65	3.83
MnO	0.09	0.06
MgO	5.67	4.18
CaO	5.87	5.42
Na_2O	3.06	3.85
K_2O	4.37	3.66
H_2O	*	4.0

*blueschist V01a modeled under fluid saturated conditions with a 99:1 molar ratio of H_2O:CO_2

4.5.1 Eclogite V01d P-T constraints

Fig. 13a shows the pseudosection diagram for the effective composition of the eclogite V01d (garnet rim and matrix composition), excluding lawsonite- and plagioclase feldspar-bearing regions that are not observed in hand sample or thin section. At higher pressures and temperatures (P > 1.1 GPa, T >

450°C), mineral assemblages are broadly consistent with phases observed as inclusions in garnets within the eclogite (white mica + omphacite + quartz + rutile ± amphibole (calcic + sodic) ± epidote). Pseudosection fields at progressively lower pressures and temperatures predict the stabilization of titanite at the expense of rutile, reproducing the matrix mineral assemblage observed in the eclogite.

Garnet compositional isopleths for X_{Prp}, X_{Grs}, and X_{Sps} are superimposed on the pseudosection diagram in Fig. 13b, and broadly show systematic increasing pyrope content and decreasing grossular and spessartine content with increasing pressure and temperature. Si-in-phengite isopleths (Fig. 13c) are shown over the 3.25–3.65 p.f.u. range that is consistent with the range of Si-in-phengite values measured in the eclogite and predict increasing Si incorporated in the phengite structure at higher pressures or lower temperatures. Isopleths correlating to the mean of the EMPA-measured garnet-rim compositions for the eclogite ($X_{\mathrm{Prp}} \approx 0.09$, $X_{\mathrm{Grs}} \approx 0.29$, $X_{\mathrm{Sps}} \approx 0.02$) yield a modeled peak temperature of ~610 ± 50°C at a pressure of ~1.7 ± 0.1 GPa for late garnet growth (white star in Fig. 13d). Combining all mineral compositional constraints including Si p.f.u of phengite rims in the matrix, and modal abundances of phengite, quartz, and epidote, the model constrains the re-equilibration of the eclogite matrix to produce the final mineral assemblage at T ~470 ±50°C and P ~1.5 ± 0.1 GPa (blue star in Fig. 13d).

4.5.2 Blueschist V01a P-T constraints

The pseudosection diagram for the effective composition of the blueschist V01a is shown in Fig. 14a, again excluding the lawsonite- and plagioclase feldspar-bearing regions due to the absence of these phases in the hand sample and thin sections. Eclogitic mineral assemblages found as inclusions in garnet in the blueschist (white mica + omphacite + quartz + rutile ± amphibole (sodic + calcic) ± epidote ± biotite) are predicted at higher pressures and temperatures (P > 1.3 GPa, T > 500°C), while lower pressures and temperatures model rutile replacement by titanite and the stabilization of chlorite in blueschist-facies assemblages.

The superimposed garnet compositional isopleths on the pseudosection diagram in Fig. 14b are consistent with the eclogite model, predicting increasing X_{Prp} and decreasing X_{Grs} and X_{Sps} with increasing pressure and temperature. Fig. 14c displays the Si-in-phengite isopleths calculated from the blueschist effective composition for the range of Si-in-phengite values measured in the samples (3.25–3.65 p.f.u.). Garnet compositional isopleths corresponding to the mean EMPA-measured garnet rim compositions for the blueschist ($X_{\mathrm{Prp}} \approx 0.10$, $X_{\mathrm{Grs}} \approx 0.27$, $X_{\mathrm{Sps}} \approx 0.02$) converge on a peak temperature of ~620 ± 50°C at a pressure of ~1.8 ± 0.1 GPa for late garnet growth in the blueschist (white star in Fig. 14d). The modeled P-T constraints for the re-equilibration of the blueschist matrix based on Si p.f.u. of matrix phengite rims, and modal abundances of phengite, quartz, and epidote are T ~380 ± 50 °C and P ~0.8 ± 0.1 GPa (blue star in Fig. 14d).

4.5.3 Geothermobarometry constraints

Garnet-clinopyroxene thermometry and Si-in-phengite barometry yielded estimates for early garnet growth of T ~460 ± 50°C and P ~1.1 ± 0.2 GPa in the blueschist and T ~440 ± 50°C and P ~1.2 ± 0.2 GPa in the eclogite. A P-T constraint for late garnet growth in the eclogite is estimated as T ~610 ± 50°C and P ~2.3 ± 0.2 GPa. A corresponding P-T constraint for late garnet growth in the blueschist was not determined due to lack of equilibrium garnet-rim–matrix-omphacite pairs in the blueschist.

5 Discussion

5.1 Origin of the blueschist-eclogite transition on Sifnos

The importance of protolith composition to the petrogenesis of the blueschists and eclogites of the Cherronisos unit on Sifnos has been well documented by previous studies of the Cycladic Blueschist Unit, which broadly support the interpretation that the exhumed blueschists on Sifnos preserve peak HP/LT conditions (Groppo et al., 2009; Matthews & Schliestedt, 1984; Mocek, 2001; Okrusch & Broecker, 1990; Schliestedt, 1986). However, the major- and trace-element compositions of our blueschist, eclogite, and mixed blueschist-eclogite samples across the blueschist-eclogite transition at Vroulidia Beach indicate a common MORB protolith with calc-alkaline affinity (Table 2, Fig. 4). Moreover, the bulk compositions of our samples are consistent with those of the phengite-rich eclogites described by Schliestedt (1986) from the same locality (samples 241 and 566 in Schliestedt, 1986). The similarity in garnet chemistry among the blueschist, eclogite, and mixed blueschist-eclogite samples (Fig. 6) further indicates that these rocks experienced a shared P–T evolution, reflecting a more nuanced petrogenetic history within the EBC exposure at Vroulidia Beach. In the following discussion, we discuss the origin of the studied blueschist-eclogite transition on Sifnos, focusing on the blueschist and eclogite end member sample chemistry, textures, and thermodynamic equilibria modeling results.

5.1.1 Prograde to peak-pressure metamorphic evolution

Insights into the prograde evolution of these rocks are provided by garnet inclusion assemblages, which record the mineral parageneses and microstructures that developed prior to peak conditions. Garnets in deformed, glaucophane-rich regions of the blueschist contain abundant tabular omphacite inclusions exhibiting a pronounced shape-preferred orientation (Figs. 5l, 10a) and crystallographic-preferred orientation (Fig. 10) that define a relict foliation not preserved elsewhere in the samples. These microstructures are consistent with the S_1 foliation described by Roche et al. (2016) and attributed to early deformation within the subduction interface. The restriction of the S_1 fabric to these domains in the blueschist suggest that deformation was locally partitioned early in the prograde history, a feature that may have influenced later fluid infiltration and reaction localization. In all samples, epidote, quartz, phengite, omphacite, and rutile occur as common inclusions within garnet cores (Figs. 3g–h, 5k–l, 7a, 10a), with epidote, quartz, and phengite present both as isolated grains and as tabular aggregates (Fig. 7a). These aggregates are interpreted as pseudomorphs after lawsonite formed through the lawsonite breakdown reaction: lws + omp → ph + ep + qz (Schliestedt, 1986). Collectively, these features record prograde metamorphic reactions from the lawsonite-blueschist into the lawsonite-eclogite facies, culminating in transformation at peak-pressure or early retrogression to epidote-eclogite facies conditions.

5.1.2 Early decompression to peak temperature conditions

The predicted peak temperature metamorphic assemblage from pseudosection modeling for the effective bulk compositions of both blueschist and eclogite samples consists of garnet + white mica + omphacite + quartz + rutile ± epidote ± amphibole ± biotite (Figs. 13a, 14a). Garnet growth and inclusion entrapment in both rock types correspond to these modeled peak temperature conditions. Inclusion assemblages within garnet cores—comprising epidote, phengite, omphacite, quartz, and rutile—are consistent with this predicted assemblage, indicating crystallization along the prograde path approaching peak pressure.

Both the blueschist and the eclogite show the same evolution of the garnet chemistry through core and rim growth—showing these samples experience the same P-T history. The trends in garnet composition during rim growth are characterized by decreasing X_{Alm} and increasing X_{Grs}, together with reversals in the trajectory of the X_{Prp} and X_{Sps} trajectories (Fig. 6), suggest the onset of decompression following peak subduction. These trends converge on the modeled garnet isopleths at ~1.7–1.8 GPa and 610–620°C (Figs. 13d, 14d), providing a robust estimate for peak-temperature conditions for the blueschist and eclogite.

5.1.3 Eclogite retrogression and matrix re-equilibration

The final matrix assemblage of the eclogite consists of omphacite + phengite + garnet + epidote + quartz + glaucophane + titanite + apatite + calcite (Figs. 3f, 5f–i). The weak foliation defined by omphacite and phengite, together with the weak CPO of omphacite in the eclogite relative to that in the blueschist (Figs. 11, 12), indicates minimal deformation during retrogression. Glaucophane occurs rarely (~1 modal %) as fine grains, often with very fine grained omphacite inclusions (Figs. 5j). Glaucophane frequently displays a 180° misorientation relationship with adjacent omphacite grains (Fig. 11e), consistent with mimetic replacement—epitaxial growth of glaucophane on the omphacite lattice due to their similar unit-cell dimensions—during retrogression (McNamara et al., 2012). This limited glaucophane growth suggests limited availability of fluids required to stabilize hydrous phases during retrogression (discussed below). Retrogression from eclogite- to blueschist-facies conditions likely occurred during slow exhumation, as indicated by the unmixing of omphacite into omphacite + jadeite lamellae in garnet inclusions (Fig. 9) and the replacement of rutile by titanite in the eclogite matrix (Matsumoto & Hirajima, 2005; Romer & Rötzler, 2003; Tsujimori et al., 2005). Eclogite pseudosection models predict an equilibrium assemblage of omphacite + white mica + garnet + epidote + amphibole + titanite + quartz at ~1.5 GPa and 470°C (Fig. 13d), consistent with the observed retrograde mineralogy. Minor untwinned calcite (~2 modal %), occurring as local masses, is not predicted by the model and likely crystalized during late exhumation after deformation had ceased.

5.1.4 Blueschist retrogression and matrix re-equilibration

The contrast between the weakly deformed eclogite matrix, and the more pervasively recrystallized blueschist assemblage we interpret as spatial variations in deformation and fluid availability during exhumation. The eclogite matrix assemblage exhibits a weak foliation and omphacite CPO, indicating limited deformation and retrogression under fluid-poor conditions. In contrast, the blueschist matrix—composed of glaucophane + phengite + garnet + omphacite + epidote + quartz + titanite + apatite + calcite + chlorite—shows a well-developed foliation (Figs. 3d,3i–k), pervasive recrystallization, and a strong CPO in glaucophane and omphacite (Fig. 12), consistent with deformation-assisted hydration and metamorphic re-equilibration during retrogression. Our blueschist pseudosection model predicts the observed re-equilibrated assemblage at ~0.8 GPa and 380°C (Fig. 14d), excluding calcite, which likely formed later during post-deformation exhumation. Mimetic replacement of omphacite by glaucophane is ubiquitous (Fig. 12e), and zonation in glaucophane reflects fluid-driven variations in Fe oxidation state (Figs. 8a,e; Groppo et al., 2009). The weaker a- and b-axis CPOs of coarse glaucophane porphyroblasts (Fig. 8c) relative to fine-grained glaucophane that fully mimics the omphacite CPO (Fig. 8b) imply the activation of diffusion-assisted creep accompanied by rigid grain rotation during exhumation. Moreover, pervasive chloritization along fractures in the remaining omphacite grains (Fig. 3k) further supports localized fluid infiltration and deformation. Together, these features indicate that deformation and fluid flow were spatially partitioned during exhumation, with eclogite domains largely fluid-poor, while adjacent blueschist zones acted as more permeable fluid-rich, deforming pathways. This rheological and permeability partitioning is consistent with observations from other shear zones (Angiboust et al., 2017; Condit & Mahan, 2018; Whitney et al., 2014), and likely played a key role in controlling the extent of retrogression and preservation of peak assemblages within the CBU on Sifnos.

5.1.5 A retrograde eclogite-blueschist transition on Sifnos

Collectively, these observations guide us to an interpretation that this exhumed blueschist-eclogite transition at Vroulidia Beach preserve a common metamorphic evolution from blueschist through peak epidote-eclogite facies conditions, followed by differential re-equilibration during exhumation. The consistent garnet chemistry and inclusion assemblages across both rock types demonstrate that they shared a P–T trajectory, while variations in deformation intensity, fluid availability, and permeability controlled the extent of retrogression and mineral re-equilibration. Fluid-assisted deformation in the eventual blueschist promoted pervasive recrystallization and growth of hydrous phases during decompression, whereas limited fluid availability in the eclogite led to the preservation of near-peak assemblages. The resulting juxtaposition of weakly retrogressed eclogite and strongly hydrated blueschist therefore reflects localized deformation and fluid pathways that progressively developed from prograde subduction through exhumation. These petrologic and microstructural relationships provide a framework for interpreting the prograde-to-retrograde evolution of this Vroulidia Beach exposure, and form the basis for the proposed P–T path reconstruction discussed below.

5.2 P-T path

In this section we reconstruct the P-T path (Fig. 15a) of a blueschist-eclogite transition from the EBC on Vroulidia Beach using the petrological and textural observations and pseudosection models and classical thermobarometry discussed above. Using classical thermobarometry, we estimate the start of garnet growth to ~1.1 GPa at ~450°C with omphacite inclusions equilibrated with garnet (1 in Fig. 15a). We estimate the growth of the garnet rims initiated with early decompression ~2.3 GPa and ~610°C (2 in Fig. 15a). These P-T constraints are consistent with the prograde section of the P-T envelope proposed by Groppo et al. (2009), and we propose that the unconstrained region of our P-T reconstruction follows this envelope during prograde subduction and deformation through the lawsonite-blueschist and -eclogite facies to peak pressures at the transition to the epidote-eclogite facies (Fig. 15b). Temperature continued to increase during early decompression, likely related to tectonic slicing of the unit from the subducting plate, reaching a peak temperature of ~610–620°C at ~1.7 GPa recorded in the garnet rim chemistry and inclusion assemblages (3 in Fig. 15a). Movement of the tectonic slice within the subduction channel towards underplating to the overriding plate record a steep decrease in temperature relative to pressure due to the slice coming in contact with cooler, subducting material at the interface, yielding a P-T constraint of ~1.5 GPa at ~470°C for the re-equilibration of the eclogite matrix (4 in Fig. 15a). This estimate for the retrograde re-equilibration of the eclogite is consistent with proposed peak metamorphic conditions on Sifnos by Schliestedt (1986; Fig. 15b). Omphacite replacement by glaucophane continued during exhumation to produce the blueschist matrix due to fluid-localization in zones of more intense deformation, with the re-equilibration of the blueschist matrix at ~0.8 GPa and ~380°C (5 in Fig. 15a). Fig. 15b shows our reconstructed P-T path along with previous estimates for Sifnos.

5.3 Implications

While our investigation does not preclude the interpretation that many of the coherent, exhumed exposures of HP/LT units from the CBU preserve prograde to peak metamorphism and deformation, it highlights the occurrence of nuanced tectonometamorphic histories of sequences within larger geological units. Blueschists originally proposed to represent peak metamorphic conditions have been reinterpreted as retrogressed blueschists in tectonic mélanges, such as the Franciscan Formation (e.g., Coleman & Lanphere, 1971) and the blueschists of the Tian Shan orogenic belt (Klemd et al., 2005; van der Straaten et al., 2008). Our results demonstrate that within the larger framework of compositional controls on the development of blueschist and eclogite lithologies at Vroulidia Beach, localized fluid infiltration through rheologically weak zones—initiated during prograde subduction—can drive selective retrogression coupled with deformation during exhumation. This highlights the value of integrating detailed petrological and microstructural analysis using modern techniques such as thermodynamic equilibrium modeling and EBSD-based textural analysis, and underscores the potential for refining our understanding of the subduction and exhumation histories of previously well-studied regions like the Cycladic Islands.

The limited preservation of prograde subduction-related deformation—expressed as a relict foliation in omphacite inclusions within garnet in the blueschist—offers little constraint on the relative strength of blueschists versus eclogites along the interface during prograde subduction. However, our investigation provide valuable insight into how deformation partitioning in these zones may channelize fluid flow and promote selective retrogression during exhumation. Interactions between deformation and fluid-mobility have been recognized as mechanisms that create zones of rheological weakness in a host of different lithologies and tectonic settings (e.g., Angiboust et al., 2017; Condit & Mahan, 2018; Jaeckel et al., 2018; Kleijbeuker et al., 2025; Soret et al., 2025; Viti et al., 2018; Donna L. Whitney et al., 2014; Yonkee et al., 2003). In this study, evidence for such fluid-deformation feedbacks signal the potential for future work on how strain was partitioned between rheologically weak and strong units within this tectonic slice, and its role in the exhumation of the Eclogite-Blueschist Complex on Sifnos. We suggest caution when assuming blueschist-eclogite rocks represent specific portions of subduction P-T paths (e.g., prograde, retrograde) without doing detailed petrologic and petrographic work.

6 Conclusions

This study investigated the feedbacks between deformation and fluid-flow in an exhumed blueschist-eclogite transition from the Eclogite-Blueschist Complex of the Cherronisos Unit exposure of the Cycladic Blueschist Unit at Vroulidia Beach, Sifnos Island. The studied blueschist-eclogite transition illustrates feedbacks between deformation and localized fluids to selectively retrogress and enhance deformation in weakened domains to produce the strongly deformed blueschists intercalated with massive eclogites along the sampled transect. This study illustrates the potential for interplay between deformation and fluid-flow to control the production of blueschist and eclogites descended from the same protolith within the context of a larger exhumed subduction terrane where variations in protolith composition exhibit a primary control on the observed mineral assemblage and compositions.

Acknowledgments

This work was funded through NSF CAREER grant EAR-2338181 to Condit, and research awards at the University of Washington through the Anthony Qamar Endowed Memorial Fund to Ott. Part of this work was conducted at the Washington Nanofabrication Facility / Molecular Analysis Facility, a National Nanotechnology Coordinated Infrastructure (NNCI) site at the University of Washington with partial support from the National Science Foundation via awards NNCI-1542101 and NNCI-2025489. Microprobe data were collected at the Mackay School of Earth Science and Engineering Microbeam Laboratory at University of Nevada, Reno, with the invaluable assistance of Joel DesOrmeau. We thank Stanley Mertzman at the X-ray Laboratory of Franklin and Marshall College for assistance with bulk sample analyses. The authors thank Besim Dragovic for helpful discussions regarding thermodynamic modeling of HP/LT lithologies in the Hellenic Subduction Zone.

Chapter 5 Figures

Figure 1. (a) Geological map of the Cycladic Blueschist Unit (CBU) on Sifnos Island, Greece (after Dragovic et al., 2015), showing study location (CBU23 Sif V samples, red star; coordinates: 37.023968, 24.654570). (b) Previously published peak P-T (blue star; Schliestedt, 1986) and P-T path estimates for the CBU on Sifnos.

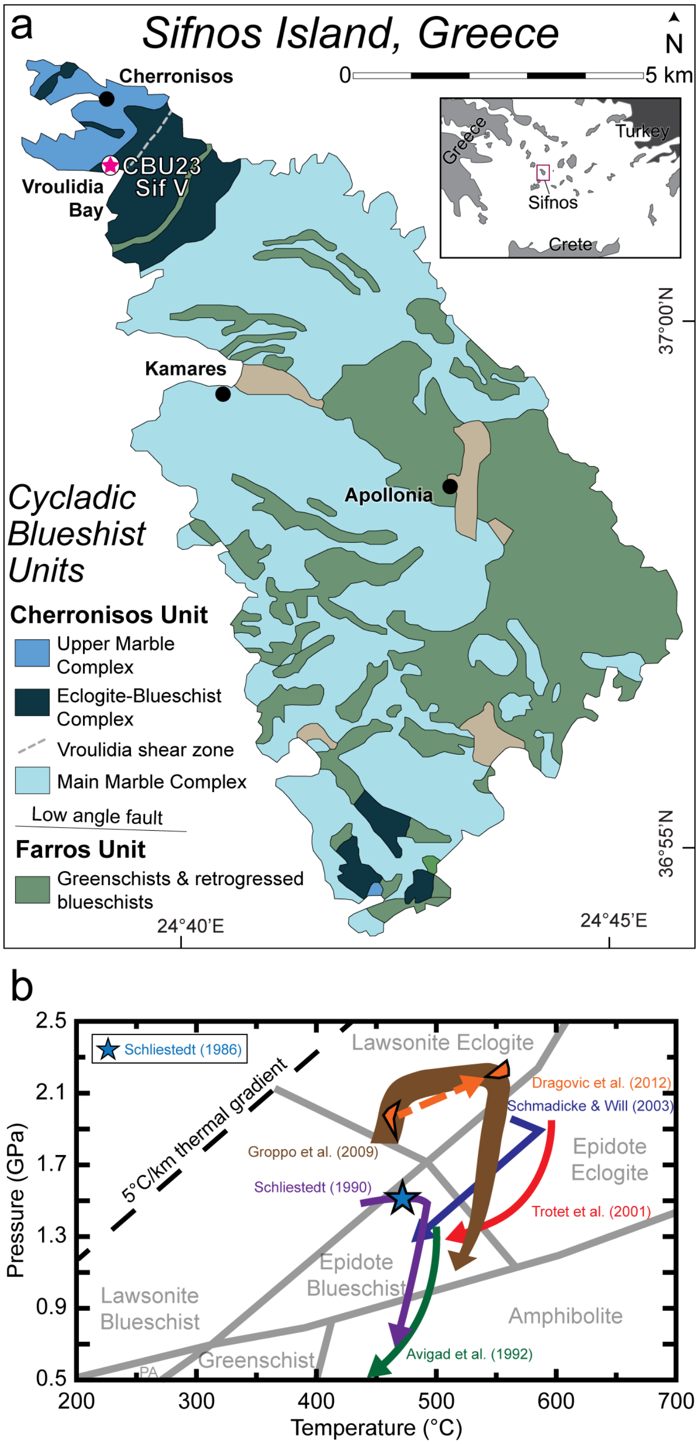

Figure 2. Field photographs of the study area on Vroulidia Beach, Sifnos Island including (a) locations of samples along blueschist-eclogite transition structurally below contact between metamafic and metasedimentary units, and detail of the sampling locations of the (b) eclogite, (c) mixed blueschist-eclogite), and (d) blueschist samples discussed in this study. Note the centimeter-scale blueschist-eclogite domains in (c). (e) An example of decimeter-scale intercalation of blueschist and eclogite domains. (f) Field photograph of massive eclogite pod (center) between penetratively deformed mica-schist (left) and blueschist (right).

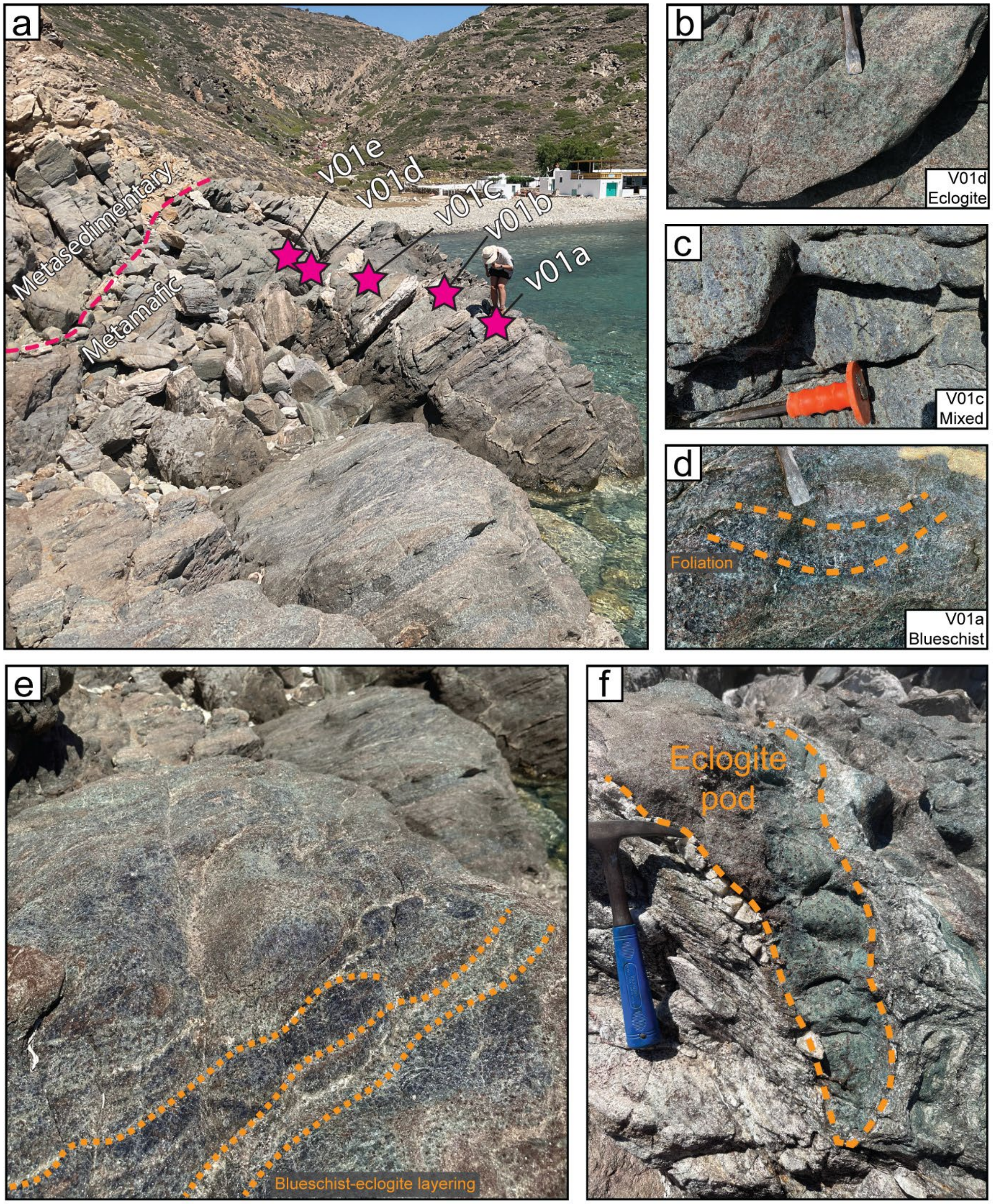

Figure 3. Photographs of the (a) blueschist, (b) mixed blueschist-eclogite, and (c) eclogite samples selected for this study. Photomicrographs of representative regions of the thin sections of the (d) blueschist, (e) mixed blueschist-eclogite, and (f) eclogite showing the variation in sample foliations. Detail of phengite, epidote, quartz, and rutile inclusions in garnet in (g) Plane-polarized light (PPL) and (h) cross-polarized light (XPL). (i-k) Photomicrographs of blueschist matrix in PPL (i,k) and XPL (j) show foliation defined by glaucophane and phengite, matrix titanite, and untwinned calcite in matrix and glaucophane fractures (i,j), and chloritization of omphacite along fractures (k). (l) PPL micrograph of a relict foliation defined by omphacite inclusions in garnet that is oblique to blueschist matrix foliation (see Fig. 10).

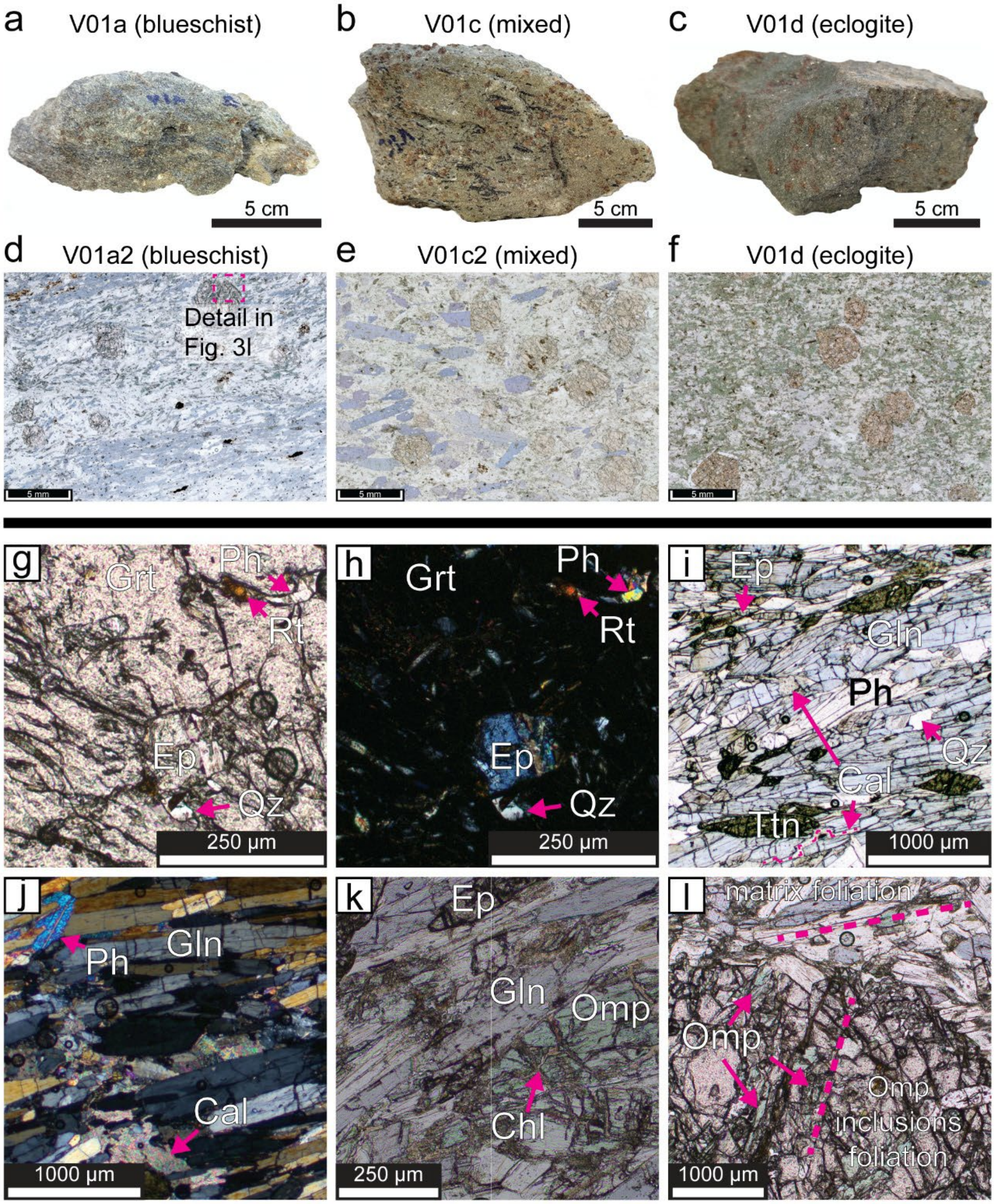

Figure 4. (a) Major element composition of the blueschist, mixed blueschist-eclogite, and eclogite included in this study. (b) Trace element distributions of the samples included in this study, normalized to mid-ocean ridge basalt (MORB) compositions (Pearce, 1979). For comparison, the average compositions of Schliestedt (1986) for blueschist and eclogite on Sifnos and trace element patterns of oceanic alkali basalt and island arc tholeiite after Pearce (1979) are included. (c) Alkalis-Fe-Mg diagram with the samples included in this study plotted alongside the blueschist, eclogite, and actinolite-bearing rocks of Schliestedt (1986) and the magma series of Kuno (1968) and Irvine and Baragar (1971).

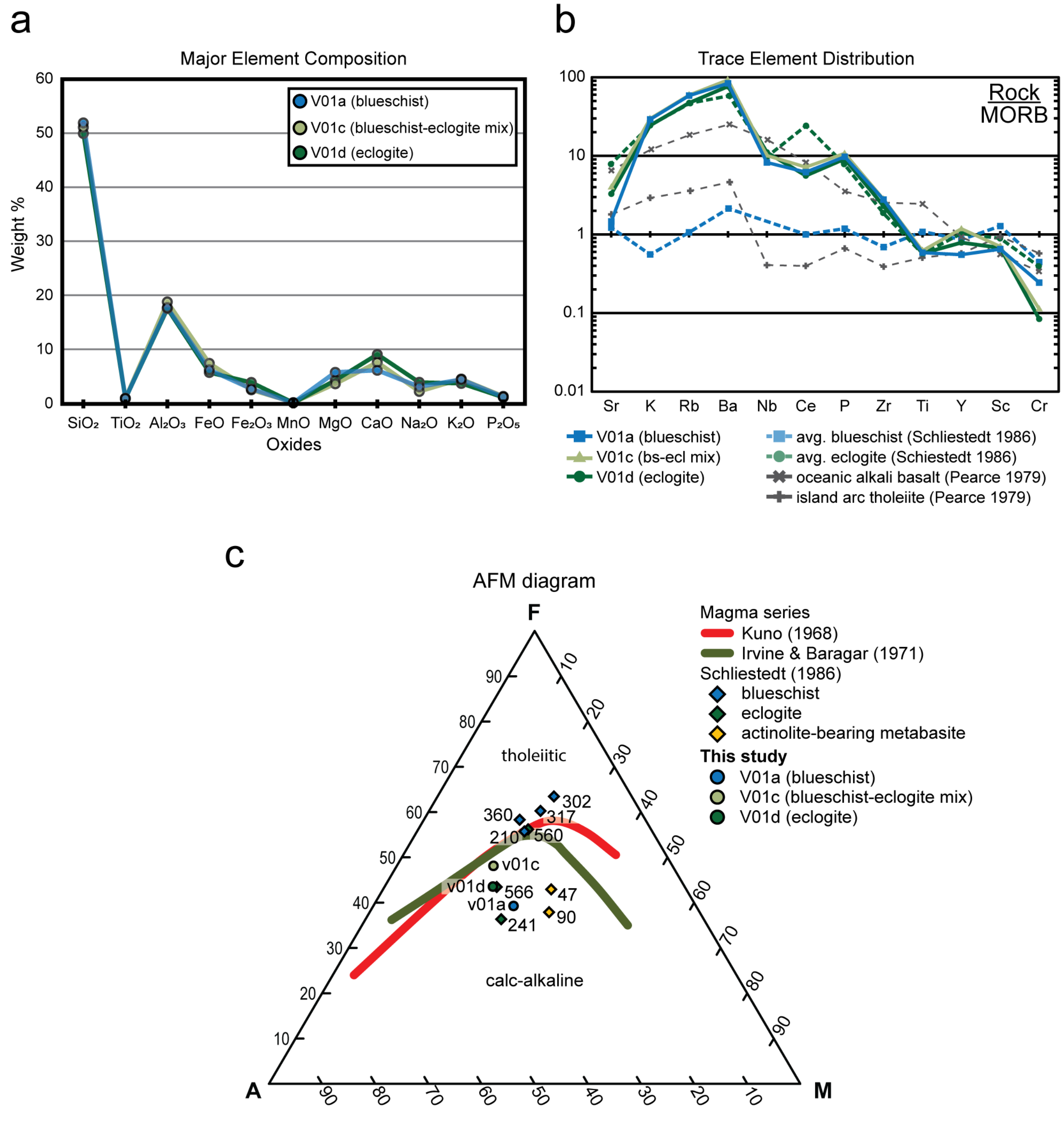

Figure 5. (a-e) Photomicrographs of the microstructures of the mixed blueschist-eclogite displaying the foliation defined by glaucophane and phengite and occurrence of omphacite, phengite, and epidote inclusions in glaucophane (a, PPL; b, XPL). Titanite commonly occurs along with untwinned calcite in matrix (c-d, PPL; e, XPL). (f-l) Microstructures of the eclogite feature a weak foliation in omphacite and phengite (f,h, PPL; g,i, XPL), untwinned calcite associated with Fe-oxide (f,g), and common titanite (f-j). (j) A rare glaucophane grain encloses omphacite inclusions. (k,l) Representative micrograph of inclusions in garnet in PPL (k) and XPL (l).

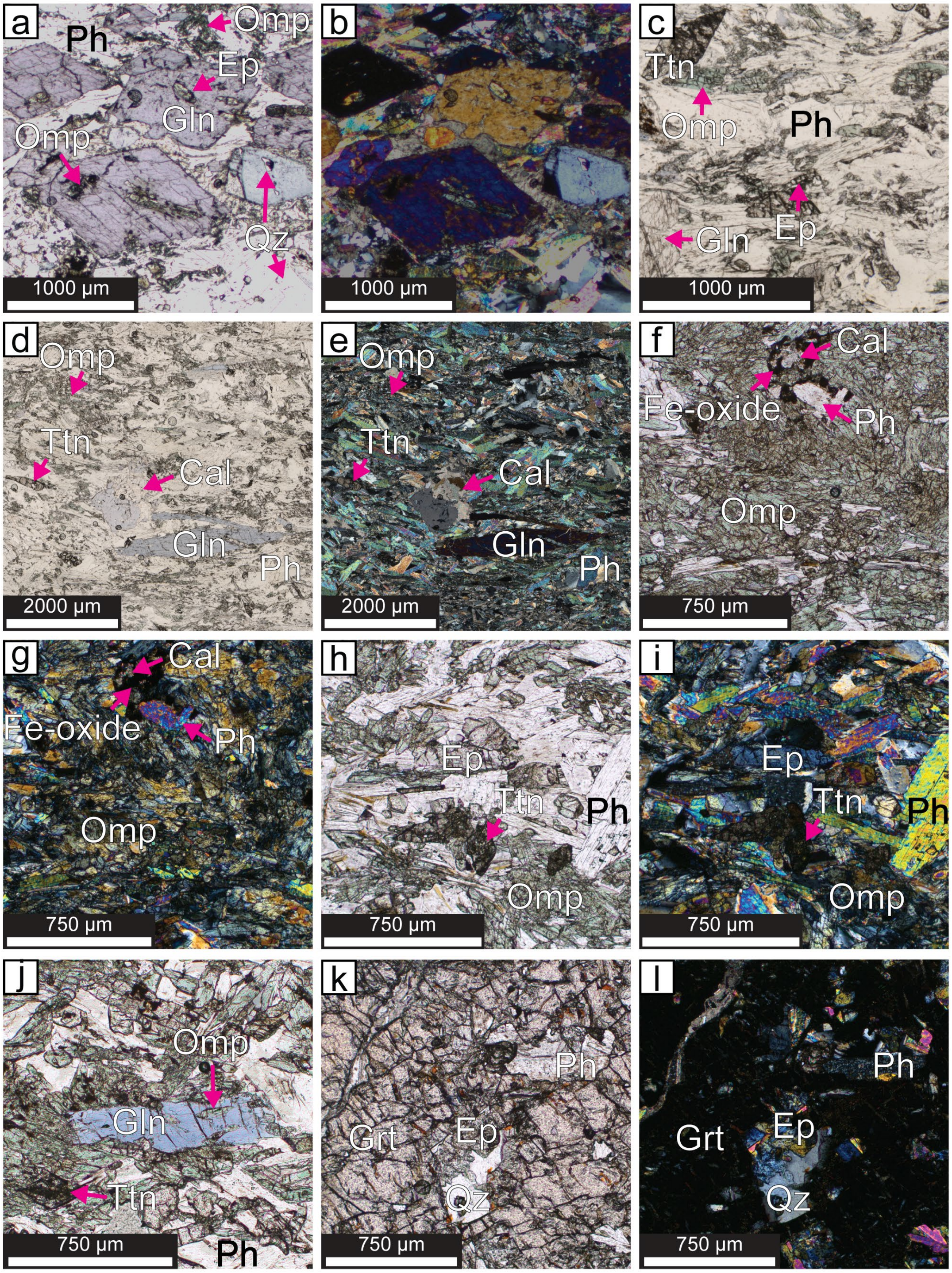

Figure 6. Locations of core-rim traverses of representative garnets and measured garnet chemistry in the (a) blueschist, (b) mixed blueschist-eclogite, and (c) eclogite samples. Garnet chemistry of the core-rim traverses shown as distance along profile from core to rim versus mole fraction of almandine (Alm; Fe-component), grossular (Grs; Ca-component), pyrope (Prp; Mg-component) and Spessartine (Sps; Mn-component).

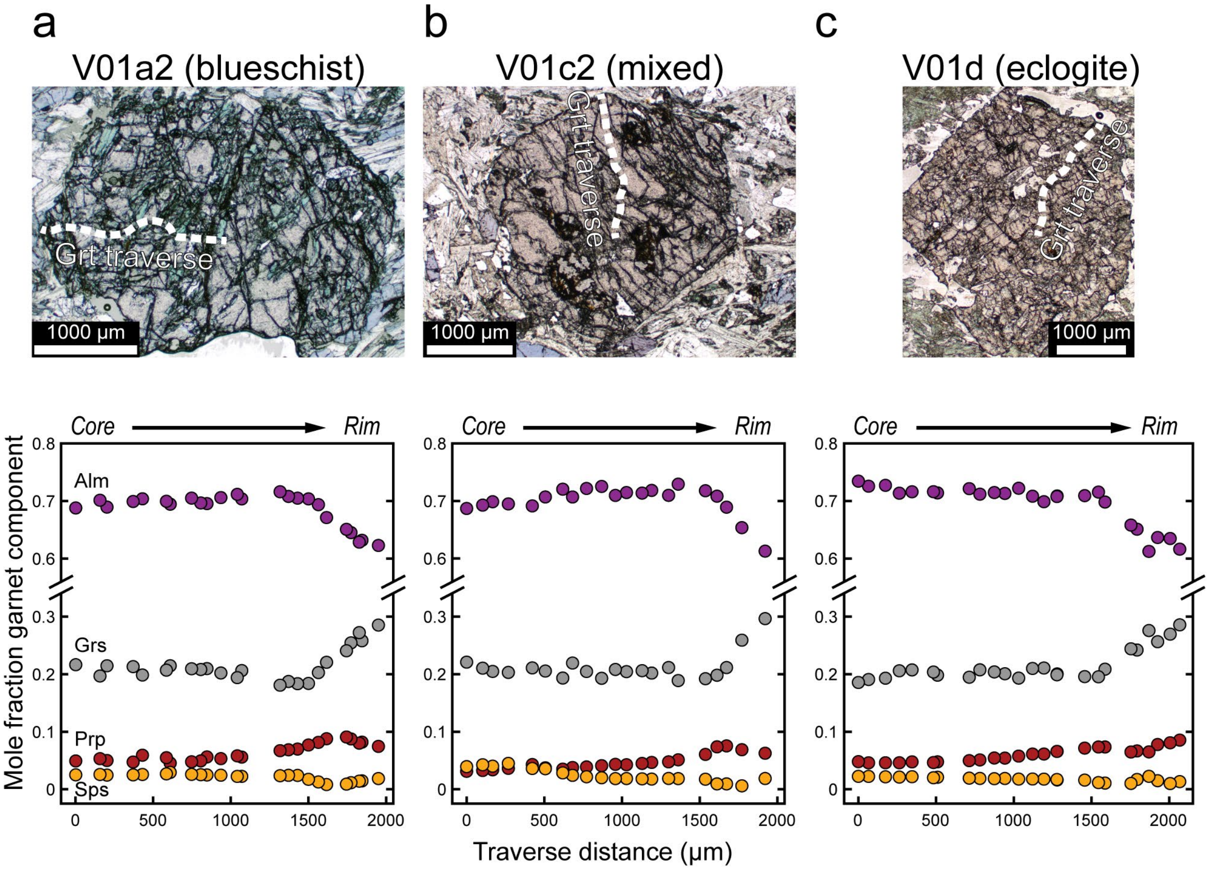

Figure 7. (a) XPL photomicrograph of phengite in garnet inclusion assemblage in the eclogite. (b) BSE image of the eclogite matrix displaying chemical zoning in phengite with cores enriched in Si, Fe, Mg and lower Al relative to the rims. (c) ternary diagram of white mica compositions of all samples showing the muscovite to celadonite apices (phengite solid-solution). (d) Na (apfu) versus Si (apfu) of phengite in all samples displayed for inclusions in garnet, and as cores and rims for phengite in the matrix of the samples.

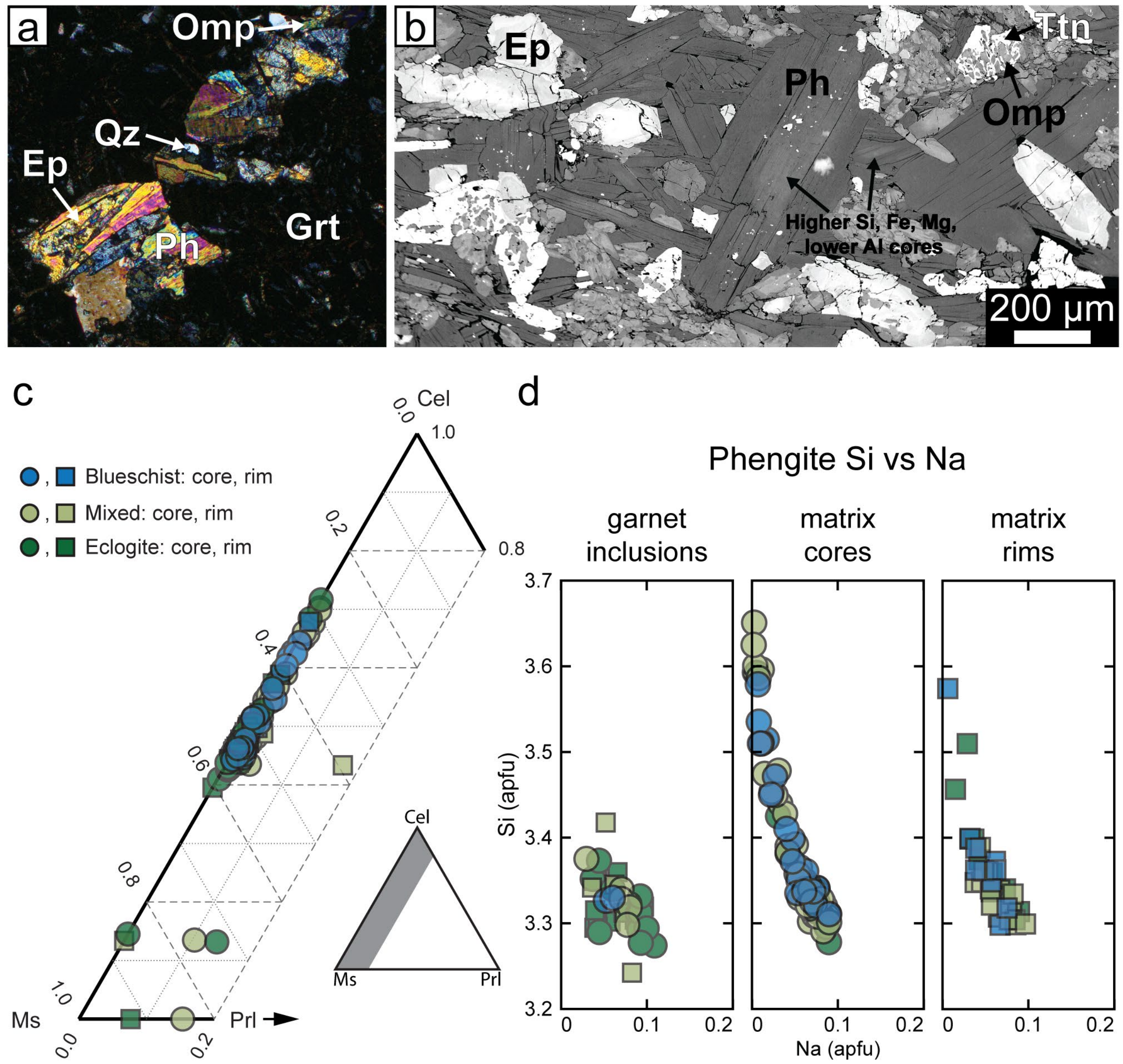

Figure 8. Chemically zoned, elongated glaucophane grains in the blueschist matrix shown in (a) PPL and (b) XPL. (c) PPL micrograph of tabular, unzoned glaucophane in the mixed blueschist-eclogite. (d) PPL micrograph of a rare, fine-grained, unzoned glaucophane grain in the omphacitic matrix of the eclogite. (e-h) sodic amphibole compositions of the blueschist and mixed blueschist-eclogite samples shown as the ferric versus ferrous iron composition (e,g) and the C-site occupancy by Al, Fe^{3+}, and Ti versus A-site occupancy by Na, K, and Ca (f,h).

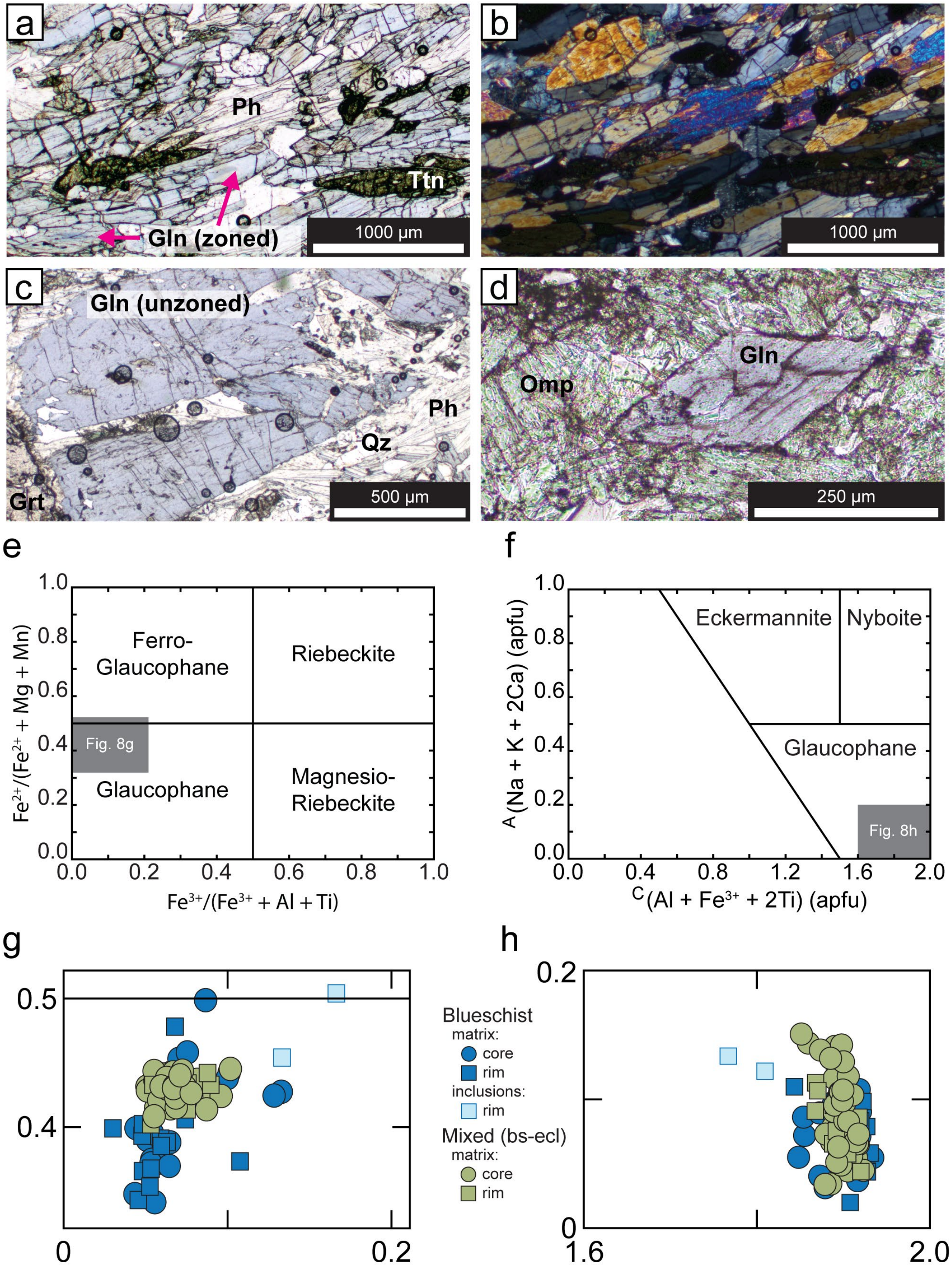

Figure 9. Pyroxene compositions for the (a) eclogite and (b) blueschist samples. The eclogite displays a miscibility gap between omphacitic and jadeitic pyroxene that are observed as lamellar structures with high/low contrast in the inset BSE-image in (a).

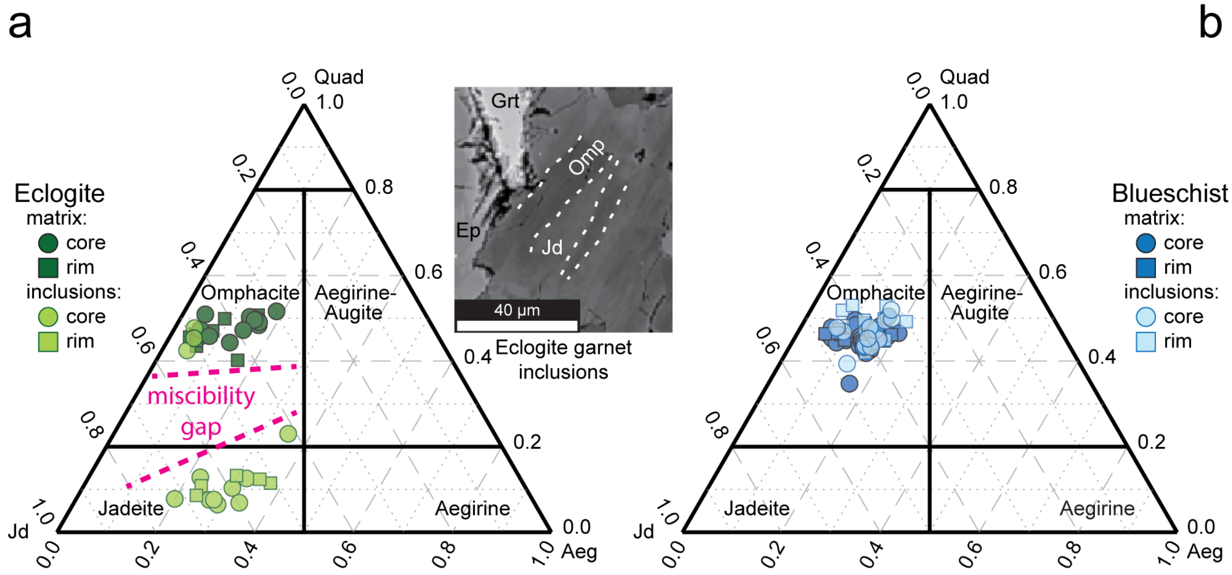

Figure 10. (a) Detailed photomicrograph of omphacite inclusions in garnet shown in Fig. 3l. (b) EBSD-map of the garnet showing the omphacite inclusions as gray bordered grains colored by orientation in the Z-direction (down) key to orientations in part (d). (c) Omphacite display a strong SPO defining a relict foliation oblique to the sample foliation. (d) Inverse pole figure key for omphacite grains in (b), where similarly colored omphacite grains preserve a relict CPO.

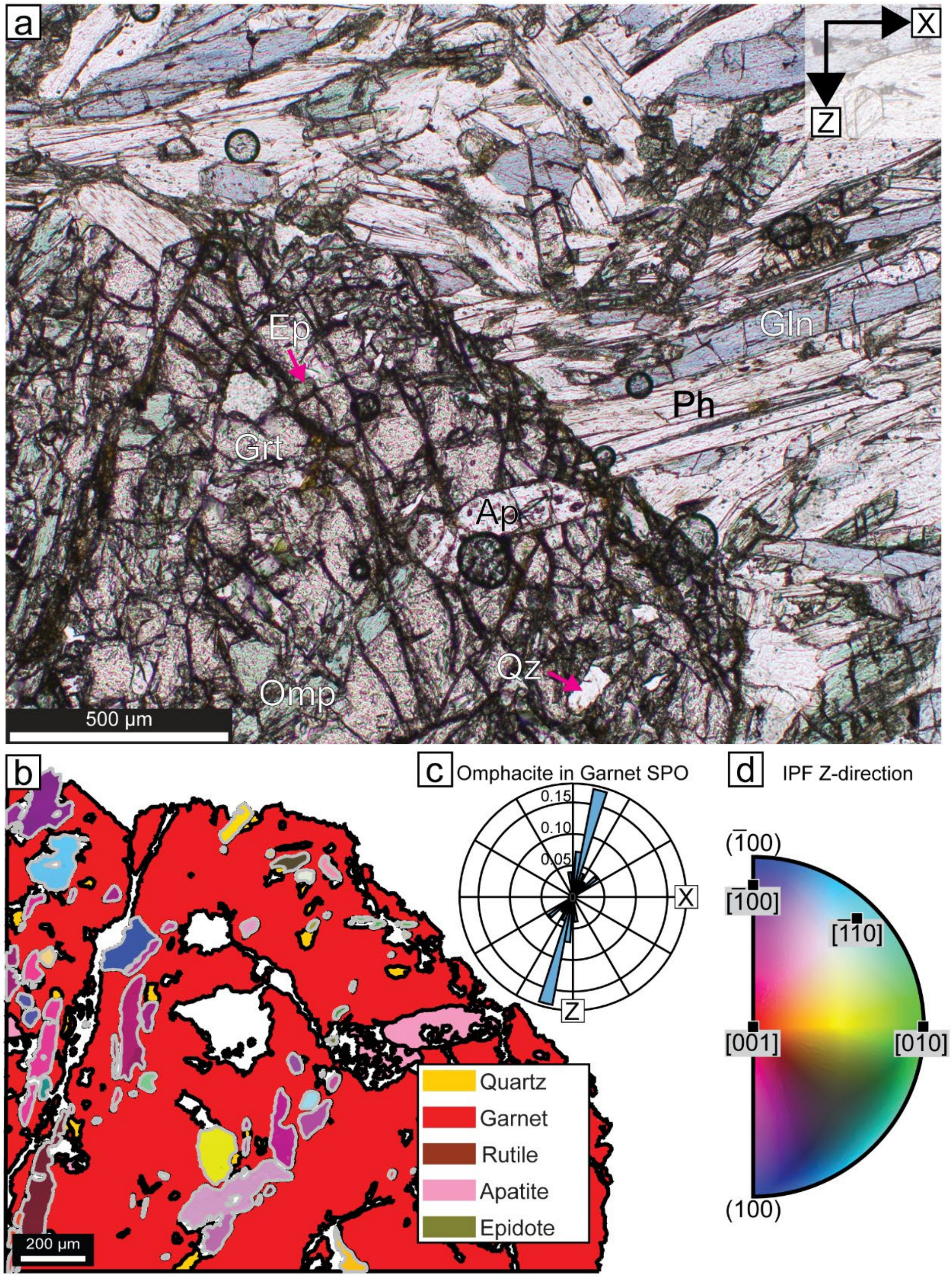

Figure 11. (a) EBSD phase map for only the omphacite and glaucophane in the eclogite. (b) Pole figures of the [100], [010], and [001] axes of omphacite for all grains, large grains (d > 5 μm), and small grains (d < 5 μm) contoured by multiples of uniform distribution. (c) Pole figures of glaucophane as described in (b). (d) Rose diagram plots of SPO in omphacite and glaucophane. (e) Misorientation angle distribution for omphacite-glaucophane neighbor pairs in eclogite matrix.

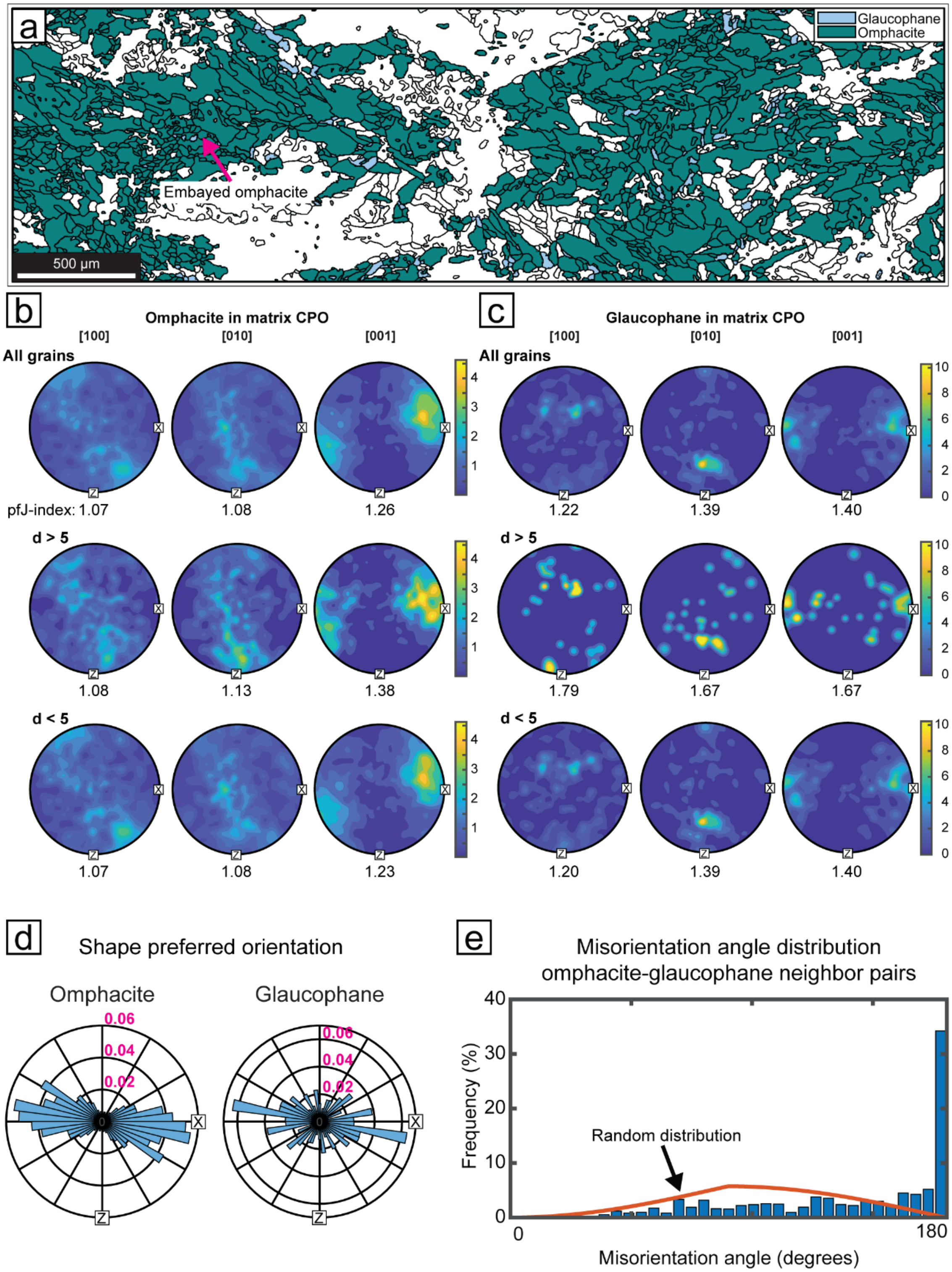

Figure 12. (a) EBSD phase map for only the omphacite and glaucophane in the blueschist. (b) Pole figures of the [100], [010], and [001] axes of omphacite for all grains, large grains (d > 5 μm), and small grains (d < 5 μm) contoured by multiples of uniform distribution. (c) Pole figures of glaucophane as described in (b). (d) Rose diagram plots of SPO in omphacite and glaucophane. (e) Misorientation angle distribution for omphacite-glaucophane neighbor pairs in blueschist matrix.

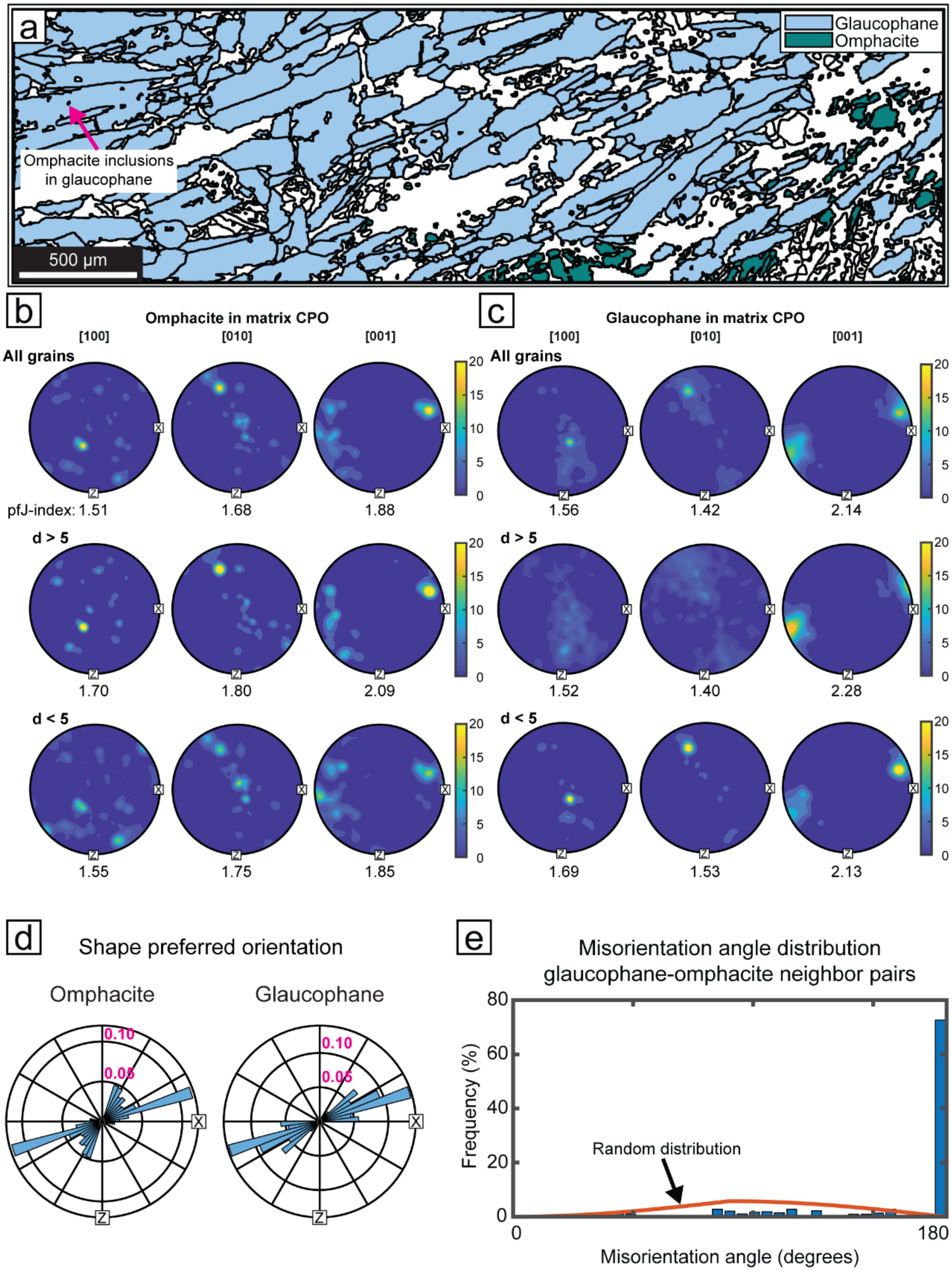

Figure 13. (a) P-T pseudosection of the effective composition of the eclogite (Table 5) with 4 wt% H_2O. (b) P-T pseudosection contoured with pyrope, grossular, and spessartine garnet compositional isopleths with bolded contours showing isopleths closest to garnet rim composition measured by microprobe. (c) P-T pseudosection contoured with Si-in-phengite isopleths for range of compositions measured in phengite. (d) P-T pseudosection with P-T constraints from garnet isopleth convergence with measured garnet rim composition (peak temperature; white star) and matrix phengite rim Si p.f.u. and matrix mineral assemblage (matrix re-equilibration; blue star).

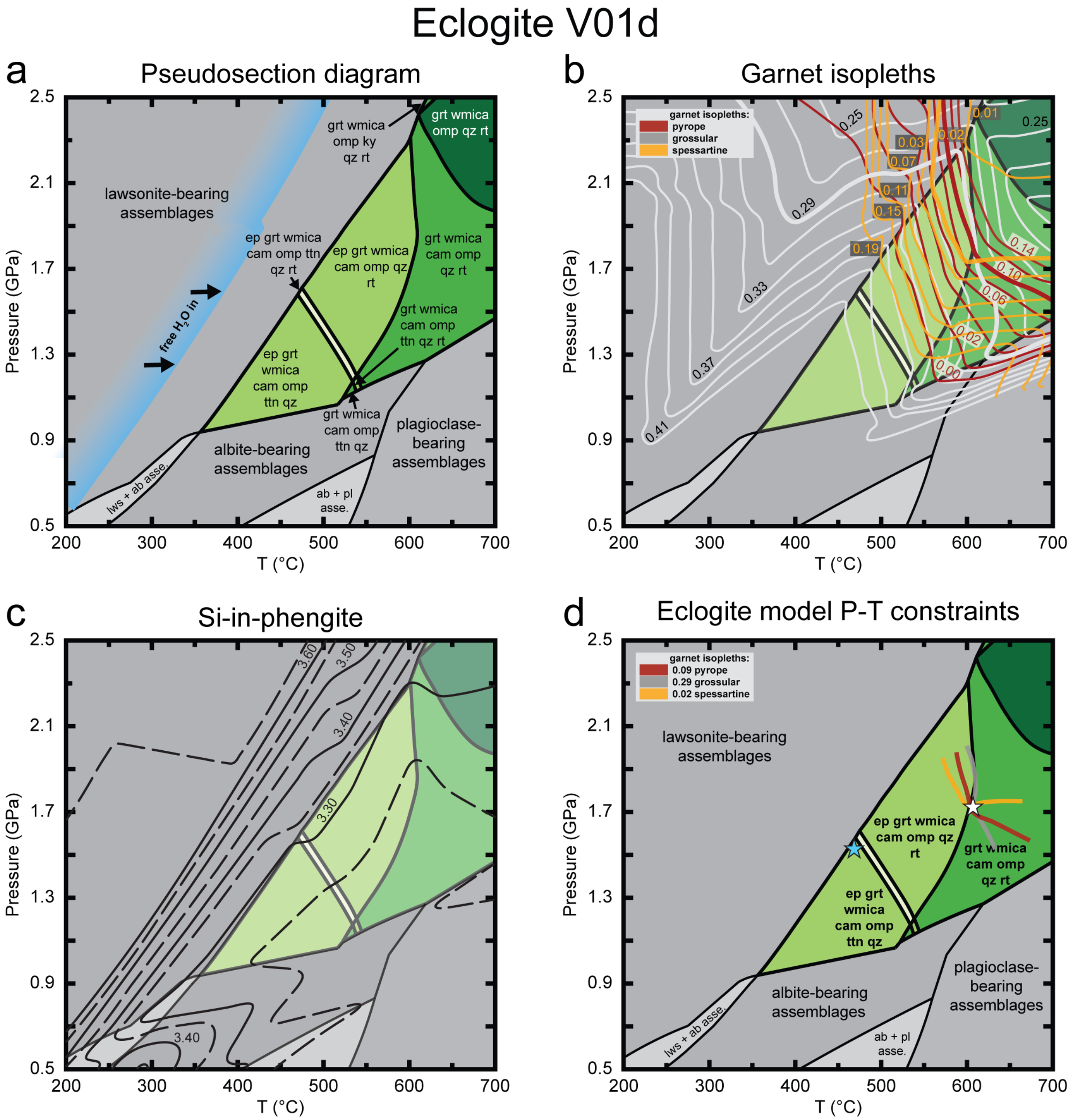

Figure 14. (a) P-T pseudosection of the effective composition of the blueschist (Table 5) under fluid-saturated conditions with a molar ratio of $H_2O:CO_2 = 99:1$. (b) P-T pseudosection contoured with pyrope, grossular, and spessartine garnet compositional isopleths with bolded contours showing isopleths closest to garnet rim composition measured by microprobe. (c) P-T pseudosection contoured with Si-in-phengite isopleths for range of compositions measured in phengite. (d) P-T pseudosection with P-T constraints from garnet isopleth convergence with measured garnet rim composition (peak temperature; white star) and matrix phengite rim Si p.f.u. and matrix mineral assemblage (matrix re-equilibration; blue star).

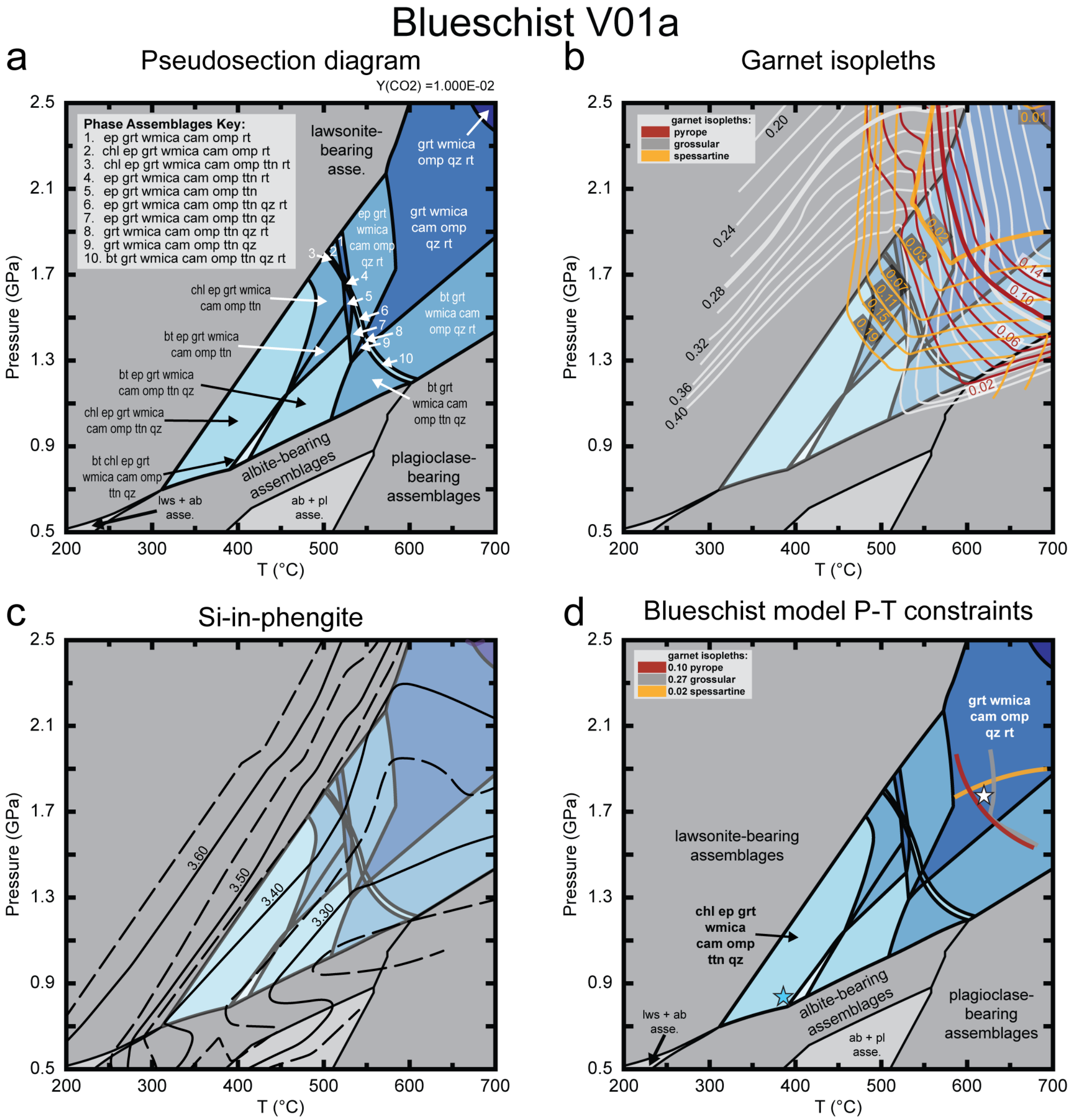

Figure 15. (a) P-T path reconstruction for the Sifnos blueschist and eclogite (this study). P-T constraints 1 and 2 were determined using the Garnet-Clinopyroxene geothermometer of Ellis and Green (1979) and Si-in-phengite barometry. Constraints 3–5 were determined from pseudosection models of the effective bulk composition (detailed in discussion). (b) P-T path reconstruction from (a) along with previously published P-T paths for Sifnos.

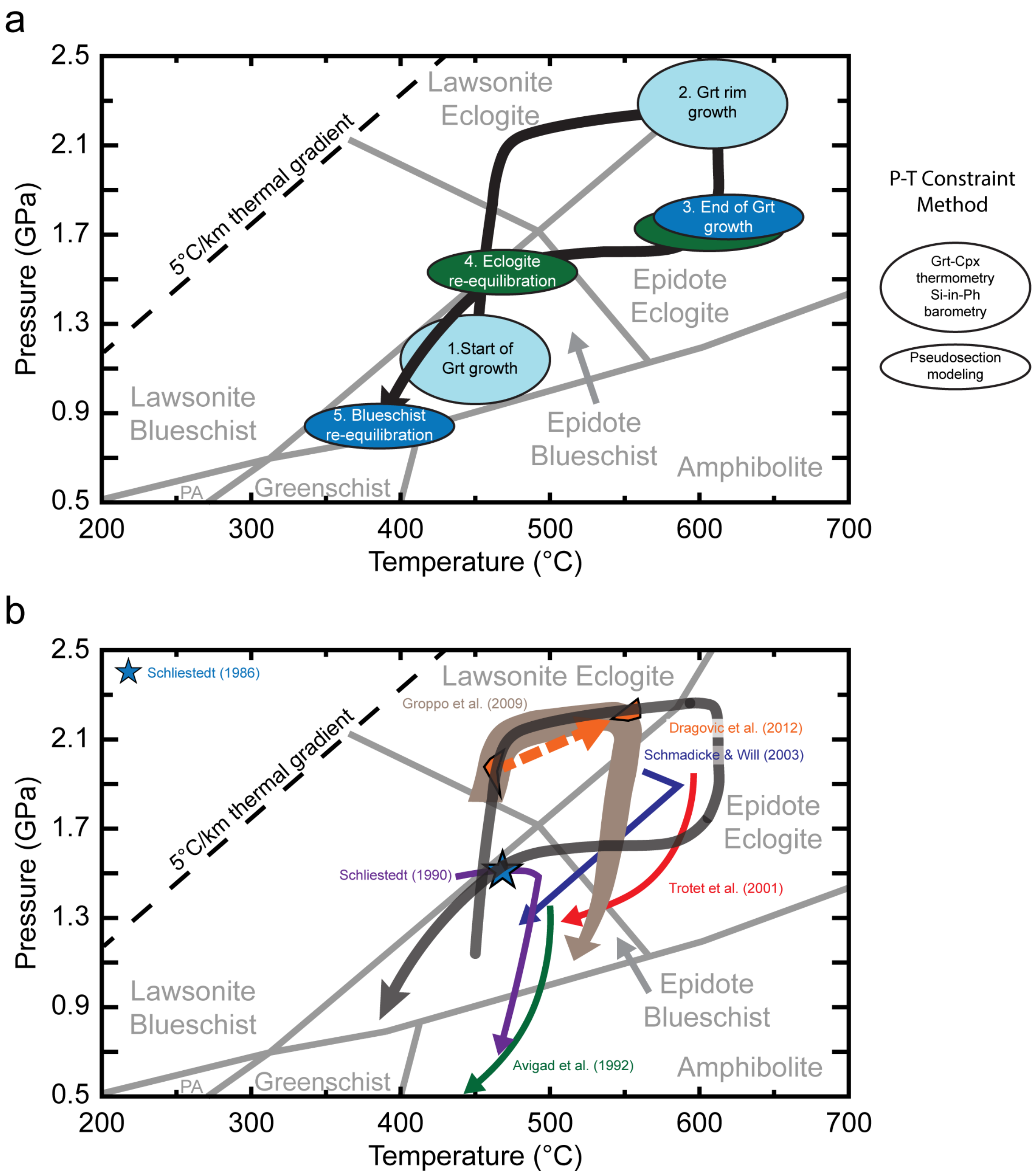

Chapter 5 References

Abbey, S. (1980). Studies in "Standard Samples" for Use In the General Analysis of Silicate Rocks and Minerals. *Geostandards Newsletter*, *4*(2), 163–190. https://doi.org/10.1111/j.1751-908X.1980.tb00283.x

Agard, P., Yamato, P., Jolivet, L., & Burov, E. (2009). Exhumation of oceanic blueschists and eclogites in subduction zones: Timing and mechanisms. *Earth-Science Reviews*, *92*(1), 53–79. https://doi.org/10.1016/j.earscirev.2008.11.002

Altherr, R., Kreuzer, H., Lenz, H., Wendt, I., Harre, W., & Durr, S. (1994). Further evidence for Late-Cretaceous low pressure/high-temperature terrane in the Cyclades, Greece. *Chemie Der Erde*, *54*, 319–328.

Angiboust, S., Yamato, P., Hertgen, S., Hyppolito, T., Bebout, G. E., & Morales, L. (2017). Fluid pathways and high-P metasomatism in a subducted continental slice (Mt. Emilius klippe, W. Alps). *Journal of Metamorphic Geology*, *35*(5), 471–492. https://doi.org/10.1111/jmg.12241

Avigad, D. (1993). Tectonic juxtaposition of blueschists and greenschists in Sifnos Island (Aegean Sea)—implications for the structure of the Cycladic blueschist belt. *Journal of Structural Geology*, *15*(12), 1459–1469. https://doi.org/10.1016/0191-8141(93)90006-V

Avigad, D., Matthews, A., Evans, B. W., & Garfunkel, Z. (1992). Cooling during the exhumation of a blueschist terrane: Sifnos (Cyclades), Greece. *European Journal of Mineralogy*, *4*(3), 619–634. https://doi.org/10.1127/ejm/4/3/0619

Bachmann, F., Hielscher, R., & Schaeben, H. (2010). Texture Analysis with MTEX – Free and Open Source Software Toolbox. *Solid State Phenomena*, *160*, 63–68. https://doi.org/10.4028/www.scientific.net/SSP.160.63

Behr, W. M., Kotowski, A. J., & Ashley, K. T. (2018). Dehydration-induced rheological heterogeneity and the deep tremor source in warm subduction zones. *Geology*, *46*(5), 475–478. https://doi.org/10.1130/G40105.1

Bröcker, M., Baldwin, S., & Arkudas, R. (2013). The geological significance of 40Ar/39Ar and Rb–Sr white mica ages from Syros and Sifnos, Greece: a record of continuous (re)crystallization during exhumation? *Journal of Metamorphic Geology*, *31*(6), 629–646. https://doi.org/10.1111/jmg.12037

Bröcker, Michael. (1990). Blueschist-to-greenschist transition in metabasites from Tinos Island, Cyclades, Greece: Compositional control or fluid infiltration? *Lithos*, *25*(1), 25–39. https://doi.org/10.1016/0024-4937(90)90004-K

Bröcker, Michael, Scherer, E. E., Xypolias, P., & Höhn, M. (2022). The timing of blueschist-facies metamorphism in the Makrotantalon Unit on Andros Island, Greece: Cretaceous and Eocene high-pressure/low-temperature events? *Geological Magazine*, *159*(8), 1437–1453. https://doi.org/10.1017/S0016756822000280

Brooks, H. L., Dragovic, B., Lamadrid, H. M., Caddick, M. J., & Bodnar, R. J. (2019). Fluid capture during exhumation of subducted lithologies: A fluid inclusion study from Sifnos, Greece. *Lithos*, *332–333*, 120–134. https://doi.org/10.1016/j.lithos.2019.01.014

Catlos, E., & Cemen, I. (2023). A Review of the Dynamics of Subduction Zone Initiation in the Aegean Region. In *Compressional Tectonics*. Retrieved from https://agupubs.onlinelibrary.wiley.com/doi/chapter-epub/10.1002/9781119773856.ch4

Clarke, G. L., Aitchison, J. C., & Cluzel, D. (1997). Eclogites and Blueschists of the Pam Peninsula, NE New Caledonia: a Reappraisal, *38*(7), 34.

Coleman, R. G., & Lanphere, M. A. (1971). Distribution and Age of High-Grade Blueschists, Associated Eclogites, and Amphibolites from Oregon and California. *Geological Society of America Bulletin*, *82*(9), 2397. https://doi.org/10.1130/0016-7606(1971)82%255B2397:DAAOHB%255D2.0.CO;2

Condit, C. B., & Mahan, K. H. (2018). Fracturing, fluid flow and shear zone development: Relationships between chemical and mechanical processes in Proterozoic mafic dykes from southwestern Montana, USA. *Journal of Metamorphic Geology*, *36*(2), 195–223. https://doi.org/10.1111/jmg.12289

Connolly, J. a. D. (1990). Multivariable phase diagrams; an algorithm based on generalized thermodynamics. *American Journal of Science*, *290*(6), 666–718. https://doi.org/10.2475/ajs.290.6.666

Connolly, J. a. D., & Petrini, K. (2002). An automated strategy for calculation of phase diagram sections and retrieval of rock properties as a function of physical conditions. *Journal of Metamorphic Geology*, *20*(7), 697–708. https://doi.org/10.1046/j.1525-1314.2002.00398.x

Dragovic, B., Samanta, L. M., Baxter, E. F., & Selverstone, J. (2012). Using garnet to constrain the duration and rate of water-releasing metamorphic reactions during subduction: An example from Sifnos, Greece. *Chemical Geology*, *314–317*, 9–22. https://doi.org/10.1016/j.chemgeo.2012.04.016

Dragovic, B., Baxter, E. F., & Caddick, M. J. (2015). Pulsed dehydration and garnet growth during subduction revealed by zoned garnet geochronology and thermodynamic modeling, Sifnos, Greece. *Earth and Planetary Science Letters*, *413*, 111–122. https://doi.org/10.1016/j.epsl.2014.12.024

Duesterhoeft, E., Quinteros, J., Oberhänsli, R., Bousquet, R., & de Capitani, C. (2014). Relative impact of mantle densification and eclogitization of slabs on subduction dynamics: A numerical thermodynamic/thermokinematic investigation of metamorphic density evolution. *Tectonophysics*, *637*, 20–29. https://doi.org/10.1016/j.tecto.2014.09.009

Ellis, D. J., & Green, D. H. (1979). An experimental study of the effect of Ca upon garnet-clinopyroxene Fe-Mg exchange equilibria. *Contributions to Mineralogy and Petrology*, *71*(1), 13–22. https://doi.org/10.1007/BF00371878

Ernst, W. G. (1975). Systematics of large-scale tectonics and age progressions in Alpine and Circum-Pacific blueschist belts. *Tectonophysics*, *26*(3), 229–246. https://doi.org/10.1016/0040-1951(75)90092-X

Flansburg, M. E., Stockli, D. F., Poulaki, E. M., & Soukis, K. (2019). Tectono-magmatic and Stratigraphic Evolution of the Cycladic Basement, Ios Island, Greece. *Tectonics*, *38*(7), 2291–2316. https://doi.org/10.1029/2018TC005436

Fuhrman, M. L., & Lindsley, D. H. (1988). Ternary-feldspar modeling and thermometry. *American Mineralogist*, *73*(3–4), 201–215.

Govindaraju, K. (1994). 1994 Compilation of Working Values and Sample Description for 383 Geostandards. *Geostandards Newsletter*, *18*(S1), 1–158. https://doi.org/10.1046/j.1365-2494.1998.53202081.x-i1

Green, E., Holland, T., & Powell, R. (2007). An order-disorder model for omphacitic pyroxenes in the system jadeite-diopside-hedenbergite-acmite, with applications to eclogitic rocks. *American Mineralogist*, *92*(7), 1181–1189. https://doi.org/10.2138/am.2007.2401

Green, E. C. R., White, R. W., Diener, J. F. A., Powell, R., Holland, T. J. B., & Palin, R. M. (2016). Activity–composition relations for the calculation of partial melting equilibria in metabasic rocks. *Journal of Metamorphic Geology*, *34*(9), 845–869. https://doi.org/10.1111/jmg.12211

Groppo, C., Forster, M., Lister, G., & Compagnoni, R. (2009). Glaucophane schists and associated rocks from Sifnos (Cyclades, Greece): New constraints on the *P–T* evolution from oxidized systems. *Lithos*, *109*(3), 254–273. https://doi.org/10.1016/j.lithos.2008.10.005

Hacker, B. R. (2008). H2O subduction beyond arcs. *Geochemistry, Geophysics, Geosystems*, *9*(3). https://doi.org/10.1029/2007GC001707

Hacker, B. R., Abers, G. A., & Peacock, S. M. (2003). Subduction factory 1. Theoretical mineralogy, densities, seismic wave speeds, and H2O contents. *Journal of Geophysical Research: Solid Earth*, *108*(B1). https://doi.org/10.1029/2001JB001127

Heilbronner, R., & Barrett, S. (2014). Volume Determinations. In R. Heilbronner & S. Barrett (Eds.), *Image Analysis in Earth Sciences: Microstructures and Textures of Earth*

Materials (pp. 173–185). Berlin, Heidelberg: Springer. https://doi.org/10.1007/978-3-642-10343-8_10

van Hinsbergen, D. J. J., Hafkenscheid, E., Spakman, W., Meulenkamp, J. E., & Wortel, R. (2005). Nappe stacking resulting from subduction of oceanic and continental lithosphere below Greece. *Geology*, *33*(4), 325–328. https://doi.org/10.1130/G20878.1

Holland, T. J. B., & Powell, R. (1998). An internally consistent thermodynamic data set for phases of petrological interest. *Journal of Metamorphic Geology*, *16*(3), 309–343. https://doi.org/10.1111/j.1525-1314.1998.00140.x

Holland, T. J. B., & Powell, R. (2011). An improved and extended internally consistent thermodynamic dataset for phases of petrological interest, involving a new equation of state for solids. *Journal of Metamorphic Geology*, *29*(3), 333–383. https://doi.org/10.1111/j.1525-1314.2010.00923.x

Irvine, T. N., & Baragar, W. R. A. (1971). A Guide to the Chemical Classification of the Common Volcanic Rocks. *Canadian Journal of Earth Sciences*, *8*(5), 523–548.

Jaeckel, K., Bebout, G. E., & Angiboust, S. (2018). Deformation-enhanced fluid and mass transfer along Western and Central Alps paleo-subduction interfaces: Significance for carbon cycling models. *Geosphere*, *14*(6), 2355–2375. https://doi.org/10.1130/GES01587.1

Jolivet, L., & Brun, J.-P. (2010). Cenozoic geodynamic evolution of the Aegean. *International Journal of Earth Sciences*, *99*(1), 109–138. https://doi.org/10.1007/s00531-008-0366-4

van Keken, P. E., Hacker, B. R., Syracuse, E. M., & Abers, G. A. (2011). Subduction factory: 4. Depth-dependent flux of H2O from subducting slabs worldwide. *Journal of Geophysical Research: Solid Earth*, *116*(B1). https://doi.org/10.1029/2010JB007922

Keppler, R., Behrmann, J. H., & Stipp, M. (2017). Textures of eclogites and blueschists from Syros island, Greece: Inferences for elastic anisotropy of subducted oceanic crust. *Journal of Geophysical Research: Solid Earth*, *122*(7), 5306–5324. https://doi.org/10.1002/2017JB014181

Kim, J., & Jung, H. (2019). New Crystal Preferred Orientation of Amphibole Experimentally Found in Simple Shear. *Geophysical Research Letters*, *46*(22), 12996–13005. https://doi.org/10.1029/2019GL085189

Kleijbeuker, L. H., Amiri, H., Hamers, M. F., & Kotowski, A. J. (2025). Quantitative Microstructural Analysis of Exhumed Epidote-Amphibolites and Plate Interface Rheology in Warm Subduction Zones. *Geochemistry, Geophysics, Geosystems*, *26*(4), e2024GC011886. https://doi.org/10.1029/2024GC011886

Klemd, R., Bröcker, M., Hacker, B. R., Gao, J., Gans, P., & Wemmer, K. (2005). New Age Constraints on the Metamorphic Evolution of the High-Pressure/Low-Temperature Belt in the Western Tianshan Mountains, NW China. *The Journal of Geology*, *113*(2), 157–168. https://doi.org/10.1086/427666

Ko, B., & Jung, H. (2015). Crystal preferred orientation of an amphibole experimentally deformed by simple shear. *Nature Communications*, *6*(1), 6586. https://doi.org/10.1038/ncomms7586

Kotowski, A. J., & Behr, W. M. (2019). Length scales and types of heterogeneities along the deep subduction interface: Insights from exhumed rocks on Syros Island, Greece. *Geosphere*, *15*(4), 1038–1065. https://doi.org/10.1130/GES02037.1

Kotowski, A. J., Cisneros, M., Behr, W. M., Stockli, D. F., Soukis, K., Barnes, J. D., & Ortega-Arroyo, D. (2022). Subduction, Underplating, and Return Flow Recorded in the Cycladic Blueschist Unit Exposed on Syros, Greece. *Tectonics*, *41*(6), e2020TC006528. https://doi.org/10.1029/2020TC006528

Kuno, H. (1968). Differentiation of Basalt Magmas. In *Basalts: The Poldevart Treatise on Rocks of Basaltic Composition* (pp. 623–688). New York: Interscience Publishers.

Lamont, T. N., Searle, M. P., Gopon, P., Roberts, N. M. W., Wade, J., Palin, R. M., & Waters, D. J. (2020). The Cycladic Blueschist Unit on Tinos, Greece: Cold NE Subduction and SW Directed Extrusion of the Cycladic Continental Margin Under the Tsiknias Ophiolite. *Tectonics*, *39*(9), e2019TC005890. https://doi.org/10.1029/2019TC005890

Laurent, V., Lanari, P., Naïr, I., Augier, R., Lahfid, A., & Jolivet, L. (2018). Exhumation of eclogite and blueschist (Cyclades, Greece): Pressure–temperature evolution determined by thermobarometry and garnet equilibrium modelling. *Journal of Metamorphic Geology*, *36*(6), 769–798. https://doi.org/10.1111/jmg.12309

Lee, J., & Jung, H. (2021). Lattice-Preferred Orientation and Seismic Anisotropy of Minerals in Retrograded Eclogites from Xitieshan, Northwestern China, and Implications for Seismic Reflectance of Rocks in the Subduction Zone. *Minerals*, *11*(4), 380. https://doi.org/10.3390/min11040380

Lister, G. S., & Raouzaios, A. (1996). The tectonic significance of a porphyroblastic blueschist facies overprint during Alpine orogenesis: Sifnos, Aegean Sea, Greece. *Journal of Structural Geology*, *18*(12), 1417–1435. https://doi.org/10.1016/S0191-8141(96)00072-7

Mainprice, D., Bachmann, F., Hielscher, R., & Schaeben, H. (2015). Descriptive tools for the analysis of texture projects with large datasets using MTEX : strength, symmetry and components. *Geological Society, London, Special Publications*, *409*(1), 251–271. https://doi.org/10.1144/SP409.8

Manzotti, P., Schiavi, F., Ballèvre, M., & Nosenzo, F. (2025). Garnet growth across the quartz–coesite transition in metapelites: equilibrium vs. kinetics. *European Journal of Mineralogy*, *37*(4), 455–482. https://doi.org/10.5194/ejm-37-455-2025

Matsumoto, K., & Hirajima, T. (2005). The coexistence of jadeite and omphacite in an eclogite-facies metaquartz diorite from the southern Sesia Zone, Western Alps, Italy. *Journal of Mineralogical and Petrological Sciences*, *100*(2), 70–84. https://doi.org/10.2465/jmps.100.70

Matthews, A., & Schliestedt, M. (1984). Evolution of the blueschist and greenschist facies rocks of Sifnos, Cyclades, Greece. *Contributions to Mineralogy and Petrology*, *88*(1), 150–163. https://doi.org/10.1007/BF00371419

McNamara, D. D., Wheeler, J., Pearce, M., & Prior, D. J. (2012). Fabrics produced mimetically during static metamorphism in retrogressed eclogites from the Zermatt-Saas zone, Western Italian Alps. *Journal of Structural Geology*, *44*, 167–178. https://doi.org/10.1016/j.jsg.2012.08.006

Michibayashi, K., & Mainprice, D. (2004). The Role of Pre-existing Mechanical Anisotropy on Shear Zone Development within Oceanic Mantle Lithosphere: an Example from the Oman Ophiolite. *Journal of Petrology*, *45*(2), 405–414. https://doi.org/10.1093/petrology/egg099

Mocek, B. (2001). Geochemical evidence for arc-type volcanism in the Aegean Sea: the blueschist unit of Siphnos, Cyclades (Greece). *Lithos*, *57*(4), 263–289. https://doi.org/10.1016/S0024-4937(01)00043-3

Nowlan, E. U., Schertl, H.-P., & Schreyer, W. (2000). Garnet–omphacite–phengite thermobarometry of eclogites from the coesite-bearing unit of the southern Dora-Maira Massif, Western Alps. *Lithos*, *52*(1), 197–214. https://doi.org/10.1016/S0024-4937(99)00091-2

Okrusch, M., & Broecker, M. (1990). Eclogites associated with high-grade blueschists in the Cyclades archipelago, Greece; a review. *European Journal of Mineralogy*, *2*(4), 451–478.

Padrón-Navarta, J. A., Sánchez-Vizcaíno, V. L., Hermann, J., Connolly, J. A. D., Garrido, C. J., Gómez-Pugnaire, M. T., & Marchesi, C. (2013). Tschermak's substitution in antigorite and consequences for phase relations and water liberation in high-grade serpentinites. *Lithos*, *178*, 186–196. https://doi.org/10.1016/j.lithos.2013.02.001

Peacock, S. M. (1993). The importance of blueschist → eclogite dehydration reactions in subducting oceanic crust. *Geological Society of America Bulletin*, *105*(5), 684–694. https://doi.org/10.1130/0016-7606(1993)105%253C0684:TIOBED%253E2.3.CO;2

Peacock, S. M. (2004). Thermal Structure and Metamorphic Evolution of Subducting Slabs. In *Inside the Subduction Factory* (pp. 7–22). American Geophysical Union (AGU). https://doi.org/10.1029/138GM02

Pearce, J. (1979). Geochemical evidence for the genesis and eruptive setting of lavas from Tethyan ophiolites. *Proceedings of the International Ophiolite Symposium Ministry of Agriculture and Natural Resources Cyprus*, 261–272.

Poulaki, E. M., Stockli, D. F., Flansburg, M. E., & Soukis, K. (2019). Zircon U-Pb Chronostratigraphy and Provenance of the Cycladic Blueschist Unit and the Nature of the Contact With the Cycladic Basement on Sikinos and Ios Islands, Greece. *Tectonics*, *38*(10), 3586–3613. https://doi.org/10.1029/2018TC005403

Reichen, L. E., & Fahey, J. J. (1962). *An improved method for the determination of FeO in rocks and minerals including garnet* (No. 1144- B). *Bulletin*. U.S. G.P.O.,. https://doi.org/10.3133/b1144B

Ring, U., Will, T., Glodny, J., Kumerics, C., Gessner, K., Thomson, S., et al. (2007). Early exhumation of high-pressure rocks in extrusion wedges: Cycladic blueschist unit in the eastern Aegean, Greece, and Turkey. *Tectonics*, *26*(2). https://doi.org/10.1029/2005TC001872

Ring, U., Glodny, J., Will, T. M., & Thomson, S. (2011). Normal faulting on Sifnos and the South Cycladic Detachment System, Aegean Sea, Greece. *Journal of the Geological Society*, *168*(3), 751–768. https://doi.org/10.1144/0016-76492010-064

Roche, V., Laurent, V., Cardello, G. L., Jolivet, L., & Scaillet, S. (2016). Anatomy of the Cycladic Blueschist Unit on Sifnos Island (Cyclades, Greece). *Journal of Geodynamics*, *97*, 62–87. https://doi.org/10.1016/j.jog.2016.03.008

Roduit, N. (n.d.). JMicroVision: Image analysis toolbox for measuring and quantifying components of high-definition images. (Version 1.3.5). Retrieved from https://jmicrovision.github.io/

Romer, R. L., & Rötzler, J. (2003). Effect of metamorphic reaction history on the U-Pb dating of titanite. In D. Vance, W. Müller, & I. M. Villa (Eds.), *Geochronology: Linking the Isotopic Record with Petrology and Textures* (Vol. 220, p. 0). Geological Society of London. https://doi.org/10.1144/GSL.SP.2003.220.01.08

Schliestedt, M. (1986). Eclogite-Blueschist Relationships as Evidenced by Mineral Equilibria in the High-Pressure Metabasic Rocks of Sifnos (Cycladic Islands), Greece. *Journal of Petrology*, *27*(6), 1437–1459. https://doi.org/10.1093/petrology/27.6.1437

Schliestedt, M., & Matthews, A. (1987). Transformation of blueschist to greenschist facies rocks as a consequence of fluid infiltration, Sifnos (Cyclades), Greece. *Contributions to Mineralogy and Petrology*, *97*(2), 237–250. https://doi.org/10.1007/BF00371243

Schliestedt, M., Altherr, R., & Matthews, A. (1987). Evolution of the Cycladic Crystalline Complex: Petrology, Isotope Geochemistry and Geochronolgy (pp. 389–428). https://doi.org/10.1007/978-94-009-4013-0_15

Schmädicke, E., & Will, T. M. (2003). Pressure–temperature evolution of blueschist facies rocks from Sifnos, Greece, and implications for the exhumation of high-pressure rocks in the Central Aegean. *Journal of Metamorphic Geology*, *21*(8), 799–811. https://doi.org/10.1046/j.1525-1314.2003.00482.x

Schneider, C. A., Rasband, W. S., & Eliceiri, K. W. (2012). NIH Image to ImageJ: 25 years of image analysis. *Nature Methods*, *9*(7), 671–675. https://doi.org/10.1038/nmeth.2089

Smye, A. J., & England, P. C. (2023). Metamorphism and Deformation on Subduction Interfaces: 2. Petrological and Tectonic Implications. *Geochemistry, Geophysics, Geosystems*, *24*(1), e2022GC010645. https://doi.org/10.1029/2022GC010645

Soret, M., Précigout, J., Stünitz, H., Raimbourg, H., Plümper, O., Osselin, F., et al. (2025). Deep crustal deformation driven by reaction-induced weakening. *Nature Communications*, *16*(1), 6407. https://doi.org/10.1038/s41467-025-60692-7

Spear, F. S., Wark, D. A., Cheney, J. T., Schumacher, J. C., & Watson, E. B. (2006). Zr-in-rutile thermometry in blueschists from Sifnos, Greece. *Contributions to Mineralogy and Petrology*, *152*(3), 375–385. https://doi.org/10.1007/s00410-006-0113-4

Spear, F. S., Wolfe, O. M., Thomas, J. B., Hubbard, J. E., Castro, A. E., & Cheney, J. T. (2024). P–T Evolution of the Cyclades Blueschist Unit: Constraints on the Evolution of a Nascent Subduction System From Zr-In-Rutile (ZiR) and Quartz-In-Garnet (QuiG) Thermobarometry. *Geochemistry, Geophysics, Geosystems*, *25*(4), e2023GC011121. https://doi.org/10.1029/2023GC011121

Stern, R. J. (2002). Subduction zones. *Reviews of Geophysics*, *40*(4). https://doi.org/10.1029/2001RG000108

van der Straaten, F., Schenk, V., John, T., & Gao, J. (2008). Blueschist-facies rehydration of eclogites (Tian Shan, NW-China): Implications for fluid–rock interaction in the subduction channel. *Chemical Geology*, *255*(1), 195–219. https://doi.org/10.1016/j.chemgeo.2008.06.037

Tinkham, D. K., & Ghent, E. D. (2005). ESTIMATING P-T CONDITIONS OF GARNET GROWTH WITH ISOCHEMICAL PHASE-DIAGRAM SECTIONS AND THE PROBLEM OF EFFECTIVE BULK-COMPOSITION. *The Canadian Mineralogist*, *43*(1), 35–50. https://doi.org/10.2113/gscanmin.43.1.35

Trotet, F., Jolivet, L., & Vidal, O. (2001). Tectono-metamorphic evolution of Syros and Sifnos islands (Cyclades, Greece). *Tectonophysics*, *338*(2), 179–206. https://doi.org/10.1016/S0040-1951(01)00138-X

Tsujimori, T., Liou, J. G., & Coleman, R. G. (2005). Coexisting retrograde jadeite and omphacite in a jadeite-bearing lawsonite eclogite from the Motagua Fault Zone, Guatemala. *American Mineralogist*, *90*(5–6), 836–842. https://doi.org/10.2138/am.2005.1699

Viti, C., Collettini, C., Tesei, T., Tarling, M. S., & Smith, S. A. F. (2018). Deformation Processes, Textural Evolution and Weakening in Retrograde Serpentinites. *Minerals*, *8*(6), 241. https://doi.org/10.3390/min8060241

Walters, J. B., & Gies, N. B. (2025). MinPlotX: A powerful tool for formula recalculation, visualization, and comparison of large mineral compositional datasets. *Mineralogia*, *56*(1), 13–22. https://doi.org/10.2478/mipo-2025-0003

Wang, Y., Zhang, L.-F., Li, Z.-H., Li, Q.-Y., & Bader, T. (2019). The Exhumation of Subducted Oceanic-Derived Eclogites: Insights From Phase Equilibrium and Thermomechanical Modeling. *Tectonics*, *38*(5), 1764–1797. https://doi.org/10.1029/2018TC005349

White, R. W., Powell, R., & Clarke, G. L. (2002). The interpretation of reaction textures in Fe-rich metapelitic granulites of the Musgrave Block, central Australia: constraints from mineral equilibria calculations in the system K2O–FeO–MgO–Al2O3–SiO2–H2O–TiO2–Fe2O3. *Journal of Metamorphic Geology*, *20*(1), 41–55. https://doi.org/10.1046/j.0263-4929.2001.00349.x

White, R. W., Powell, R., Holland, T. J. B., Johnson, T. E., & Green, E. C. R. (2014). New mineral activity–composition relations for thermodynamic calculations in metapelitic systems. *Journal of Metamorphic Geology*, *32*(3), 261–286. https://doi.org/10.1111/jmg.12071

Whitney, D. L., & Evans, B. W. (2010). Abbreviations for names of rock-forming minerals. *American Mineralogist*, *95*(1), 185–187. https://doi.org/10.2138/am.2010.3371

Whitney, Donna L., Teyssier, C., Seaton, N. C. A., & Fornash, K. F. (2014). Petrofabrics of high-pressure rocks exhumed at the slab-mantle interface from the “point of no return” in a subduction zone (Sivrihisar, Turkey). *Tectonics*, *33*(12), 2315–2341. https://doi.org/10.1002/2014TC003677

Yonkee, W. A., Parry, W. T., & Bruhn, R. L. (2003). Relations between progressive deformation and fluid-rock interaction during shear-zone growth in a basement-cored thrust sheet, Sevier orogenic belt, Utah. *American Journal of Science*, *303*(1), 1–59. https://doi.org/10.2475/ajs.303.1.1

Zlatkin, O., Avigad, D., & Gerdes, A. (2018). New Detrital Zircon Geochronology From the Cycladic Basement (Greece): Implications for the Paleozoic Accretion of Peri-Gondwanan Terranes to Laurussia. *Tectonics*, *37*(12), 4679–4699. https://doi.org/10.1029/2018TC005046

Zuluaga, C. A., Stowell, H. H., & Tinkham, D. K. (2005). The effect of zoned garnet on metapelite pseudosection topology and calculated metamorphic P-T paths. *American Mineralogist*, *90*(10), 1619–1628. https://doi.org/10.2138/am.2005.1741

Chapter 6: Conclusions and Future Work

The principle of uniformitarianism, first developed by James Hutton and popularized by Charles Lyell, proposes that the processes we observe in the Earth system today have also been active in shaping the Earth through its history. In this context, exhumed subduction terranes are a lodestar that guides subduction-zone scientists in unravelling the dynamics of active subduction zones and their role in plate tectonics. This thesis addressed outstanding questions about mafic blueschists, a high-pressure/low-temperature lithology central to the chemical and mechanical behavior of the ductilely-deforming subduction interface. By applying modern, cutting edge techniques, including electron backscatter diffraction (EBSD)-based microstructural analyses and petrological modeling of phase equilibria to the ancient archives of exhumed subduction zone rocks, this work provides novel insights into the rheological and metamorphic evolution of blueschists during subduction and exhumation. This chapter summarizes these key findings and outlines promising directions for future research.

Mafic blueschists are a common lithology along the subduction interface from the base of the seismogenic zone to the sub-arc depths (~>30-90km), yet this important lithology cannot be studied in situ within active subduction margins. By constraining the range of seismic anisotropy for a suite of lawsonite- and epidote-blueschists from a globally expansive inventory of blueschists exhumed from a wide range of peak P-T conditions, this work offers a refined tool to improve seismic imaging of subsurface structure in active subduction zones. Blueschists generate substantial P-wave anisotropy (AVp), with magnitudes up to ~20% that display a strong positive correlation with the modal abundance of glaucophane and the strength of the crystallographic preferred orientation (CPO) of the phase produced by deformation. The deformation-induced alignment of glaucophane is linked to not only the magnitude of predicted anisotropy, but the CPO-type of the sodic amphibole is correlated with the Vp pattern of fast- and slow-P-wave propagation directions, influencing the character of the seismic-anisotropy pattern. These results highlight the importance of the ubiquitous amphibole in the anisotropic signal generated by mafic blueschists. While shear wave splitting delay times up to ~0.1 s are not substantial and may not prove useful for imaging the subsurface of subduction zones, receiver function analysis provides an alternative approach to improve seismic imaging of blueschists at the subduction interface. Blueschists commonly display AVp values ~10%, and the subset of seven samples in this investigation that generate anisotropies of this magnitude represent a tractable path for future investigations of the extent of mafic blueschists at the subduction interface. The Voigt-Reuss-Hill-averaged elastic stiffness matrices for the blueschists in this study can be integrated into synthetic receiver function models as blueschist layers to map the extent of blueschist along the subduction interface. Furthermore, the reduction in AVp magnitudes associated with eclogitization signals the potential for determining the depth of the blueschist-eclogite transition in active subduction zones.

The central role of glaucophane deformation in the seismic anisotropy motivated a detailed microstructural investigation of the deformation mechanisms active at the pressure-temperature conditions relevant to the base of the seismogenic zone. Specifically, I wanted to understand how these CPOs actually form, and what mechanisms they record. In a novel method combining weighted Burgers vector analysis with misorientation-based mother-daughter inheritance analysis on glaucophane in a lawsonite blueschist that equilibrated at ~300°C and 1.0 GPa in the Catalina Schist, dislocation creep was demonstrated to be an important deformation mechanism in the subducting slab downdip of the transition from seismic to aseismic deformation. Dislocation creep is governed by a power-law constitutive relationship, with the implication that the subduction interface downdip of the seismogenic zone is a highly stress-sensitive environment. The deformation of mafic blueschist in the subducting slab is likely a key contributor to plate coupling behavior and observed convergence velocities in subduction zones—an implication that directly motivated the experimental work to derive a flow law for dislocation creep in glaucophane.

To quantify the relationship between stress and strain rate in blueschists deformed by dislocation creep, a suite of deformation experiments were conducted on glaucophane aggregates prepared from a metabasic blueschist host rock from Sifnos Island, Greece. Constant displacement rate, load-stepping, and temperature-stepping experiments were conducted in a Griggs-type apparatus to constrain the stress exponent (n = 5.3), activation energy (Q = 392 kJ mol-1), and pre-exponential factor (A = 160 MPa-5.3 s-1) parameters in a flow law for dislocation creep for glaucophane (blueschist). The experimentally constrained flow law was extrapolated to natural conditions for the subduction interface along with flow laws for related subduction zone lithologies and deformation mechanisms. Key findings from this study are the prediction that aseismic, viscous deformation in the subducting slab is initiated by dislocation creep in glaucophane ~350°C and transitions to grain-size-sensitive mechanisms at higher temperatures, finer grain sizes, and elevated pore-fluid pressures. Furthermore, predictions of blueschist strength align with field observations that suggest blueschist is weaker than eclogite and stronger than serpentinite—yet predict a substantially greater rheological strength relative to quartz-bearing (metasedimentary) lithologies. The rheological models in this study highlight a critical discrepancy between stress estimates of tens of MPa at the creeping region of the subduction interface based on field observations and the predictions of monomineralic flow laws, which are orders of magnitude higher (~1 GPa). Future studies that integrate polyphase rheology, fluid behavior, and field constraints to account for the chemical and mechanical effects of phase mixing, grain- and phase-boundary sliding, fluid-mediated mechanisms, and the interplay between these mechanisms in real, polyphase rocks are required to predict the state of stress and deformation more accurately along the subduction interface in active subduction zones.

The importance of the interaction between deformation mechanisms and fluid flow in subduction zone lithologies were explored further in the example of an exhumed blueschist-eclogite transition at Vroulidia Beach on Sifnos Island, Greece. Previous work on Sifnos interpreted the exposed lithologies of the Eclogite-Blueschist Complex as representative of peak P-T conditions during subduction based on evidence for blueschist and eclogite petrogenesis from protoliths of tholeiitic and calc-alkaline composition, respectively. Through an interdisciplinary approach combining optical petrography, bulk- and mineral-scale geochemical analyses, and phase equilibrium modeling, the results of the investigation yield an alternative hypothesis for the petrogenesis of the studied blueschist-eclogite transition on Sifnos. I propose the transition is the expression of limited prograde deformation during subduction that established fluid pathways that consequently promoted selective retrogression of and localized deformation into blueschists during exhumation. The interplay between deformation, fluid-localization, and retrograde metamorphism produced the observed field relationship of deformed retrograde blueschist domains intercalated with preserved, weakly-deformed eclogites from near-peak P-T conditions. This work demonstrates the potential for nuanced metamorphic histories within the context of larger coherent terranes and the importance of standardizing the practice of interdisciplinary studies that combine detailed microstructural and petrological methodologies as the bedrock that underlies the interpretation that blueschist-eclogite rocks are representative of specific portions of subduction P-T paths.

Collectively, the chapters of this dissertation provide first order constraints on the geophysical signatures, deformation mechanisms, and rheology of the sodic amphibole glaucophane and, by extension, mafic blueschist at the subduction interface. This work has demonstrated that glaucophane plays a central role in deformation along the subduction interface, and may govern viscous creep in the subducting slab in cold, mature, subduction zones. By pairing field- and microstructural-based evidence for dislocation creep with one of the first experimentally derived flow laws for this amphibole, this dissertation quantifies the behavior of blueschist in stress and strain space and predict how temperature, grain size, and pore-fluid pressure influence the transition between grain-size-sensitive and grain-size-insensitive creep—providing a framework for incorporating blueschist into geodynamic and rheological models of subduction. Moreover, the new constraints on blueschist seismic anisotropy and reconstruction of blueschist-eclogite metamorphic pathways in exhumed HP/LT terranes highlight the power of interdisciplinary approaches for interpreting the deep structure of active margins and the preserved histories of exhumed subduction complexes, respectively. Taken together, these investigations advance our first-order understanding of the rheology, deformation, and geophysical fingerprints of blueschists—laying a foundation for future efforts to bridge micro-scale observations with macro-scale processes and dynamics in subduction zones.

Appendices

Appendix 1. Supporting Information for Chapter 2: Seismic Anisotropy of Mafic Blueschists: EBSD-based constraints from the exhumed rock record

Jason N. Ott[1], Cailey B. Condit[1], Vera Schulte-Pelkum[2], Rachel Bernard[3], and Matej Pec[4]

[1]Department of Earth and Space Sciences, University of Washington, Seattle, WA, USA

[2]Cooperative Institute for Research in Environmental Sciences and Department of Geological Sciences, University of Colorado, Boulder, CO, USA

[3]Geology Department, Amherst College, Amherst, MA, USA

[4]Department of Earth, Atmospheric and Planetary Sciences, Massachusetts Institute of Technology, Cambridge, MA, USA

Contents of this file

Figures S1 to S8, Tables S1, S2

Introduction

Figure S1 displays photomicrographs of regions of the sample thin sections sized to illustrate the mineralogy and textures that contain the target representative regions selected for EBSD data collection and analysis. Measurements of fabric strength as pole figures of the CPOs in glaucophane, epidote, lawsonite, and phengite are presented for the full set of indexed orientations in Fig. S2, and as 1 point per grain based on the mean orientation of each grain in Fig. S3 for all samples included in this study. A representative subset of the range of CPOs of samples are included in the main text as Fig. 5. Figure S4 includes the full set of calculated seismic properties for all samples in this study including Vp, Vs_1, and Vs_2 velocities, anisotropies, velocity ratios, and Vs polarizations. Discussion in the text is primarily related to Vp anisotropy (AVp), but all seismic properties are included in Fig. S4 for completeness. Figure S5 displays a ternary plot of the hexagonal, orthorhombic, and tetragonal+monoclinic+triclinic components of the Voigt elastic stiffness matrices after conducting a symmetry decomposition analysis and subtracting the isotropic components of the elastic stiffness matrices. Figure S6 displays the AVp %, AVs_1 %, AVs_2 %, and max AVs % (shear wave splitting percentage) of all samples in order of increasing AVp %. Stereographic projections of Vp and AVp % for 2-phase rock recipe models of all samples are included in Fig. S7. A representative example of an epidote blueschist and a lawsonite blueschist were included in the text (Figs. 9a-b) and the full set of models were used as the basis for Fig. 9c-e. The calculated seismic anisotropies of all samples as AVp, AVs (max shear wave splitting), AVs_1, and AVs_2 are plotted in Fig. S8 as a function of pressure, temperature, and temperature/pressure from the estimates in the literature (Table 1) to investigate the data for trends in the magnitude of anisotropy and metamorphic grade.

Relative error and error % of the modal abundances calculated from the areal EBSD maps relative to the number of grains indexed per phase (after method of Heilbronner and Barrett, 2014) are presented in Table S1. Table S2 includes all texture measurements for glaucophane, epidote, lawsonite, and phengite, measured as 1 point per grain and from full EBSD dataset (uploaded as a separate file). Table S3 includes the results of the symmetry decomposition analysis (after Browaeys and Chevrot, 2004) of the Voigt elastic stiffness matrices into the isotropic, hexagonal, orthorhombic, and other lower symmetries (tetragonal + monoclinic + triclinic symmetry). These data were used as the basis for Fig S5.

All stereographic projections and texture measurements in the supplementary material were produced with the MTEX 5.7.0 toolbox for MATLAB (Mainprice et al., 2011).

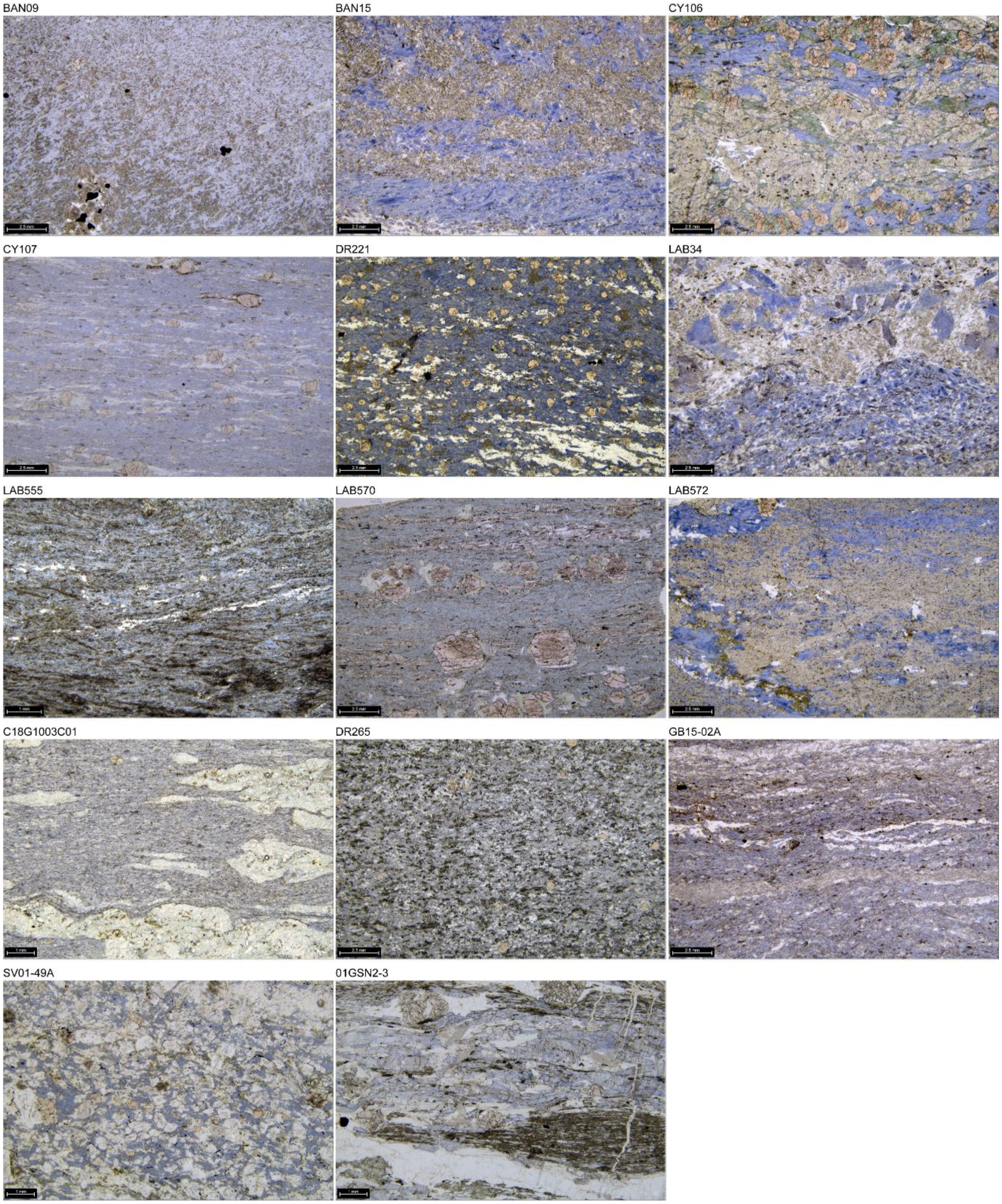

Figure S1. Photomicrographs of regions of the thin sections displaying the mineralogy and textures of the samples included in the anisotropy study. Selected target regions over which EBSD data were collected is contained within each photomicrograph.

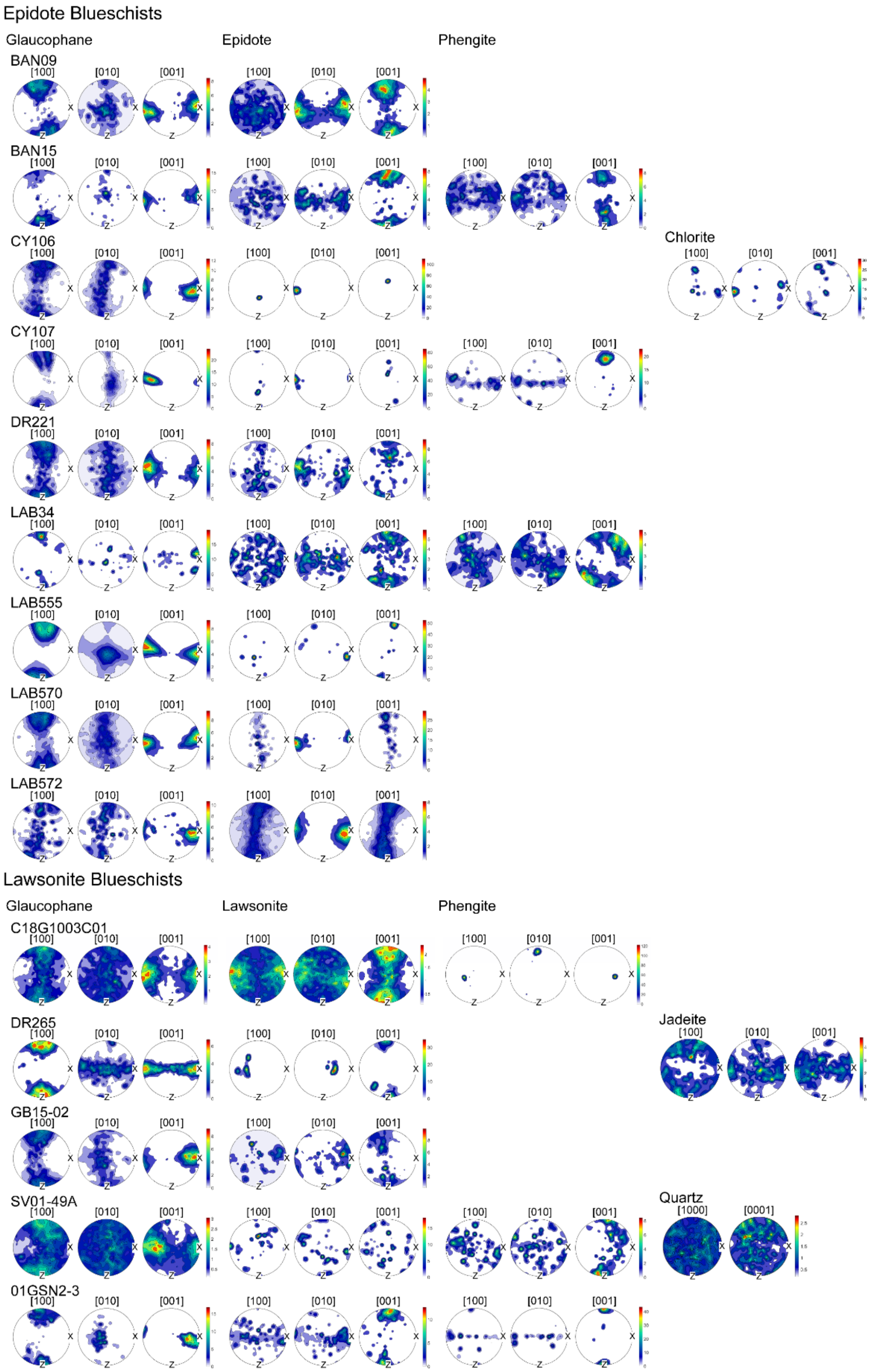

Figure S2. CPO measured as the full set of EBSD-indexed orientations for the crystallographic axes of the major anisotropic phases for all samples in this study.

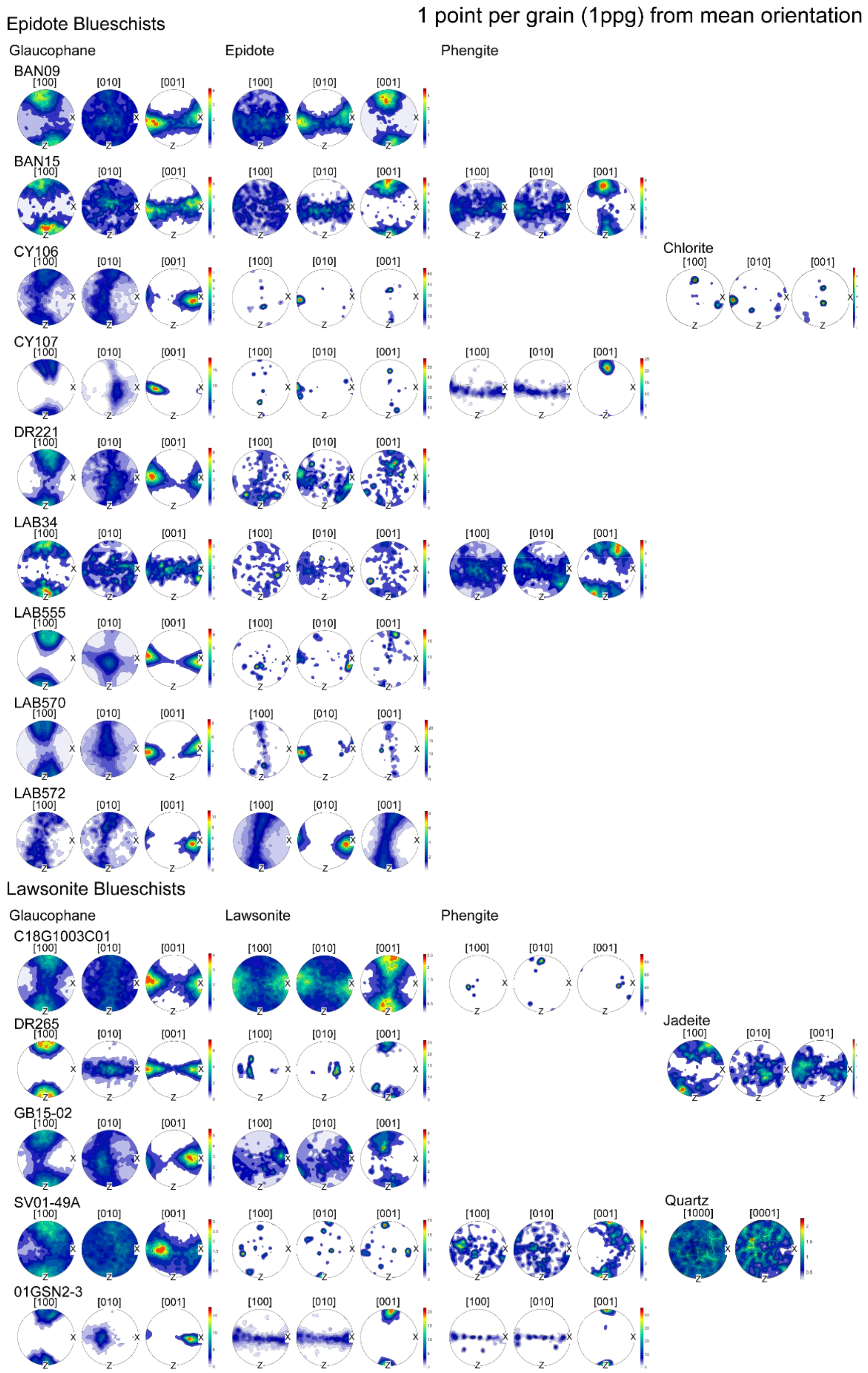

Figure S3. CPO measured as one point-per-grain using the mean grain orientation (1ppg) for the crystallographic axes of the major anisotropic phases for all samples in this study.

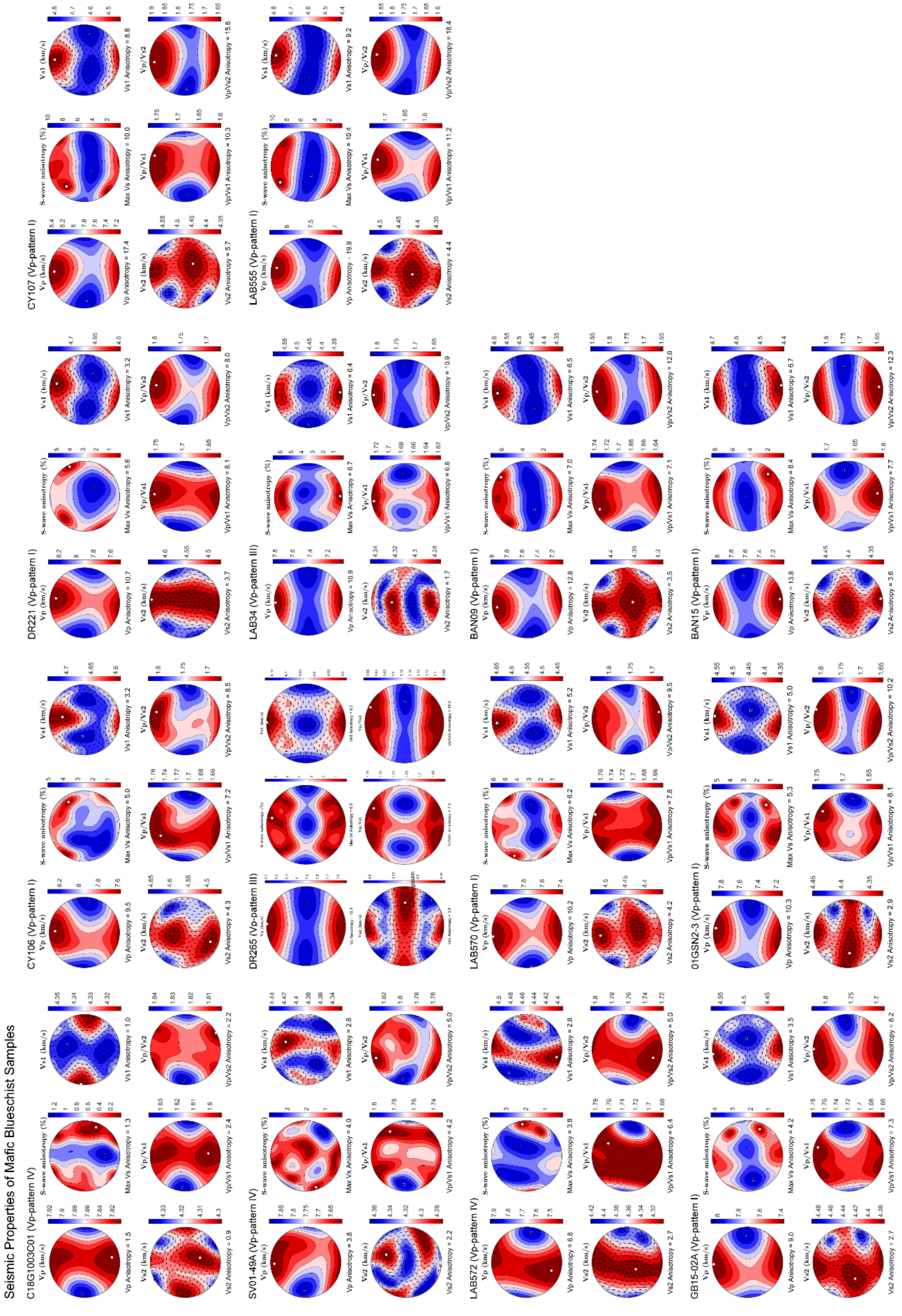

Figure S4. Calculated seismic properties, including Vp, Vs_1, and Vs_2 velocities and polarizations, anisotropies, and velocity ratios.

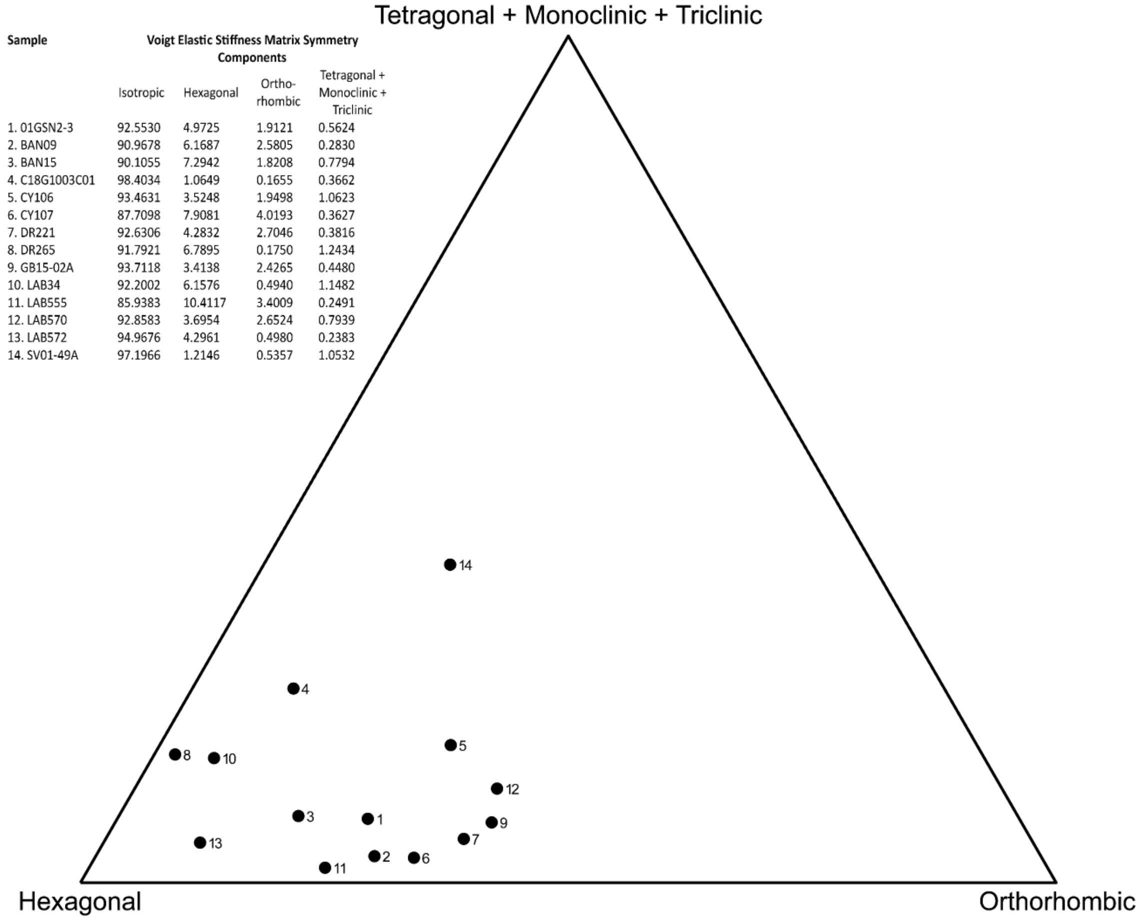

Sample	Voigt Elastic Stiffness Matrix Symmetry Components			
	Isotropic	Hexagonal	Ortho-rhombic	Tetragonal + Monoclinic + Triclinic
1. 01GSN2-3	92.5530	4.9725	1.9121	0.5624
2. BAN09	90.9678	6.1687	2.5805	0.2830
3. BAN15	90.1055	7.2942	1.8208	0.7794
4. C18G1003C01	98.4034	1.0649	0.1655	0.3662
5. CY106	93.4631	3.5248	1.9498	1.0623
6. CY107	87.7098	7.9081	4.0193	0.3627
7. DR221	92.6306	4.2832	2.7046	0.3816
8. DR265	91.7921	6.7895	0.1750	1.2434
9. GB15-02A	93.7118	3.4138	2.4265	0.4480
10. LAB34	92.2002	6.1576	0.4940	1.1482
11. LAB555	85.9383	10.4117	3.4009	0.2491
12. LAB570	92.8583	3.6954	2.6524	0.7939
13. LAB572	94.9676	4.2961	0.4980	0.2383
14. SV01-49A	97.1966	1.2146	0.5357	1.0532

Figure S5. Symmetry decomposition of the Voigt elastic stiffness matrices (after Browaeys and Chevrot, 2004) displayed on a ternary diagram after subtracting out the isotropic component of the symmetry. This visualization shows the extent to which each sample's elastic stiffness matrix can be represented by hexagonal, orthorhombic, or other (tetragonal + monoclinic + triclinic) symmetry classes.

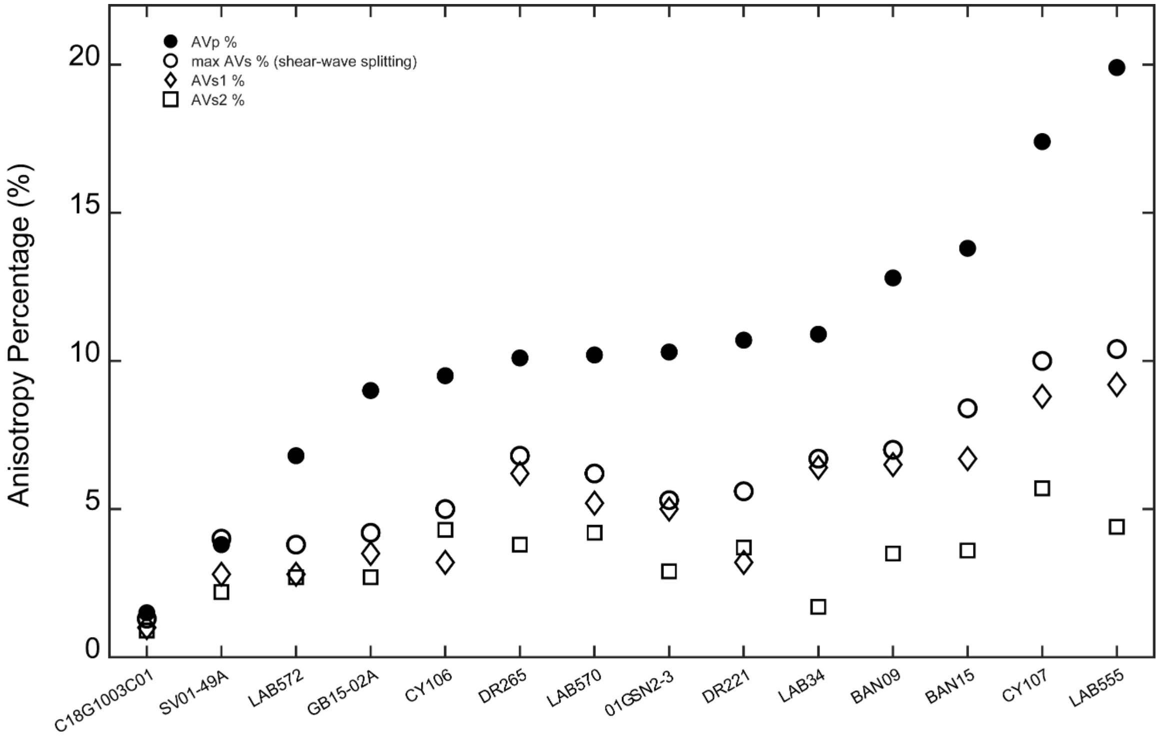

Figure S6. The calculated seismic anisotropies of each sample as the AVp %, max AVs % (max shear wave splitting percentage), and anisotropy of the fast shear wave,AVs_1, and slow shear wave AVs_2. The horizontal axis is ordered from left to right by increasing AVp % of samples.

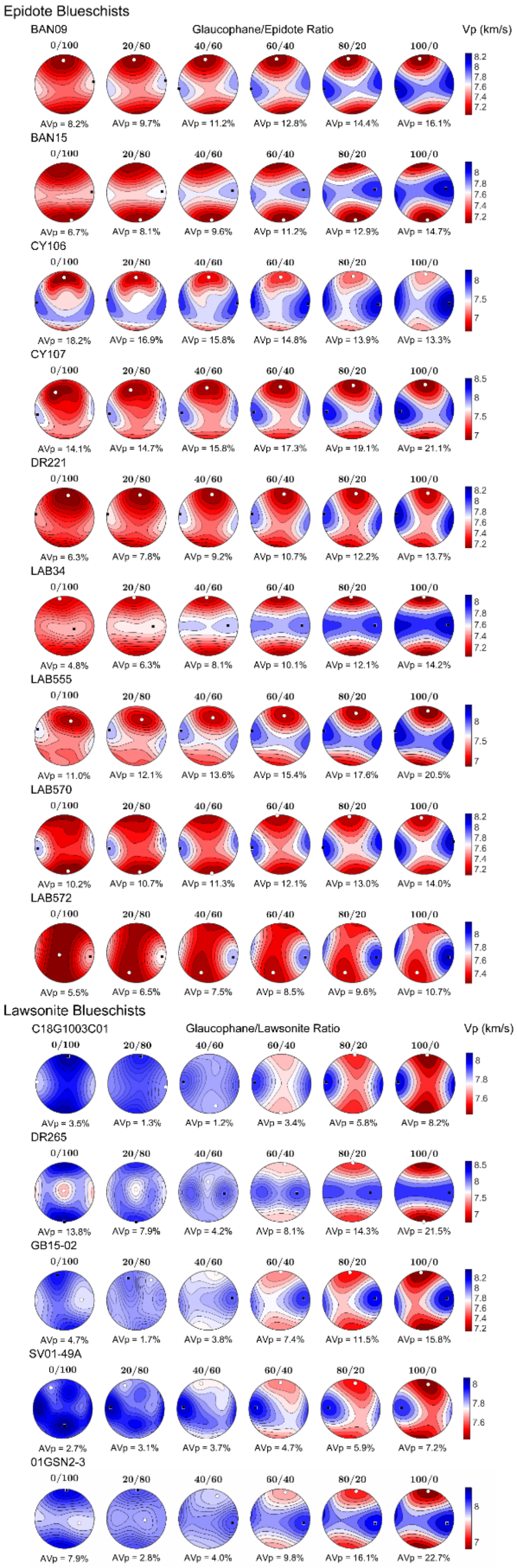

Figure S7. Equal-area upper hemisphere stereographic projections of P-wave velocities (in km/s) and AVp % for the range of gln/ep ratios for epidote blueschists and the range of gln/lws ratios for lawsonite blueschists for all 2-phase rock recipe models

Seismic anisotropy shown for P-waves (AVp %), shear-wave splitting (AVs %), S_1-waves (AVs1 %), and S_2-waves (AVs2 %) with respect to estimates of peak pressure, temperature, and temperature/pressure for exhumed subduction terranes from the literature. Length of horizontal bars represent the max/min estimates of P, T or T/P in each case. Blue bars are lawsonite blueschists, olive-green bars are epidote blueschists.

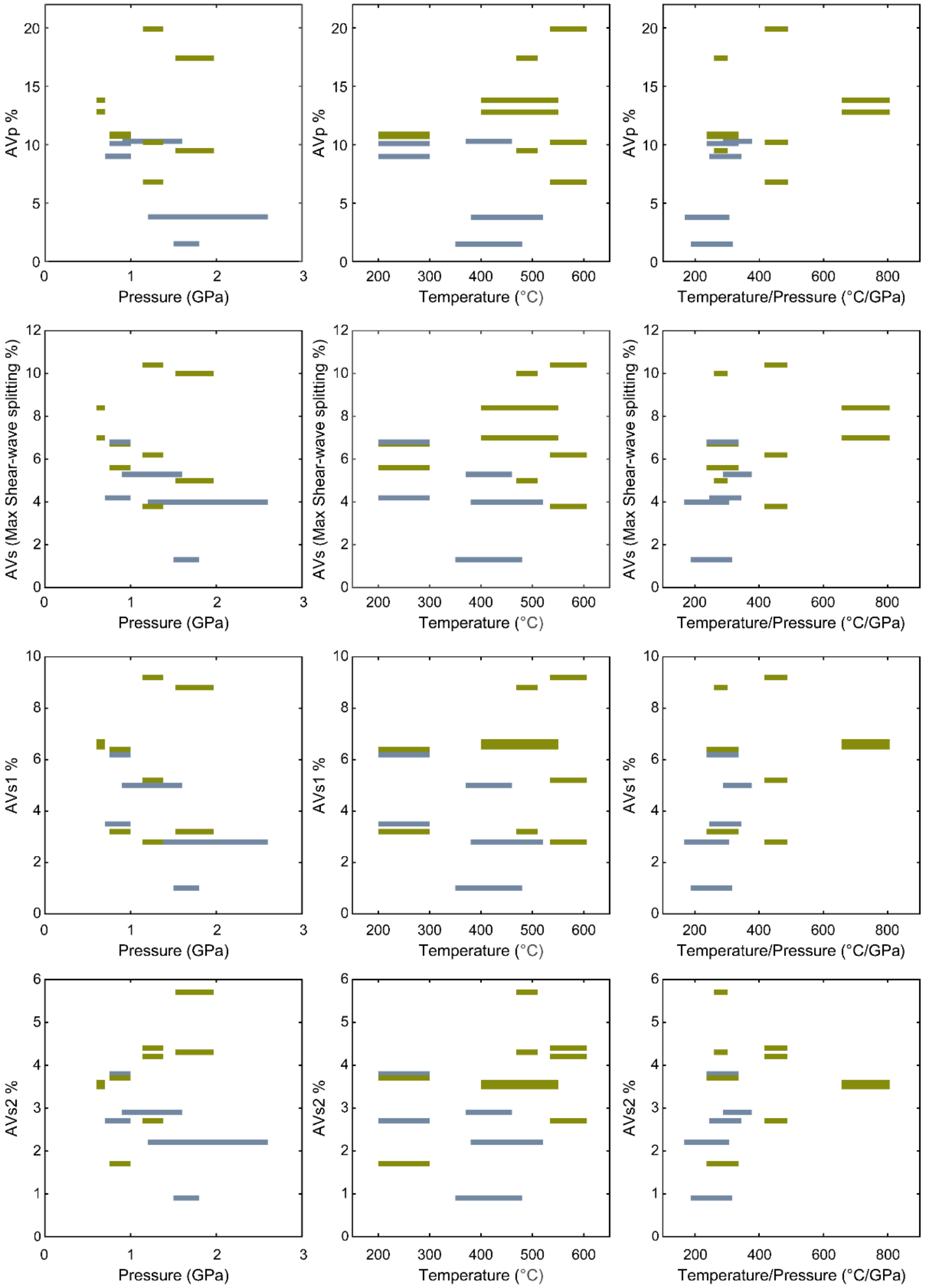

Figure S8. Magnitude of the calculated anisotropy in AVp, AVs (max shear wave splitting), AVs_1, and AVs_2 as a function of pressure, temperature, and temperature/pressure based on estimates from the literature (Table 1). Lawsonite blueschist shown as blue bars, and epidote blueschist shown as olive-green bars.

Table S1. Relative error and error % of the modal abundances calculated from the areal EBSD maps relative to the number of grains indexed per phase after method of Heilbronner and Barrett, 2014.

Table S1: Relative error of modal abundances

Relative Error = 1/sqrt(N) with N=number of grains of phase in map   % error = (Rel. Err.)*(Modal %)   (Heilbronner & Barrett, 2014)

Mineral abbreviations after Whitney & Evans, 2010

	01GSN2-3					**CY106**					**GB15-02A**					**LAB572**			
	Modal %	# Grains	Rel. error	% error		Modal %	# Grains	Rel. error	% error		Modal %	# Grains	Rel. error	% error		Modal %	# Grains	Rel. error	% error
Gln	45.74	1869	0.0231	1.06	Gln	58.89	5414	0.0136	0.80	Gln	61.56	6509	0.0124	0.76	Gln	36.94	1445	0.0263	0.97
Ep	0.03	23	0.2085	0.01	Ep	11.29	1260	0.0282	0.32	Ep					Ep	55.39	12807	0.0088	0.49
Lws	18.7	1208	0.0288	0.54	Lws					Lws	20.64	2889	0.0186	0.38	Lws				
Ph	4.04	855	0.0342	0.14	Ph	0.78	289	0.0588	0.05	Ph	0.56	451	0.0471	0.03	Ph	0.91	106	0.0971	0.09
Grt	3.13	28	0.1890	0.59	Grt	14.48	71	0.1187	1.72	Grt	4.46	463	0.0465	0.21	Grt	1.77	9	0.3333	0.59
Jd	3.17	1060	0.0307	0.10	Jd					Jd					Jd	3.27	210	0.0690	0.23
Omp	0.12	54	0.1361	0.02	Omp	4.64	924	0.0329	0.15	Omp	0.01	10	0.3162	0.00	Omp	0.06	39	0.1601	0.01
Qz	24.83	1550	0.0254	0.63	Qz	1.32	295	0.0582	0.08	Qz	12.74	3328	0.0173	0.22	Qz	0.29	128	0.0884	0.03
Chl	0.04	14	0.2673	0.01	Chl	7.68	2179	0.0214	0.16	Chl					Chl	0.05	17	0.2425	0.01
Rt	0.21	58	0.1313	0.03	Rt	0.93	287	0.0590	0.05	Rt	0.02	34	0.1715	0.00	Rt	1.32	493	0.0450	0.06

	BAN09					**CY107**					**LAB34**					**SV01-49A**			
	Modal %	# Grains	Rel. error	% error		Modal %	# Grains	Rel. error	% error		Modal %	# Grains	Rel. error	% error		Modal %	# Grains	Rel. error	% error
Gln	60.86	6097	0.0128	0.78	Gln	77.87	5473	0.0135	1.05	Gln	62.18	875	0.0338	2.10	Gln	41.61	7913	0.0112	0.47
Ep	38.1	3351	0.0173	0.66	Ep	0.28	48	0.1443	0.04	Ep	28.89	762	0.0362	1.05	Ep				
Lws					Lws					Lws					Lws	42.91	523	0.0437	1.88
Ph	0.01	6	0.4082	0.00	Ph	8.57	1488	0.0259	0.22	Ph	8.12	2810	0.0189	0.15	Ph	1.51	280	0.0598	0.09
Grt	0.31	3	0.5774	0.18	Grt	11.93	11	0.3015	3.60	Grt	0.49	18	0.2357	0.12	Grt	0.85	18	0.2357	0.20
Jd	0.01	9	0.3333	0.00	Jd					Jd					Jd	2.69	265	0.0614	0.17
Omp					Omp	0.12	15	0.2582	0.03	Omp	0.02	7	0.3780	0.01	Omp	0.08	21	0.2182	0.02
Qz	0.71	320	0.0559	0.04	Qz	0.51	88	0.1066	0.05	Qz					Qz	9.89	2198	0.0213	0.21
Chl					Chl	0.69	200	0.0707	0.05	Chl	0.14	47	0.1459	0.02	Chl	0.21	50	0.1414	0.03
Rt					Rt	0.04	17	0.2425	0.01	Rt	0.15	64	0.1250	0.02	Rt	0.22	50	0.1414	0.03

	BAN15					**DR221**					**LAB555**			
	Modal %	# Grains	Rel. error	% error		Modal %	# Grains	Rel. error	% error		Modal %	# Grains	Rel. error	% error
Gln	85.78	1679	0.0244	2.09	Gln	81.6	3634	0.0166	1.35	Gln	95.75	50782	0.0044	0.42
Ep	10.35	848	0.0343	0.36	Ep	5.59	561	0.0422	0.24	Ep	0.58	180	0.0745	0.04
Lws					Lws					Lws				
Ph	3.8	1872	0.0231	0.09	Ph	0.28	84	0.1091	0.03	Ph	0.08	90	0.1054	0.01
Grt					Grt	11.91	60	0.1291	1.54	Grt				
Jd					Jd					Jd	0.08	94	0.1031	0.01
Omp					Omp					Omp	0.1	106	0.0971	0.01
Qz					Qz	0.08	19	0.2294	0.02	Qz	3.07	537	0.0432	0.13
Chl					Chl	0.13	58	0.1313	0.02	Chl	0.28	438	0.0478	0.01
Rt	0.07	41	0.1562	0.01	Rt	0.41	54	0.1361	0.06	Rt	0.06	33	0.1741	0.01

	C18G1003C01					**DR265**					**LAB570**			
	Modal %	# Grains	Rel. error	% error		Modal %	# Grains	Rel. error	% error		Modal %	# Grains	Rel. error	% error
Gln	43.02	6036	0.0129	0.55	Gln	64.22	3697	0.0164	1.06	Gln	54.65	10160	0.0099	0.54
Ep				0.00	Ep	0.07	44	0.1508	0.01	Ep	32.63	417	0.0490	1.60
Lws	56.26	7542	0.0115	0.65	Lws	18.84	241	0.0644	1.21	Lws				
Ph	0.03	7	0.3780	0.01	Ph	0.68	213	0.0685	0.05	Ph	0.2	110	0.0953	0.02
Grt	0.28	8	0.3536	0.10	Grt	0.77	4	0.5000	0.39	Grt	9.33	5	0.4472	4.17
Jd	0.31	65	0.1240	0.04	Jd	14.9	1238	0.0284	0.42	Jd				
Omp	0.05	14	0.2673	0.01	Omp	0.1	49	0.1429	0.01	Omp				
Qz	0.01	1	1.0000	0.01	Qz	0.41	180	0.0745	0.03	Qz	2.34	243	0.0642	0.15
Chl	0.04	12	0.2887	0.01	Chl					Chl	0.29	171	0.0765	0.02
Rt					Rt					Rt	0.56	176	0.0754	0.04

Table S2: Symmetry Decomposition of Voigt Elastic Stiffness Matrices

After Browaeys and Chevrot (2004)

Sample	Voigt Elastic Stiffness Matrix Symmetry Components (%)			
	Isotropic	Hexagonal	Ortho-rhombic	Tetragonal + Monoclinic + Triclinic
1. 01GSN2-3	92.5530	4.9725	1.9121	0.5624
2. BAN09	90.9678	6.1687	2.5805	0.2830
3. BAN15	90.1055	7.2942	1.8208	0.7794
4. C18G1003C01	98.4034	1.0649	0.1655	0.3662
5. CY106	93.4631	3.5248	1.9498	1.0623
6. CY107	87.7098	7.9081	4.0193	0.3627
7. DR221	92.6306	4.2832	2.7046	0.3816
8. DR265	91.7921	6.7895	0.1750	1.2434
9. GB15-02A	93.7118	3.4138	2.4265	0.4480
10. LAB34	92.2002	6.1576	0.4940	1.1482
11. LAB555	85.9383	10.4117	3.4009	0.2491
12. LAB570	92.8583	3.6954	2.6524	0.7939
13. LAB572	94.9676	4.2961	0.4980	0.2383
14. SV01-49A	97.1966	1.2146	0.5357	1.0532

Table S2. Symmetry decomposition of the Voigt elastic stiffness matrix into the representation of the isotropic, hexagonal, orthorhombic, and other lower symmetries (tetragonal + monoclinic + triclinic). After the method of Browaeys and Chevrot (2004).

Appendix 2. Supporting Information for Chapter 3: Dislocation creep of glaucophane in mafic blueschists during subduction: weighted Burgers vector analysis from the Catalina Schist

Supplements:

I. METHODS AND MATERIALS

A. Sample Preparation and Petrography

The garnet blueschist block is a deformed polymetamorphic metabasaltic lawsonite blueschist emplaced within the mélange of the lawsonite blueschist unit of the Catalina Schist subduction complex (Bebout and Barton, 1993; Penniston-Dorland and Harvey, 2023; Platt and Schmidt, 2024) located at 33°22’N 118°28’W on Pimu’nga (Santa Catalina Island, CA, USA; Fig. S1). A structurally oriented thin section was prepared from the sample, cut perpendicular to the foliation and parallel to the lineation, such that the X-Z plane is contained in the plane of the thin section. The mineral assemblage of the sample as determined by optical petrography and EBSD data analysis is glaucophane (55%) + lawsonite (15%) + phengite (<10%) + garnet (5%) + quartz (10%) + titanite (<5%). The hand sample displays and foliation and lineation, and the foliation in the thin section is defined by a shape preferred orientation and layer segregation of glaucophane, lawsonite, and phengite (Fig. S2). Glaucophane and lawsonite grains are frequently elongated up to ~1 mm in length (Fig. S2A). Garnet occurs within glaucophane-rich layers as hypidiomorphic to allotriomorphic grains up to ~500 µm in diameter, and as small (<50 µm) idiomorphic to hypidiomorphic inclusions in glaucophane porphyroblasts (Figs. S2B). Titanite appears in the matrix (up to ~200 µm) and as small (<50 µm) inclusions in glaucophane and lawsonite porphyroblasts (Figs. S2B,C). Glaucophane and lawsonite are in textural equilibrium (Figs. S2A,C), suggesting that much of the glaucophane growth occurred while the sample was at lawsonite blueschist facies conditions (based on the abundance of lawsonite and the presence of titanite inclusions in both lawsonite and glaucophane grains). Some lawsonite grains in a quartz-rich region of the sample show erosion of tabular lawsonite grains by quartz, suggesting lawsonite may have been reacting out late during the GB block’s subduction history (Fig. S2D). Glaucophane commonly shows evidence of intragranular deformation including undulatory extinction (Fig. S2E,F) and subgrain structures (Fig. S2F), and core-mantle structures with fine-grained mantles most frequently clustered at the tips of elongated grains (Fig. S2).

B. Petrological modelling

Phase diagrams were constructed using Perple_X 6.6.6 (Connolly and Petrini, 2002) and the thermodynamic database of Holland and Powell (2011; hp62ver) with the components SiO_2-TiO_2-Al_2O_3-FeO-Fe_2O_3-MgO-CaO-Na_2O-K_2O assuming H_2O-saturated conditions. The pure phases ilmenite (ilm; ilm_nol), margarite (ma), and andradite (andr) were excluded in consideration of the requirements for solution models that were implemented. The following solid solution models were included: feldspar (Fuhrman and Lindsley, 1988), olivine (Holland and Powell, 1998), spinel (White et al., 2002), omphacite (Green et al., 2007), carpholite and sudoite (Massonne and Willner, 2008), epidote (Holland and Powell, 2011), antigorite (Padrón-Navarta et al., 2013), biotite, chlorite, chloritoid, ilmenite, garnet, mica, and orthopyroxene (White et al., 2014), and clinoamphibole (Green et al., 2016). Brucite, stilpnomelane, and pumpellyite were treated as ideal solid solutions. The P-T model was constructed for the garnet blueschist block bulk composition (in weight %) of SiO_2 (50.11), TiO_2 (1.766), Al_2O_3 (14.55), FeO (10.46), Fe_2O_3 (2.21), MgO (5.16), CaO (5.10), Na_2O (3.94%), and K_2O (1.63) as reported by Awalt (2013).

C. EBSD methods

Data collection

EBSD data were collected using a ThermoFisher-Scientific Apreo variable-pressure scanning electron microscope (SEM) with an Oxford Instruments Symmetry 2 EBSD detector at the University of Washington Molecular Analysis Facility. The thin section was polished for 2 hours with a Bruker Vibromet 2 vibratory polisher using a 0.06 µm-diameter amorphous colloidal silica suspension. The sample was coated in a 5 nm layer of carbon and mounted to a stage with a fixed 70° tilt. EBSD data was collected using a 20 kV accelerating voltage and 32 nA current at a working distance of 13 mm.

The base EBSD map was collected over a 3.1 mm by 3.8 mm representative region of the sample using a step size of 3.6 µm and an exposure time of 20 ms. The base EBSD map was used for the major microstructural analysis including phase percentages, crystallographic preferred orientation (CPO), shape preferred orientation (SPO), kernel average misorientation (KAM), misorientation distribution analyses, and textural measurements (pfJ-index; Michibayashi and Mainprice, 2004). The weighted Burgers vector (WBV) and inheritance (mother-daughter) analyses were conducted on higher resolution maps collected on selected 500 µm by 350 µm regions using a step size of 1 µm. The EBSD (Kikuchi) patterns were indexed using the Oxford HKL database (for quartz) and the American Mineralogist database (all other phases) packaged with Oxford's AZtec software.

EBSD data reduction and microstructural analysis

Orientation analysis and grain reconstruction using EBSD (Fig. 1) quantifies deformation preserved in Gln at the intra- and inter-granular scales through characterization of SPO and CPO (e.g., Prior et al., 1999). All EBSD data reduction and analysis were conducted with the MTEX 5.10.0 toolbox for MATLAB (Bachmann et al., 2010; Mainprice et al., 2011). Low confidence data with a mean angular deviation greater than 1° were removed from the crystallographic reference dataset were removed. Grain reconstruction was performed with a low-angle (subgrain) boundary threshold of ≥ 2° and a high-angle (grain boundary) threshold of 10° (Figs. 1A,C). Grains with fewer than three measurements were filtered from the dataset. CPO is plotted as equal-area upper-hemisphere pole figures represented by one-point-per-grain using the mean orientation of each grain. Pole figure contours are multiples of uniform distribution (m.u.d.) and all pole figures contours are scaled equally (Fig. 1B). The textural strength was calculated as the pole-figure J-index (pfJ-index) after Michibayashi and Mainprice (2004) as

$$pfJ_{hkl} = \int P_{hkl}(\alpha,\beta)^2 d\omega$$

with *hkl* as the Miller index of the crystallographic axis, the spherical coordinates of an orientation is (α,β), $P_{hkl}(\alpha,\beta)$ is the fraction of all measured orientations of a crystallographic axis with a given orientation, and $d\omega$ is the element of differentiation. The pfJ-index ranges from 1 for a random (untextured) CPO to infinity for a single-crystal orientation. The SPO is displayed as a polar plot histogram of the longest axis of the glaucophane grains, weighted by grain area (Fig. 1D). The random and neighboring grain pair misorientation distributions were calculated from the orientation distribution function fit to the set of glaucophane grain mean orientations using an 8° half-width (Fig. 1E).

D. Weighted Burgers vector (WBV) analysis

A full description of the theoretical basis and mathematical formulation of weighted Burgers vector analysis and its application to geological investigations is included in the work of Wheeler et al. (2024). In this work we apply WBV analysis to full EBSD maps (Fig. 2; Figs. S4,6-12) using the differential method to image geometrically necessary dislocations and subgrain boundaries, and illustrate trends in WBV direction over full EBSD maps. These trends are compared to WBV directions calculated by applying the integral WBV method to individual segments of subgrain boundaries (Fig. 2). WBV calculations were conducted using the implementation included in the MTEX 5.10.0 toolbox for MATLAB (Bachmann et al., 2010; Mainprice et al., 2011) with stencil and tile sizes of 9 pixels for the differential and integral methods respectively (see section 2 of Wheeler et al., 2024). Calculated WBVs were filtered using a minimum threshold of twice the typical assumed orientation error for EBSD data (0.02 radians) to minimize WBV errors (section 2.4.1 of Wheeler et al., 2024) and inverse pole figures are plotted using the calcDensity function of MTEX weighted by the length of the WBVs to minimize the effect of low dislocation densities, which may also be error prone, on observed trends in the WBV. As noted in earlier studies, EBSD of a 2D map area does not yield the full Nye dislocation tensor, but also cannot contain “phantom directions”, thus, WBV analysis provides a minimum constraint on the geometrically necessary dislocations present in the sample (Wheeler et al., 2009, 2024; Chauve et al., 2017).

The WBV does not decompose the calculated vectors into components representing individual dislocation types, and our analysis does not make assumptions about the dislocation types present to attempt decomposition of the WBVs into individual slip systems. We observed WBVs of subgrain boundary segments frequently lie on the great circle connecting the slip vector of multiple slip systems that have been observed in glaucophane using transmission electron microscopy (e.g., Reynard et al., 1989), implying contributions from multiple slip systems (Fig. 2).

II. SUPPLEMENTAL FIGURES

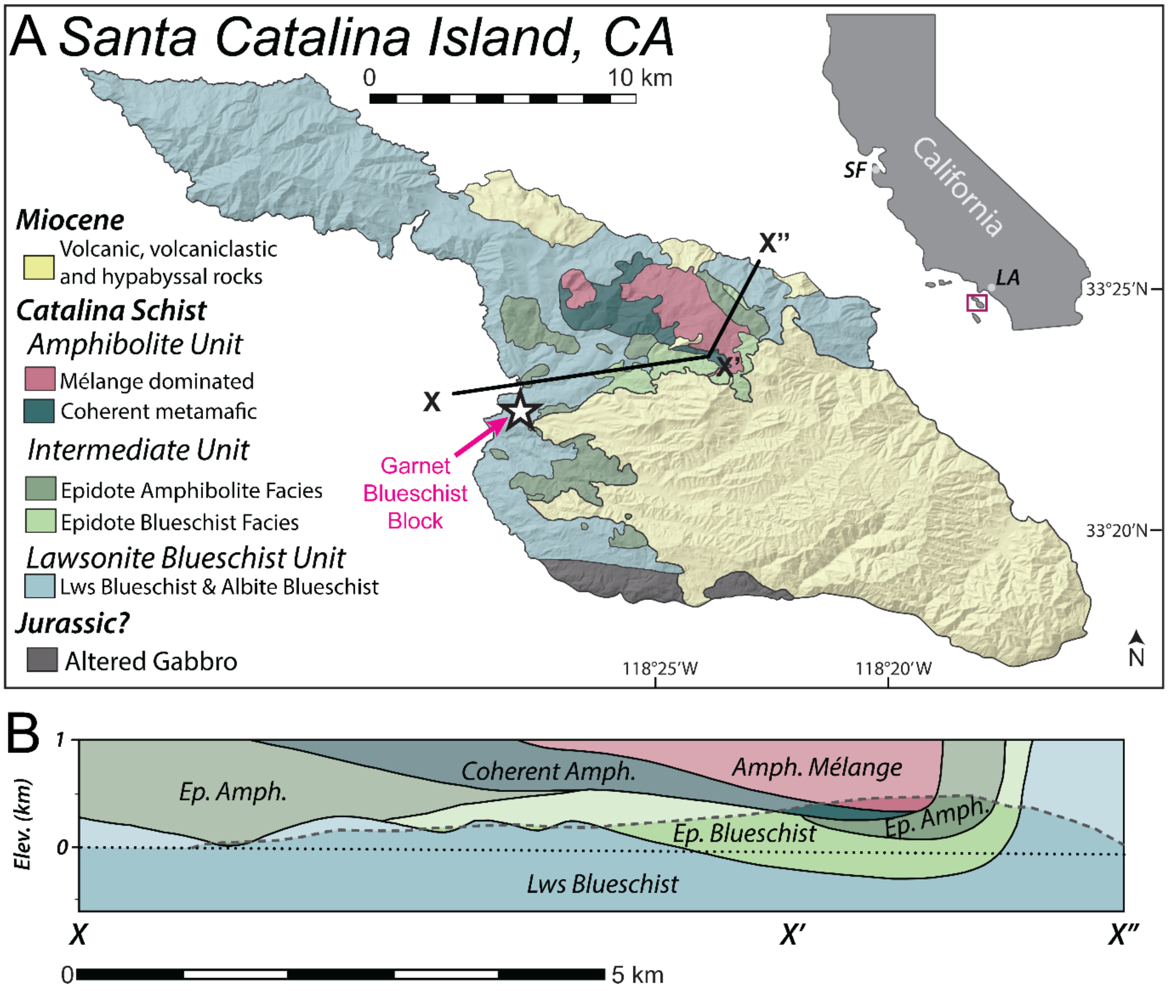

Fig. S1. (A) Geologic map of the lithotectonic units of the Catalina Schist based on Platt and Schmidt (2024) illustrating the structural relationships of the units that crop out. Location of the garnet blueschist block (33°22'N 118°28'W) is marked with a white star. **(B)** X–X'–X" cross section reconstruction of the subsurface contacts between the structural units. Mélange zones are described in all lithotectonic units of the Catalina Schist (Bebout and Barton, 1993; Penniston-Dorland and Harvey, 2023).

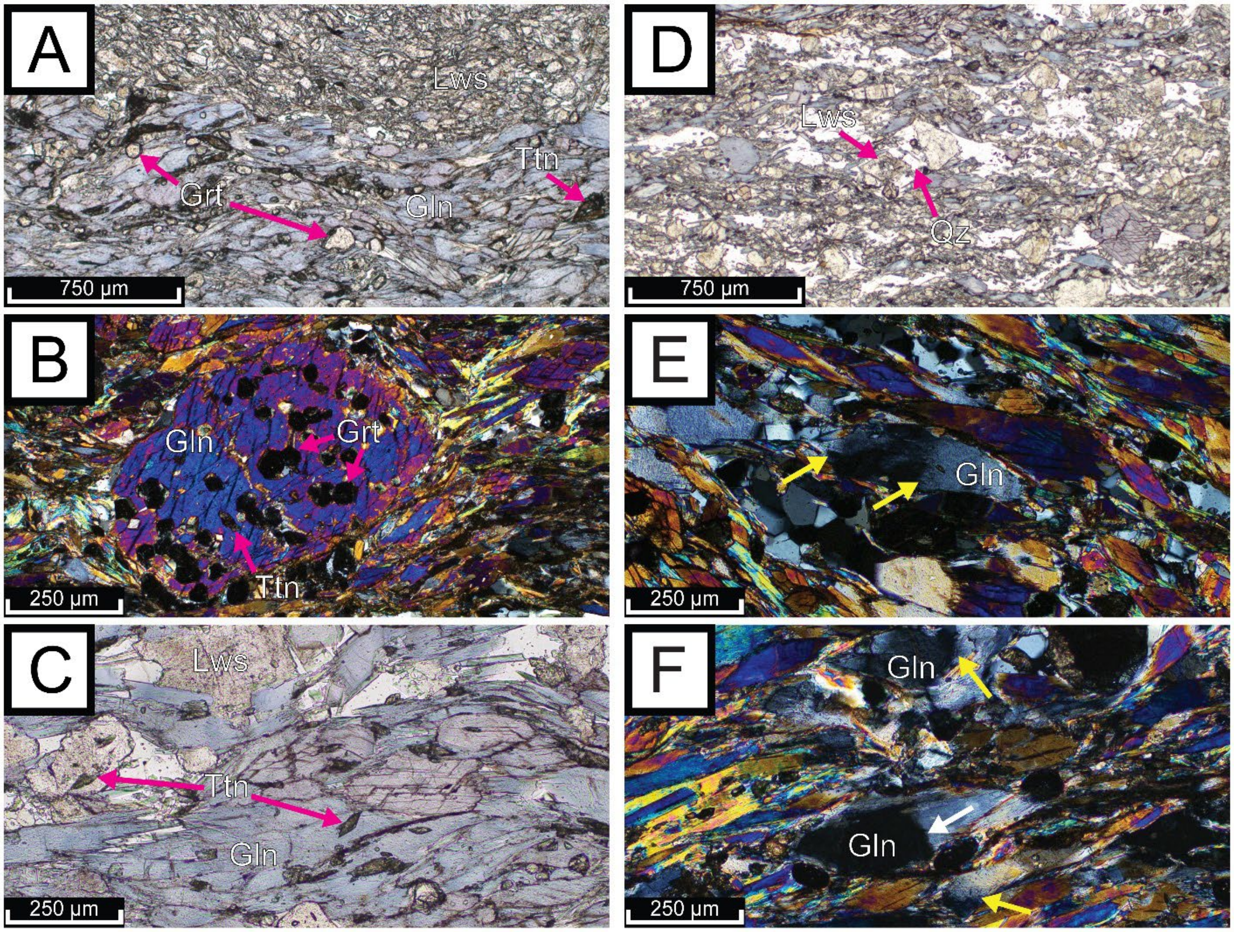

Fig. S2. (A) Boundary between glaucophane- and lawsonite-rich domains shows abundant hypidiomorphic and allotriomorphic garnets, and titanite in the matrix. Small platelets of phengite appear interstitially in the lawsonite-domain. **(B)** A glaucophane porphyroblast containing many small (<50 µm), idiomorphic garnet and allotriomorphic titanite inclusions. **(C)** Glaucophane and lawsonite in textural equilibrium. Both phases frequently contain titanite inclusions. **(D)** Lawsonite grains in quartz-rich region of sample showing erosion of tabular lawsonite grains by quartz. **(E)** XPL image of undulatory extinction in glaucophane grain (yellow arrows). **(F)** XPL image of subgrain boundary (white arrow) and undulatory extinction (yellow arrows) in glaucophane.

Fig. S3. (A) Pseudosection model of garnet blueschist block from composition reported in methods: petrological modelling (section I.B.) and **(B)** modal abundances of clinoamphibole (glaucophane), omphacite, lawsonite, garnet, titanite, and rutile extracted from Perple_X model on 2D grid from 0.5-2.0 GPa and 200-700°C. Pseudosection model and modal abundances were used to construct Fig. 4A in main text. Mineral abbreviations after Whitney and Evans (2010).

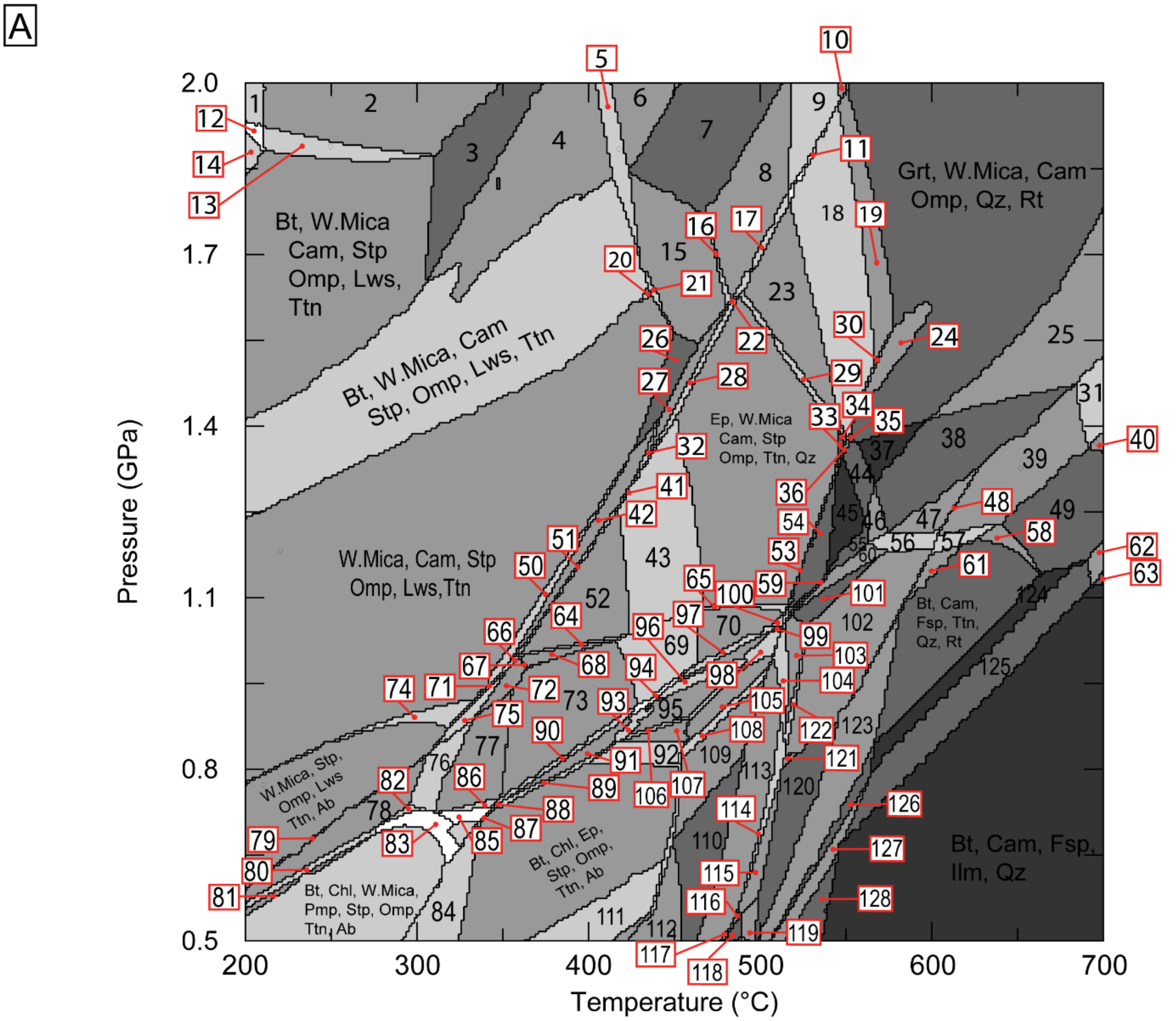

1. Bt, Chl, W.Mica, Cam, Stp, Lws, Ttn, Rt
2. Bt, W.Mica, Cam, Stp, Lws, Ttn, Rt
3. Bt, W.Mica, Cam, Stp, Lws, Ttn
4. Bt, W.Mica, Cam, Stp, Omp, Lws, Ttn
5. Bt, W.Mica, Cam, Stp, Omp, Lws, Ttn, Rt
6. Bt, W.Mica, Cam, Stp, Omp, Lws, Rt
7. W.Mica, Cam, Stp, Omp, Lws, Rt
8. W.Mica, Cam, Stp, Omp, Lws, Qz, Rt
9. Grt, W.Mica, Cam, Stp, Omp, Lws, Qz, Rt
10. Grt, W.Mica, Cam, Omp, Lws, Qz, Rt
11. Ep, Grt, W.Mica, Cam, Stp, Omp, Lws, Qz, Rt
12. Bt, Chl, W.Mica, Cam, Stp, Omp, Lws, Ttn, Rt
13. Bt, W.Mica, Cam, Stp, Omp, Lws, Ttn, Rt
14. Bt, Chl, W.Mica, Cam, Stp, Omp, Lws, Ttn
15. W.Mica, Cam, Stp, Omp, Lws, Ttn, Rt
16. W.Mica, Cam, Stp, Omp, Lws, Ttn, Qz, Rt
17. Ep, W.Mica, Cam, Stp, Omp, Lws, Qz, Rt
18. Ep, Grt, W.Mica, Cam, Stp, Omp, Qz, Rt
19. Ep, Grt, W.Mica, Cam, Omp, Qz, Rt
20. Chl, W.Mica, Cam, Stp, Omp, Omp, Lws, Ttn
21. W.Mica, Cam, Stp, Omp, Omp, Lws, Ttn, Rt
22. Ep, W.Mica, Cam, Stp, Omp, Lws, Ttn, Qz, Rt
23. Ep, W.Mica, Cam, Stp, Omp, Qz, Rt
24. Grt, W.Mica, Cam, Cam, Omp, Qz, Rt
25. Bt, Grt, W.Mica, Cam, Omp, Qz, Rt
26. W.Mica, Cam, Stp, Omp, Lws, Ttn
27. Ep, W.Mica, Cam, Stp, Omp, Lws, Ttn
28. Ep, W.Mica, Cam, Stp, Omp, Lws, Ttn, Qz
29. Ep, W.Mica, Cam, Stp, Omp, Ttn, Qz, Rt
30. Ep, Grt, W.Mica, Cam, Omp, Qz, Rt
31. Bt, Grt, W.Mica, Cam, Fsp, Omp, Qz, Rt
32. Ep, W.Mica, Cam, Stp, Omp, Lws, Ttn
33. Ep, W.Mica, Cam, Stp, Ttn, Qz
34. Ep, W.Mica, Cam, Stp, Ttn, QZ, Rt
35. Ep, Grt, W.Mica, Cam, Omp, Ttn, Qz, Rt
36. Ep, W.Mica, Cam, Omp, Ttn, Qz, Rt
37. W.Mica, Cam, Omp, Qz, Rt
38. Bt, W.Mica, Cam, Omp, Qz, Rt
39. Bt, W.Mica, Cam, Fsp, Omp, Qz, Rt
40. Bt, Grt, Cam, Fsp, Omp, Qz, Rt
41. Ep, W.Mica, Cam, Stp, Omp, Lws, Ttn, Qz
42. W.Mica, Cam, Stp, Omp, Lws, Ttn
43. Ep, W.Mica, Cam, Stp, Omp, Ttn, Qz
44. W.Mica, Cam, Omp, Ttn, Qz, Rt
45. W.Mica, Cam, Omp, Ttn, Qz
46. Bt, W.Mica, Cam, Omp, Ttn, Qz, Rt
47. Bt, W.Mica, Cam, Omp, Ab, Qz, Rt
48. Bt, W.Mica, Cam, Fsp, Omp, Ab, Qz, Rt
49. Bt, Cam, Fsp, Omp, Qz, Rt
50. W.Mica, Cam, Stp, Omp, Lws, Ttn
51. W.Mica, Cam, Stp, Omp, Lws, Ttn, Qz
52. W.Mica, Cam, Stp, Omp, Ttn, Qz
53. W.Mica, Cam, Stp, Omp, Ttn, Qz
54. W.Mica, Cam, Omp, Ttn, Qz
55. Bt, W.Mica, Cam, Omp, Ttn, Qz
56. Bt, W.Mica, Cam, Omp, Ttn, Ab, Qz, Rt
57. Bt, W.Mica, Cam, Fsp, Omp, Ttn, Qz, Rt
58. Bt, Cam, Fsp, Omp, Ttn, Qz, Rt
59. Bt, W.Mica, Cam, Omp, Ttn, Qz
60. Bt, W.Mica, Cam, Omp, Ttn, Ab, Qz
61. Bt, W.Mica, Cam, Fsp, Ttn, Qz, Rt
62. Bt, Cam, Fsp, Ilm, Omp, Qz, Rt
63. Bt, Cam, Fsp, Ilm, Omp, Qz
64. W.Mica, Cam, Stp, Omp, Ttn, Ab, Qz
65. Ep, W.Mica, Cam, Stp, Omp, Ttn, Ab, Qz
66. W.Mica, Cam, Stp, Omp, Lws, Ttn, Ab
67. W.Mica, Stp, Omp, Lws, Ttn, Ab, Qz
68. W.Mica, Stp, Omp, Ttn, Ab, Qz
69. Ep, W.Mica, Cam, Stp, Omp, Ttn, Ab
70. Ep, W.Mica, Cam, Stp, Omp, Ttn, Ab
71. W.Mica, Cam, Stp, Omp, Omp, Lws, Ttn, Ab
72. W.Mica, Stp, Omp, Lws, Ttn, Ab
73. Ep, W.Mica, Stp, Omp, Ttn, Ab
74. W.Mica, Cam, Stp, Omp, Lws, Ttn, Ab
75. W.Mica, Stp, Omp, Lws, Ttn, Ab
76. W.Mica, Pmp, Stp, Omp, Ttn, Ab
77. W.Mica, Pmp, Stp, Omp, Ttn, Ab
78. W.Mica, Pmp, Stp, Omp, Ttn, Ab
79. W.Mica, Pmp, Stp, Omp, Lws, Ttn, Ab
80. Bt, W.Mica, Pmp, Stp, Omp, Omp, Ttn, Ab
81. Bt, W.Mica, Pmp, Stp, Omp, Ttn, Ab
82. Chl, W.Mica, Pmp, Stp, Omp, Ttn, Ab
83. Bt, Chl, W.Mica, Pmp, Stp, Omp, Ttn, Ab
84. Bt, Chl, Ep, Pmp, Stp, Omp, Ttn, Ab

85. Bt, Chl, W.Mica, Pmp, Stp, Omp, Ttn, Ab
86. Bt, W.Mica, Pmp, Stp, Omp, Ttn, Ab
87. Bt, Chl, Ep, W.Mica, Stp, Omp, Ttn, Ab
88. Bt, Chl, Ep, W.Mica, Stp, Omp, Ttn, Ab
89. Bt, Chl, Ep, W.Mica, Stp, Omp, Ttn, Ab
90. Bt, Ep, W.Mica, Stp, Omp, Ttn, Ab
91. Bt, Ep, W.Mica, Stp, Omp, Ttn, Ab
92. Bt, Chl, Ep, Cam, Stp, Omp, Ttn, Ab
93. Bt, Ep, W.Mica, Cam, Stp, Omp, Ttn, Ab
94. Bt, Ep, W.Mica, Cam, Stp, Omp, Ttn, Ab
95. Bt, Ep, W.Mica, Cam, Stp, Ttn, Ab
96. Bt, Ep, W.Mica, Cam, Stp, Ttn, Ab
97. Bt, Ep, W.Mica, Cam, Stp, Omp, Ttn, Ab
98. Bt, Ep, W.Mica, Cam, Stp, Ttn, Ab
99. Bt, Ep, W.Mica, Cam, Stp, Omp, Ttn, Ab
100. Ep, W.Mica, Cam, Stp, Omp, Ttn, Ab
101. Bt, W.Mica, Cam, Ttn, Ab, Qz
102. Bt, W.Mica, Cam, Ttn, Ab, Qz, Rt
103. Bt, W.Mica, Cam, Stp, Ttn, Ab, Qz
104. Bt, Ep, W.Mica, Cam, Stp, Ttn, Ab, Qz
105. Bt, Ep, Cam, Stp, Ttn, Ab
106. Bt, Chl, Ep, W.Mica, Cam, Stp, Ttn, Ab
107. Bt, Chl, Ep, Cam, Stp, Ttn, Ab
108. Bt, Ep, Cam, Stp, Omp, Ttn, Ab
109. Bt, Ep, Cam, Stp, Omp, Ttn, Ab
110. Bt, Ep, Cam, Stp, Ttn, Ab
111. Bt, Chl, Ep, Stp, Omp, Ttn, Ab
112. Bt, Chl, Ep, Cam, Stp, Ttn, Ab
113. Bt, Ep, Cam, Stp, Ttn, Ab, Qz
114. Bt, Ep, Cam, Stp, Ttn, Ab, Qz, Rt
115. Bt, Cam, Stp, Ttn, Ab, Qz, Rt
116. Bt, Chl, Cam, Stp, Ttn, Ab, Qu
117. Bt, Chl, Ep, Cam, Stp, Ttn, Ab, Qz
118. Bt, Chl, Cam, Ttn, Ab, Qz
119. Bt, Chl, Cam, Ttn, Ab, Qz, Rt
120. Bt, Cam, Ttn, Ab, Qz, Rt
121. Bt, Ep, Cam, Ttn, Ab, Qz, Rt
122. Bt, W.Mica, Cam, Stp, Ttn, Ab, Qz, Rt
123. Bt, Cam, Fsp, Ttn, Ab, Qz, Rt
124. Bt, Cam, Fsp, Qz, Rt
125. Bt, Cam, Fsp, Ilm, Qz, Rt
126. Bt, Cam, Fsp, Ab, Qz, Rt
127. Bt, Cam, Fsp, Ilm, Ab, Qz, Rt
128. Bt, Cam, Fsp, Ilm, Ab, Qz

B

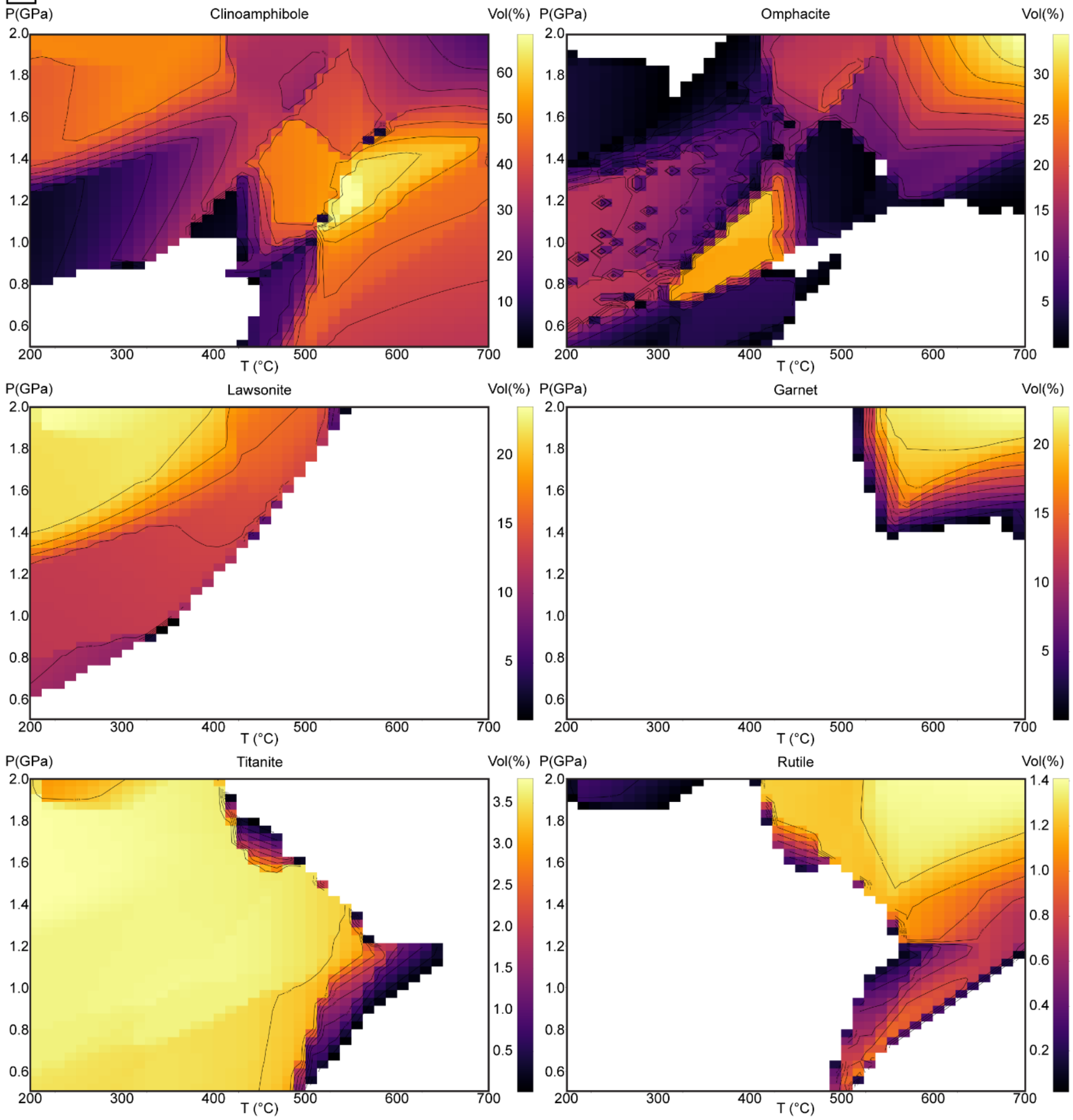

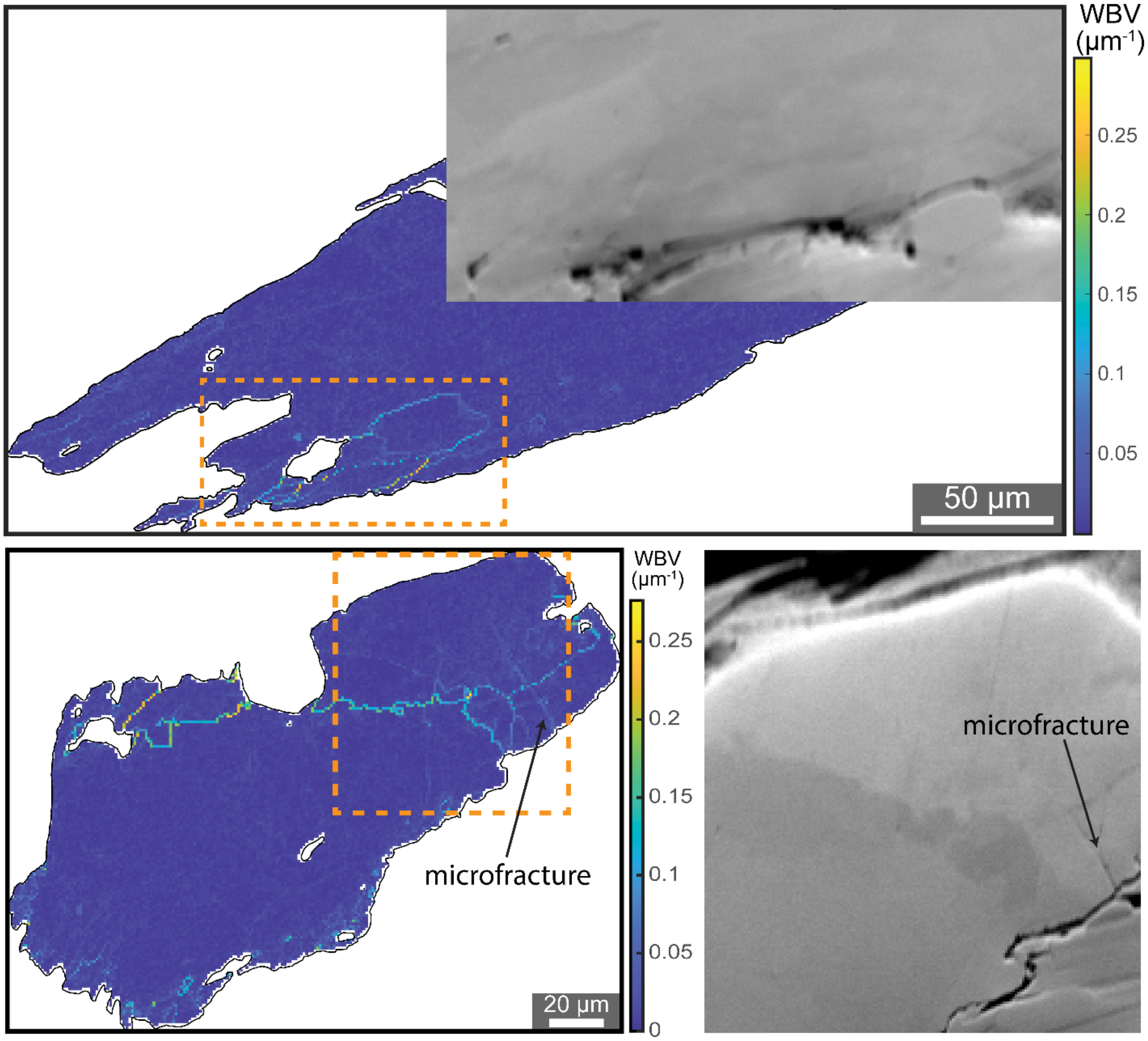

Fig. S4. Weighted Burgers vector magnitude maps of selected grains discussed in main text and Figure 2 (top and bottom left) illustrate subgrain boundary structures within the glaucophane grains. Scanning electron microscope images of the orange bounded regions were captured using the forescatter detector (FSD) (top inset, bottom right), and illustrate changes in orientation (variations in grayscale color) across the glaucophane grains and along subgrain boundaries. Black arrows denote an example of a microfracture within a grain.

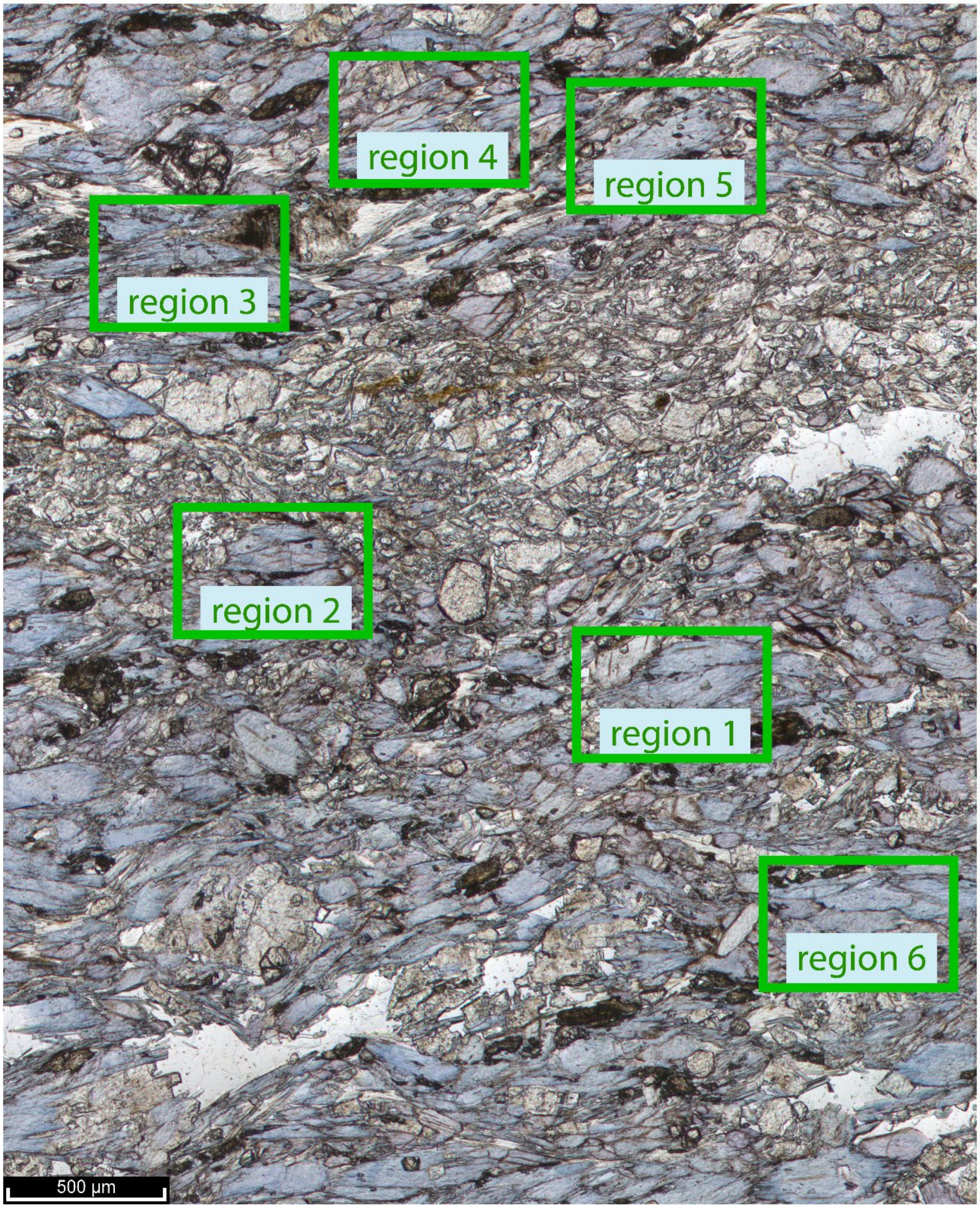

Fig. S5. Plane-polarized light micrograph including representative region of sample mapped by EBSD (Fig 1A), with green boxes denoting the regions mapped at higher resolution (1 micrometer step size) for WBV analysis (Figs. S7-12).

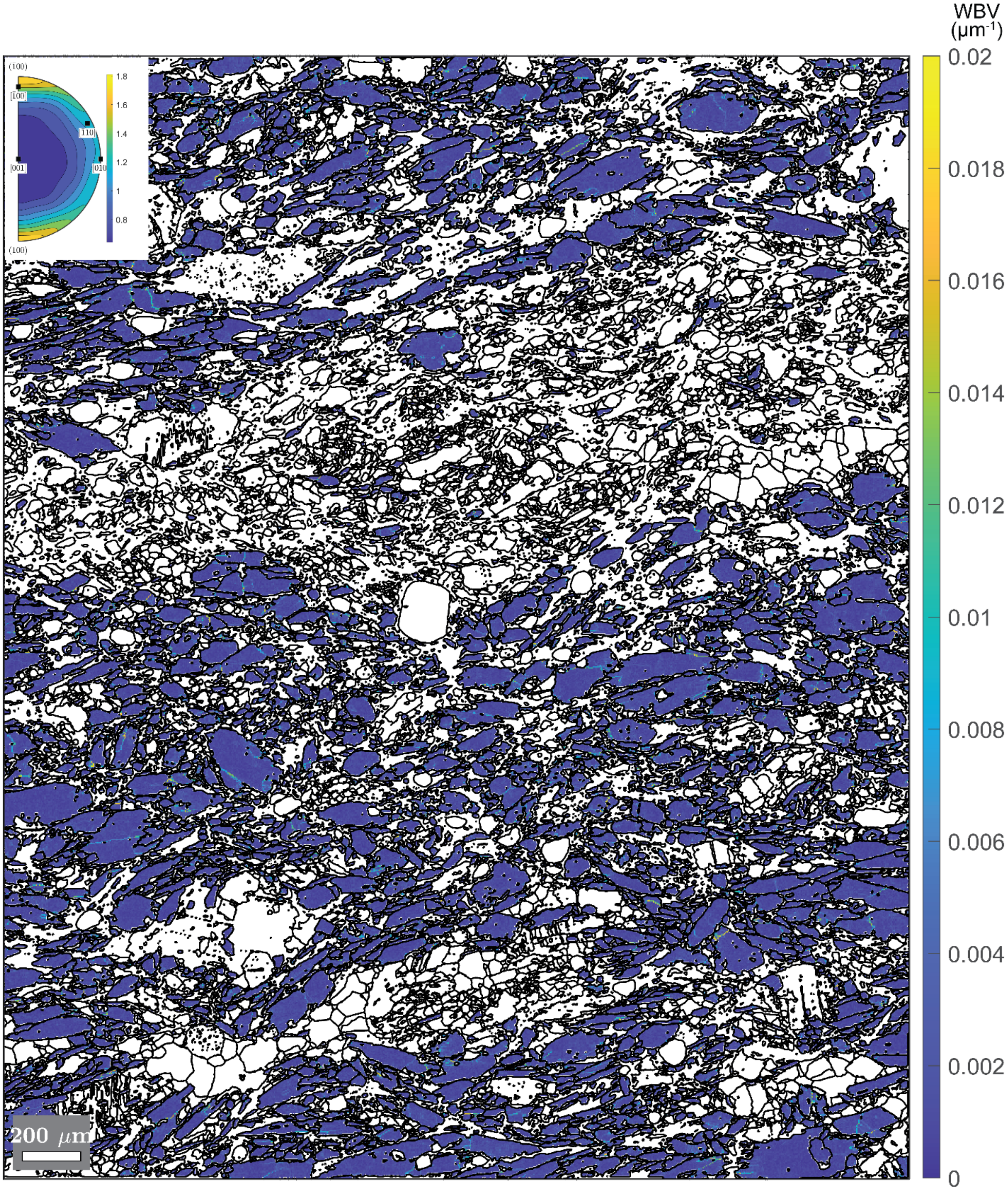

Fig. S6. WBV magnitude map of glaucophane calculated using differential method on 3x3 stencil (section I.D.) for full representative EBSD map. Inset is inverse pole figure (IPF) of WBV direction weighted by WBV length.

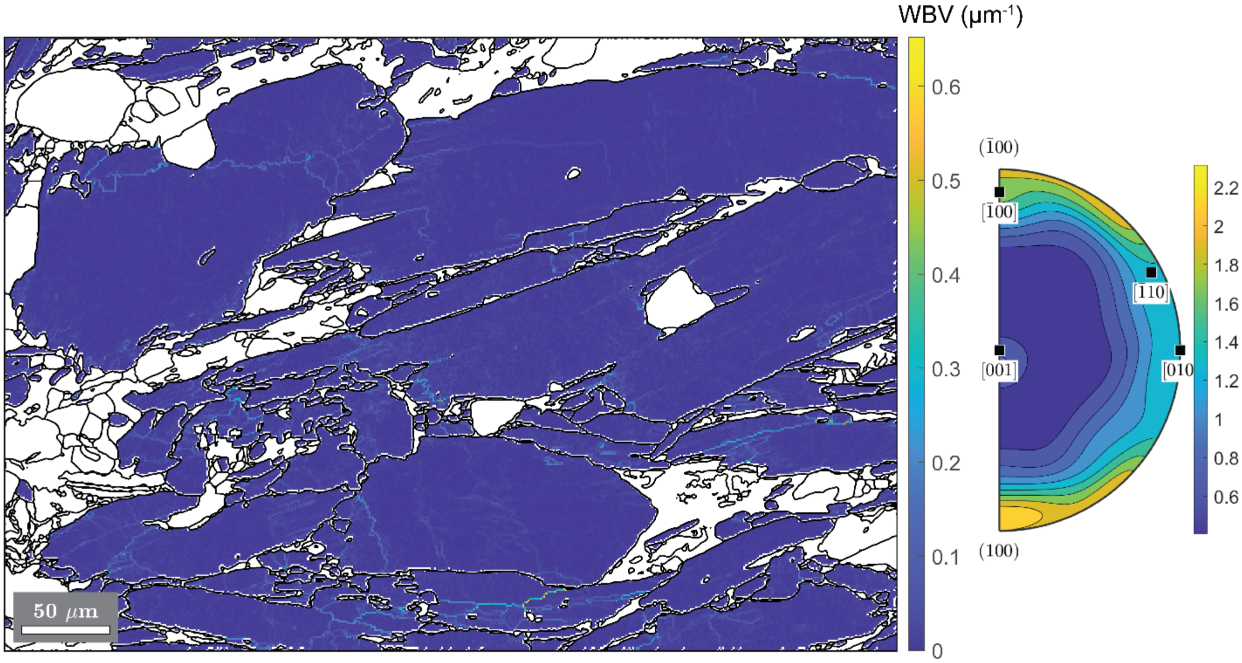

Fig. S7. WBV magnitude map of glaucophane in region 1 (Fig. S5) calculated using differential method on 3x3 stencil. Plotted on the right is an IPF of WBV direction weighted by WBV length.

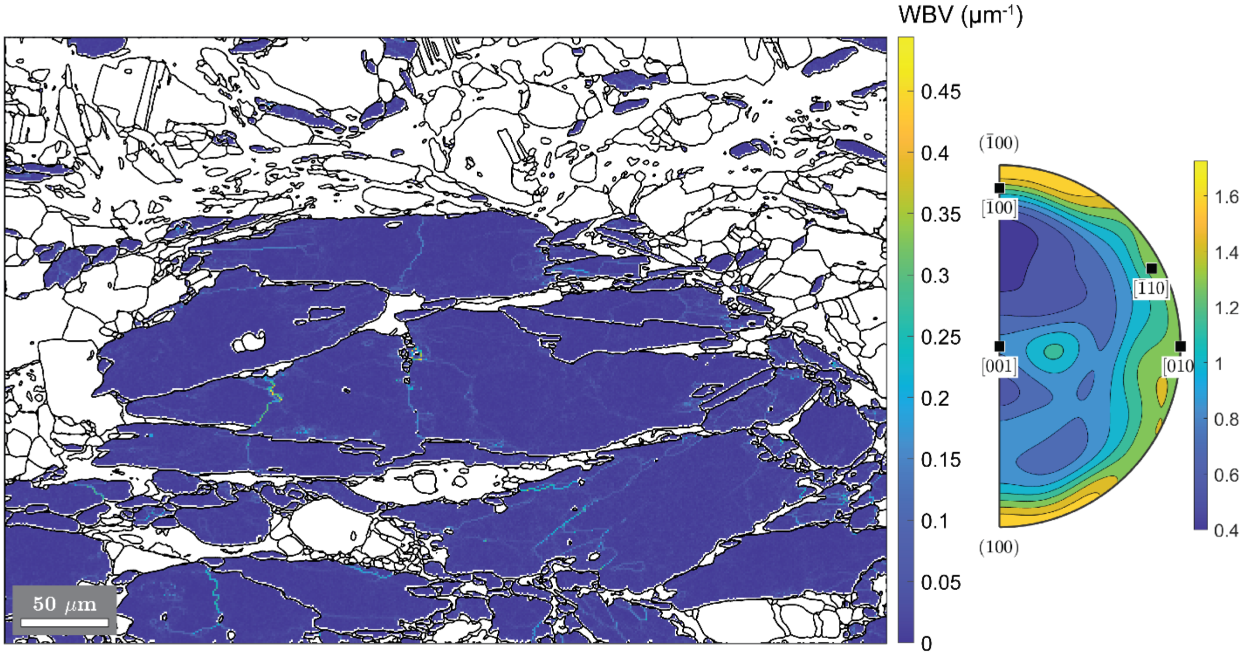

Fig. S8. WBV magnitude map of glaucophane in region 2 (Fig. S5) calculated using differential method on 3x3 stencil. Plotted on the right is an IPF of WBV direction weighted by WBV length.

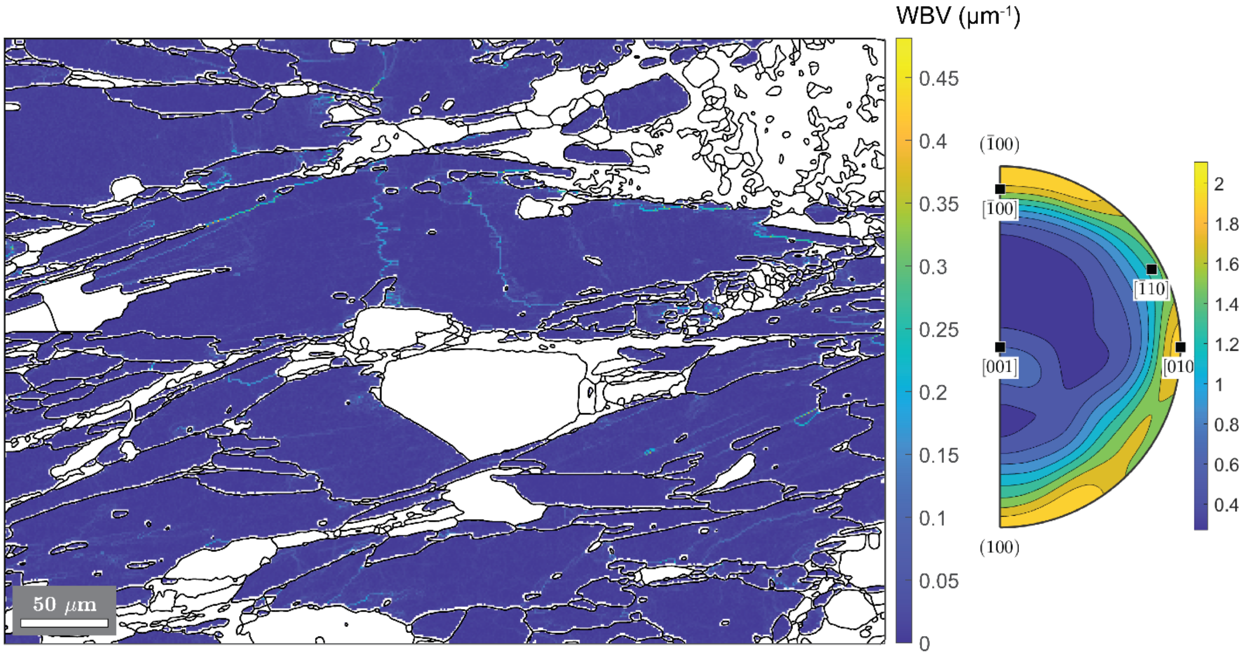

Fig. S9. WBV magnitude map of glaucophane in region 3 (Fig. S5) calculated using differential method on 3x3 stencil. Plotted on the right is an IPF of WBV direction weighted by WBV length.

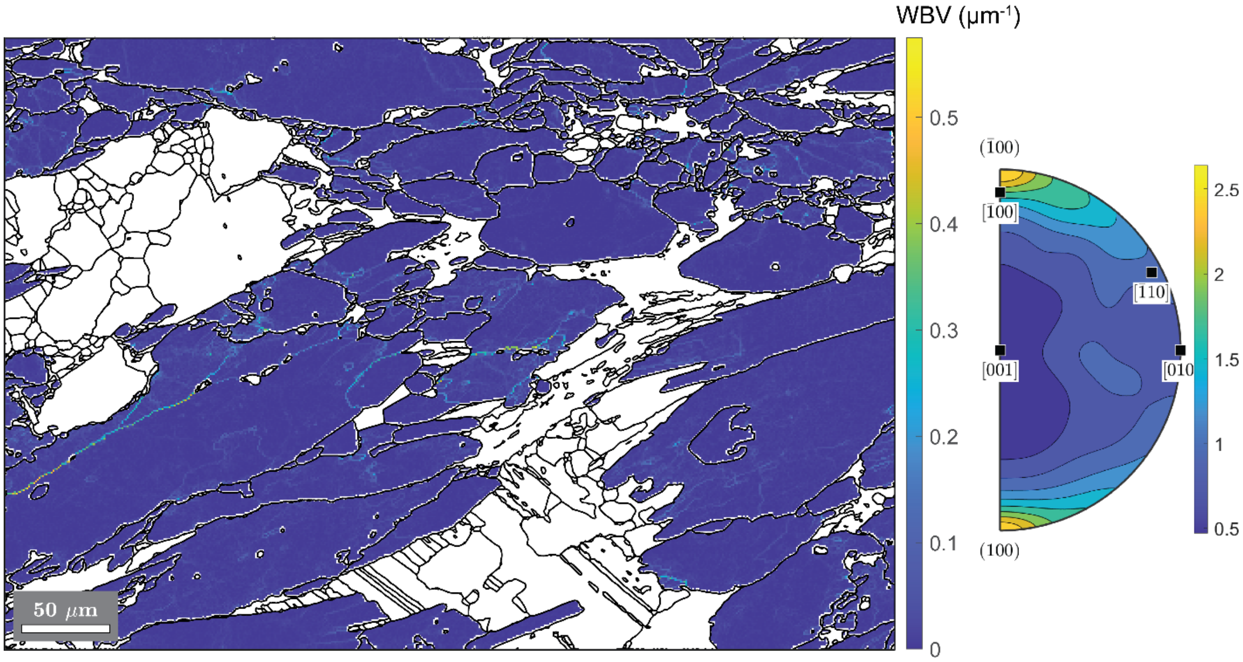

Fig. S10. WBV magnitude map of glaucophane in region 4 (Fig. S5) calculated using differential method on 3x3 stencil. Plotted on the right is an IPF of WBV direction weighted by WBV length.

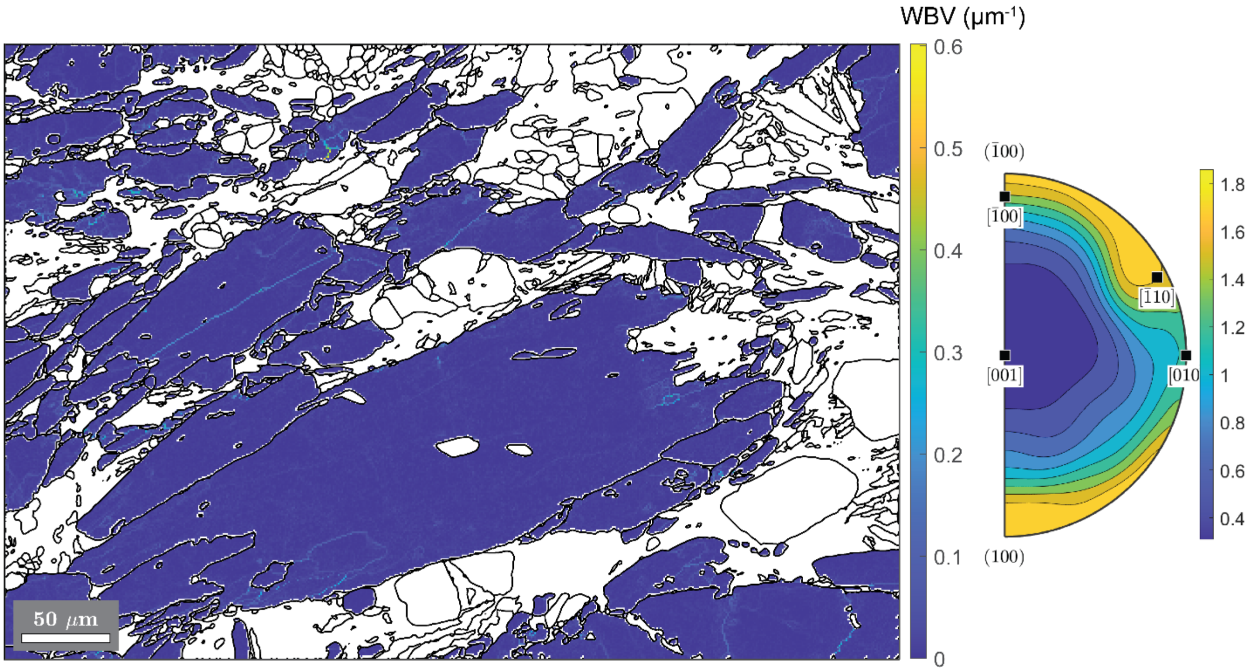

Fig. S11. WBV magnitude map of glaucophane in region 5 (Fig. S5) calculated using differential method on 3x3 stencil. Plotted on the right is an IPF of WBV direction weighted by WBV length.

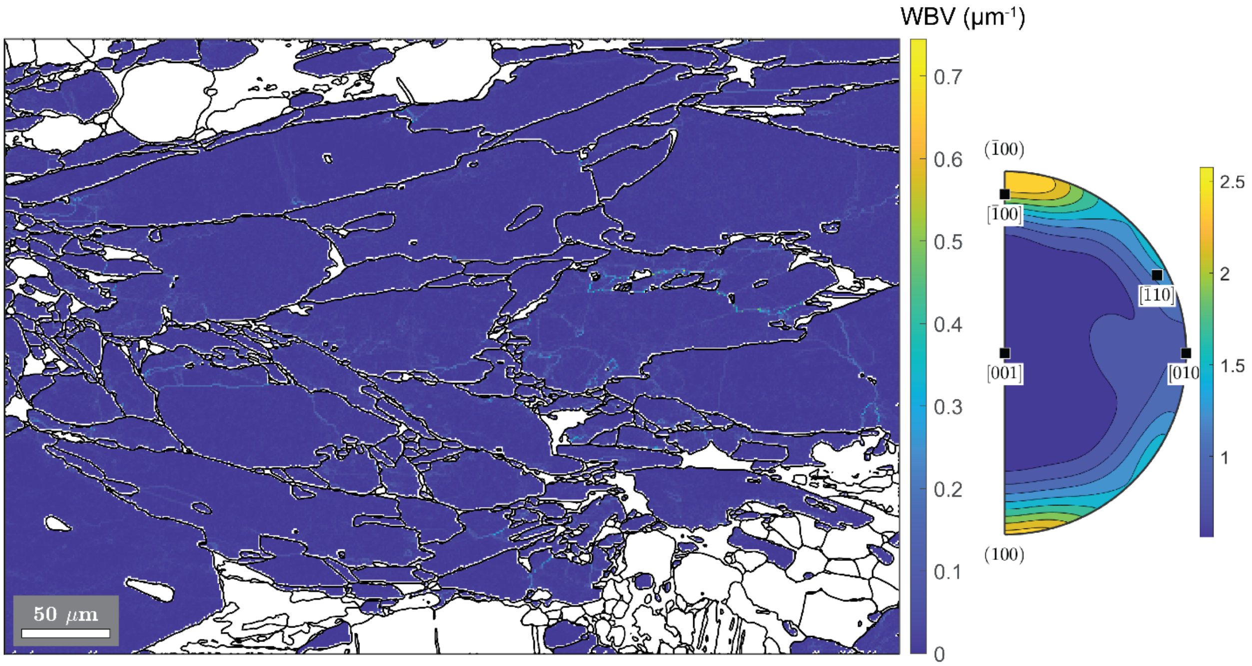

Fig. S12. WBV magnitude map of glaucophane in region 6 (Fig. S5) calculated using differential method on 3x3 stencil. Plotted on the right is an IPF of WBV direction weighted by WBV length.

REFERENCES CITED

Awalt, M., 2013, Petrology and Pseudosection Modeling of a Garnet-Blueschist Block-In-Mélange, Santa Catalina Island, California [Undergraduate Honors Thesis]: Macalester College, 77 p., https://digitalcommons.macalester.edu/geology_honors/15.

Bachmann, F., Hielscher, R., and Schaeben, H., 2010, Texture Analysis with MTEX – Free and Open Source Software Toolbox: Solid State Phenomena, v. 160, p. 63–68, doi:10.4028/www.scientific.net/SSP.160.63.

Bebout, G.E., and Barton, M.D., 1993, Metasomatism during subduction: products and possible paths in the Catalina Schist, California: Chemical Geology, v. 108, p. 61–92, doi:10.1016/0009-2541(93)90318-D.

Chauve, T., Montagnat, M., Piazolo, S., Journaux, B., Wheeler, J., Barou, F., Mainprice, D., and Tommasi, A., 2017, Non-basal dislocations should be accounted for in simulating ice mass flow: Earth and Planetary Science Letters, v. 473, p. 247–255, doi:10.1016/j.epsl.2017.06.020.

Connolly, J. a. D., and Petrini, K., 2002, An automated strategy for calculation of phase diagram sections and retrieval of rock properties as a function of physical conditions: Journal of Metamorphic Geology, v. 20, p. 697–708, doi:10.1046/j.1525-1314.2002.00398.x.

Fuhrman, M.L., and Lindsley, D.H., 1988, Ternary-feldspar modeling and thermometry: American Mineralogist, v. 73, p. 201–215.

Green, E., Holland, T., and Powell, R., 2007, An order-disorder model for omphacitic pyroxenes in the system jadeite-diopside-hedenbergite-acmite, with applications to eclogitic rocks: American Mineralogist, v. 92, p. 1181–1189, doi:10.2138/am.2007.2401.

Green, E.C.R., White, R.W., Diener, J.F.A., Powell, R., Holland, T.J.B., and Palin, R.M., 2016, Activity–composition relations for the calculation of partial melting equilibria in metabasic rocks: Journal of Metamorphic Geology, v. 34, p. 845–869, doi:10.1111/jmg.12211.

Holland, T.J.B., and Powell, R., 2011, An improved and extended internally consistent thermodynamic dataset for phases of petrological interest, involving a new equation of state for solids: Journal of Metamorphic Geology, v. 29, p. 333–383, doi:10.1111/j.1525-1314.2010.00923.x.

Holland, T.J.B., and Powell, R., 1998, An internally consistent thermodynamic data set for phases of petrological interest: Journal of Metamorphic Geology, v. 16, p. 309–343, doi:10.1111/j.1525-1314.1998.00140.x.

Mainprice, D., Hielscher, R., and Schaeben, H., 2011, Calculating anisotropic physical properties from texture data using the MTEX open-source package: Geological Society, London, Special Publications, v. 360, p. 175–192, doi:10.1144/SP360.10.

Massonne, H.-J., and Willner, A.P., 2008, Phase relations and dehydration behaviour of psammopelite and mid-ocean ridge basalt at very-low-grade to low-grade metamorphic conditions: European Journal of Mineralogy, p. 867–879, doi:10.1127/0935-1221/2008/0020-1871.

Michibayashi, K., and Mainprice, D., 2004, The Role of Pre-existing Mechanical Anisotropy on Shear Zone Development within Oceanic Mantle Lithosphere: an Example from the Oman Ophiolite: Journal of Petrology, v. 45, p. 405–414, doi:10.1093/petrology/egg099.

Padrón-Navarta, J.A., Sánchez-Vizcaíno, V.L., Hermann, J., Connolly, J.A.D., Garrido, C.J., Gómez-Pugnaire, M.T., and Marchesi, C., 2013, Tschermak's substitution in antigorite and consequences for phase relations and water liberation in high-grade serpentinites: Lithos, v. 178, p. 186–196, doi:10.1016/j.lithos.2013.02.001.

Penniston-Dorland, S.C., and Harvey, K.M., 2023, Constraints on tectonic processes in subduction mélange: A review of insights from the Catalina Schist (CA, USA): Geosystems and Geoenvironment, v. 2, p. 100190, doi:10.1016/j.geogeo.2023.100190.

Platt, J.P., and Schmidt, W.L., 2024, Is the Inverted Field Gradient in the Catalina Schist Terrane Primary or Constructional? Tectonics, v. 43, p. e2023TC008021, doi:10.1029/2023TC008021.

Prior, D.J. et al., 1999, The application of electron backscatter diffraction and orientation contrast imaging in the SEM to textural problems in rocks: American Mineralogist, v. 84, p. 1741–1759, doi:10.2138/am-1999-11-1204.

Reynard, B., Gillet, P., and Willaime, C., 1989, Deformation mechanisms in naturally deformed glaucophanes: a TEM and HREM study: European Journal of Mineralogy, v. 1, p. 611–624, doi:10.1127/ejm/1/5/0611.

Wheeler, J., Mariani, E., Piazolo, S., Prior, D. j., Trimby, P., and Drury, M. r., 2009, The weighted Burgers vector: a new quantity for constraining dislocation densities and types using electron backscatter diffraction on 2D sections through crystalline materials: Journal of Microscopy, v. 233, p. 482–494, doi:10.1111/j.1365-2818.2009.03136.x.

Wheeler, J., Piazolo, S., Prior, D.J., Trimby, P.W., and Tielke, J.A., 2024, Using crystal-lattice distortion data for geological investigations: the weighted Burgers vector method: Journal of Structural Geology, v. 179, p. 105040, doi:10.1016/j.jsg.2023.105040.

White, R.W., Powell, R., and Clarke, G.L., 2002, The interpretation of reaction textures in Fe-rich metapelitic granulites of the Musgrave Block, central Australia: constraints from mineral equilibria calculations in the system K2O–FeO–MgO–Al2O3–SiO2–H2O–TiO2–Fe2O3: Journal of Metamorphic Geology, v. 20, p. 41–55, doi:10.1046/j.0263-4929.2001.00349.x.

White, R.W., Powell, R., Holland, T.J.B., Johnson, T.E., and Green, E.C.R., 2014, New mineral activity–composition relations for thermodynamic calculations in metapelitic systems: Journal of Metamorphic Geology, v. 32, p. 261–286, doi:10.1111/jmg.12071.

Whitney, D.L., and Evans, B.W., 2010, Abbreviations for names of rock-forming minerals: American Mineralogist, v. 95, p. 185–187, doi:10.2138/am.2010.3371.

Appendix 3. Supporting Information for Chapter 4: Experimental constraints on the strength of subducting oceanic crust: a dislocation creep flow law for blueschist (glaucophane)

Jason N. Ott[1], Cailey B. Condit[1], and Matěj Peč[2]

[1]Department of Earth and Space Sciences, University of Washington, Seattle, WA, USA

[2]Department of Earth, Atmospheric and Planetary Sciences, Massachusetts Institute of Technology, Cambridge, MA, USA

Contents of this file

Text S1 to S5

Figures S1 to S16

Table S1

Text S1. Starting material and sample assembly

The starting material for the glaucophane deformation experiments was separated from a metabasic blueschist sample from Sifnos, Greece previously investigated by Schliestedt (1986; Table S1) and hosted in the blueschist collection at the University of Washington. This glaucophane-rich blueschist is predominantly glaucophane (> 45 modal percent) with the remainder of the mineral assemblage composed of epidote, chloritoid, garnet, phengite, quartz, and minor rutile. Glaucophane composition in the Sifnos blueschists has been previously constrained to near end-member composition by Schliestedt (1986; Table S1). The host blueschist was crushed to particle sizes under ~200 µm in diameter at the Western Washington University rock prep lab, and the particles were sieved to select a particle size range of 100–120 µm. The Franz magnetic separator at the University of Washington was used to isolate glaucophane, followed by hand-picking of glaucophane grains using an optical microscope for sample purity (removal of glaucophane with inclusions and other phases including epidote-group minerals with similar magnetic susceptibilities). The selected glaucophane fraction was ground using an agate auto mortar-and-pestle, and a grain size aliquot of 10–20 µm was prepared by using Stokes settling in ethanol (e.g., Ronde, 2004). The starting material was kept nominally dry by storing the glaucophane powder in a drying oven at ~100°C until immediately prior to loading and weld-sealing the sample jacket.

Sample assemblies were prepared by loading 0.15 g of the starting material into an 6.75 mm outer diameter, 0.2 mm wall thickness gold jacket between two alumina forcing blocks with a diameter of 6.3 mm that were precut to 45°, and the completed sample assembly was weld-sealed between 0.2 mm-thick gold endcaps (Fig. 1a). The sample was placed between the upper and lower alumina pistons and the assembly surrounded by solid NaCl-salt medium, a graphite resistivity furnace, and a 25.4 mm-diameter outer NaCl-salt medium. A K-type thermocouple was placed in contact with the center of the shear zone to control temperature, and the ~50 mm-long sample assembly was loaded into a water-cooled pressure vessel between two copper washers that provide the electrical contact with the graphite furnace. The completed experimental assembly was capped by a soft, deformable lead (Pb) plug to allow transmission of the load to the sample from the σ_1 and σ_3 tungsten-carbide pistons. A detailed schematic of the experimental apparatus and sample assembly is included in Figure 1 of Pec and Al Nasser (2021).

Text S2. Experimental methods

The deformation experiments were conducted at the Rock Deformation Laboratory at Massachusetts Institute of Technology Department of Earth, Atmospheric and Planetary Sciences in a Sanchez Technologies Solid Medium Deformation Apparatus (Griggs-type triaxial deformation apparatus) described in Ghaffari and Pec (2020) in detail. During each experiment, the pressure and temperature were gradually increased to 1.5 GPa and 650°C over 4–6 hours, then the samples were hot-pressed at nominally hydrostatic conditions for 16 hours.

After completing the hot-press, the σ_1 piston was hydraulically advanced until reaching the "hit-point" of contact with the sample, and the samples were deformed by either (1) constant displacement rate at a constant temperature, (2) load-stepping at a constant temperature, or (3) temperature-stepping at a constant load. Constant displacement rate tests were conducted by advancing the σ_1 piston at a hydraulic pump rate of either 0.25 mL/min or 0.025 mL/min to reach shear strain rates of $\sim 5 \times 10^{-4}$ s^{-1} and $\sim 5 \times 10^{-5}$ s^{-1}, respectively. The load-stepping experiment (101JO) was conducted by advancing the σ_1 piston at 0.25 mL/min until approaching the peak strength of the sample based on the stress-strain curve of the constant displacement rate experiment at the same conditions (100JO). The test was then conducted by setting the load to a series of constant values and monitoring the displacement rate curves until nominally steady-state conditions (over 10–30 minutes) were reached before each subsequent load-step. The temperature stepping experiment (152JO) was also conducted by advancing the piston at 0.25 mL/min until approaching peak strength of the sample, then setting a constant load and monitoring the displacement rate curves until steady-state conditions were reached before each subsequent temperature-step.

At the completion of each test, the samples were quenched by reducing the temperature to 200°C at a rate of 300°C/min while also reducing the differential stress from the σ_1 piston to preserve the deformation microstructures. The experiments were then gradually brought to standard conditions by simultaneously reducing the temperature, confining pressure, and axial load, and the sample assemblies were recovered. During the depressurization a small differential stress (~100 MPa) was maintained to minimize unloading cracks. A post-experiment examination was completed on assembly for Pb-leaks between the tungsten carbide pistons and packing rings, thermocouple positioning, damage or tears to the gold sample-jacket, or any other indicators that might reflect on the validity of the mechanical data.

Text S3. Mechanical data analysis

Experimental data were recorded at a 1 Hz sampling rate including the axial load, the confining pressure, the position of the σ_1 and σ_3 pistons, the sample temperature, and the furnace power (in Volts and Amperes). The mechanical data were processed in Matlab, using the application newRig (Pec, 2018). The raw mechanical data is used to determine the "hit-point" at which the σ_1 piston contacts the sample by linear regression fits to the "run-in" curve, corresponding to the penetration of the lead plug by the σ_1 piston, and the nominally "elastic" loading curve where strain is applied to the sample. The intersection of the two regression lines is the hit-point at which the differential stress and shear strain is set to zero. The data are then corrected for the stiffness of the deformation rig (0.016 mm/kN) and “friction” associate with the driving in of the σ_1 piston into the high-pressure environment of the pressure vessel (1.42 kN/mm).

Shear zone thicknesses measured from the hot-pressed (undeformed) sample and the deformed samples are entered as parameters to determine the amount of sample thinning, and with the axial displacement from the mechanical data and the sample geometry (shear zone is oriented at a 45° angle to the direction of the σ_1 piston), are used to resolve the vertical displacement into pure and simple shear components. Assuming that sample thinning occurs continuously over the experiment, and that the overlap of the forcing blocks is a maximum at the start of the experiment and continually decreases through the experiment, the newRig application calculates the normal and shear stresses from the mechanical data, as well as the finite and instantaneous shear strain (γ) and shear strain rate ($\dot{\gamma}$; Pec, 2018). The shear stresses were then corrected for the solid NaCl salt assembly using the calibration of Holyoke and Kronenberg (2010) which was validated for our apparatus (Ortega-Arroyo et al., 2025). Finally, the shear stress and strain-rate ($\dot{\gamma}$) results from newRig were converted to equivalent (eq) stress and strain-rates using the relationships:

$$\sigma_{eq} = \sqrt{3} * \sigma_{shear}$$

and:

$$\dot{\varepsilon}_{eq} = \dot{\gamma}/\sqrt{3}$$

as detailed in Paterson and Olgaard (2000) to ensure that our flow law derived under general shear will be consistent with experimental flow laws derived in axial-compression geometry experiments.

Text S4. Microstructural data analysis

Data collection: Electron backscatter diffraction (EBSD) data were obtained at the University of Washington’s Molecular Analysis Facility (MAF) using a ThermoFisher-Scientific Apreo variable-pressure scanning electron microscope (SEM) equipped with an Oxford Instruments Symmetry 2 EBSD detector. The thin sections were prepared with a Bruker Vibromet 2 vibratory polisher for 2 hours, using a 0.06 µm amorphous colloidal silica suspension. After polishing, the sample was coated with a ~5 nm carbon layer and mounted to the stage at a fixed tilt angle of 70°. EBSD measurements were collected under a 20 kV accelerating voltage, 3.2 nA beam current, and a 13 mm working distance.

The EBSD maps were collected on ~125 µm × 85 µm regions of the center of the shear zone of the samples using a 0.25 µm step size and 20 ms exposure time. These datasets provided the basis for microstructural characterization, including phase proportions, crystallographic preferred orientation (CPO), shape preferred orientation (SPO), misorientation-to-mean-orientation (mis2mean) maps, misorientation angle distributions, grain orientation spread (GOS) maps, weighted Burgers vector analysis (Wheeler et al., 2024), linear-intercept grain size analysis (e.g., Hansen et al., 2011; Fig. S14), and textural analyses (pfJ-index; Michibayashi & Mainprice, 2004). Kikuchi patterns were indexed with the Oxford HKL database for quartz and the American Mineralogist database for other phases, both accessed through Oxford’s AZtec software. Backscattered electron (BSE) images were collected at the University of Washington MAF on the ThermoFisher-Scientific Apreo variable-pressure SEM using the T1 detector under a 20 kV accelerating voltage and a 1.6 nA beam current at a 10 mm working distance with the thin-section surface oriented normal to the electron beam.

EBSD data reduction and microstructural analysis: EBSD orientation analysis and grain reconstruction (Figs. 2,S1–S2,S4–S7) were used to assess deformation in glaucophane at both intra- and inter-granular scales, through evaluation of SPO and CPO (e.g., Prior et al., 2009). Data reduction and analysis were performed with the MTEX 5.10.0 toolbox in MATLAB (Bachmann et al., 2010; Mainprice et al., 2011). Measurements with a mean angular deviation exceeding 1° were discarded. Grain reconstruction applied a ≥ 2° threshold for subgrain boundaries and 10° for grain boundaries, with grains containing fewer than three points excluded.

CPO results are presented as equal-area, upper-hemisphere pole figures, plotted one point per grain based on mean orientations. Pole figure contours are given in multiples of uniform distribution (m.u.d.), with consistent scaling across all pole figures (Figs. 2b,f,j). Textural strength was quantified using the pole-figure J-index (pfJ-index; Michibayashi & Mainprice, 2004), defined as:

$$pfJ_{hkl} = \int P_{hkl}(\alpha,\beta)^2 d\omega$$

where *hkl* denotes the Miller index, (α,β) are spherical coordinates, $P_{hkl}(\alpha,\beta)$ represents the fraction of orientations for a crystallographic axis at a given orientation, and $d\omega$ is the differential element. The pfJ-index ranges from 1 (random orientation distribution) to infinity (single-crystal). The SPO is displayed in the main text as a polar plot histogram (rose diagram) of the longest axis of the glaucophane grains, weighted by grain area (Figs. 2c,g,k), and supplemented by Paror, Surfor, and characteristic shape SPO analysis (Figs. S3,S8,S9). The random and neighboring grain pair misorientation distributions were calculated from the orientation distribution function fit to the set of glaucophane grain mean orientations using an 8° half-width (Fig. 2d,h,l).

Text S5. Electron probe microanalysis

Glaucophane compositions in hot-pressed and experimentally deformed samples were analyzed using a JEOL JXA-8200 Superprobe electron microprobe at the Massachusetts Institute of Technology Electron Microprobe Facility. Operating conditions were 15 kV accelerating voltage, 10 nA beam current, and a focused beam. Formula recalculations were performed in the application MinPlotX (Walters & Gies, 2025), with Fe^{3+} estimated and a TiOH correction applied based on measured Ti-contents (Table S1). Structural assignments in MinPlotX follow the assignment criteria of Leake et al. (1997) and Hawthorne et al. (2012).

Figure S1.

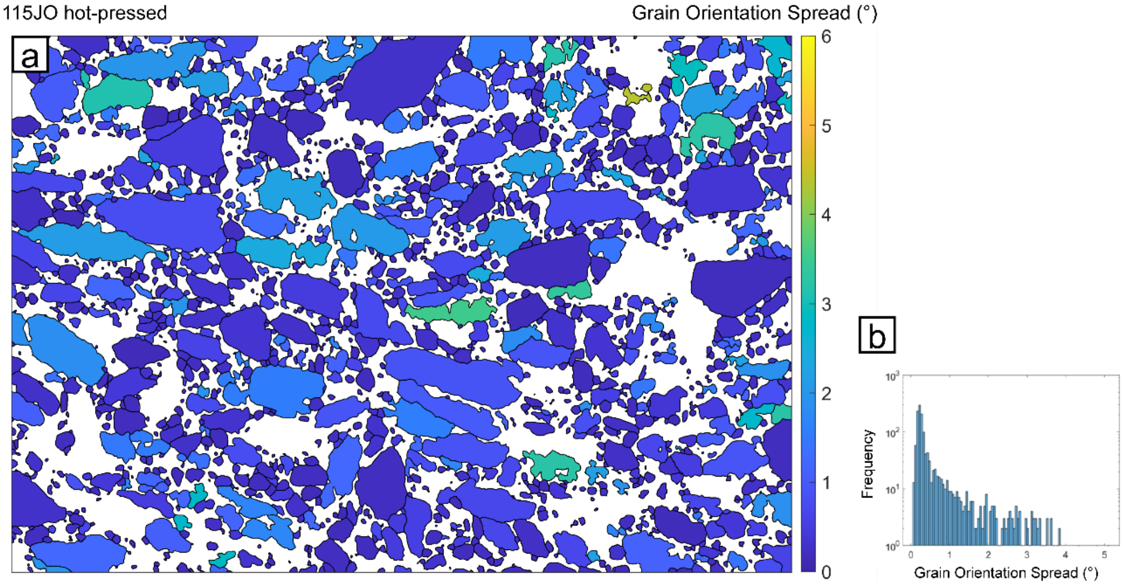

Figure S2.

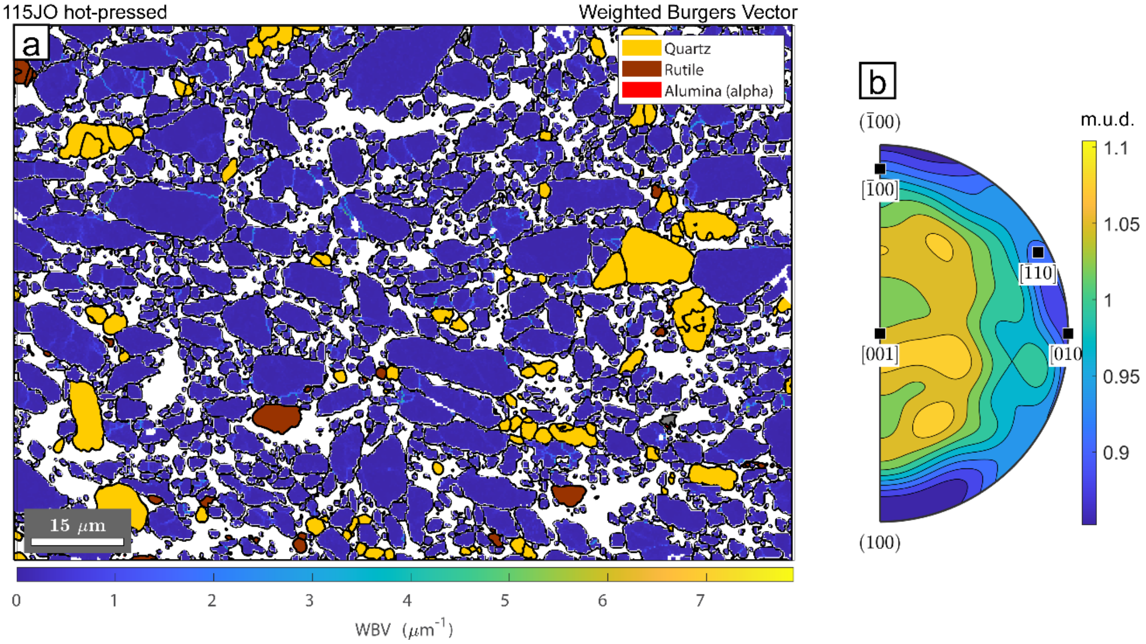

Figure S1. (a) Grain Orientation Spread (GOS) map of glaucophane in the hot-pressed, but otherwise undeformed sample (115JO) showing low average misorientations (low strain). (b) Histogram of the GOS in glaucophane as log frequency versus GOS in degrees.

Figure S2. (a) Weighted Burgers vector (WBV) map of glaucophane in the hot-pressed, but otherwise undeformed sample (115JO) displays few regions with high dislocation density organized into subgrain boundaries. (b) Probability density of WBV-direction (weighted by length) with contours scaled as multiples of uniform distribution (m.u.d.). WBVs are near uniformly distributed in hot-pressed sample.

Figure S3.

115JO Glaucophane SPO: Paror, Surfor, and Characteristic Grain Shape

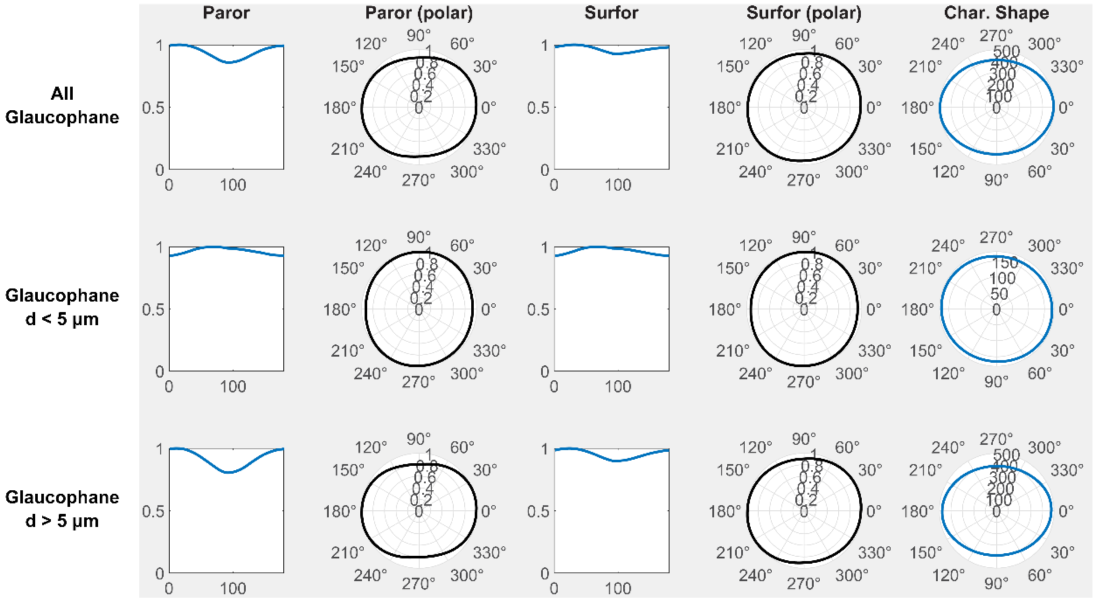

Figure S3. Shape preferred orientation (SPO) analysis of glaucophane grains from the hot-pressed, but otherwise undeformed sample (115JO). The rows show results for all measured glaucophane (top), grains with diameters < 5 µm (middle), and grains with diameters > 5 µm (bottom). Columns display (from left to right): **Paror** (parallel-to-orientation ratio, a measure of the degree of grain alignment), **Paror (polar)** plots (orientation of grain long axes), **Surfor** (surface orientation ratio, quantifying grain boundary alignment), **Surfor (polar)** plots, and c**haracteristic grain shape** rose diagrams (distribution of grain aspect ratios and orientations). Together, these metrics illustrate the development of an SPO in the hot-pressed sample that is weak in the fine-grained glaucophane, with coarse-grained glaucophane displaying a SPO that complements the CPO—with the grain elongation direction aligned to the shear plane (horizontal). For details of SPO calculation methods, see Heilbronner and Barrett (2014).

Figure S4.

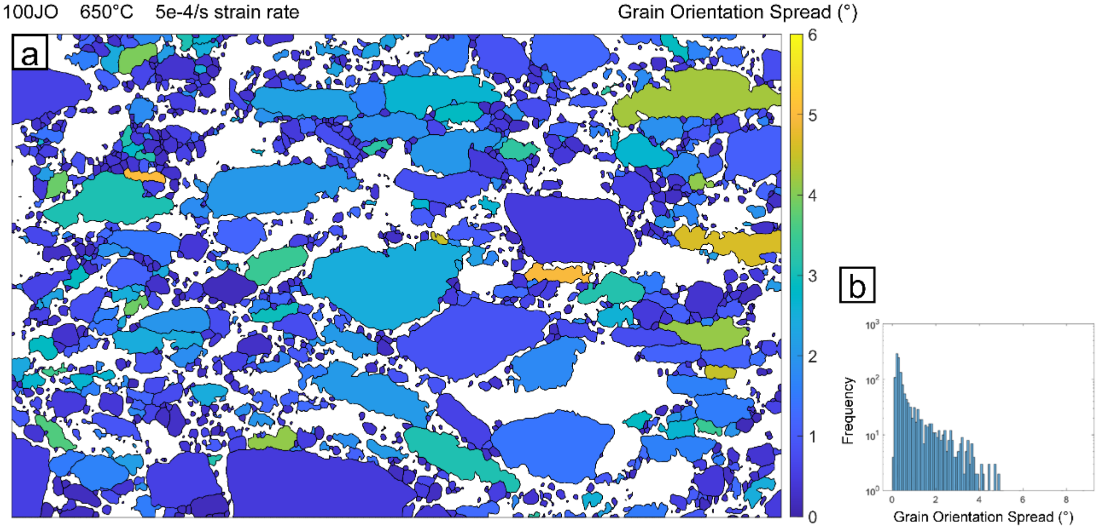

Figure S5.

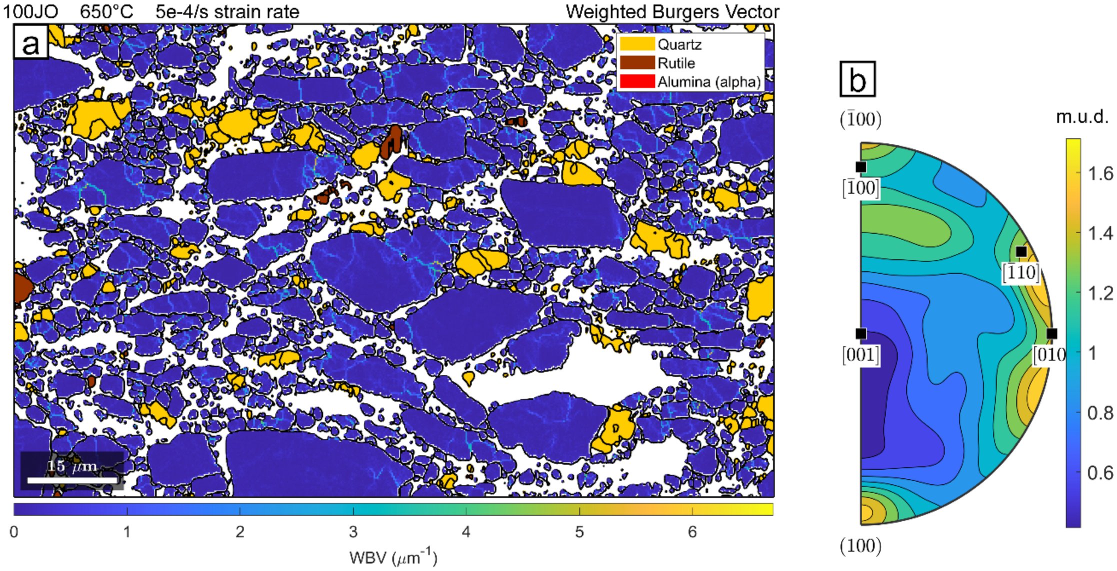

Figure S4. (a) GOS map of glaucophane in the sample deformed at 650°C and 5e-4/s (100JO), showing increased average misorientations in comparison to the hot-pressed sample (Fig. S1) signifying increased strain preserved in glaucophane grains. (b) Histogram of the GOS in glaucophane as log frequency versus GOS in degrees.

Figure S5. (a) Weighted Burgers vector (WBV) map of glaucophane in the sample deformed at 650°C and 5e-4/s (100JO), frequently shows networks of lobate, interconnected subgrain boundaries. (b) Probability density of WBV-direction (weighted by length) with contours scaled as multiples of uniform distribution (m.u.d.). WBVs show density maxima near <100>- and <110>-directions, consistent with active pure and mixed character slip systems previously observed in naturally deformed glaucophane (Ott et al., 2025; Reynard et al., 1989).

Figure S6.

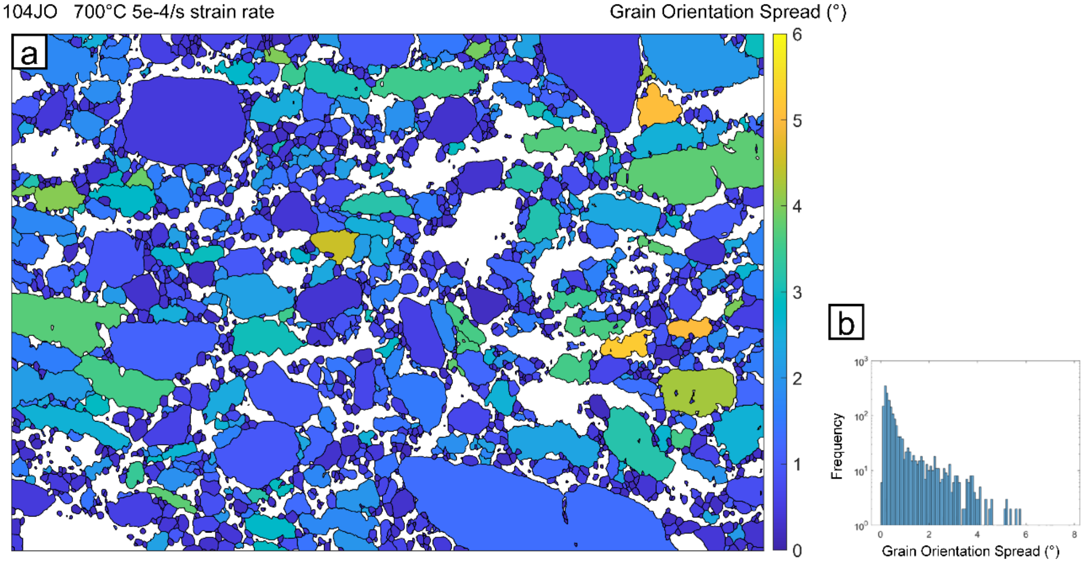

Figure S7.

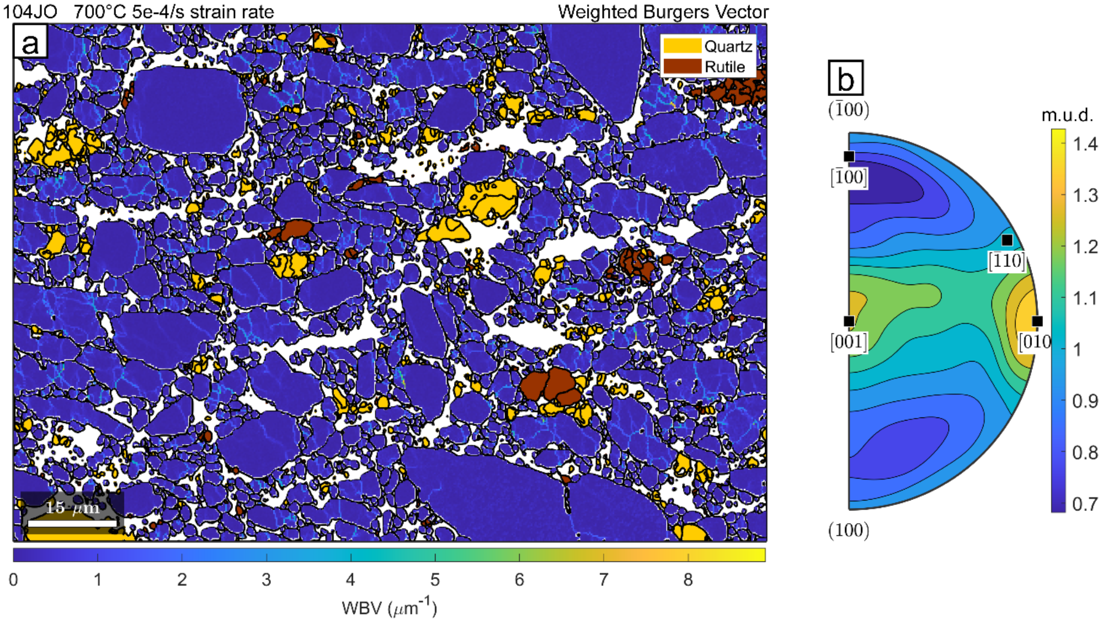

Figure S6. (a) GOS map of glaucophane in the sample deformed at 700°C and 5e-4/s (104JO) shows increased intragranular strain compared to the sample deformed at 650°C and 5e-4/s (100JO), (Fig. S4). (b) Histogram of the GOS in glaucophane as log frequency versus GOS in degrees.

Figure S7. (a) Weighted Burgers vector (WBV) map of glaucophane in sample the sample deformed at 700°C and 5e-4/s (104JO) shows extensive networks of lobate, interconnected subgrain boundaries. (b) Probability density of WBV-direction (weighted by length) with contours scaled as multiples of uniform distribution (m.u.d.). WBVs density maxima near <010>- and <001>-directions, no longer evidence of <110> WBV-direction.

Figure S8.

100JO Glaucophane SPO: Paror, Surfor, and Characteristic Grain Shape

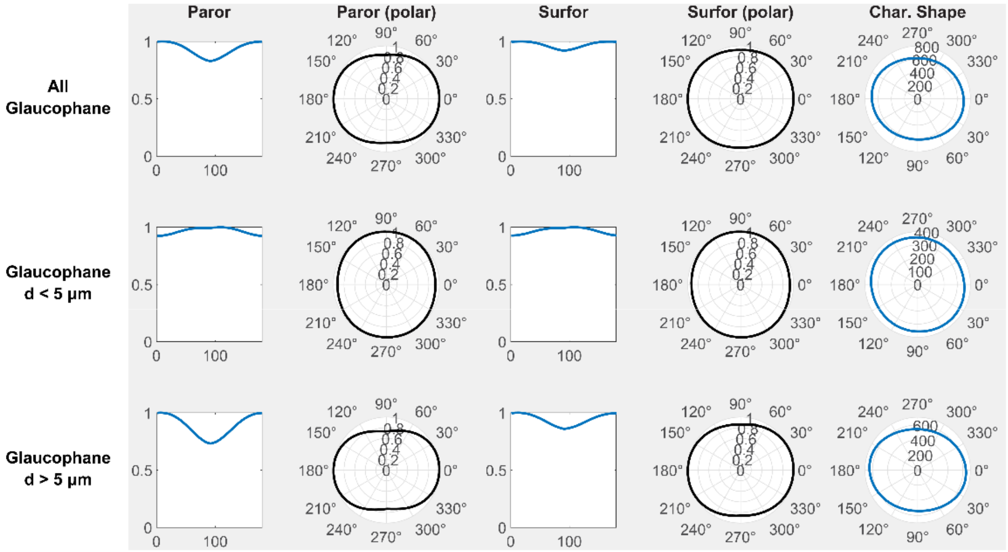

Figure S9.

104JO Glaucophane SPO: Paror, Surfor, and Characteristic Grain Shape

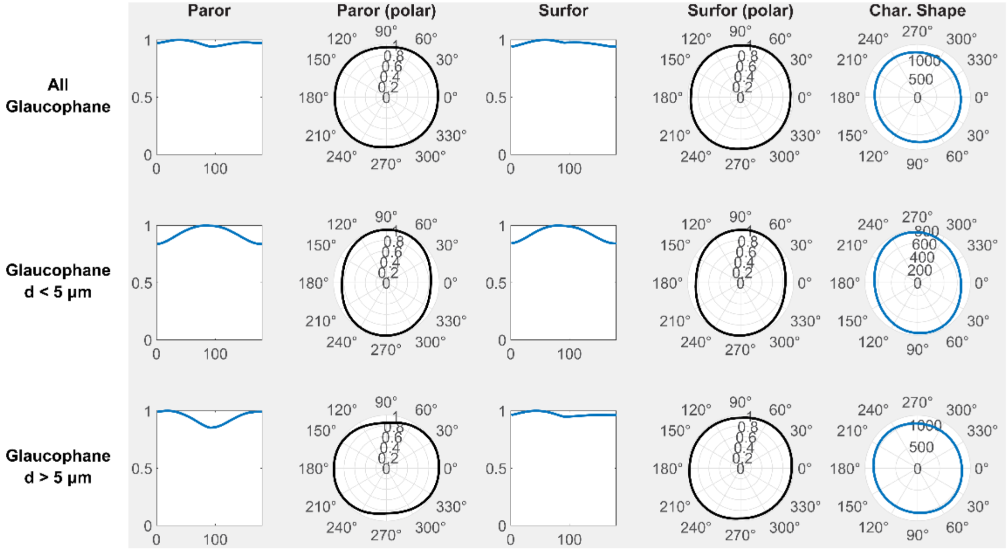

Figure S8. SPO analysis of glaucophane grains from sample the sample deformed at 650°C and 5e-4/s (100JO). Rows and columns as described in Figure S3. Similar to the hot-pressed sample, fine-grained glaucophane shows weaker SPO than the coarse-grains. Coarse grains are elongated with the shear plane (horizontal).

Figure S9. SPO analysis of glaucophane grains from sample the sample deformed at 700°C and 5e-4/s (104JO). Rows and columns as described in Figure S3. Unlike the lower-T test (Fig. S8), fine-grained glaucophane now shows SPO with elongation direction normal to shear plane. Paror plots show moderate SPO in coarse glaucophane grains, but with near-equant characteristic shape.

Figure S10. 115JO Hot-pressed sample

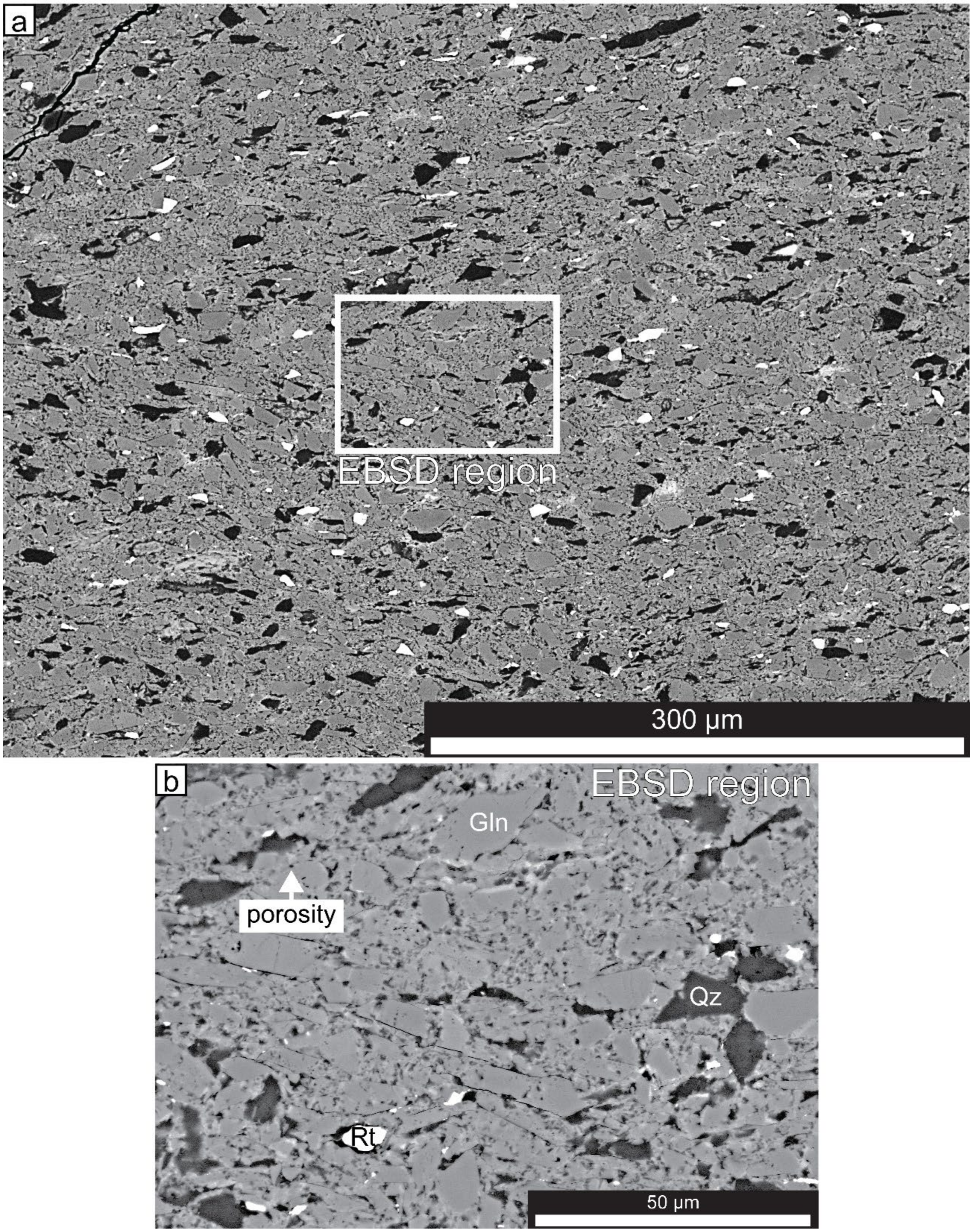

Figure S10. (a) Backscatter electron (BSE) image of the center of the shear zone in the hot-pressed, but otherwise undeformed sample (115JO), illustrating the distribution of phases in the sample and commonly angular grain boundaries. (b) Detail of boxed region in (a) highlights porosity in the hot-pressed sample.

Figure S11.

100JO 650°C 5e-4 strain rate

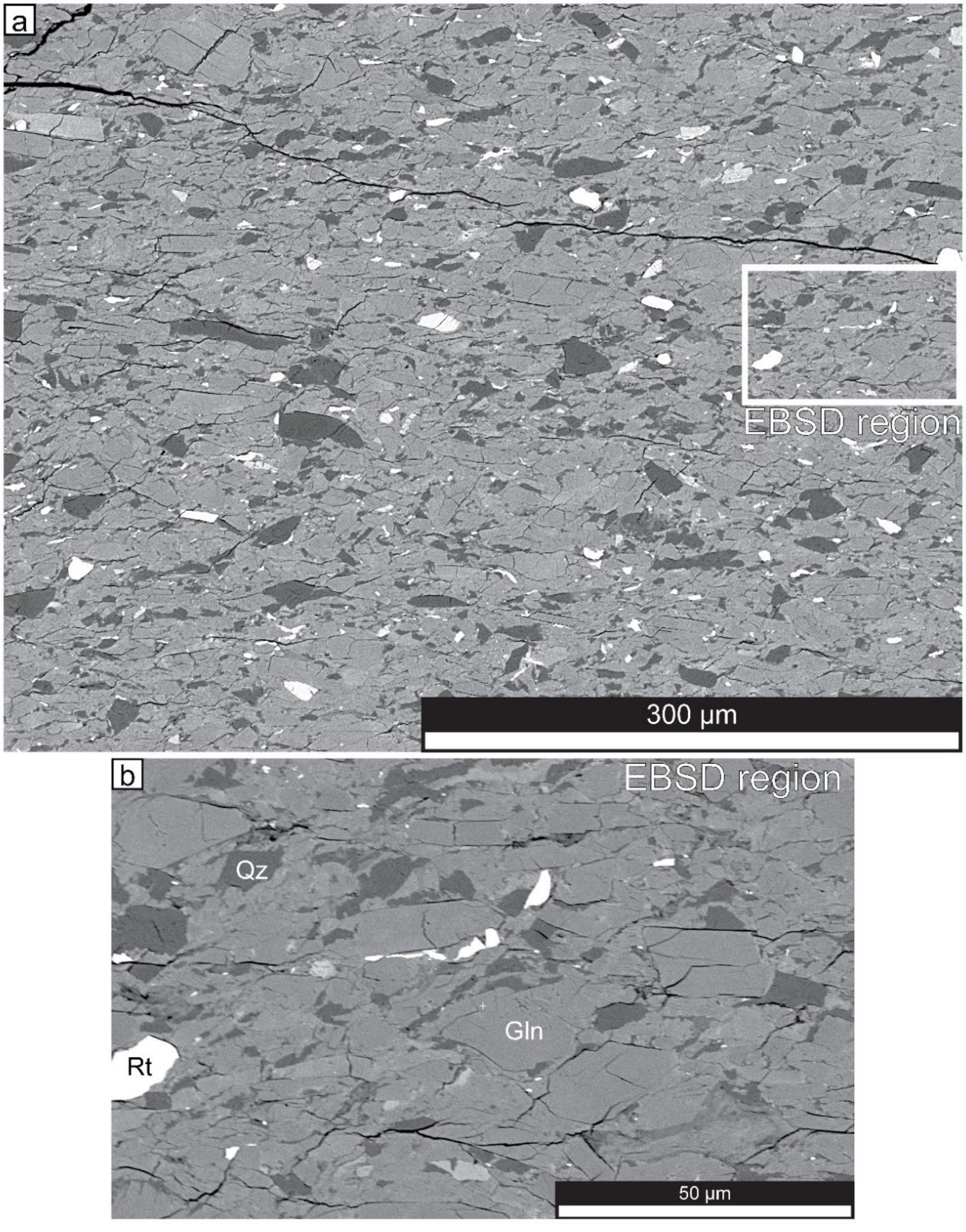

Figure S11. (a) BSE image of the center of the shear zone in the sample deformed at 650°C and 5e-4/s (100JO), illustrating the distribution of phases in the sample and local development of rounded grain boundaries. (b) Detail of boxed region in (a).

Figure S12.

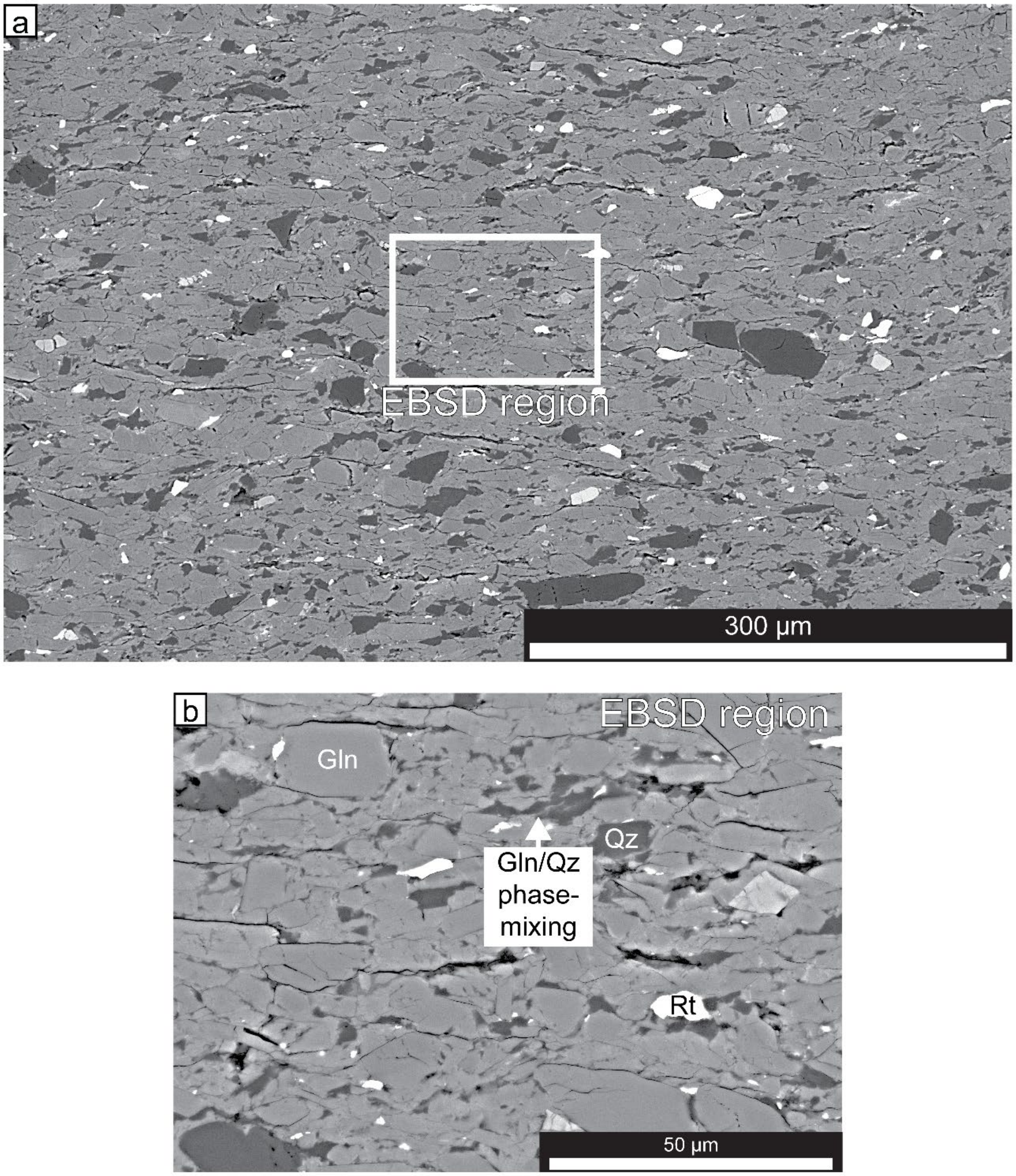

Figure S12. (a) Backscatter electron (BSE) image of the center of the shear zone in the sample deformed at 700°C and 5e-4/s (104JO), illustrating the distribution of phases in the sample and widespread development of lobate/rounded grain boundaries. (b) Detail of boxed region in (a) highlights regions of phase-mixing between glaucophane and quartz.

Figure S13.

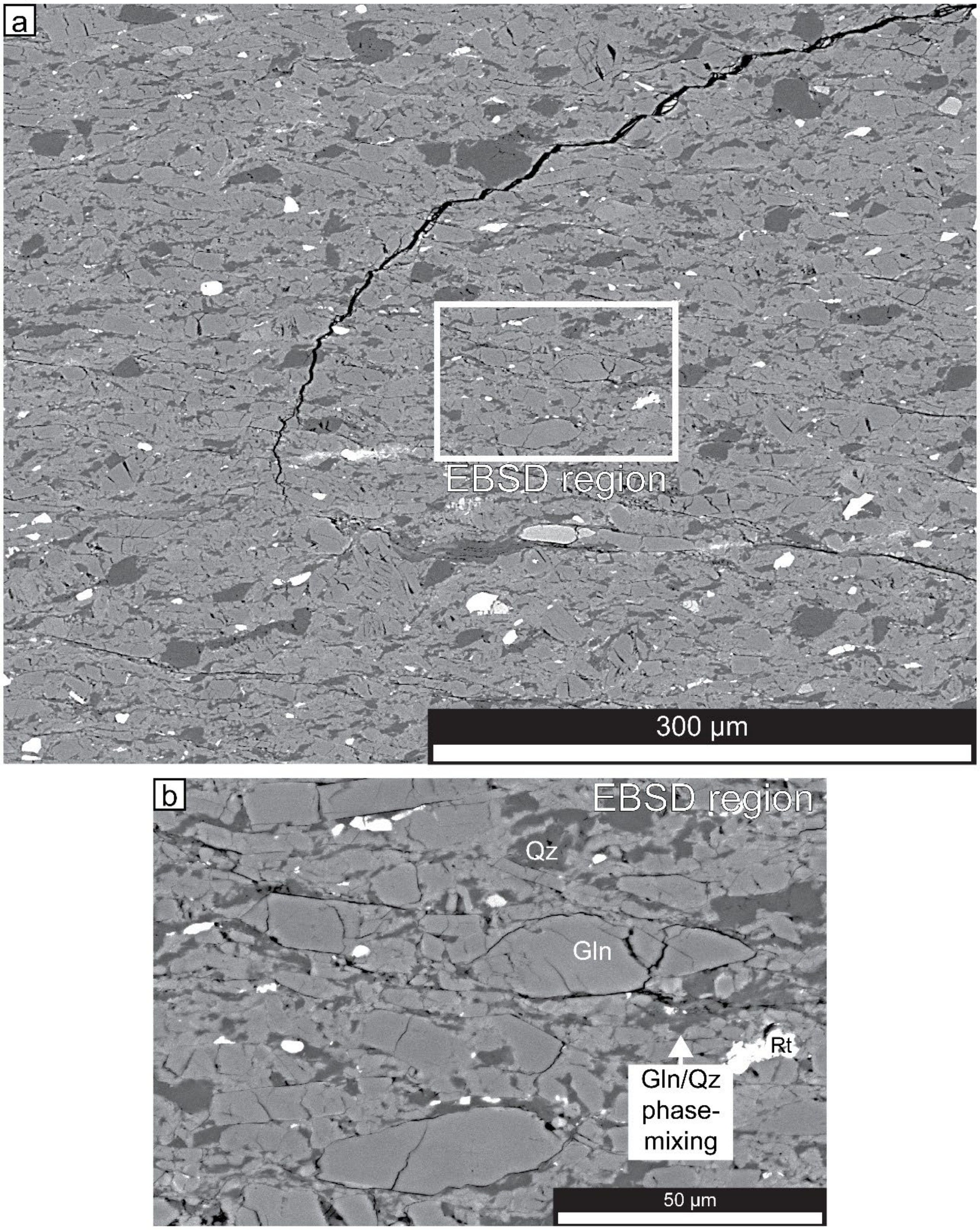
103JO 750°C 5e-4 strain rate

Figure S13. (a) Backscatter electron (BSE) image of the center of the shear zone in the sample deformed at 750°C and 5e-4/s (103JO), illustrating the distribution of phases in the sample and widespread development of lobate/rounded grain boundaries. (b) Detail of boxed region in (a) highlights the widespread phase-mixing between glaucophane and quartz in the sample, with some mixing zones additionally incorporating rutile.

Figure S14. Line-intercept glaucophane grain size distributions

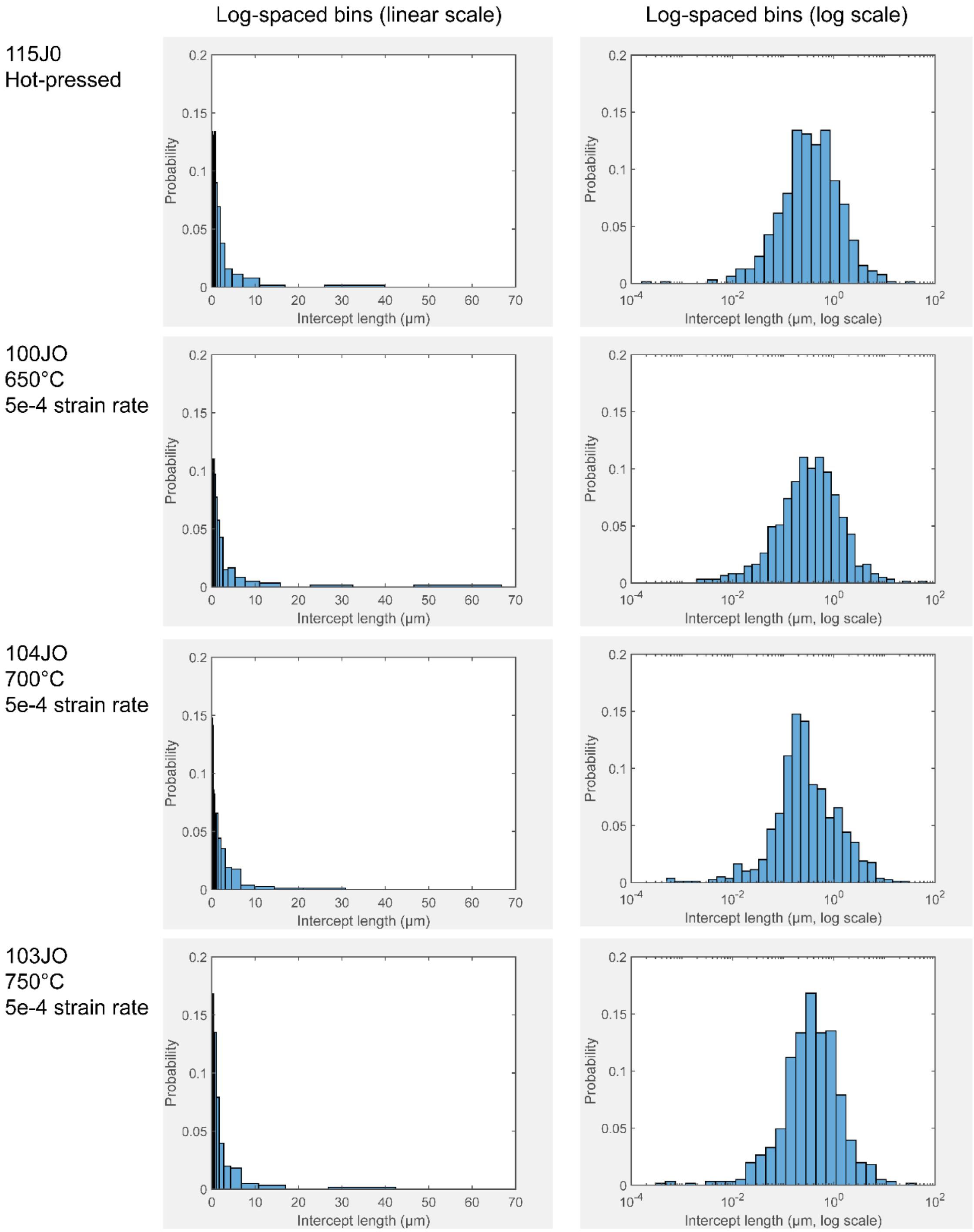

Figure S14. Grain size distributions measured by the linear-intercept method for the hot-pressed sample and samples deformed at 650°C, 700°C, and 750°C at a strain rate of ~5e-4/s shown as log-spaced bins on a linear scale (left) and log scale (right; after Hansen et al., 2011). Samples deformed at higher temperatures show increasing fractions of smaller (recrystallized) grains while the distributions display only minor differences.

Figure S15.

Sodic-amphiboles classification diagram

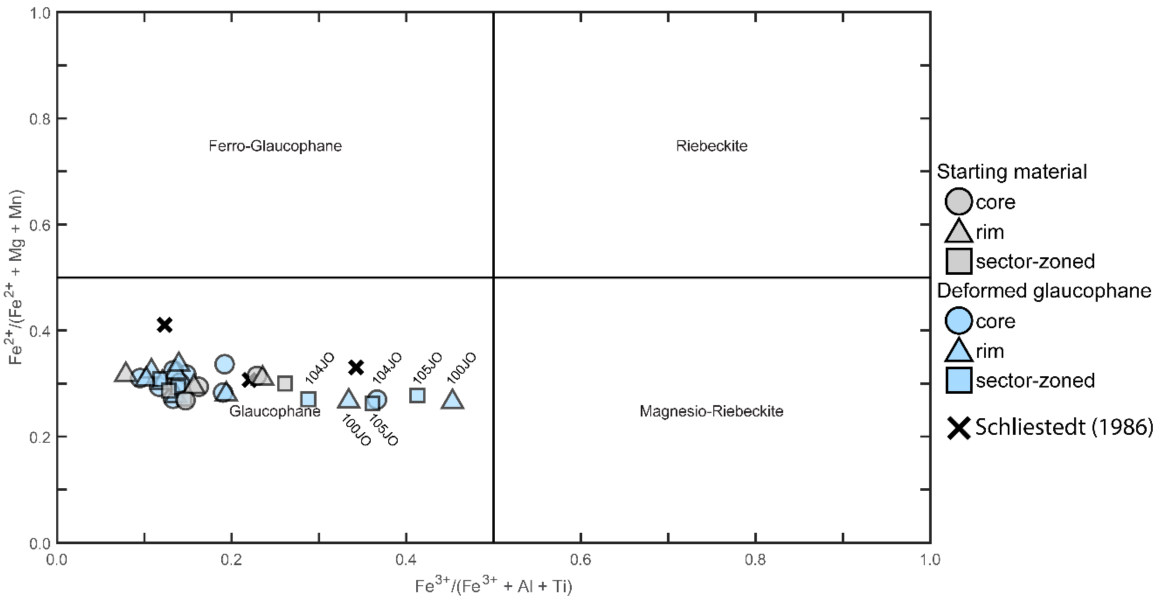

Figure S15. Electron microprobe analysis (EMPA) measured compositions of glaucophane starting material and deformation experiment products with reported glaucophane compositions of Schliestedt (1986). Compositions are reported in Table S1.

Figure S16. Glaucophane deformation experiment 102JO

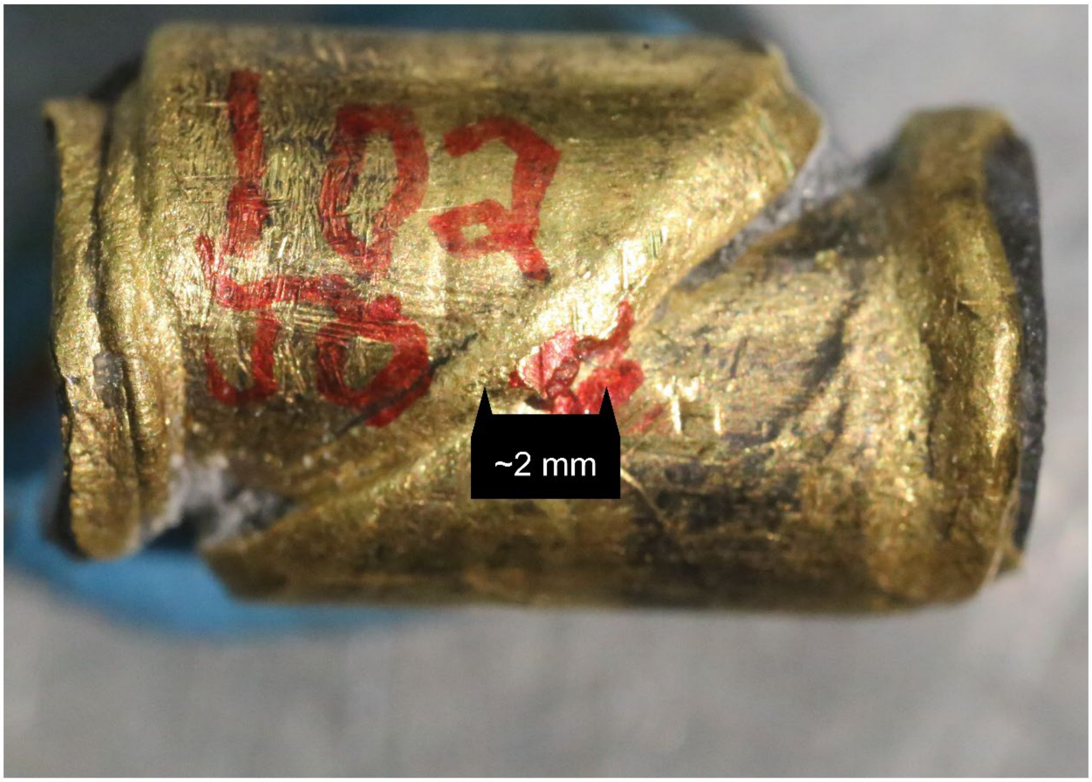

Figure S16. Recovered sample deformed at 650°C and ~5e-5/s (102JO) displaying approximately 2 mm of offset between the final position of the thermocouple tip and the center of the shear zone.

Table S1: Electron Microprobe Measured Compositions of Glaucophane Experimental Products

													Recalculated	
No.	T(°C)	SiO_2	TiO_2	Al_2O_3	Cr_2O_3	*FeO	MnO	MgO	CaO	Na_2O	K_2O	Total	*FeO	*Fe_2O_3
105JO_1c	700	57.72	0.00	9.63	0.00	11.86	0.04	10.91	0.64	7.56	0.02	98.38	9.63	9.63
105JO_1r	700	57.70	0.00	9.88	0.00	11.73	0.03	10.81	0.71	7.49	0.02	98.37	9.66	2.30
105JO_2a	700	58.15	0.00	10.10	0.00	11.07	0.03	11.25	0.60	7.58	0.02	98.80	8.90	2.41
105JO_2b	700	58.79	0.00	6.15	0.03	15.46	0.10	11.69	0.44	6.04	0.05	98.74	9.37	6.77
105JO_3a	700	57.96	0.00	10.47	0.00	10.96	0.05	10.81	0.45	7.59	0.01	98.30	9.08	2.09
105JO_3b	700	58.05	0.00	7.03	0.00	13.41	0.06	11.83	0.45	7.73	0.03	98.59	8.00	6.02
105JO_4c	700	57.77	0.00	9.93	0.00	11.83	0.04	10.49	0.19	7.48	0.01	97.74	9.74	2.33
105JO_4r	700	58.31	0.00	9.91	0.00	12.03	0.01	10.39	0.22	7.71	0.01	98.59	9.82	2.46
100JO_1c	650	57.19	0.03	10.09	0.09	10.30	0.04	11.74	1.19	7.40	0.04	98.10	8.33	2.19
100JO_1r	650	57.75	0.06	10.07	0.07	11.15	0.02	10.55	0.31	7.65	0.00	97.63	9.47	1.87
100JO_2c	650	57.38	0.00	9.11	0.04	12.78	0.06	10.28	0.43	7.35	0.03	97.46	9.82	3.29
100JO_2r	650	57.60	0.00	6.38	0.11	14.79	0.04	11.16	0.17	7.52	0.02	97.80	7.55	8.05
100JO_3c	650	57.64	0.01	9.41	0.04	11.28	0.06	11.27	0.61	7.73	0.04	98.09	9.22	2.29
100JO_3r	650	57.86	0.01	6.18	0.03	15.46	0.08	12.32	0.43	5.47	0.03	97.87	11.09	4.86
100JO_4c	650	55.55	0.00	9.59	0.09	10.09	0.03	10.63	0.62	7.02	0.03	93.65	8.36	1.93
100JO_4r	650	57.14	0.00	9.96	0.05	10.38	0.04	11.41	0.76	7.44	0.03	97.22	8.32	2.28
104JO_1c	650	57.27	0.11	8.62	0.00	11.72	0.02	11.67	0.69	7.65	0.01	97.76	9.01	3.01
104JO_1r	650	57.77	0.04	8.90	0.00	11.72	0.03	11.59	0.68	7.40	0.01	98.15	8.84	3.20
104JO_2c	650	57.64	0.03	10.78	0.00	10.58	0.03	10.81	0.37	7.93	0.00	98.17	9.08	1.66
104JO_2r	650	57.82	0.01	10.49	0.00	10.86	0.04	10.86	0.35	7.61	0.00	98.03	8.94	2.14
104JO_3a	650	56.40	0.01	9.90	0.00	10.34	0.05	11.50	1.03	7.29	0.01	96.53	8.18	2.40
104JO_3b	650	57.35	0.12	7.16	0.00	13.50	0.08	12.01	1.06	6.51	0.03	97.82	9.54	4.40
104JO_4c	650	56.33	0.00	6.78	0.00	14.76	0.05	12.12	0.39	7.42	0.02	97.87	9.91	5.39
104JO_4r	650	57.79	0.00	10.46	0.00	10.60	0.03	10.78	0.23	7.82	0.00	97.71	8.99	1.79
115JO_1c		57.47	0.03	9.53	0.00	11.52	0.02	11.32	0.79	7.49	0.02	98.19	9.09	2.70
115JO_1r		57.37	0.07	9.70	0.00	11.46	0.04	11.42	0.74	7.80	0.02	98.62	9.14	2.58
115JO_2a		58.34	0.07	7.55	0.00	14.24	0.05	11.34	0.36	6.06	0.07	98.08	10.46	4.20
115JO_2b		57.89	0.07	10.27	0.00	10.65	0.04	11.28	0.60	7.60	0.02	98.41	8.65	2.22
115JO_3c		56.98	0.00	8.33	0.00	13.29	0.06	11.39	1.30	7.31	0.04	98.69	10.15	3.48
115JO_3r		56.93	0.01	8.40	0.00	13.27	0.06	11.41	1.27	7.28	0.03	98.66	10.01	3.62
115JO_4c		57.35	0.00	10.20	0.02	10.52	0.02	11.73	1.12	7.37	0.03	98.36	8.29	2.48
115JO_4r		58.17	0.01	10.50	0.00	10.48	0.05	10.84	0.37	7.92	0.02	98.35	9.26	1.36

**Measured FeO used to recalculate FeO and Fe_2O_3 in MinPlotX from amphibole stoichiometry (Walters & Gies, 2025)*

Measured Compositions of Glaucophane Reported in Schliestedt (1986)

No.	SiO_2	TiO_2	Al_2O_3	FeO	Fe_2O_3	MgO	CaO	Na_2O	Total
303	57.6	0	8.9	7.2	5.75	10.7	0.5	7.30	97.95
360 (core)	56.5	0	7.5	7.8	7.65	10.0	0.4	7.05	96.90
360 (rim)	56.9	0	10.1	10.2	3.35	8.8	0.2	7.40	96.95

References

Bachmann, F., Hielscher, R., & Schaeben, H. (2010). Texture Analysis with MTEX – Free and Open Source Software Toolbox. *Solid State Phenomena*, *160*, 63–68. https://doi.org/10.4028/www.scientific.net/SSP.160.63

Ghaffari, H. O., & Pec, M. (2020). An ultrasound probe array for a high-pressure, high-temperature solid medium deformation apparatus. *Review of Scientific Instruments*, *91*(8), 085117. https://doi.org/10.1063/5.0004035

Hansen, L. N., Zimmerman, M. E., & Kohlstedt, D. L. (2011). Grain boundary sliding in San Carlos olivine: Flow law parameters and crystallographic-preferred orientation. *Journal of Geophysical Research: Solid Earth*, *116*(B8). https://doi.org/10.1029/2011JB008220

Hawthorne, F. C., Oberti, R., Harlow, G. E., Maresch, W. V., Martin, R. F., Schumacher, J. C., & Welch, M. D. (2012). Nomenclature of the amphibole supergroup. *American Mineralogist*, *97*(11–12), 2031–2048. https://doi.org/10.2138/am.2012.4276

Heilbronner, R., & Barrett, S. (2014). *Image Analysis in Earth Sciences: Microstructures and Textures of Earth Materials* (pp. 173–185). Berlin, Heidelberg: Springer. https://doi.org/10.1007/978-3-642-10343-8_10

Holyoke, C. W., & Kronenberg, A. K. (2010). Accurate differential stress measurement using the molten salt cell and solid salt assemblies in the Griggs apparatus with applications to strength, piezometers and rheology. *Tectonophysics*, *494*(1), 17–31. https://doi.org/10.1016/j.tecto.2010.08.001

Leake, B. E., Woolley, A. R., Arps, C. E. S., Birch, W. D., Gilbert, M. C., Grice, J. D., et al. (1997). Nomenclature of amphiboles; report of the subcommittee on amphiboles of the International Mineralogical Association, Commission on New Minerals and Mineral Names. *The Canadian Mineralogist*, *35*(1), 219–246.

Mainprice, D., Hielscher, R., & Schaeben, H. (2011). Calculating anisotropic physical properties from texture data using the MTEX open-source package. *Geological Society, London, Special Publications*, *360*(1), 175–192. https://doi.org/10.1144/SP360.10

Michibayashi, K., & Mainprice, D. (2004). The Role of Pre-existing Mechanical Anisotropy on Shear Zone Development within Oceanic Mantle Lithosphere: an Example from the Oman Ophiolite. *Journal of Petrology*, *45*(2), 405–414. https://doi.org/10.1093/petrology/egg099

Ortega-Arroyo, D., O'Ghaffari, H., Peč, M., Gong, Z., Fu, R. R., Ohl, M., et al. (2025). "Lab-Quakes": Quantifying the Complete Energy Budget of High-Pressure Laboratory Failure. *AGU Advances*, *6*(5), e2025AV001683. https://doi.org/10.1029/2025AV001683

Ott, J. N., Condit, C. B., Pec, M., & Journaux, B. (2025). Dislocation creep of glaucophane in mafic blueschists during subduction: Weighted Burgers vector analysis from the Catalina Schist (California, USA). *Geology*, *53*(6), 529–534. https://doi.org/10.1130/G53025.1

Paterson, M. S., & Olgaard, D. L. (2000). Rock deformation tests to large shear strains in torsion. *Journal of Structural Geology*, *22*(9), 1341–1358. https://doi.org/10.1016/S0191-8141(00)00042-0

Pec, M. (2018). newRig (Version Beta). Retrieved from https://mpec.scripts.mit.edu/peclab/software/

Pec, M., & Al Nasser, S. (2021). Formation of Nanocrystalline and Amorphous Materials Causes Parallel Brittle-Viscous Flow of Crustal Rocks: Experiments on Quartz-Feldspar Aggregates. *Journal of Geophysical Research: Solid Earth*, *126*(5), e2020JB021262. https://doi.org/10.1029/2020JB021262

Prior, D. J., Mariani, E., & Wheeler, J. (2009). EBSD in the Earth Sciences: Applications, Common Practice, and Challenges. In A. J. Schwartz, M. Kumar, B. L. Adams, & D. P. Field (Eds.), *Electron Backscatter Diffraction in Materials Science* (pp. 345–360). Boston, MA: Springer US. https://doi.org/10.1007/978-0-387-88136-2_26

Reynard, B., Gillet, P., & Willaime, C. (1989). Deformation mechanisms in naturally deformed glaucophanes: a TEM and HREM study. *European Journal of Mineralogy*, *1*(5), 611–624. https://doi.org/10.1127/ejm/1/5/0611

Ronde, A. A. de. (2004). *Mineral reaction and deformation in Plagioclase-Olivine composites : an experimental study* (Thesis). University_of_Basel. https://doi.org/10.5451/unibas-003550982

Schliestedt, M. (1986). Eclogite-Blueschist Relationships as Evidenced by Mineral Equilibria in the High-Pressure Metabasic Rocks of Sifnos (Cycladic Islands), Greece. *Journal of Petrology*, *27*(6), 1437–1459. https://doi.org/10.1093/petrology/27.6.1437

Walters, J. B., & Gies, N. B. (2025). MinPlotX: A powerful tool for formula recalculation, visualization, and comparison of large mineral compositional datasets. *Mineralogia*, *56*(1), 13–22. https://doi.org/10.2478/mipo-2025-0003

Wheeler, J., Piazolo, S., Prior, D. J., Trimby, P. W., & Tielke, J. A. (2024). Using crystal-lattice distortion data for geological investigations: the weighted Burgers vector method. *Journal of Structural Geology*, *179*, 105040. https://doi.org/10.1016/j.jsg.2023.105040

Appendix 4. Supporting Information for Chapter 5: Constraining the Nature and Significance of an Exhumed Blueschist-Eclogite Transition, Sifnos Island, Greece

Figure S1. (a) Si-in-phengite compositional isopleths extracted from Perple_X pseudosection model for the bulk composition of the blueschist sample (V01a in Table 2). (b) Si-in-phengite compositional isopleths extracted from Perple_X pseudosection model for the bulk composition of the eclogite sample (V01d in Table 2).

a Si-in-phengite isopleths: blueschist V01a

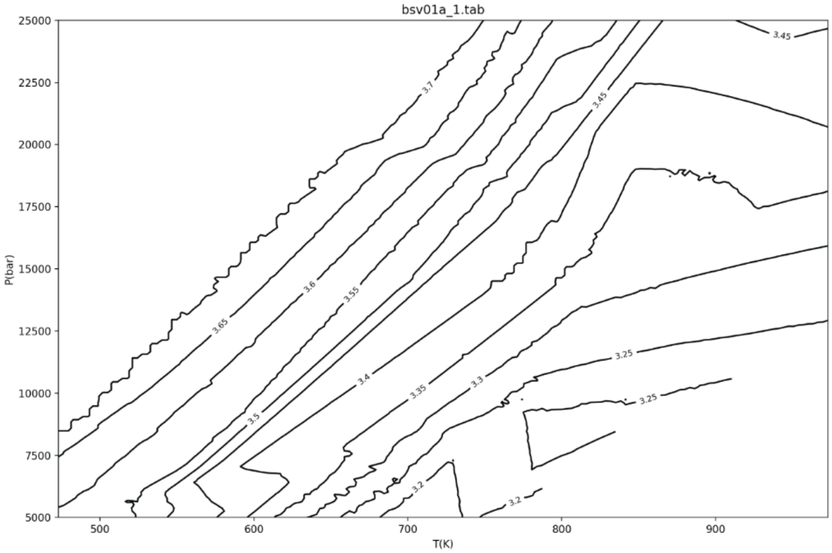

V01a modeled composition:

SiO2	51.69
TiO2	0.88
Al2O3	17.64
FeO	6.18
Fe2O3	9.52
MnO	0.12
MgO	5.71
CaO	6.09
Na2O	3.06
K2O	4.37

b Si-in-phengite isopleths: eclogite V01d

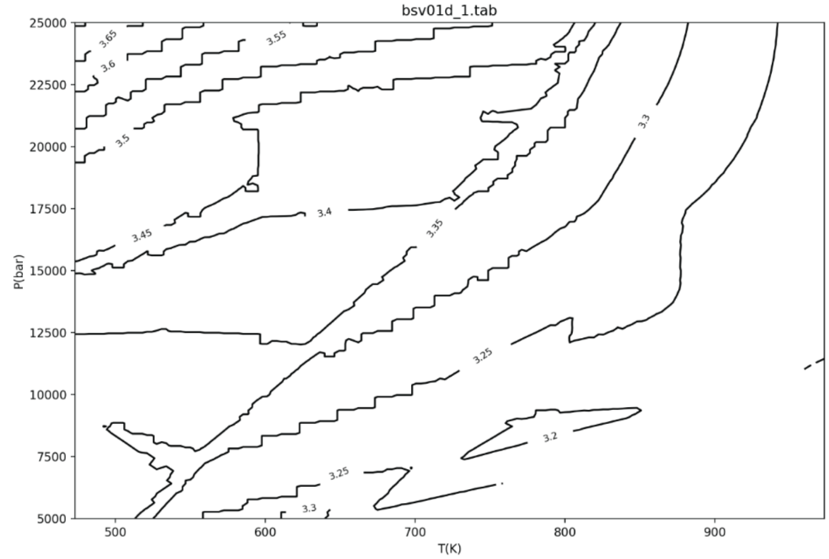

V01d modeled composition:

SiO2	49.58
TiO2	0.86
Al2O3	17.40
FeO	5.66
Fe2O3	10.12
MnO	0.09
MgO	4.24
CaO	8.98
Na2O	3.85
K2O	3.66